



University  
of Glasgow

Wright, Paul James (2019) *The energetics of small solar flares and brightenings*. PhD thesis.

<https://theses.gla.ac.uk/41187/>

Copyright and moral rights for this work are retained by the author

A copy can be downloaded for personal non-commercial research or study, without prior permission or charge

This work cannot be reproduced or quoted extensively from without first obtaining permission in writing from the author

The content must not be changed in any way or sold commercially in any format or medium without the formal permission of the author

When referring to this work, full bibliographic details including the author, title, awarding institution and date of the thesis must be given

Enlighten: Theses

<https://theses.gla.ac.uk/>  
[research-enlighten@glasgow.ac.uk](mailto:research-enlighten@glasgow.ac.uk)

# The Energetics of Small Solar Flares and Brightenings

**Paul James Wright**  
MPhys (Soton)

Astronomy and Astrophysics Group  
School of Physics and Astronomy  
Kelvin Building  
University of Glasgow  
Glasgow, G12 8QQ  
Scotland, U.K.



University  
of Glasgow

Presented for the degree of  
Doctor of Philosophy  
The University of Glasgow  
2019

---

This thesis is my own composition except where indicated in the text.  
No part of this thesis has been submitted elsewhere for any other degree  
or qualification.

**Copyright © 2019 by Paul James Wright**

14th April 2019

---

*She dreams in colour, she dreams in loadct, 39*

# Acknowledgements

Throughout my PhD studies, I have received a wide range of help and support. First and foremost I must extend a heartfelt thanks to Dr Iain Hannah. It has been a pleasure to be your first PhD student, and to have you as my primary supervisor. We have undoubtedly learned a lot, and without your patience, this work would have not been possible. Dr Alec Mackinnon, thank you for being my secondary supervisor and reading through the final chapters of this thesis. I must also thank my internal and external examiners, Professor Lyndsay Fletcher and Professor Robert Walsh.

On a more personal note, it goes without saying that this journey would not have been nearly as enjoyable if it wasn't for the colleagues and friends. Thank you to all of you in 604 (and 614/616), you are all highly talented individuals who will no doubt go on to do amazing things. It has been a true pleasure. It is true what they say: People Make Glasgow.

Thank you, Ben, Stephen, and Tony. You were the best cohort I could have asked for, and the most easily convinced to come to the pub! Ben & Jenni, Alasdair & Lindsey, thank you for inviting me to your weddings. I will never forget the feeling of sitting in the backseat of that car from Tavistock to Bristol and flying through the Lake District in my Fiat Panda days after passing my driving test.

Dina, you have an incredible heart. It's a pleasure to be able to call you my academic sister, and I look forward to seeing you defend your thesis and graduate. Kyle, I will miss hearing your constant huffing and puffing and your affectionately named "Kyle problems". A bit of cardio once in a while won't kill you. Juntao, shine on you crazy diamond.

Paulo, thank you for the continual advice and conversation while coming to getting coffee throughout the day. You are one of the kindest people I have ever met. Natasha, you were the best office mate I could have asked for. You provided endless advice,

support, and a tropical climate in dreary Scotland. You both have admirable work ethics, and I am delighted to see you both move on to better things!

To those of you outside of Glasgow: my undergraduate friends in Southampton, my undergraduate tutor Professor Malcolm Coe, and my friends and colleagues at the Harvard-Smithsonian Center for Astrophysics; NASA Goddard Space Flight Center; SETI; Lockheed Martin; and elsewhere, thank you for helping me get where I am today.

Finally, Mum and Dad, thank you for your patience and support.

# Abstract

This thesis concentrates on a long-standing problem in heliophysics—the coronal heating problem. The work in this thesis investigates this problem in two main ways. The first has been to initiate the novel, yet highly successful, approach of trying to observe the smallest distinguishable heating events with a highly sensitive hard X-ray telescope, optimised for targets outside of the solar system (*NuSTAR*; Chapters 4, 5); the second approach has been to study the unresolved ensemble of even smaller events by studying the properties of pixel-level time series (Chapters 6, 7, 8).

Chapter 1 provides a background of the coronal heating problem, with specific emphasis on the observational signatures of nanoflare heating. This is followed by an overview of the advancements of coronal imaging and spectroscopy, and the instruments used throughout this thesis are introduced (Chapter 2). Chapter 3 introduces the basics of atomic line spectroscopy and the concept of the differential emission measure. A number of techniques that are utilised throughout this thesis to recover the thermal properties of the corona are described and demonstrated with both spectroscopic and narrowband EUV observations.

Chapter 4 provides an introduction to the *NuSTAR* hard X-ray astrophysics telescope. While *NuSTAR* is an astrophysics mission, this chapter demonstrates that *NuSTAR* is able to provide scientifically useful observations of the Sun, and these observations have advanced our understanding of various coronal phenomena including active region microflares. Chapter 5 presents observations and analysis of the first *NuSTAR* microflare where the combination of *SDO/AIA*, *Hinode/XRT*, and *NuSTAR* observations have allowed the differential emission measure to be constrained over an unprecedented temperature range. While no non-thermal emission was observed in this microflare, upper-limits consistent with a null detection are derived, and thermal energetics are discussed.

From Chapter 6, this thesis concentrates on the unresolved nanoflare ensemble. Chapter 6 describes the concept of time-lag analysis, a technique to determine the temporal offset of two channels by investigating EUV light curves from *SDO/AIA*. Time-lag analysis is presented on a number of active region features and the 94 Å (Fe XVIII) – 335 Å time-lag is introduced in order to separate the hot and cool components of the *SDO/AIA* 94 Å channel. Chapter 7 builds on the work of Chapter 6 by introducing the concept EM time-lag analysis, where time-lag analysis is performed on the emission measure distribution in order to understand if the *true* time-lag signature (in temperature) is masked by the multi-thermal nature of *SDO/AIA*. For the channel pair used within this chapter, EM time-lag analysis appears to generally agree with *SDO/AIA* time-lag analysis however, there are a number of differences that will be discussed.

Finally, Chapter 8 presents a test case demonstration of wavelet analysis on EUV time series. Wavelet analysis is first introduced, followed by wavelet coherency, and local intermittency measure, each of which could be valuable tools in the search for the signatures of the coronal heating mechanism.

# Contents

<b>Acknowledgements</b>	<b>iii</b>
<b>Abstract</b>	<b>v</b>
<b>List of Figures</b>	<b>xii</b>
<b>List of Tables</b>	<b>xviii</b>
<b>1 Introduction</b>	<b>1</b>
1.1 The Sun's Atmosphere . . . . .	1
1.1.1 Heating Mechanisms . . . . .	2
1.2 Solar Flares . . . . .	4
1.3 Nanoflares . . . . .	6
1.3.1 Modelling . . . . .	6
1.3.2 High <i>vs.</i> Low Frequency . . . . .	7
1.3.3 Observations . . . . .	8
1.3.3.1 Low-Temperature EM slope . . . . .	10
1.3.3.2 High-Temperature (> 5 MK) Emission . . . . .	10
1.3.3.3 Doppler Shifts . . . . .	12
1.3.3.4 Time Series Analysis . . . . .	12
<b>2 The Current Picture of Multi-thermal Observations of an Active Region</b>	<b>14</b>
2.1 EUV Observations . . . . .	14
2.1.1 <i>Hinode's</i> Extreme-Ultraviolet Imaging Spectrometer . . . . .	16
2.1.2 <i>Solar Dynamics Observatory's</i> Atmospheric Imaging Assembly . . . . .	18
2.1.3 Sounding Rockets & Future Missions . . . . .	19
2.2 Soft X-ray Observations . . . . .	22

2.2.1	<i>Hinode</i> X-Ray Telescope ( <i>Hinode</i> /XRT) . . . . .	24
2.2.2	Sounding Rockets & Future Missions . . . . .	25
2.3	Hard X-Ray Observations . . . . .	27
2.3.1	Advancements in Hard X-Ray Observations . . . . .	28
2.4	Summary . . . . .	29
<b>3</b>	<b>Temperature Diagnostics</b> . . . . .	<b>30</b>
3.1	Spectral Lines . . . . .	30
3.2	Differential Emission Measure (DEM) . . . . .	32
3.2.1	Inverse Problems . . . . .	35
3.2.2	A Direct Approach . . . . .	37
3.3	Difficulties in Reconstructing the DEM . . . . .	40
3.4	DEM Reconstruction Techniques . . . . .	41
3.4.1	Tikhonov Regularised Inversion (RI) . . . . .	42
3.4.1.1	Error Estimation . . . . .	43
3.4.1.2	Tikhonov Regularisation DEM Examples . . . . .	44
3.4.2	Iterative Least-Squares Approach . . . . .	49
3.4.2.1	Error Estimation . . . . .	49
3.4.2.2	Iterative Least-Squares DEM Examples . . . . .	49
3.4.3	Markov-Chain Monte-Carlo MCMC[M] . . . . .	54
3.4.4	Basis Pursuit . . . . .	55
3.4.4.1	Basis Functions . . . . .	56
3.4.4.2	The Method . . . . .	57
3.4.4.3	Basis Pursuit DEM Examples . . . . .	58
3.5	Summary . . . . .	61
<b>4</b>	<b><i>NuSTAR</i> Hard X-ray Imaging Spectroscopy</b> . . . . .	<b>62</b>
4.1	Overview . . . . .	62
4.2	<i>NuSTAR</i> Instrument . . . . .	65
4.2.1	Focusing Optics . . . . .	65
4.2.1.1	Wolter-Type Telescopes . . . . .	67
4.2.1.2	Ghost-Rays & Stray Light . . . . .	69
4.2.2	Detectors . . . . .	71
4.2.2.1	Detector & Electronics Throughput . . . . .	73

4.2.2.2	GRADE . . . . .	74
4.2.2.3	Pileup . . . . .	75
4.2.3	Astrometric Alignment . . . . .	76
4.3	Data Processing . . . . .	76
4.3.1	NuSTARDAS . . . . .	76
4.4	Overview of <i>NuSTAR</i> Solar Science Goals, Observations, and Results . . . . .	78
4.4.1	<i>NuSTAR</i> Solar Science Goals . . . . .	78
4.4.2	<i>NuSTAR</i> Solar Observations . . . . .	79
4.4.2.1	September 10, 2014 . . . . .	81
4.4.2.2	November 1, 2014 . . . . .	81
4.4.2.3	December 11, 2014 . . . . .	83
4.4.2.4	April 25, 2015 & September 2, 2015 . . . . .	85
4.4.2.5	Further Observations: 2016 - Present . . . . .	86
4.5	Summary . . . . .	87
<b>5</b>	<b>The First <i>NuSTAR</i> Microflare</b> . . . . .	<b>89</b>
5.1	<i>SDO/AIA</i> and <i>Hinode/XRT</i> Event Overview . . . . .	90
5.2	<i>NuSTAR</i> Event Overview . . . . .	95
5.3	<i>NuSTAR</i> Data Analysis . . . . .	97
5.3.1	<i>NuSTAR</i> Spectral Fitting . . . . .	99
5.4	Multi-thermal Microflare Emission . . . . .	102
5.4.1	Comparison of <i>NuSTAR</i> , <i>Hinode/XRT</i> & <i>SDO/AIA</i> . . . . .	102
5.4.2	Differential Emission Measure . . . . .	105
5.5	Microflare Energetics . . . . .	109
5.5.1	Thermal Energy . . . . .	109
5.5.2	<i>NuSTAR</i> Non-Thermal Limits . . . . .	110
5.6	Discussion and Conclusions . . . . .	113
<b>6</b>	<b>EUV Time Series Analysis</b> . . . . .	<b>116</b>
6.1	Time-Lag Analysis: <i>SDO/AIA</i> . . . . .	117
6.2	Time-Lag Analysis of an Active Region: Example Pixel Time-lags . . . . .	119
6.2.1	<i>SDO/AIA</i> Temperature Response Functions . . . . .	121
6.2.2	Diffuse Emission, Pixel 1, Viall & Klimchuk (2012) . . . . .	123
6.2.3	Active Region Fan Loop, Pixel 2 . . . . .	129

6.2.4	Active Region Core/Loop Pixel, Pixel 3 . . . . .	132
6.2.5	Loop Footpoint, Pixel 4 . . . . .	135
6.2.6	Summary . . . . .	136
6.3	Time-Lag Analysis of an Active Region: Time-Lag Maps . . . . .	138
6.3.1	Further <i>SDO/AIA</i> Channel Pairs . . . . .	142
6.3.2	Discussion . . . . .	143
6.4	Testing with Model Time Series . . . . .	144
6.4.1	EBTEL Diffuse Emission Simulation: Corona . . . . .	144
6.4.1.1	Simulation Setup, <a href="#">Viall &amp; Klimchuk (2013, 2015)</a> . . . . .	146
6.4.2	EBTEL Diffuse Emission Simulation: Transition Region Response	149
6.4.2.1	Further Mechanisms for Zero Time-lags: In-Phase Time Series . . . . .	150
6.4.3	Steady Heating . . . . .	151
6.5	Summary . . . . .	152
<b>7</b>	<b>EM Time Series Analysis</b>	<b>155</b>
7.1	Active Region DEM . . . . .	156
7.1.1	EM (Temperature) Time-lags . . . . .	157
7.1.2	Diffuse Emission Pixel; Pixel 1 . . . . .	162
7.1.3	Active Region Fan Loop; Pixel 2 . . . . .	173
7.1.4	Active Region Core/Loop; Pixel 3 . . . . .	181
7.1.5	Loop Footpoint; Pixel 4 . . . . .	189
7.1.6	Summary . . . . .	195
7.2	Testing with Model Time Series . . . . .	197
7.2.1	EBTEL Diffuse Emission Simulation: Corona . . . . .	197
7.2.2	EBTEL Diffuse Emission Simulation: Transition Region . . . . .	201
7.2.3	Steady Heating “Simulations” . . . . .	203
7.3	Discussions and Conclusions . . . . .	204
7.3.1	Summary . . . . .	208
7.3.2	Further Work: Alternative DEM Methods . . . . .	208
<b>8</b>	<b>Wavelet Analysis</b>	<b>211</b>
8.1	Demonstrating Wavelet Analysis . . . . .	212
8.2	Wavelet Coherence . . . . .	216

---

8.3	Local Intermittency Measure . . . . .	219
8.4	Discussion and Future Work . . . . .	221
<b>9</b>	<b>Conclusions and Future Work</b>	<b>222</b>
9.1	<i>NuSTAR</i> Microflares . . . . .	222
9.2	Time-Lag Analysis . . . . .	223
9.3	EM Time-Lag Analysis . . . . .	225
9.4	Wavelet Analysis . . . . .	230
	<b>Bibliography</b>	<b>232</b>

# List of Figures

1.1	An active region in EUV and X-rays . . . . .	3
1.2	Tangled and twisted magnetic strands . . . . .	4
1.3	Frequency distribution of solar flares . . . . .	5
1.4	Temperature evolution of a coronal strand . . . . .	8
1.5	Various EMD forms of the loop apex . . . . .	9
2.1	NOAA AR 11259 observed with <i>Hinode</i> /EIS . . . . .	17
2.2	NOAA AR 11259 as observed by <i>SDO</i> /AIA . . . . .	19
2.3	<i>SDO</i> /AIA temperature response functions for the six optically-thin EUV filter channels . . . . .	20
2.4	NOAA AR 11259 observed with <i>Hinode</i> /XRT . . . . .	23
2.5	Temperature response functions for the nine <i>Hinode</i> /XRT filters . . . . .	24
2.6	<i>Hinode</i> /EIS and <i>MaGIXS</i> emission lines . . . . .	25
3.1	<i>Hinode</i> /EIS contribution functions, and <i>SDO</i> /AIA temperature response functions . . . . .	36
3.2	<i>Hinode</i> /EIS contribution functions and EM-loci for a multi-thermal plasma	38
3.3	<i>Hinode</i> /EIS EM-loci for two isothermal plasmas . . . . .	40
3.4	Regularised Inversion <i>Hinode</i> /EIS emission measure distribution . . . . .	45
3.5	Regularised Inversion <i>Hinode</i> /EIS $\mathbf{R}_\lambda \mathbf{K}$ matrix . . . . .	45
3.6	Regularised Inversion <i>Hinode</i> /EIS emission measure distributions . . . . .	46
3.7	Regularised Inversion <i>Hinode</i> /EIS $\mathbf{R}_\lambda \mathbf{K}$ matrices . . . . .	46
3.8	Regularised Inversion <i>SDO</i> /AIA emission measure distributions . . . . .	48
3.9	Regularised Inversion <i>SDO</i> /AIA $\mathbf{R}_\lambda \mathbf{K}$ matrix . . . . .	48
3.10	xrt_dem_iterative2.pro <i>SDO</i> /AIA emission measure distribution and $\chi^2$ iterations . . . . .	50

3.11	xrt_dem_iterative2.pro <i>SDO/AIA</i> emission measure distribution and 300 MC iterations . . . . .	51
3.12	xrt_dem_iterative2.pro <i>Hinode/EIS</i> emission measure distribution and $\chi^2$ iterations . . . . .	52
3.13	xrt_dem_iterative2.pro <i>Hinode/EIS</i> emission measure distribution and 300 MC iterations . . . . .	53
3.14	MCMC emission measure distribution with 300 MC iterations . . . . .	54
3.15	Basis Pursuit emission measure distributions for Dirac-delta functions and Gaussians with $a = \{0.1, 0.2, 0.6\}$ . . . . .	59
3.16	Basis Pursuit emission measure distributions for Dirac-delta functions and Gaussians with $a = \{0.1, 0.2\}$ . . . . .	59
3.17	Basis Pursuit emission measure distributions for Dirac-delta functions and Gaussians with $a = \{0.1\}$ . . . . .	59
4.1	Schematics of <i>NuSTAR</i> in the stowed, and deployed configurations, with an accompanying photograph in the stowed formation . . . . .	63
4.2	Photographs of <i>NuSTAR</i> mast, one of the optics modules, and the one of the detector modules . . . . .	64
4.3	Optical constants and reflectance of gold over 0.1 – 10 keV . . . . .	67
4.4	Wolter-I optical configuration . . . . .	68
4.5	Comparison of a microflare observed by <i>RHESSI</i> and <i>FOXSI</i> . . . . .	69
4.6	Various reflection geometries through Wolter-I optics . . . . .	70
4.7	Three <i>NuSTAR</i> solar mosaic observations that display ghost-ray patterns . . . . .	72
4.8	Simulated and observed <i>NuSTAR</i> ghost-ray patterns . . . . .	73
4.9	The $3 \times 3$ pixel morphology of <i>GRADES</i> 0 – 26 . . . . .	75
4.10	Five <i>NuSTAR</i> spectra from <a href="#">Hannah et al. (2016)</a> . . . . .	83
4.11	<i>NuSTAR</i> observations near the limb, <a href="#">Marsh et al. (2017)</a> . . . . .	84
4.12	Time evolution of the 2 – 4, and 4 – 8 keV <i>NuSTAR</i> (FPMA) hard X-ray images from <a href="#">Glesener et al. (2017)</a> . . . . .	86
4.13	Overview of one of the three quiet Sun flares from <a href="#">Kuhar et al. (2018)</a> . . . . .	87
5.1	Combined <i>NuSTAR</i> , <i>SDO/AIA</i> , <i>Hinode/XRT</i> image of the Sun on 29th April 2015 . . . . .	90

5.2	Overview of <i>SDO/AIA</i> 94 Å Fe XVIII and <i>Hinode/XRT</i> during times of <i>NuSTAR</i> observations . . . . .	91
5.3	Comparison of AR 12333 from <i>SDO/AIA</i> and <i>Hinode/XRT</i> at the times of <i>NuSTAR</i> observations . . . . .	93
5.4	Time profiles of the different <i>Hinode/XRT</i> and <i>SDO/AIA</i> channels from the loop region of AR 12333 . . . . .	94
5.5	<i>NuSTAR</i> observation summary . . . . .	95
5.6	<i>NuSTAR</i> mosaics, and co-temporal <i>RHESSI</i> observations on April 29, 2015 . . . . .	96
5.7	<i>NuSTAR</i> 2.5 – 4.5 keV maps for the four time intervals it observed AR 12333 . . . . .	98
5.8	<i>SDO/AIA</i> 94 Å Fe XVIII maps overplotted with shifted contours from <i>Hinode/XRT</i> , and <i>NuSTAR</i> 2.5 – 4.5 keV and 4.5 – 6.5 keV emission) . . . . .	99
5.9	<i>NuSTAR</i> spectra for the regions shown in Figure 5.8, at different stages of flare evolution with time . . . . .	102
5.10	Additional model fits to the <i>NuSTAR</i> spectrum for the impulsive phase of the microflare . . . . .	103
5.11	Comparison of <i>Hinode/XRT</i> and <i>SDO/AIA</i> 94 Å Fe XVIII fluxes during the microflare’s impulsive phase, to the synthetic values obtained from the <i>NuSTAR</i> spectral fit . . . . .	104
5.12	DEMs obtained during the impulsive phase of the microflare . . . . .	106
5.13	DEM obtained during the pre-flare phase . . . . .	107
5.14	EMDs obtained during the pre-flare and impulsive phase of the microflare . . . . .	108
5.15	X-ray flux spectrum . . . . .	111
5.16	Non-thermal upper-limits as a function of $E_c$ and $\delta$ . . . . .	113
6.1	NOAA AR 11082 observed in six <i>SDO/AIA</i> channels . . . . .	120
6.2	<i>SDO/AIA</i> temperature response functions . . . . .	122
6.3	Visualisation of positive time-lags in temperature . . . . .	123
6.4	<i>SDO/AIA</i> light curves for a pixel of diffuse emission, Pixel 1 . . . . .	124
6.5	Cross-correlation value as a function of temporal offset for a pixel of diffuse emission, Pixel 1 . . . . .	125
6.6	NOAA AR 11082 shown for <i>SDO/AIA</i> 94 Å, and <i>SDO/AIA</i> 94 (Fe XVIII) Å . . . . .	126

6.7	Cross-correlation value as a function of temporal offset for a pixel of diffuse emission, Pixel 1 . . . . .	127
6.8	Visualisation of time-lags including the 94 Å (Fe XVIII) – 335 Å channel pair . . . . .	128
6.9	<i>SDO/AIA</i> light curves for a pixel of fan loop emission, Pixel 2 . . . . .	129
6.10	Cross-correlation value as a function of temporal offset for a pixel of fan loop emission, Pixel 2 . . . . .	130
6.11	Cross-correlation value as a function of temporal offset for a pixel of fan loop emission, Pixel 2 . . . . .	131
6.12	<i>SDO/AIA</i> light curves for a pixel of active region core/loop emission, Pixel 3 . . . . .	132
6.13	Cross-correlation value as a function of temporal offset for a pixel of active region core/loop emission, Pixel 3 . . . . .	133
6.14	Cross-correlation value as a function of temporal offset for a pixel of active region core/loop emission, Pixel 3 . . . . .	134
6.15	<i>SDO/AIA</i> light curves for a pixel of fan loop footpoint emission, Pixel 4	135
6.16	Cross-correlation value as a function of temporal offset for a pixel of fan loop footpoint emission, Pixel 4 . . . . .	136
6.17	Summary of time-lag pairs for Pixels (1 – 4) . . . . .	137
6.18	Time-lag maps for the 94 Å – 335 Å and 94 Å (Fe XVIII) – 335 Å channel pairs . . . . .	139
6.19	Time-lag and Cross-correlation histograms for the <i>SDO/AIA</i> 94 Å – 335 Å and the 94 Å (Fe XVIII) – 335 Å channel pairs . . . . .	139
6.20	Cross-Correlation maps for the 94 Å – 335 Å and 94 Å (Fe XVIII) – 335 Å channel pairs . . . . .	140
6.21	Time-lag maps for the 94 Å – 335 Å and 94 Å (Fe XVIII) – 335 Å channel pairs where cross-correlation > 0.2 . . . . .	141
6.22	Time-lag and Cross-correlation histograms for the <i>SDO/AIA</i> 94 Å – 335 Å and the 94 Å (Fe XVIII) – 335 Å channel pairs with cross-correlation values > 0.2 . . . . .	141
6.23	Time-lag maps for six sets of channel pairs . . . . .	143
6.24	Time-lag histograms for six channel pairs . . . . .	144
6.25	Cross-correlation histograms for six channel pairs . . . . .	145

6.26	Cross-correlation value as a function of temporal offset for EBTEL coronal simulations . . . . .	147
6.27	Cross-correlation value as a function of temporal offset for EBTEL (coronal) simulations . . . . .	148
6.28	Cross-correlation value as a function of temporal offset for EBTEL transition region simulations . . . . .	150
6.29	Light curves and cross-correlation value as a function of offset for “steady” light curves . . . . .	152
7.1	<i>SDO</i> /AIA temperature response functions . . . . .	158
7.2	NOAA AR 11082 in six <i>SDO</i> /AIA channels displayed in order of temperature bins ( <b>A</b> – <b>F</b> ) . . . . .	159
7.3	Regularised Inversion DEM maps ( <b>A</b> – <b>F</b> ) . . . . .	160
7.4	<i>SDO</i> /AIA time-lag maps for 193 Å – 171 Å and the EM time-lag map for the corresponding <b>B</b> - <b>C</b> channel pair . . . . .	161
7.5	Light curves of a pixel of diffuse emission, Pixel 1 . . . . .	163
7.6	Cross-correlation value as a function of temporal offset . . . . .	168
7.7	250 × 250 pixel time-lag map for <i>SDO</i> /AIA 193 Å – 171 Å . . . . .	169
7.8	Time-lag maps for <i>SDO</i> /AIA and EM analysis . . . . .	170
7.9	Time-lag maps for <i>SDO</i> /AIA and EM analysis . . . . .	171
7.10	<i>SDO</i> /AIA observations at the start of the two-hour time series . . . . .	171
7.11	Light curves of a pixel from the 8 × 12 pixel region that is seen to have <i>zero</i> time-lags in both <i>SDO</i> /AIA and EM time-lag maps . . . . .	172
7.12	Light curves of a pixel of fan loop emission, Pixel 2 . . . . .	174
7.13	Cross-correlation value as a function of offset for the pixel of fan loop emission, Pixel 2 . . . . .	177
7.14	250 × 250 pixel time-lag map for <i>SDO</i> /AIA 193 Å – 171 Å . . . . .	178
7.15	Time-lag maps for <i>SDO</i> /AIA and EM analysis . . . . .	179
7.16	<i>SDO</i> /AIA images of the rectangular region chosen to encompass the pixel of fan loop emission, Pixel 2 . . . . .	180
7.17	Light curves of a pixel of active region core/loop emission, Pixel 3 . . . . .	182
7.18	Cross-correlation value as a function of offset for the pixel of active region core/loop emission, Pixel 3 . . . . .	185
7.19	250 × 250 pixel time-lag map for <i>SDO</i> /AIA 193 Å – 171 Å . . . . .	186

7.20	Time-lag maps for <i>SDO</i> /AIA and EM analysis . . . . .	187
7.21	<i>SDO</i> /AIA images of the rectangular cutout region chosen to encompass the pixel of core/loop emission, Pixel 3 . . . . .	188
7.22	Light curves for the pixel of fan loop footpoint emission, Pixel 4 . . . . .	190
7.23	Cross-correlation value as a function of offset for the pixel of fan loop footpoint emission, Pixel 4 . . . . .	191
7.24	250 × 250 pixel time-lag map for the observed <i>SDO</i> /AIA 193 Å – 171 Å channel pair . . . . .	192
7.25	Time-lag maps for the pixel of loop footpoint emission, Pixel 4 . . . . .	193
7.26	<i>SDO</i> /AIA 171 Å and 193 Å images for the cutout region shown in Fig- ure 7.24 . . . . .	194
7.27	Cross-correlation value as a function of offset for <i>SDO</i> /AIA EBTEL coronal simulations . . . . .	199
7.28	Cross-correlation value as a function of offset for <i>SDO</i> /AIA EBTEL coronal simulations . . . . .	200
7.29	Cross-correlation value as a function of offset for <i>SDO</i> /AIA EBTEL Transition Region simulations . . . . .	202
7.30	Cross-correlation as a function of offset for “steady” heating simulations	203
7.31	Basis Pursuit DEM maps . . . . .	210
8.1	Wavelet and Fourier analysis of the 155-hour <i>SDO</i> /AIA 335 Å time series	215
8.2	Wavelet coherency and phase between <i>SDO</i> /AIA 193 Å, and 171 Å time series . . . . .	217
8.3	Wavelet Coherency and phase between DEM-synthesised <i>SDO</i> /AIA 193 Å, and 171 Å time series . . . . .	218
8.4	LIM <sup>2</sup> for the 155 hour <i>SDO</i> /AIA 335 Å time series . . . . .	220
9.1	DeepEM temperature maps in comparison to <i>SDO</i> /AIA images and Ba- sis Pursuit temperature maps . . . . .	229

# List of Tables

2.1	List of Key Diagnostic Lines to be Observed by <i>MaGIXS</i> . . . . .	26
3.1	<i>Hinode</i> /EIS Observations of an Active Region Core (Warren <i>et al.</i> , 2012) . . . . .	39
4.1	Summary of <i>NuSTAR</i> & <i>RHESSI</i> Specifications . . . . .	65
5.1	Summary of Thermal Energies of NOAA AR 12333 . . . . .	110

# Chapter 1

## Introduction

The coronal heating problem—understanding how the upper atmosphere of the Sun is heated to, and sustained at temperature over a million degrees Kelvin ( $> 1\text{MK}$ ), while the photosphere below remains at  $\sim 6000\text{ K}$ —remains one of the most prominent challenges in astrophysics. If the assumption is made that the only heating mechanism of the corona is through thermal conduction, a gradual drop-off in temperature would be expected; the temperature of the corona rises a few orders of magnitude over this few hundred kilometre region, and thus the atmosphere must be continuously heated by another process (e.g. [Klimchuk, 2015](#)).

This chapter will briefly introduce the structure of the solar atmosphere in § 1.1 before discussing possible heating mechanisms (§ 1.1.1). This thesis is focused on small heating events by flares, and § 1.2 will provide a general overview of flares, before concentrating on nanoflares (§ 1.3).

### 1.1 The Sun’s Atmosphere

Early spectroscopic observations of the corona revealed unexpected emission lines, thought to be from a new element: “coronium”. These lines were later determined to be from highly ionised (9 – 13-times) Iron ([Grotrian, 1939](#); [Edlén, 1943](#)), and it was clear that the corona was composed of fully ionised high-temperature gas (that interacts with the magnetic field).

The Sun’s atmosphere starts at the photosphere where the temperature is around

$\sim 5700$  K (and is close to being a blackbody radiator), and the opacity to optical light drops to zero. Noticeably, the photosphere contains dark regions on the surface that are known as sunspots and are the locations of strong magnetic fields, and are associated with active regions (§ 1.1). The chromosphere spans  $\sim 2000$  km and is located directly above the photosphere. It is optically thick, sitting at a temperature  $\sim 10^4$  K. Above the chromosphere is the transition region. This region is a thin  $\sim 100$  km layer between the chromosphere and corona over which the temperature rises from  $10^4$  K to 1 MK ( $10^6$  K). The corona is the outermost layer of the Sun, it is a highly non-uniform environment which reflects its magnetic structure. As the plasma- $\beta \ll 0$ , magnetic fields dominate, and the corona consists of *coronal loops* on many scales with both closed and open magnetic field present.

One interesting feature of the solar corona are active regions. These regions are located above groups of sunspots where the magnetic fields are the strongest, and temperatures hottest. Figure 1.1 shows an active region observed at 1 MK (by the Atmospheric Imaging Assembly on-board the *Solar Dynamics Observatory SDO/AIA* Pesnell *et al.*, 2012; Lemen *et al.*, 2012), and at  $> 2$  MK, observed by the X-ray telescope on-board *Hinode* (Kosugi *et al.*, 2007; Golub *et al.*, 2007).

There are a myriad of loops that populate active regions and in the solar corona in general (and are generally thought to consist of fundamental ‘strands’, e.g. Brooks *et al.*, 2012). Patterns in the EUV images called ‘moss’ (Figure 1.1, *left*,  $\sim 1$  MK; Berger *et al.*, 1999; Martens *et al.*, 2000), are the footpoints (where magnetic field lines emerge from the photosphere) of short high-temperature loops that form in the core of the active region, ‘core loops’, which are most easily observed in X-rays (Figure 1.1, *right*). There are also evolving cooler loops surrounding the core most clearly observable at  $\sim 1$  MK, often referred to as ‘EUV loops’, and at the periphery of active regions long-lived fan structures are present.

### 1.1.1 Heating Mechanisms

The exact mechanism behind the multi-million degree corona is most likely the result of multiple heating mechanisms, each of which may dominate in different situations and coronal region: wave heating may dominate in quiet solar corona (McIntosh *et al.*, 2011), and reconnection of braided magnetic field may heat active regions and loops (e.g. Parker, 1983). Regardless of heating mechanism, any model has to be able to

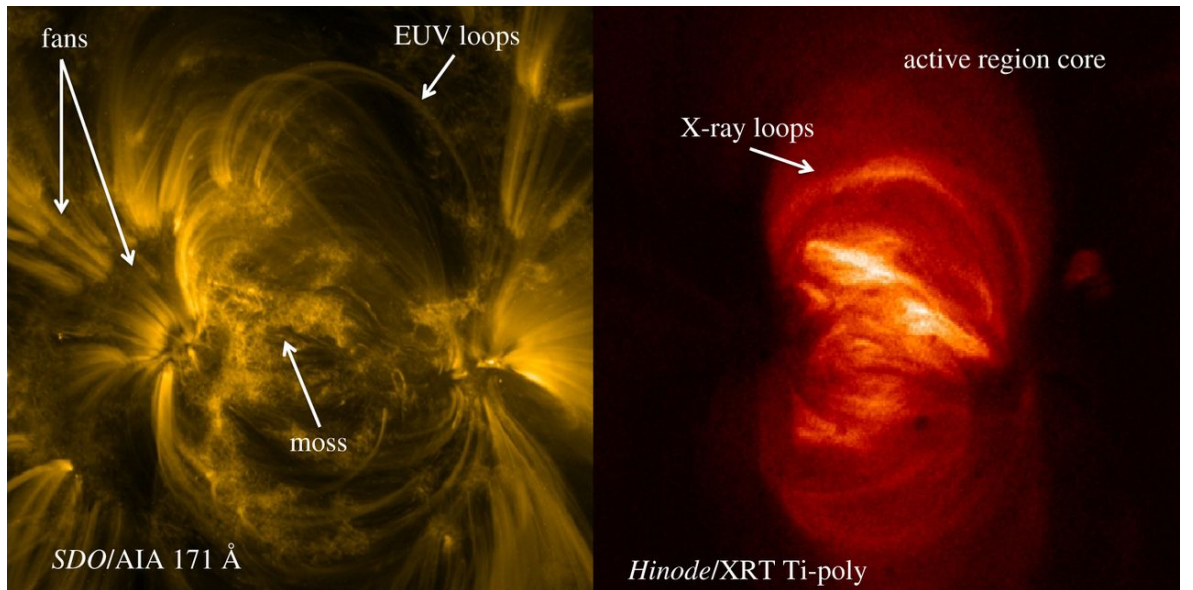


Figure 1.1: *Left:* An example active region in a narrow-band EUV filter centred on  $171 \text{ \AA}$ , 1 MK. *Right:* X-Ray image. Adapted from [Schmelz & Winebarger \(2015\)](#).

sustain the radiative and conductive energy losses that are observed in both active regions and the quiet Sun ([Withbroe & Noyes, 1977](#)). Historically these mechanisms are split in to AC (alternating current), and DC (direct current), where AC refers to the dissipation of waves, and DC refers to magnetic stresses (e.g. [Klimchuk, 2006](#)).

Following the discovery of impulsive hard X-ray events ( $10^{24-27}$  erg, [Lin \*et al.\*, 1984](#)), [Parker \(1988\)](#) proposed the idea of ‘nanoflares’ to heat the corona. These nanoflares, with energies *nine* orders of magnitude smaller than larger flares ( $10^{32}$  erg), were proposed to heat the corona assuming they were occurring sufficiently often.

By gradually stressing the individual magnetic strands threading the corona (see [Figure 1.2](#)), a build up of the energy stored in the field would occur until the energy is released by reconnection—a topological change of magnetic field resulting in a lower energy state. In the largest solar flares this reconnection then leads to direct heating, bulk motion, and particle acceleration. The non-thermal particles will lose their energy to the background plasma via Coulomb collisions, heating the material. If this is also present in the smallest events these nanoflares would then provide intermittent energy input that would appear to steadily heat the corona and we would also expect to observe similar, yet smaller, non-thermal signatures as present in the largest flares. Recently, observations from *Hi-C* (§ 2.1.3) have observed such braiding in an active

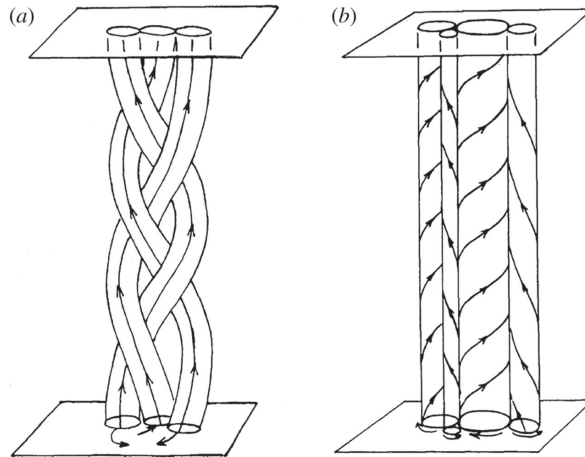


Figure 1.2: Tangled (a) and twisted (b) magnetic strands. This Figure is reproduced from [Parker \(1983\)](#).

region ([Cirtain \*et al.\*, 2013](#)).

## 1.2 Solar Flares

Solar flares are rapid releases of energy in the corona and are typically characterised by impulsive emission in hard X-rays (HXRs;  $> 10$  keV) followed by brightening in soft X-rays (SXR) and extreme ultraviolet (EUV) indicating that electrons have been accelerated as well as material heated. Solar flares are observed to occur over many orders of magnitude, with the largest events releasing up to  $10^{32}$  erg ([Fletcher \*et al.\*, 2011](#)).

The classification of solar flares is based upon the peak SXR flux obtained by *GOES* in the  $1-8 \text{ \AA}$  range, and are classified over *six* orders of magnitude from X-class ( $> 10^{-4} \text{ W m}^{-2}$ ) down to A/B-class microflares. What is particularly important for heating of the solar corona is that smaller flares are observed to occur considerably more often than large flares with their frequency distribution behaving as a negative power-law ([Hudson, 1991](#)). This is described as

$$\frac{dN}{dW} \sim W^{-\alpha}, \quad (1.1)$$

where  $N$  is the number of events and  $W$  is the flare energy.

Figure 1.3 shows the flare frequency distribution of flares and microflares as a function of thermal energy, as observed by many different authors. This flare frequency dis-

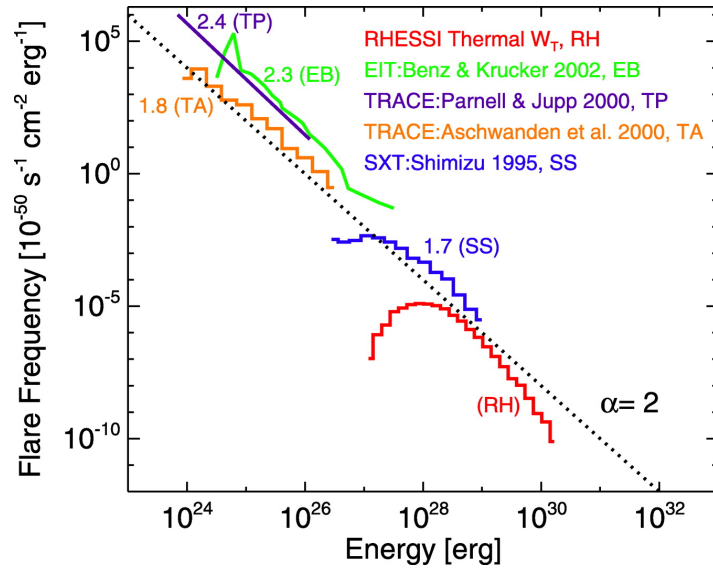


Figure 1.3: Flare frequency distribution as a function of thermal energy for observations from *SOHO*/EIT (Benz & Krucker, 2002); *TRACE* (Parnell & Jupp, 2000; Aschwanden *et al.*, 2000); *Yohkoh*/SXT (Shimizu, 1995); and *RHESSI* (Hannah *et al.*, 2008). For each study  $\alpha$  is provided, and a dotted line indicates  $\alpha = 2$ . This Figure is from Hannah *et al.* (2008).

tribution is shown for observations from *SOHO*/EIT (Benz & Krucker, 2002); *TRACE* (Parnell & Jupp, 2000; Aschwanden *et al.*, 2000); *Yohkoh*/SXT (Shimizu, 1995); and *RHESSI* (Hannah *et al.*, 2008). The left of the distribution has been obtained in the EUV and SXR from quiet Sun observations, while the HXR study by Hannah *et al.* (2008) concentrates on active region events.

The reported power-law indices for each distribution is seen to range from  $2.7 < \alpha < 1.5$ , and these distributions are taken from different instruments, using different detection routines, where different energies have been determined, and assumptions made (see Parnell & De Moortel, 2012). It is therefore not completely clear if small flares heat the corona, and an important point is that Parnell (2004) were able to determine 1200 different power-law index values (derived for both the quiet Sun and active regions) where these power-law indices range from  $-2.5 < \alpha < -1.6$ . It is not immediately clear how small flares can be, and if the flare frequency distribution is steep enough (requiring  $\alpha > 2$ , Hudson, 1991) so that there are enough small events to keep the solar atmosphere consistently heated, but what is clear is that this may not be the best method to determine if nanoflares do indeed heat the corona.

The most comprehensive study used five years of observations of flares and microflares in the hard X-rays from *RHESSI* (*Reuven Ramaty High Energy Solar Spectroscopic Imager*; Lin *et al.*, 2002). *RHESSI* observations have shown that microflares occur exclusively in active regions, like larger flares, as well as heating material  $> 10$  MK and accelerating electrons to  $> 10$  keV (Christe *et al.*, 2008; Hannah *et al.*, 2008, 2011). Although energetically these events are about *six* orders of magnitude smaller than large flares it shows that the same physical processes are at work to impulsively release energy.

Prior to the launch of the *Nuclear Spectroscopic Telescope Array* (*NuSTAR*, Harrison *et al.*, 2013, Chapter 4) satellite there had only been limited SXR spectroscopic observations from *SphinX* (Gburek *et al.*, 2011) or indirect evidence of non-thermal emission from *IRIS* observations (e.g. Testa *et al.*, 2014) from flares beyond *RHESSI*'s sensitivity. There is now increasing number of hard X-ray microflare observations of events smaller than GOES A-class (see Chapter 4.4.2), and it is crucial to probe how small flares can be while still remaining distinct, and how their properties relate to flares and microflares in order to further understand their contribution to coronal heating.

## 1.3 Nanoflares

### 1.3.1 Modelling

Popular methods for modelling coronal loops involve a number of 0-D and 1-D hydrodynamic codes such as the 1-D HYDRAD code (Bradshaw & Cargill, 2013), and there are other approaches in the literature (e.g. Peres, 2000; Warren *et al.*, 2002; Ugarte-Urra *et al.*, 2006; Sarkar & Walsh, 2008). One method that has been extensively used to model the coronal (and transition region) response to nanoflare heating is the Enthalpy-Based Thermal Evolution of Loops, EBTEL (Klimchuk *et al.*, 2008; Cargill *et al.*, 2012; Cargill *et al.*, 2012).

EBTEL is a 0-D hydrodynamics code where “0-D” refers to the lack of spatial resolution, and the general assumptions are that the density, pressure, and temperature can be defined as the spatial averages. Such simulations are important as they are computationally efficient which allows the parameter space to be explored efficiently. As described in Klimchuk *et al.* (2008), the basic idea behind EBTEL is to equate an

enthalpy flux of evaporating or condensing plasma with any excess or deficit in the heat flux relative to the transition region radiation loss rate. An excess heat flux drives evaporative upflows, while a deficient heat flux is compensated for by condensation downflows (see Klimchuk *et al.*, 2008). EBTEL was originally developed by Klimchuk *et al.* (2008) as an improvement to the cooling model of Cargill (1994). EBTEL accommodates any time-dependent heating profile, can include background heating, and accounts for both thermal conduction and radiation throughout the evolution (in contrast, the Cargill model assumes that only one operates at any time). Furthermore, EBTEL has options for non-thermal electron beam heating, and finally, EBTEL is unique in that it provides both the time-dependent DEM of the transition region footpoints in addition to the coronal DEM which is important to the work in this thesis (see Chapter 6).

### 1.3.2 High *vs.* Low Frequency

The frequency at which coronal loops are heated is still a matter of debate, and the frequency of heating is important as it strongly influences both the instantaneous and time-averaged properties of the plasma.

The difference between the two scenarios is the time between successive reheating events ( $\tau_{reheat}$ ) compared to the plasma cooling time ( $\tau_{cool}$ ; the time for the plasma to cool via radiation and conduction). There are two extreme examples: the high-frequency ( $\tau_{reheat} \ll \tau_{cool}$ ), and low frequency ( $\tau_{reheat} \gg \tau_{cool}$ ) scenarios, where both are heated by nanoflares at different frequencies.

Figure 1.4 shows the temporal evolution of the coronal strand in the high-frequency (*left*) and low-frequency (*right*) scenarios. In the high-frequency scenario (see Figure 1.4(a)) the time between successive reheating events is insignificant compared to the time it takes the strand to cool, and as such the temperature fluctuates around a mean value. This would imply that the temperature distribution of the plasma would be narrow. Conversely, in the low frequency scenario (see Figure 1.4(b)) the time between successive heating events is significant, and the plasma has time to cool before being reheated. It is clear that there would be a much wider range of plasma temperature in this scenario (Figure 1.4(b)), with a substantial amount of material at cooler temperatures (Mulu-Moore *et al.*, 2011; Tripathi *et al.*, 2011; Bradshaw *et al.*, 2012; Reep *et al.*, 2013; Cargill, 2014).

### 1.3.3 Observations

As direct observations of the heating process are not yet possible—these events happen on scales much smaller than the resolvable limits with the present-day instrumentation—studies use indirect methods to try understand the heating process.

One of the methods to study the heating of the plasma is to study the so-called *differential emission measure* (DEM, Chapter 3). While DEM inversion, and the methods to perform this inversion are discussed in detail in Chapter 3, the DEM provides an insight in to the temperature distribution of the corona, and is a measure of the squared electron density  $n_e(T)$  along the line-of-sight,  $h$ :

$$\text{DEM} = \xi(T) = n_e^2 \frac{dh}{dT} [\text{cm}^{-5}\text{K}^{-1}] \quad (1.2)$$

and it is also possible to use the *emission measure distribution* (EMD) interchangeably

$$\text{EMD} = \xi(T) dT = n_e^2 dh [\text{cm}^{-5}] \quad (1.3)$$

The shape of the EMD is a powerful tool to constrain heating mechanisms. Unfortunately however, recovery of the DEM (and therefore the EMD) is an ill-posed inversion problem, and there are a large number of solutions that will recover the observed data. Regardless, with sufficient spectroscopic observations over a wide range

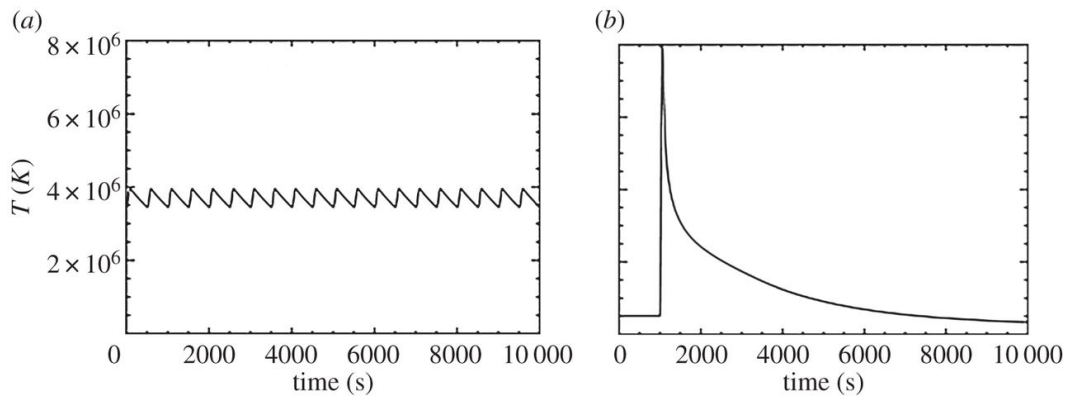


Figure 1.4: Temperature evolution of a coronal strand heated by (a) high-frequency and (b) low frequency nanoflares computed with EBTEL. This Figure is adapted from Klimchuk, 2015.

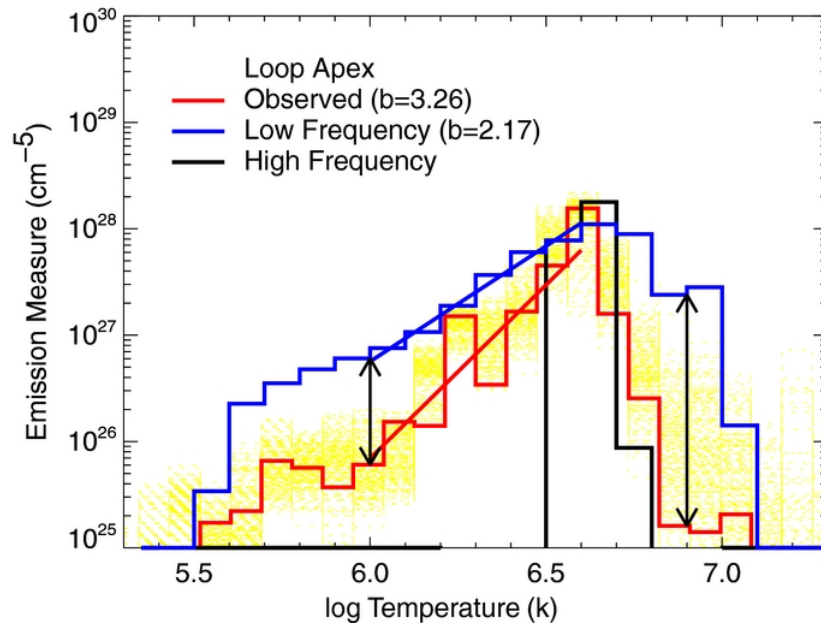


Figure 1.5: Various EMD forms for the loop apex. The low-, and high-frequency simulations (cf. Figure 1.4) are shown in blue and black. The observed EMD for the loop apex is shown in red. This Figure is adapted from Warren *et al.* (2011).

in temperature (such as those from Hinode/EIS, § 2.1.1), the shape of the temperature distribution can be reasonably well-constrained, and the distribution studied.

Figure 1.4 implies that in the high-frequency scenario there will be a narrow distribution of temperature (isothermal), and in the low frequency scenario this distribution will be larger with a substantial amount of material at lower temperatures (multi-thermal). To provide additional context, Figure 1.5 shows two simulated emission measure distributions for high-, and low-frequency heating in addition to the observed distribution for a loop apex, (Warren *et al.*, 2011). Figure 1.5 shows the low-frequency simulation (blue) in comparison to the high-frequency scenario (black). This behaviour is consistent with what is seen in Figure 1.4, and it is clear that the frequency of heating affects both the low-, and high-temperature components of the EMD, with the low-frequency nanoflares producing less steep low-temperature slopes than high-frequency nanoflares.

### 1.3.3.1 Low-Temperature EM slope

The power-law coefficients of both the low-, and high-temperature slopes of the emission measure distribution ( $T^\alpha$ , for  $\log_{10}T = 6.0 - EM_{peak}$ ;  $T^\beta$ , for  $\log_{10}T > EM_{peak}$ , where  $EM_{peak} \sim 10^{6.5-6.6}$ ) provide an insight in to the frequency of nanoflare heating, however, spectroscopic observations from current instruments are weaker at temperatures  $> 5$  MK, and are only able to well-constrain the EMD up to  $\log_{10}T \sim 6.7 - 6.8$  (5 – 6 MK).

For the low-temperature component of the EMD, loop heating models predict that the low-frequency nanoflares can only account for  $1 < \alpha < 3$  (e.g. Bradshaw *et al.*, 2012), however, several authors have analysed active region EMDs resulting in a range of low-temperature slope values from  $\alpha = 1.9 - 5.2$  (Warren *et al.*, 2011; Warren *et al.*, 2012; Winebarger *et al.*, 2011; Tripathi *et al.*, 2011; Schmelz & Pathak, 2012) providing cases for both high- and low frequency heating. There are uncertainties in the determination of this slope (e.g. Testa *et al.*, 2012), and there is also the argument that a range of observed slopes can be explained if there are various nanoflare frequencies along the line of sight (Cargill, 2014; López Fuentes & Klimchuk, 2016).

While the power-law coefficient of the low-temperature slope of the EMD can provide an insight in to the heating scenario at a given time in the active regions life, it is also interesting to understand how the heating evolves with time, and how this changes spatially within the active region itself. Recent analyses of the evolution of active region emission (e.g. Ugarte-Urra & Warren, 2012) suggested that the heating is consistent with that of low frequency during the early stage of their evolution, tending to a scenario more consistent with high-frequency nanoflare heating during the latter part (the value of  $\alpha$  increases over time). Del Zanna *et al.* (2015) determine a similar value at the first and second appearance ( $\alpha \sim 4.4, 4.6$ ), and perform DEM analysis throughout an active region showing that the slopes varying significantly ( $\pm 1$ ) within an active region core.

### 1.3.3.2 High-Temperature ( $> 5$ MK) Emission

The presence of a hot component ( $> 5$  MK) is an indication of low-frequency nanoflare heating, and is commonly referred to as the “smoking-gun” of low-frequency nanoflares (Klimchuk 2017). Observation of this component in temperature space is difficult as

it is expected to be weak, however there have been a number of studies focused on observing this hot plasma.

*Ko et al. (2009)* observed Ca XVII ( $\sim 6$  MK) line with *Hinode*/EIS, while *Teriaca et al. (2012)* observed the Fe XVIII ( $\sim 7$  MK) emission line with *SUMER*, and *Brosius et al. (2014)* obtained persistent observations of  $\sim 9$  MK plasma within an active region (Fe XIX). Using DEM analysis, *Testa et al. (2011)* utilised *Hinode*/EIS, and Soft X-ray observations from *Hinode*/XRT, and *Schmelz et al. (2009b)*; *Reale et al. (2009b)* used *Hinode*/XRT, claiming detection of plasma  $> 10$  MK in a non-flaring active region. In those studies, the high-temperature component would have been observable with *RHESSI*. By further combining the *Hinode*/XRT observations with *RHESSI* upper-limits it was possible to further constrain the high-temperature component (*Schmelz et al., 2009a*; *Reale et al., 2009a*). An important point to note with such studies is that *Winebarger et al. (2012)* demonstrated that a high-temperature blind-spot exists where *Hinode*/EIS and *Hinode*/XRT are insensitive to plasma at temperatures  $> 6$  MK, and emission measures  $< 10^{27}$  cm $^{-5}$ . This blind-spot was located by calculating how much additional emission can be added to a single temperature bin without increasing the modelled intensities in any *Hinode*/XRT filter or *Hinode*/EIS spectral line (see Figure 2 *Winebarger et al., 2012*). More recently, *Wright et al. (2017)* (Chapter 5) used *NuSTAR* to demonstrate that *Hinode*/XRT overestimated the high-temperature component when used for DEM analysis (suggesting a correction factor be applied to the temperature response functions).

While non-equilibrium ionisation effects can diminish the intensity of hot spectral lines (e.g. *Bradshaw & Klimchuk, 2011*), this is not a problem with X-ray observations where bremsstrahlung dominates. There have been a number of full-disk observations: *McTiernan (2009)* observed temperatures of 6 – 8 MK with *RHESSI*; *Miceli et al. (2012)* observed temperatures around 6.6 MK with *CORONAS-photon*/SphinX; and *Caspi et al. (2015)* observed temperatures of 11 MK with the X-123 spectrometer. Using *NuSTAR* (*Harrison et al., 2013*), *Hannah et al. (2016)* were able to constrain the emission down to an order of magnitude lower than EUNIS (*Brosius et al., 2014*) and SMM/FCS (*Del Zanna & Mason, 2014*), and while the results of the initial *NuSTAR* observations will be presented in detail in § 4.4.2, *Marsh et al. (2018)* (§ 4.4.2.3) were also able to demonstrate that *NuSTAR* (and *FOXSI*, § 2.3.1) observations were consistent with low-frequency heating.

While the EMD can probe the heating mechanism, limited studies of the low-temperature component exist as spectroscopic observations are required to fully constrain temperature-space. As has been discussed, the ability for current solar instrumentation to constrain the high-temperature component of the EMD is also limited (e.g. O’Dwyer *et al.*, 2011; Winebarger *et al.*, 2012). Observations with new instruments are required (e.g. *NuSTAR*, Chapter 4; *MaGIXS*, § 2.2.2) in order to constrain the high-temperature component of the EMD.

### 1.3.3.3 Doppler Shifts

There are a number of studies that investigate Doppler shifts (Tripathi *et al.*, 2012; Winebarger *et al.*, 2013; Dadashi *et al.*, 2012). In this case of Doppler shifts in the EUV spectral lines (observed by *Hinode*/EIS), models predict that high- and low frequency scenarios should have different velocity characteristics at the loop footpoints. For example, if high-frequency heating is taking place (see Figure 1.4) and is distributed uniformly over the loop (e.g. Testa *et al.*, 2014), no strong flows would be detectable at the loop footpoints (Winebarger *et al.*, 2013). In the low-frequency case however, upflows of plasma would be detected in these lines, and when the loop cools and drains the footprints would exhibit red-shifts. Observations of these Doppler shifts of EUV lines have so far proven to be inconclusive for either heating scenario (Dadashi *et al.*, 2012; Tripathi *et al.*, 2012; Winebarger *et al.*, 2013).

### 1.3.3.4 Time Series Analysis

With the wealth of high-cadence, high-resolution narrowband observations obtained by the *Solar Dynamics Observatory* and *Hinode*, an alternative approach to study heating of the solar corona has been through intensity variations either within a time series, or between multiple time series. While individual nanoflares are un-resolvable, numerous approaches exist in the literature in order to observe the unresolved ensemble.

Katsukawa & Tsuneta (2001) and Sakamoto *et al.* (2008) discovered intensity fluctuations (with *Yohkoh*/SXT and *TRACE* observations) above what is predicted by photon noise alone, consistent with an unresolved ensemble of nanoflares. With *Hinode*/XRT, Terzo *et al.* (2011) determined that these distributions are also skewed (and Jess *et al.*, 2014, applied similar analysis to chromospheric observations). The same

---

behaviour leads a power-law in the Fourier Power Spectra (Ireland *et al.*, 2015; Auchère *et al.*, 2016; Cadavid *et al.*, 2014; Battams *et al.*, 2019).

Finally, Viall & Klimchuk (2011, 2012) introduced the concept of time-lag analysis (see Chapter 6). By measuring the time-lags between two channels with different temperature response functions from data obtained by *SDO/AIA*, Viall & Klimchuk (2012) notably observe cooling in the majority of active region *SDO/AIA* pixels, consistent with a low-frequency heating scenario of strong and weak nanoflares. There is the question of whether these signatures are masked by the underlying multi-thermal nature of the *SDO/AIA* temperature response functions, and this will be investigated in Chapter 7.

## Chapter 2

# The Current Picture of Multi-thermal Observations of an Active Region

This chapter will address the current state of coronal active region observations and is split into three sections corresponding to the EUV, soft-, and hard X-ray regimes. First, a brief overview of the advancement in observations of coronal active regions will be presented, and each individual section will then lead into a discussion of the current instrumentation that is available for such observations. For context, emphasis is placed on the multi-instrument observations of NOAA AR 11259—an active region with good coverage from multiple instruments.

### 2.1 EUV Observations

Regular state-of-the-art EUV observations of coronal active regions are currently obtained through both imaging spectroscopy by the Extreme-ultraviolet Imaging Spectrometer on the *Hinode* satellite (*Hinode*/EIS, § 2.1.1; Kosugi *et al.*, 2007; Culhane *et al.*, 2007), and by direct imaging using the Atmospheric Imaging Assembly onboard the *Solar Dynamics Observatory* (*SDO*/AIA, § 2.1.2; Pesnell *et al.*, 2012; Lemen *et al.*, 2012), but the earliest EUV monitoring observations were as a result of the launch of the *Orbiting Solar Observatory* satellite series (*OSO* 1 - 8) which began in the early 1960's (See Tousey, 1963, for a review of the EUV Sun leading up to *OSO*-1).

The *OSO* series, which observed through to the 1980's brought with it a wide range of observations including the first observations in the EUV regime with a non-imaging

spectrometers and spectroheliographs. Particular observational highlights include the 1' spatial resolution observations of hundreds of EUV active region flares over the 300 – 1400 Å range by the Harvard College Observatory (HCO) and Naval Research Lab (NRL) experiments on *OSO-4* and *OSO-5*, and the HCO EUV instrument recorded over 4000 spectroheliograms in  $\sim 50$  lines/continuum wavelengths over a one month period in 1967.

With the progression of the *OSO* programme, the HCO instrument was further improved to a 35'' spatial resolution (*OSO-6*), and by this point the instruments from NRL and HCO had recorded a large number of spectroheliograms over a range of wavelengths. By the launch of *OSO-7* in 1971 the EUV spectroheliograph was imaging with a spatial resolution of  $\sim 20''$  (and spectral resolution of 0.8 Å over 120 – 400 Å), however, these images still could not resolve individual loops.

It wasn't until the *manned* solar observatory—*Skylab*—that the multi-thermal time-dependent picture of the Sun was first probed. Operating between May 1973 and February 1974, *Skylab* carried six major instruments including two EUV instruments, the HCO EUV spectrometer/spectroheliometer (Reeves *et al.*, 1977b,a, 280 – 1350 Å, with a spectral resolution 1.6 Å), and NRL's EUV spectroheliograph (170 – 630 Å; 2'' resolution, and 0.03 Å spectral resolution). The HCO spectrometer provided a list of line intensities to be determined for various solar phenomena (Vernazza & Reeves, 1978), and the NRL instrument provided flare spectra (e.g. Feldman *et al.*, 1988).

After the short duration of *Skylab*, the launch of the *Solar Maximum Mission (SMM)* during the solar maximum year of 1980 was a true turning point for observations of the Sun. *SMM* covered a complete solar cycle with an unprecedented instrument package for solar physics. *SMM* was designed to cover a wide range of wavelengths covering the visible up to gamma rays, and for EUV observations, *SMM*'s Ultraviolet Spectrometer/Polarimeter (*SMM/UVSP*) covered the 1150 – 3600 Å range with a resolution of 2''.

Six years after *SMM* re-entered the atmosphere, the *Solar and Heliospheric Observatory (SOHO)* (Domingo *et al.*, 1995) was launched. At the time of writing, *SOHO* has been operating for over 20 years and until August 2013 provided EUV observations of the Sun over three wavebands (171 Å, 195 Å, 284 Å; sensitive to 1 – 2 MK coronal plasma) with the EUV Imaging Telescope (*SOHO/EIT*) observing at a resolution of 2.5'' every few hours (Delaboudinière *et al.*, 1995). In addition to *SOHO/EIT*, the

Coronal Diagnostic Spectrometer (*SOHO/CDS*; [Harrison et al., 1995](#)) operated in the 150 – 800 Å range with a similar resolution to its predecessor (*SMM/UVSP*).

Further improvement on *SOHO/EIT* was to come from the launch of the *Transition Region And Coronal Explorer, TRACE*, in 1998 ([Handy et al., 1999](#)). Until 2010, TRACE provided an improved (1'') resolution images over a limited (8.5'') field-of-view with EUV filters similar to that of EIT (171 Å, 195 Å, 284 Å).

Moving to the present day, current observations in the EUV are obtained by both the *Hinode* satellite, and the *Solar Dynamics Observatory* (both of which will be described in detail in subsequent sections). The first of these, *Hinode* (formerly *Solar-B*; [Kosugi et al., 2007](#)), is a Japanese-led mission that was launched in 2006, and consists of three instruments designed to study the heating and dynamics of the solar corona. For EUV studies, *Hinode* includes the Extreme-ultraviolet Imaging Spectrometer (EIS, [Culhane et al. \(2007\)](#); § 2.1.1) and an imaging spectrometer designed to observe the EUV at chromospheric and coronal temperatures (with a spatial resolution of 2''). It should be noted that *Hinode* also includes the X-ray Telescope (XRT, § 2.2.1; [Golub et al., 2007](#); [Kano et al., 2008](#)), a broadband SXR telescope (1'' resolution) that will be discussed in § 2.2.1. The second is the *Solar Dynamics Observatory (SDO)*, launched in 2010 as part of the ‘Living with a Star’ program and provides a wealth of information with regards to the solar atmosphere and dynamics through observations with three instruments including the Atmospheric Imaging Assembly (AIA)—a full-disk narrow-band EUV imager that provides images at a spatial resolution of 1.5'' (0.6'' pixel size), and cadence of 12 s.

### 2.1.1 *Hinode*’s Extreme-Ultraviolet Imaging Spectrometer

The Extreme-ultraviolet Imaging Spectrometer on *Hinode*, (*Hinode/EIS*)—the successor to *SOHO/CDS*—is a normal-incidence EUV imaging spectrometer able to observe over two energy ranges corresponding to the short-, (SW, 170 – 210 Å) and long wavebands (LW, 250 – 290 Å). *Hinode/EIS* is able to perform observations over these two wavebands (which include spectral lines corresponding to a wide range of temperatures: 0.04 MK, 0.25 MK, 1.0 MK < T < 20 MK; [Kosugi et al., 2007](#)) using the same set of optics with multi-layer coatings on both the primary mirror and grating (see [Culhane et al., 2007](#)).

Observations can be configured with a choice of two slit (1'', 2''), or two slot sizes

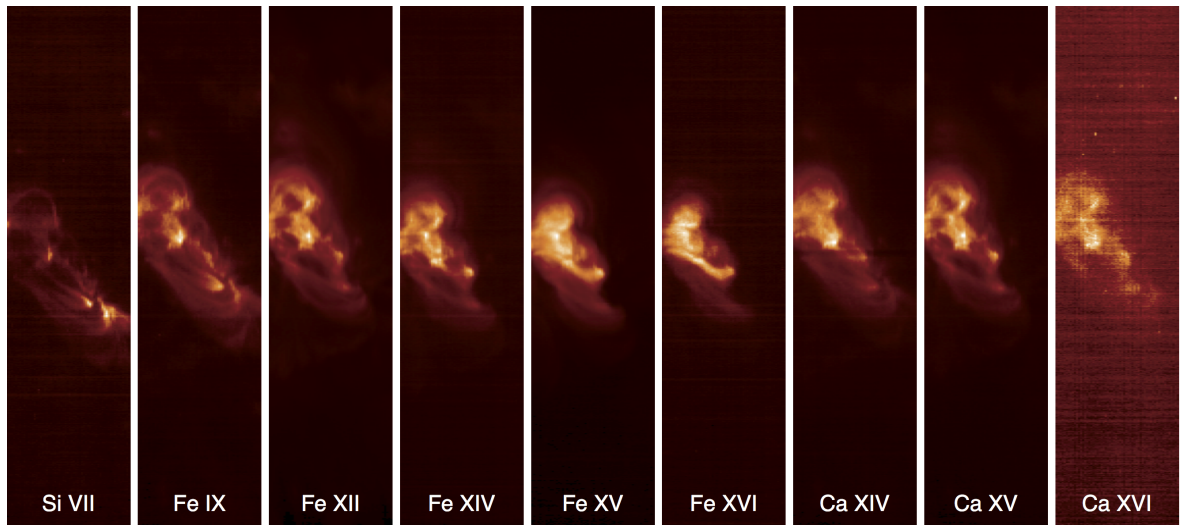


Figure 2.1: *Hinode*/EIS raster images of NOAA AR 11259 from  $\log_{10}T = 5.8 - 6.7$  K (left to right), in the region of the low-temperature slope of the emission measure distribution ( $\log_{10}T = 6.0 - \sim 6.6$ ), § 1.3.3.1. Each image is the integrated line intensity from Gaussian fitting.

( $40''$  or  $266''$ ), each with a maximum possible length of  $512''$ ; the light enters the instrument and passes through entrance filters before being dispersed by the grating on to the two CCDs, each with a spatial resolution of  $2''$  (pixel size of  $1''$ ) and a  $0.047 \text{ \AA}$  *pre-launch* full-width half-maximum (FWHM) of the optics.

Regardless of slit or slot choice, observations of the solar target can be obtained by performing either a *sit-and-stare* observation, or by obtaining a *raster*. While a *sit-and-stare* observation is self-explanatory, rastering is a powerful tool for observations of active regions. This technique allows a larger field-of-view to be studied by rotating the primary mirror after each consecutive exposure (usually  $\mathcal{O}(2 - 10 \text{ s})$  for active region observations). As *Hinode*/EIS scans across these regions, for each exposure a dispersed spectrum is recorded in each pixel, and an image is a data-cube containing a spectrum in each pixel. Image-like data can therefore be recovered by fitting a Gaussian (or multiple Gaussian) to a specific line in each pixel.

An example of such an image (obtained by rastering over NOAA AR 11259) for a set of Gaussian fitted lines can be seen in Figure 2.1. Figure 2.1 shows the reconstructed image ( $120'' \times 512''$ ) by Gaussian fitting lines after rastering right to left (West to East) along the  $x$ -direction. This is shown for *nine* emission lines ranging from  $\log_{10}T = 5.8 - 6.7$  K (where the emission measure distribution is well-constrained, § 1.3.3.1),

and highlights the multi-thermal temperature distribution of active regions; it should be noted that due to the nature of rastering there is a hidden temporal component in the  $x$ -direction.

While observations with *Hinode*/EIS can provide excellent diagnostics and allow the temperature distribution, density, flow and abundance information to be derived, *Hinode* suffered a problem one of its downlink transition systems, and now relies on a slower downlink speed (Shimizu, 2009). This directly impacts the amount and quality of data that is downloaded. In addition, obtaining multiple observations in the raster mode are also slow compared to the timescale of active region dynamics, and therefore the EUV spectroscopy provided by *Hinode*/EIS is frequently complemented by the wealth of high-cadence narrowband measurements obtained by *SDO*/AIA.

### 2.1.2 *Solar Dynamics Observatory's Atmospheric Imaging Assembly*

*SDO*/AIA is a set of four dual-channel 20 cm telescopes which together, share a total of ten narrowband filters. *SDO*/AIA is capable of imaging the Sun over a  $40'^2$  field-of-view, extending out to  $+0.5 R_{\odot}$ , on to a  $4096 \times 4096$  pixel CCD at cadence of 12s, and spatial resolution of  $1.5''$  ( $0.6''$  pixel size). For the observation of optically-thin coronal emission, *SDO*/AIA comprises six EUV filter channels centred on Fe lines at  $131 \text{ \AA}$  (Fe VIII, XXI),  $T \sim 0.4 \text{ MK}$  and  $T \sim 10 \text{ MK}$ ;  $171 \text{ \AA}$  (Fe IX),  $T \sim 0.6 \text{ MK}$ ;  $193 \text{ \AA}$  (Fe XII, XXIV),  $T \sim 1.5 \text{ MK}$ ;  $211 \text{ \AA}$  (Fe XIV),  $T \sim 2 \text{ MK}$ ;  $335 \text{ \AA}$  (Fe XVI),  $T \sim 2.5 \text{ MK}$ ; and  $94 \text{ \AA}$  (Fe XVIII),  $T \sim 6 \text{ MK}$ , in addition to the chromospheric He II ( $304 \text{ \AA}$ ,  $T \sim 50,000 \text{ K}$ ) line, UV and visible wavelengths.

The multi-thermal *SDO*/AIA EUV images for the same region as those in Figure 2.1 are shown in Figure 2.2 for a similar time. Figure 2.2 shows a NOAA AR 11259 for the six coronal EUV channels. The  $120'' \times 512''$  *Hinode*/EIS field-of-view is overplotted within this  $600'' \times 600''$  region for reference. The temperature response functions for these six *SDO*/AIA filter channels are shown in Figure 2.3, clearly highlighting the multi-thermal nature of the filter channels. These temperature response functions were calculated from the effective areas and using the CHIANTI atomic database v7.1.3 (Dere *et al.*, 1997, Landi *et al.*, 2013).

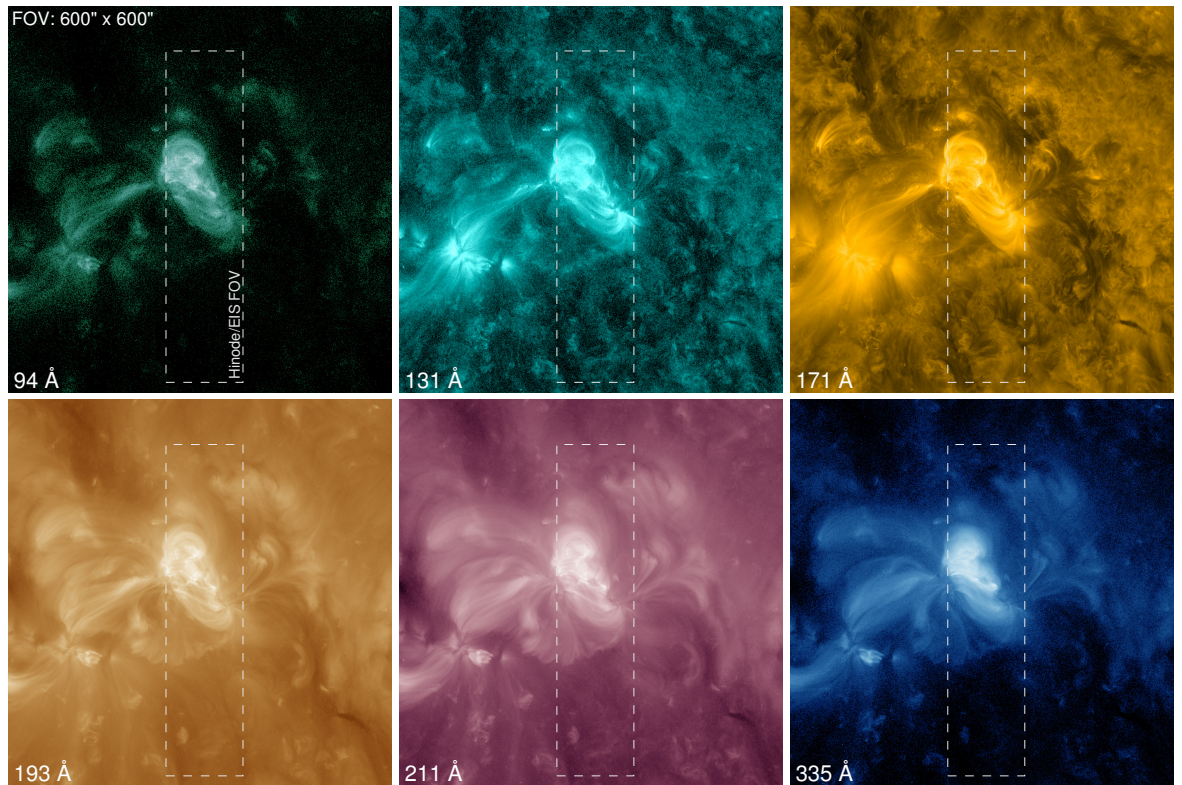


Figure 2.2: NOAA AR 11259 as observed by *SDO/AIA* in its six optically-thin EUV filters. These images are shown over a  $600'' \times 600''$  region, with the  $120'' \times 512''$  *Hinode/EIS* field-of-view (see Figure 2.1) overplotted.

### 2.1.3 Sounding Rockets & Future Missions

In order to further develop hardware for future missions—and obtain immediate cutting-edge observations—sounding rockets provide an easy, low-cost, low-risk, short-schedule access to space. Naturally, a number of improvements to EUV spectroscopy and direct imaging have been obtained as the result of recent EUV sounding rockets, two of which are the *Extreme Ultraviolet Normal Incidence Spectrograph*, *EUNIS*, and the *High Resolution Coronal Imager*, *Hi-C*.

***EUNIS*** – *EUNIS* (*EUNIS-13*<sup>1</sup>) is a two-channel imaging spectrograph that observes the Sun with high spatial resolution ( $\sim 3 - 4''$ ) in the  $300 - 370 \text{ \AA}$  and  $525 - 635 \text{ \AA}$  wavebands (Brosius *et al.*, 2014). From observations with *EUNIS-13*, Brosius *et al.* (2014) observed ubiquitous, faint emission of the Fe XIX line (with a peak forma-

<sup>1</sup>referring to the launch date of 2013-April-23

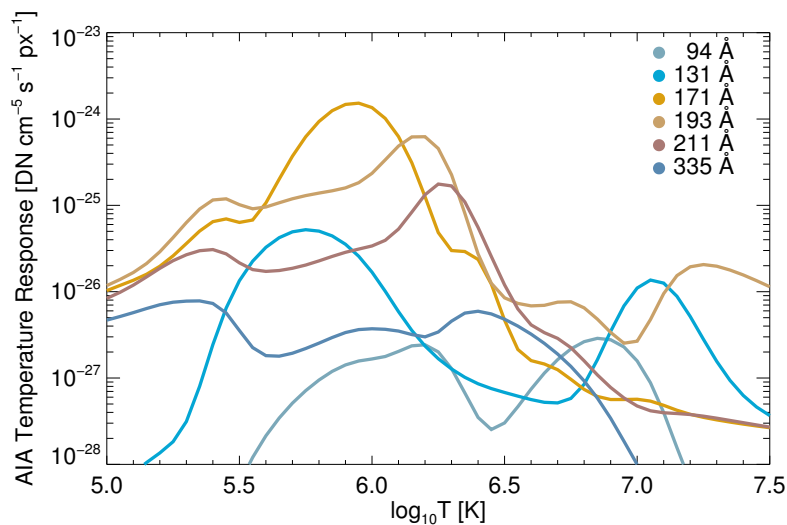


Figure 2.3: *SDO/AIA* temperature response functions for the six optically-thin EUV filter channels, highlighting the multi-thermal nature of the *SDO/AIA* instrument.

tion temperature of  $T = 8.9$  MK) throughout an active region, likely to be the result of nanoflare heating (§ 1.3.3.2).

***Hi-C*** – A natural continuation to the *SDO/AIA* instrument involves increasing to higher resolution, and higher cadence observations of the solar corona. To obtain such observations the *High-Resolution Coronal Imager (Hi-C)* (Cirtain *et al.*, 2013; Kobayashi *et al.*, 2014) was first flown on a NASA sounding rocket in 2012. *Hi-C* is a high-resolution ( $0.2''$ , high-cadence (1.4 s for the  $1024 \times 1024$ , and 5.5 s for  $4096 \times 4096$  pixel images) normal-incidence narrow-band telescope—a continuation of *TRACE* and *SDO/AIA*—and observed a narrow wavelength range centred on the Fe XII 193 Å line (cf. *SDO/AIA* 193 Å) with a  $4096 \times 4096$  pixel CCD (plate scale of  $0.1'' \text{ px}^{-1}$ ). These observations were the highest resolution of any coronal imager to date, and importantly, showed evidence for braiding (unresolved by *SDO/AIA*), followed by reconnection and heating (Cirtain *et al.*, 2013). Recently, *Hi-C* was flown again in May 2018 ("*Hi-C* 2.1").

In addition to sounding rockets there are a number of EUV instruments in currently in development,

**EUI** – The Extreme Ultraviolet Imager (EUI, P. Rochus, PI, Belgium<sup>2</sup>) will be launched on *Solar Orbiter* (Müller *et al.*, 2013) in 2019. The EUI is a suite of three telescopes with two high-resolution imagers, and a third full Sun imager that will continuously monitor the Sun in 174 Å and 304 Å (a “hot”, and “cool” channel) up to 2 solar radii. The high-resolution imager will have a resolution of 1”, in two channels 174 Å, and 1216 Å. Based on the original launch date of January 2017, *Solar Orbiter* was planned to have a period of 168 days during its nominal mission, approaching a minimum radius of 0.284 AU, and vary between a solar latitude of  $\pm 35$  (see Figure 3 of Müller *et al.*, 2013, for the mission profile with an assumed launch of January 2017). These observations would therefore complement the current observations from 1 AU that are obtained by *SDO/AIA*.

**SPICE** – Similarly to EUI, the Spectral Imaging of the Coronal Environment (SPICE, Fludra *et al.*, 2013) will be launched as part of *Solar Orbiter*. SPICE is a high-resolution EUV spectrometer which will operate over two wavebands: 704 – 790 Å, and 973 – 1049 Å, and will address *Solar Orbiter*’s science goals in a similar manner to *Hinode/EIS*, but observing plasma on the solar disk in the temperature range  $10,000 \text{ K} < T < 10 \text{ MK}$ , and on time-scales of seconds to tens of minutes.

**MUSE** – The Multi-Slit Solar Explorer (*MUSE*, Tarbell, 2017; Lemen *et al.*, 2017) is a proposed SMall EXplorer (SMEX) mission with a high-resolution, high-cadence *Hi-C*-like imager and a multi-slit (35 slits over the field-of-view) EUV spectrograph (0.3”; 1 – 4 s, Tarbell & De Pontieu, 2017) to further understand the dynamics, and probe the mechanisms responsible for energy release in the solar corona.

---

<sup>2</sup><http://eui.sidc.be/index.php>

## 2.2 Soft X-ray Observations

Solar X-rays were first detected in August 1948 using a V-2 rocket with beryllium windows, and photographic imaging (Tousey *et al.*, 1951; Hirsh, 1983; Bray *et al.*, 1991); the first detected X-ray emission from flares was obtained in 1956, and the direct evidence for active region X-ray emission was obtained in 1958 (Kreplin, 1961). It was, however, the 1960's that brought the advent of on-disk imaging. The first X-ray image of the solar corona was obtained by a pinhole camera with a five minute exposure, launched on an Areobee sounding rocket (Friedman, 1963).

While many subsequent images of the X-ray Sun were obtained by pinhole cameras, by 1966 the finest images of the X-ray Sun were obtained using a multi-filter grazing-incidence telescope by a team at NASA's Goddard Space Flight Center (GSFC). Over a period of two years following these observations numerous rocket flights by both GSFC and American Science and Engineering (AS&E) had clearly demonstrated the possibilities with grazing-incidence telescopes. While AS&E *claimed* a resolution down to 'several arcseconds' in their best observations, a summary of eight rocket flights between 1963 and 1973 demonstrated the clear improvement of resolution preceding the *Skylab* mission. By March 1973 a rocket flight recorded active region loop definition surpassing that obtained on the subsequent *Skylab* mission (Vaiana *et al.*, 1973a,b). It was these sounding rocket observations that led to the discovery of X-ray active region loops, and loops connecting regions of opposite magnetic polarity (Vaiana *et al.*, 1968, 1973b). The morphology of the X-ray corona was seen to be consisting of these arch-like loops, and this revealed distinctions between coronal structures (e.g. active regions, coronal holes, bright points, etc.; Vaiana & Rosner, 1978).

In addition to the two EUV instruments, *Skylab* also carried two grazing-incidence soft X-ray telescopes with  $\sim 2''$  spatial resolution (3.5–60 Å, AS&E; 3–53 Å, Marshall Space Flight Center, MSFC). While the resolution may have been trumped by the rocket programme, these telescopes recorded tens of thousands of exposures on film, and by the end of the *Skylab* mission the AS&E X-ray telescope had provided close to 32,000 X-ray photographs of the Sun (maximum resolution of  $\sim 2''$ ). These observations allowed study of active region evolution (from emergence to spreading, a few rotations later, Golub *et al.*, 1982), confirming that the X-ray corona is filled with coronal loops (Rosner *et al.*, 1978).

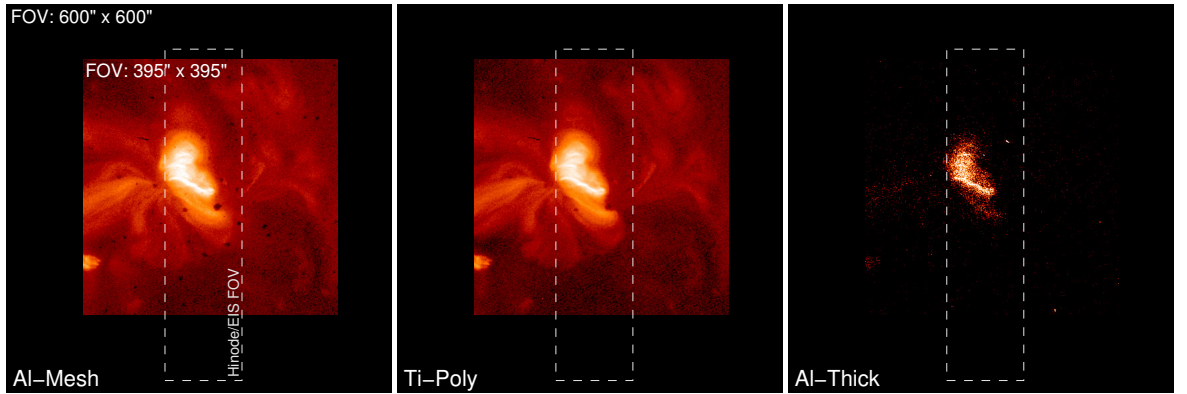


Figure 2.4: *Hinode*/XRT observations of NOAA AR 11259 with with three filters: Al-Mesh; Ti-Poly; Al-Thick (*left to right*). These images are  $395'' \times 395''$  and are plotted over the same  $600'' \times 600''$  field-of-view, including the *Hinode*/EIS field-of-view, as previously shown in Figure 2.2.

As has been mentioned, the turning point in solar observations came with *SMM*. The *SMM* mission in 1980 enabled the study of the solar corona over many regimes including soft X-rays using two spectrometers: a Bent Crystal Spectrometer (BCS;  $1.7 - 3.2 \text{ \AA}$ ) which spatially integrated over a  $6'$  field-of-view; and a Flat Crystal Spectrometer (FCS;  $1.4 - 22 \text{ \AA}$ ) with a maximum field-of-view of  $7'$  and a resolution of  $14''$ . These instruments covered a number of lines including Fe lines up to Fe XXVI ( $T \sim 60 \text{ MK}$ , [Acton et al., 1980](#)) and obtained spectroscopy of coronal flares (e.g. [MacNeice et al., 1985](#)).

*Yohkoh* (*Sunbeam*; previously *Solar-A*, [Ogawara et al., 1991](#)) followed *SMM* in 1991, and consisted of four instruments including the soft X-ray Telescope (SXT; [Tsuneta et al., 1991](#)) that observed temperatures  $\gtrsim 1.5 \text{ MK}$ , with a full-disk resolution of  $5''$ , and a  $2.5''$  resolution for partial frame images; the wide-band spectrometer (WBS; [Yoshimori et al., 1991](#)) which covered the Soft X-ray to gamma ray regime; and a Bragg Crystal Spectrometer (BCS, [Culhane et al., 1991](#)) which covered four spectral lines, and spatially integrated over the full-disk, with a similar spectral resolution to *SMM* but with a  $10\times$  increase in sensitivity. Using *Yohkoh*/SXT, [Hara et al. \(1992\)](#) were the first to report indications of plasma between 5 and 6 MK in active regions.

Since *Yohkoh*, regular space-based observations of the soft X-ray corona have been by obtained by the grazing-incidence X-Ray Telescope on board the *Hinode* (*Sunrise*; formerly *Solar-B*) satellite (*Hinode*/XRT), however, the *MaGIXS* sounding rocket will

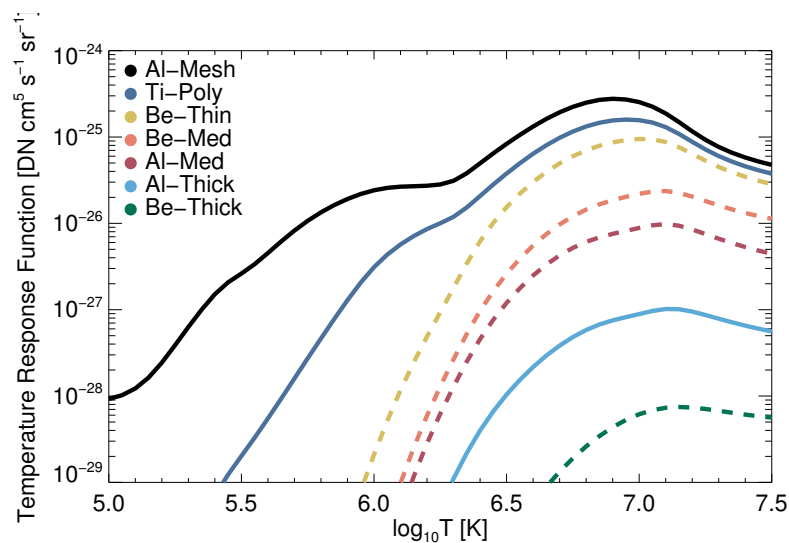


Figure 2.5: Temperature response functions for the nine *Hinode*/XRT filters. The three temperature response functions for the images shown in Figure 2.4 are shown as solid lines, with the remaining six temperature response functions shown as dashed lines.

provide the eagerly anticipated observation of the soft X-ray spectra for the analysis of active region temperature distribution (§ 2.2.2).

### 2.2.1 *Hinode* X-Ray Telescope (*Hinode*/XRT)

*Hinode*'s X-ray Telescope (XRT; Kosugi *et al.*, 2007, Golub *et al.*, 2007) is a broadband grazing-incidence instrument (Wolter-I design) with a high temporal and spatial resolution.

*Hinode*/XRT is equipped with nine broadband filters with the nomenclature generally referencing the constituent element and relative thickness (e.g. for Beryllium ( $^4\text{Be}$ ), there are three filters: Be-Thin; Be-Med; Be-Thick), and can image soft X-rays over  $6 - 60 \text{ \AA}$  ( $1 - 30 \text{ MK}$ ; see Figure 2.4). These *Hinode*/XRT observations can be obtained with a variety of field-of-views which range from high-cadence (2 s) active region observations, to  $35' \times 35'$ , full-disk synoptic images. Regardless of observational mode, these images are incident on a CCD with a resolution of  $2048 \times 2048$  pixels, with a pixel size of  $1''$  (spatial resolution of  $2''$ ).

An set of example *Hinode*/XRT observations are shown in Figure 2.4. Figure 2.4 shows NOAA AR 11259 (as also observed by *Hinode*/EIS and *SDO*/AIA; see Figure 2.1

and Figure 2.2) for three filters (Al-Mesh, Ti-Poly, Al-Thick, *left to right*). For these observations the *Hinode*/XRT field-of-view was  $\sim 395'' \times 395''$ , and is plotted over the same  $600'' \times 600''$  region as *SDO*/AIA in Figure 2.2. These observations show the bright X-ray loops in the core of the active region (cf. Figure 1.1). In addition to the images, the temperature response functions for all nine *Hinode*/XRT channels are shown in Figure 2.5, clearly showing temperature sensitivity over a wide range of temperatures.

### 2.2.2 Sounding Rockets & Future Missions

The *Marshall Grazing Incidence X-ray Spectrometer* (*MaGIXS*, Kobayashi *et al.*, 2011, 2018) is a grazing-incidence, soft X-ray spectrometer designed to cover the 0.5 – 2.0 keV (6 – 24 Å) range with a spatial resolution of 5'', and wavelength resolution of 0.05 Å. *MaGIXS* will be flown on a NASA sounding rocket in 2019, and will be able to probe the nature of active region heating through temperature diagnostics provided by sensitive observations of high-temperature lines (see Table 2.1).

An active region DEM (§ 1.3.3.1, and Chapter 3; e.g. Warren *et al.*, 2012) can be currently constrained up to approximately  $\log_{10}T = 6.8$  by EUV lines from *Hinode*/EIS, but with such soft X-ray observations could be constrained up to  $\log_{10}T = 7.3$  (Figure 2.6), providing constraints on coronal heating mechanism. Figure 2.6 shows the key *Hinode*/EIS spectral lines along with the key *MaGIXS* lines indicating the difference in temperature sensitivity.

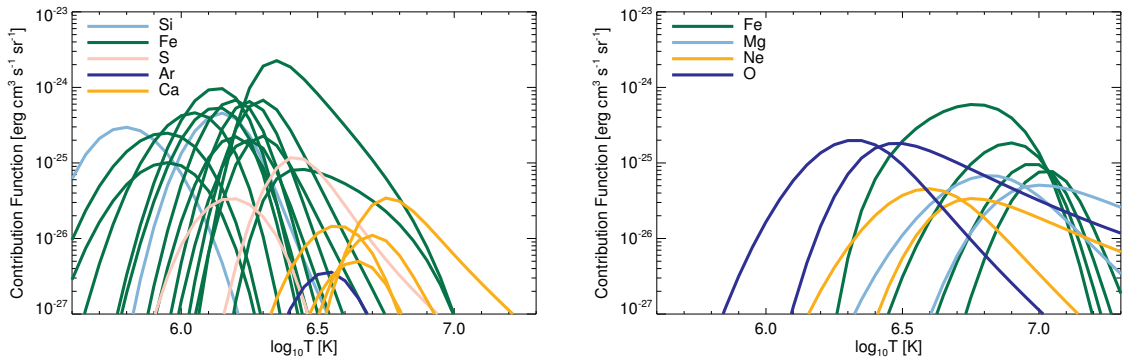


Figure 2.6: *Left*: *Hinode*/EIS lines observed for NOAA AR 11259; *Right*: Key *MaGIXS* lines as described in Table 2.1.

Table 2.1. List of Key Diagnostic Lines to be Observed by *MaGIXS*

<i>MaGIXS</i> Emission Lines	Wavelength (Å)	$\log_{10}T$ (K)
Fe XX	12.85	7.0
Fe XIX	13.53	6.8
Fe XVIII	14.21	6.8
Fe XVII	15.01	6.6
Mg XII	8.42	6.9
Mg XI	9.16	6.4
Ne X	12.13	6.6
Ne IX	13.45	6.2
O VIII	18.97	6.4
O VII	21.60	6.3

Note. — Key diagnostic lines observed by *MaGIXS*, ordered in decreasing temperature; extracted from [Kobayashi \*et al.\* \(2018\)](#).

## 2.3 Hard X-Ray Observations

Hard X-ray observations have been regularly obtained from space since the launch of the *OSO* series, but it was *SMM* that carried the first in-orbit instrument capable of imaging hard X-rays: the hard X-ray Imaging Spectrometer (*SMM/HXIS*, van Beek *et al.*, 1980). *SMM/HXIS* imaged hard X-ray flares with a resolution of  $32''$  (down to  $8''$  in the fine field-of-view), but the energy sensitivity ( $\lesssim 30$  keV) limited observations to only thermal emission. This limitation was eliminated with the hard X-ray Telescope on *Yohkoh* (*Yohkoh/HXT*) which was able to image over four bands ranging from  $14 - 93$  keV, at a resolution of  $5 - 8''$  (Kosugi *et al.*, 1991).

Since *Yohkoh*, and until October 2018, the *Reuven Ramaty High Energy Solar Spectroscopic Imager* (*RHESSI*; Lin *et al.*, 2002) had been the sole solar-dedicated hard X-ray imaging spectrometer. Launched in 2002, *RHESSI* was built on the rotational modulation collimator (RMC) technology that was pioneered by *Yohkoh/HXT* and the astrophysics mission, *Hinotori* (*Firebird*, ASTRO-A) which also observed numerous solar flares (Tanaka, 1983). *RHESSI* observed photons from 3 keV to 17 MeV at a resolution of  $< 1$  keV at  $3 - 100$  keV which increases with higher energy ( $\sim 5$  keV at 3 MeV). Since X-rays are not easily focused (for a full discussion of focusing optics see Chapter 4), spatial information from *RHESSI* was obtained through its use of nine cooled Germanium detectors each located behind a RMC. *RHESSI* rotated once every four seconds and this rotation leads to full Sun observations as the grids in each collimator block and unblock X-rays resulting in a modulation pattern. The modulations in each detector, combined with the known axis-spin timing and grid spacings allowed an image to be reconstructed from a Fourier transform. The resulting images have a resolution of  $\sim 2.3''$  at  $3 - 100$  keV,  $7''$  at  $100 - 400$  keV, and  $36''$  at  $400$  keV– $15$  MeV.

While *RHESSI* has provided over a decade of observations of the Sun which includes the observation of thousands of flares ranging in energy from large X-class down to A-class microflares, *RHESSI* was unable to observe non-flaring active regions (a single paper discusses *RHESSI* observations of the non-flaring Sun, McTiernan, 2009), or detect emission from the quiet Sun (Hannah *et al.*, 2010). In order to obtain regular observations of both flares ( $< A$ -class), and non-flaring active regions, more sensitive instrumentation is therefore required.

### 2.3.1 Advancements in Hard X-Ray Observations

EUV and X-ray observations of the Sun began with sounding rockets, and to this day sounding rockets are still vital in driving forward instrumentation development, and advancing our understanding of solar phenomena. It has been over 15 years since *RHESSI* was launched in to orbit, but the recent decade has brought with it the technological advancements required to focus photons  $> 10$  keV.

As part of the work presented in this thesis, NASA's *NuSTAR* (*Nuclear Spectroscopic Telescope Array*; Harrison *et al.*, 2013) mission—an astrophysics mission that was not designed for heliophysics—has been occasionally directed towards the Sun to observe the HXR signatures various phenomena including microflares and non-flaring active regions. These observations—the most sensitive of their kind—together with the dual-telescope focusing optics instrument, and results from the heliophysics campaign will be described further in Chapters 4 and 5. In addition to *NuSTAR*, the *FOXSI* sounding rockets (and the proposed SMEX mission of the same name) utilise similar technology but with heliophysics as a focus.

The *Focusing Optics X-ray Solar Imager* (*FOXSI*, Krucker *et al.*, 2013) sounding rocket observes a field-of-view of  $16'$  square, and a resolution approaching  $9''$ . Like *NuSTAR*, *FOXSI* utilises a conical approximation to the Wolter-I configuration, but with a reduced (2 m) focal length that is limited by the sounding rocket payload bay. *FOXSI* has been flown in 2012 (*FOXSI-1*,  $\sim 4 - 15$  keV; Krucker *et al.*, 2013, 2014) and 2014 (*FOXSI-2*,  $\sim 4 - 20$  keV; Christe *et al.*, 2016), and with an updated payload, *FOXSI-3* flew in September 2018<sup>3</sup>. With the decommissioning of *RHESSI*, a *FOXSI*-SMEX mission would greatly complement the wide range of solar observations being regularly obtained and provide dedicated direct imaging observations of hard x-ray events.

In addition to *FOXSI*, and the proposed *FOXSI*-SMEX, the Spectrometer/Telescope for Imaging X-rays (STIX, Benz *et al.*, 2012), will be launched as part of *Solar Orbiter*. STIX will provide thermal and non-thermal imaging spectroscopy from  $4 - 150$  keV by utilising a Fourier-transform imaging system that is similar to those used by *RHESSI* (and HXT on *Yohkoh*). As discussed previously, unlike *NuSTAR* and *FOXSI*, *Solar Orbiter* will orbit the Sun, and STIX will therefore provide an additional perspective

<sup>3</sup><http://foxsi.umn.edu/launches/foxsi-3>

of HXR events.

## 2.4 Summary

This chapter has provided an overview of the past, present, and future observations of the solar corona, with concentration on the present multi-thermal coronal observations of active regions, united by observations of a common target: NOAA AR 11259. Together the instruments presented in this chapter can be used for various analyses, such as recovering the plasma temperature distribution (the differential emission measure (DEM), Chapter 3)—a major focus of this thesis.

Chapter 3 will present and compare the DEMs determined from spectroscopic and narrowband EUV data from a number of recovery techniques. These results will be compared, and temperature maps will be later presented; DEMs determined in this way can then be combined with observations of soft, and hard X-Ray spectra to further constrain the high-temperature emission (Chapter 5) and place limits on the non-thermal energetics in the smallest flares; and finally, a variety of analysis techniques can be used with the recovered light curves in temperature to understand the heating of the solar corona (Chapters 6, and 8).

# Chapter 3

## Temperature Diagnostics

This thesis concentrates on the coronal heating problem by investigating both the smallest distinguishable heating events, and the unresolved ensemble of even smaller events. In this thesis these two approaches both involve recovery differential emission measure (DEM). This chapter therefore introduces an overview of spectral line emission before discussing how this emission can be used to provide temperature diagnostics, including the recovery of the DEM, an ill-posed inverse problem. There are a large number of methods available in the literature to recover the DEM and § 3.4 will introduce four of these methods that have been used within this thesis. These include Tikhonov Regularised Inversion; an iterative least-squares approach; a Markov-Chain Monte-Carlo approach; and finally a recent technique based on the concept of sparsity. Each of these methods will be discussed and demonstrated before being applied in later chapters.

### 3.1 Spectral Lines

The emission of spectral lines from neutral atoms, or ions, occurs when an electron transitions from one energy state to another through de-excitation. In the transition region and corona the emission spectrum is dominated by the emission from ions, and the observed wavelength,  $\lambda$ , is calculated from the difference in energy ( $E$ ) between the two energy levels as

$$E = \frac{hc}{\lambda}, \quad (3.1)$$

where  $h$  is Planck's constant, and  $c$  is the speed of light.

For the case of the corona the atmosphere is both hot and has low density, and as such, the atmosphere is assumed to be optically thin. In the optically thin scenario, a photon will travel freely from the source to the observer, but for higher densities and lower temperatures photons may be scattered or absorbed and re-emitted before reaching the observed (the plasma is known as optically thick).

The *emissivity* of an optically-thin spectral line (wavelength of  $\lambda_{ij}$ ), produced by the spontaneous transition from an upper-level  $j$ , to a lower-level  $i$ , can be described as

$$\epsilon(\lambda_{ij}) = \frac{hc}{4\pi\lambda_{ij}} N_j(Z^{+r}) A_{ji} [\text{erg cm}^{-3} \text{ s}^{-1} \text{ sr}^{-1}] \quad (3.2)$$

where  $Z^{+r}$  is an  $r$ -times ionised element  $Z$ ;  $A_{ji}$  is the Einstein coefficient, which is the *spontaneous transition probability* (see [Aschwanden, 2004](#));  $N_j(Z^{+r})$  is the number density of the level  $j$  from the emitting ion; and  $z$  corresponds observing along the line-of-sight.

Equivalently, the intensity of an optically-thin spectral line associated with this spontaneous transition is given by

$$I(\lambda_{ij}) = \frac{hc}{4\pi\lambda_{ij}} \int N_j(Z^{+r}) A_{ji} dz [\text{erg cm}^{-2} \text{ s}^{-1} \text{ sr}^{-1}]. \quad (3.3)$$

In order to calculate the intensity described in Equation 3.3, the number density  $N_j(Z^{+r})$  needs to first be calculated. For coronal plasma the rate of ionisation and recombination are on much longer time-scales than processes occurring between the energy levels of the ion (e.g. collisional excitations, de-excitations, and spontaneous radioactive decay, [Del Zanna & Mason, 2018](#)). The population of the upper-level  $j$  is therefore calculated as

$$N_j(Z^{+r}) = \frac{N_j(Z^{+r})}{N(Z^{+r})} \frac{N(Z^{+r})}{N(Z)} \frac{N(Z)}{N_H} \frac{N_H}{N_e} N_e \quad (3.4)$$

where here, the terms are defined as:  $\frac{N_j(Z^{+r})}{N(Z^{+r})}$ , the population level of  $j$  relative to the number density of the ion  $Z^{+r}$ ;  $\frac{N(Z^{+r})}{N(Z)}$ , is the ionisation ratio (e.g. [Mazzotta et al., 1998](#));  $\frac{N(Z)}{N_H} \equiv Ab(Z)$  is the elemental abundance (relative to hydrogen); and finally (for the solar corona),  $\frac{N_H}{N_e} \approx 0.83$ , is the hydrogen abundance relative to the electron number density ([Meyer, 1985](#)). With these defined, it is customary to redefine Equation 3.3 as

$$I(\lambda_{ij}) = \int G(N_e, T, \lambda_{ij}) N_e N_H dz, \quad (3.5)$$

where the combined atomic physics is represented by the *contribution function*, which can be defined with or without the elemental abundance ( $C$ , or  $G$ ):

$$G(N_e, T, \lambda_{ij}) = Ab(Z)C(N_e, T, \lambda_{ij}), \quad (3.6)$$

where,

$$C(N_e, T, \lambda_{ij}) = A_{ji} \frac{h\nu_{ij}}{4\pi} \frac{N_j(Z^{+r})}{N_e N(Z^{+r})} \frac{N(Z^{+r})}{N(Z)} [\text{erg cm}^{-2} \text{ s}^{-1} \text{ sr}^{-1}]. \quad (3.7)$$

An important point about Equation 3.5, is that this can then be rewritten in terms of the amount of plasma along the line-of-sight (the differential emission measure, DEM, Craig & Brown, 1976) as will be discussed in § 3.2.

The contribution functions in Equation 3.7 are determined by atomic physics calculations, and are obtainable (for a large number of lines) from the CHIANTI atomic database<sup>1</sup> (Dere *et al.*, 1997; Landi *et al.*, 2013). CHIANTI also provides a set of elemental abundances (e.g. Feldman, 1992) in order to calculate  $G(n_e, T)$  (Equation 3.6).

## 3.2 Differential Emission Measure (DEM)

The formalism of DEM analysis was first developed by Pottasch (1963), and later by Jefferies *et al.* (1972), Withbroe (1975), Jordan (1976) and Craig & Brown (1976); a detailed treatment for the solar context can be found in Bruner & McWhirter (1988). The method of recovering the DEM from spectroscopic data (e.g. *Hinode*/EIS) is based on a number of assumptions of the emitting source such that optical depths within the source are negligible; collisions dominate the excitation and ionisation processes, and the excitation processes are in statistical equilibrium; electrons and ions have Maxwellian velocity distribution characterised by the same temperature; and finally, the elemental composition does not vary within the corona. As the plasma is assumed to be both optically thin, and in thermal equilibrium (via collisions), any single volume element of plasma is radiatively decoupled from any other volume element, such that the plasma can be described as a collection of quasi-isothermal plasmas (of varying

<sup>1</sup><http://www.chiantidatabase.org/>

temperature) each occupying a different volume element. The intensity of a given spectral line ( $I_\alpha$ ) from one of these quasi-isothermal plasma elements can be represented as

$$I_\alpha = \iiint_V G(n_e(\mathbf{r}), T) n_e^2(\mathbf{r}) d^3\mathbf{r}. \quad (3.8)$$

This is the intensity emitted by the source for an emission line  $\alpha$ , where  $n_e(\mathbf{r})$  is the electron density at a position  $\mathbf{r}$  within the volume, and  $G(n_e, T)$ , is the contribution function which includes all necessary atomic physics of the line formation.

A change of variables allows Equation 3.8 to be rewritten as an integral over temperature (cf. [Craig & Brown, 1976](#)). To perform this change in variables, the volume element  $d^3\mathbf{r}$  can be represented as a surface at a position  $\mathbf{r}$ ,  $d^3\mathbf{r} = dS d\mathbf{r}$ , and by dividing the emitting region into isothermal surfaces,  $dS_T$ , the volume element can be represented as

$$d^3\mathbf{r} = dS \left( \frac{d\mathbf{r}}{dT} \right) dT = |\nabla T|^{-1} dS_T dT. \quad (3.9)$$

Here,  $\nabla T$  is the temperature gradient, and  $|\nabla T|^{-1}$  is the inverse of the magnitude of the temperature gradient. The volume of the of the plasma in the temperature range  $T, T + dT$  can then be calculated as the integral over the surface  $S_T$ ,

$$dV_i = \left( \iint_{S_T} |\nabla T|^{-1} dS \right)_i dT, \quad (3.10)$$

where  $i$  has been used to indicate each of the surfaces with a constant temperature. The total volume in the range  $T$  to  $T + dT$  is therefore  $dV = \phi(T)dT$ , where

$$\phi(T) = \sum_{i=1}^N \left( \iint_{S_T} |\nabla T|^{-1} dS \right)_i, \quad (3.11)$$

is the sum over a number of disjoint surfaces of constant temperature.

The line intensity (Equation 3.8) can be described as

$$I_\alpha = \sum_{i=1}^N \int_T \left\{ \iint_{S_T} G(n_e(\mathbf{r}), T) n_e^2(\mathbf{r}) |\nabla T|^{-1} dS \right\}_i dT, \quad (3.12)$$

or equivalently,

$$I_\alpha = \int_T G(n_e(\mathbf{r}), T) \sum_{i=1}^N \left\{ \iint_{S_T} n_e^2(\mathbf{r}) |\nabla T|^{-1} dS \right\}_i dT. \quad (3.13)$$

The emission measure differential in temperature, the *differential emission measure*,  $\xi(T)$ , can be defined as

$$DEM = \xi(T) = \sum_{i=1}^N \left( \iint_{S_T} n_e^2(\mathbf{r}) |\nabla T|^{-1} dS \right)_i, \quad (3.14)$$

so that the line intensity can be written in a simpler form as

$$I_\alpha = \int_T G(n_e(\mathbf{r}), T) \xi(T) dT, \quad (3.15)$$

cf. Equation 3.5. Here, the quantity  $\xi(T)$  arises from the change in variables from volume in Equation 3.8 to an integral in temperature. Equation 3.15 shows the motivation behind the DEM formalisation in that the observable is more straightforwardly related to a combination of physical properties of the emitting source.

Equation 3.14 can be further simplified under the assumption that the density depends only on the position within the surface ( $S_T$ ). If one defines a mean square electron density over all surfaces (weighted with respect to the temperature gradient over those surfaces):

$$n^2(T) = \frac{\xi(T)}{\phi(T)} = \frac{\sum_{i=1}^N \left( \iint_{S_T} n_e^2(\mathbf{r}) |\nabla T|^{-1} dS \right)_i}{\sum_{i=1}^N \left( \iint_{S_T} |\nabla T|^{-1} dS \right)_i}, \quad (3.16)$$

with a constant density across all surfaces,  $n^2(T) \equiv n_e^2(T)$ , which is the electron density at a temperature (T), therefore Equation 3.14 can be written as

$$\xi_V(T) = n_e^2 \frac{dV}{dT} [\text{cm}^{-3} \text{ K}^{-1}], \quad (3.17)$$

which is the differential emission measure in volume. It is also useful to define the column emission measure (the amount of plasma along the line-of-sight) which is achieved

by dividing Equation 3.17 by the observed area of the emitting source ( $\text{cm}^2$ ). The column differential emission measure for a plasma with a constant density is given by

$$\xi_c(T) = n_e^2 \frac{dh}{dT} [\text{cm}^{-5} \text{K}^{-1}] \quad (3.18)$$

where  $n_e(h(T))$  is the electron density along the line-of-sight,  $h$ , and from this point we define  $\xi(T) \equiv \xi_c(T)$ . To compare to the EM-loci (§ 3.2.2), we can also interchangeably use the *emission measure distribution* (EMD),

$$\xi(T) dT = n_e^2 dh [\text{cm}^{-5}]. \quad (3.19)$$

In order to reconstruct the DEM, multiple measurements of  $I_\alpha$  (for multiple lines) need to be obtained, and it is necessary to address the problem of solving Equation 3.15 for  $\xi(T)$ .

### 3.2.1 Inverse Problems

Finding the differential emission measure/emission measure distribution is a widely-used technique throughout solar and stellar astrophysics returning the temperature distribution of the underlying emitting plasma by combining the line intensity, or narrow-band filter measurements. However, the direct recovery is an inverse problem: the observed intensity is the convolution of the emission lines, or filters sensitivity to temperature, and the physical properties of the underlying plasma. The basic idea is that if one samples enough of the temperature range, it is in theory possible to recover information about the underlying plasma by inversion; however, due to the nature of this problem any attempt to reconstruct the DEM leads to substantial noise amplification.

In a *continuous problem* of the form

$$d(x) = \int_a^b g(x, \epsilon) m(\epsilon) d\epsilon, \quad (3.20)$$

such as that in Equation 3.15,  $d(x)$  is the observable;  $g(x, \epsilon)$  is the kernel that encodes all physics relating a model ( $m(\epsilon)$ ; the DEM,  $\xi(T)$ , in Equation 3.15) to the data. In these types of equations the interval  $[a, b]$  may be finite or infinite.

Equations in this general form—where the model is unknown—are referred to as Fredholm integral equations of the first kind (e.g. Courant & Hilbert, 1953). The Fred-

holm Equation (Equation 3.20, and therefore Equation 3.15) is a continuous-continuous forward problem. However, in physics we generally only measure a finite number of data points so this is an idealised representation of the problem. In order to solve this problem we generally need to discretise these equations, and this can be represented as  $d = \mathbf{G}m$  in the case of Equation 3.20 (e.g. Craig & Brown, 1976). Equation 3.15 is *well-posed* (in the sense of Hadamard) if for all input data:

1. a solution *exists*: for a set of observations, a DEM(T) solution exists.
2. the solution is *unique*: there is one DEM(T) that represents the observations.
3. the solution is *stable*: for a set of observations that produces a DEM(T), a small change in the input observations cannot produce large deviation of the DEM(T).

Unsurprisingly, the Fredholm equation of the first kind (therefore Equation 3.15) is a classic ill-posed inverse problem, and these three cases indicate pitfalls of differential emission measure inversion (Craig & Brown, 1976).

In order to obtain the line-of-sight DEM,  $\xi(T)$ , from a finite set of spectroscopic or narrowband measurements, such as those obtained by *Hinode*/EIS and *SDO*/AIA, the original problem (Equation 3.15) must be rewritten as a set of linear equations and thus, the integral equation

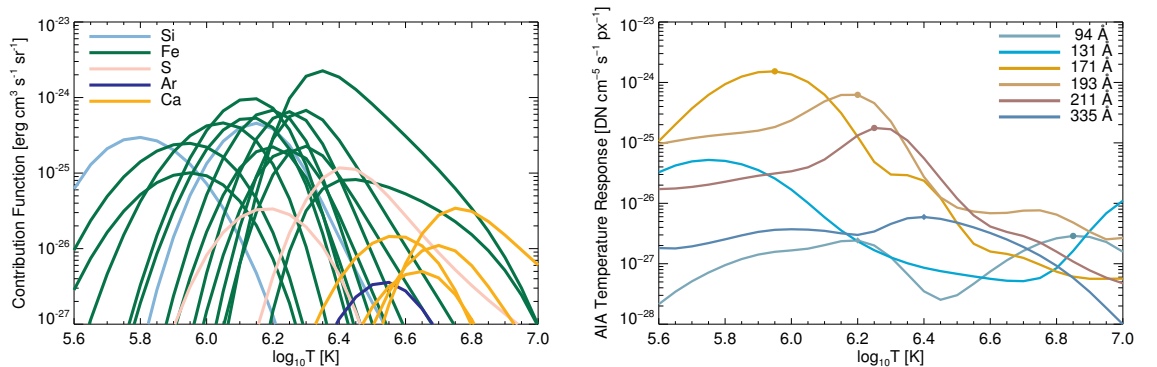


Figure 3.1: *Left*: Contribution functions for 22 spectral lines observed by *Hinode*/EIS (cf. Warren *et al.*, 2012). Each element is colour coded by ion. *Right*: Temperature response functions for the *six* optically thin *SDO*/AIA channels.

$$g_i = \int_T K_i(T) \xi(T) dT, \quad (3.21)$$

can be written in the discretized form

$$g_i = \sum_{j=1}^N \mathbf{K}_{i,j} \xi(T_j), \quad (3.22)$$

where as before,  $g_i$  is the observable. This is either the integrated intensity ( $I_\alpha$ , Equation 3.15) for a given spectral line ( $i = 0, \dots, N$ ), or the imaged data number (DN) for a specific narrowband filter,  $i$ ;  $\xi(T_j)$  is the DEM at over a discrete temperature range ( $j = 0, \dots, M$ ) corresponding to the temperature range and resolution required. In this case, for spectroscopic data,  $\mathbf{K}_{i,j} \equiv \mathbf{G}_{i,j}$ , which corresponds to the contribution function of the line transition over the same temperature range (Equation 3.15; Figure 3.1, *left*). For the application to narrowband data, such as those observed by *SDO/AIA*, the same equations hold but in that case  $\mathbf{K}_{i,j}$  represents the physics of the emission lines *and* the instrumental response: *the temperature response function* (Figure 3.1, *right*). For the generalised case, the set of linear equations in matrix form are therefore

$$g_i = \mathbf{K}_{i,j} \xi(T_j). \quad (3.23)$$

It must be noted that due to the ill-posed nature of this problem, any attempt to reconstruct the DEM directly (i.e.,  $\xi(T_j) = \mathbf{K}_{i,j}^{-1} g_i$ , where  $M = N$ , and  $\mathbf{K}^{-1}$  is the inverse of the matrix  $\mathbf{K}$ ) leads to substantial noise amplification (Craig & Brown, 1977).

### 3.2.2 A Direct Approach

Prior to discussing the process of trying to solve the set of linear equations in Equation 3.23, a direct approach to determining the temperature distribution along the line-of-sight using only the observed line intensities and their contribution functions, is to plot the emission measure loci (EM-loci). The EM-loci for an observed spectral line,  $\alpha$  is defined as  $I_\alpha/G(n_e, T)$ , and together represent the theoretical maximum of the emission measure distribution. Independently, each EM-loci represents an upper-limit of the  $EM(T_i)$  when *all EM* is at  $T = T_i$ . For an isothermal plasma ( $T = T_c$ ) all of the EM-loci curves will meet at the point defined as  $T_c$ , EM. This is however only true if

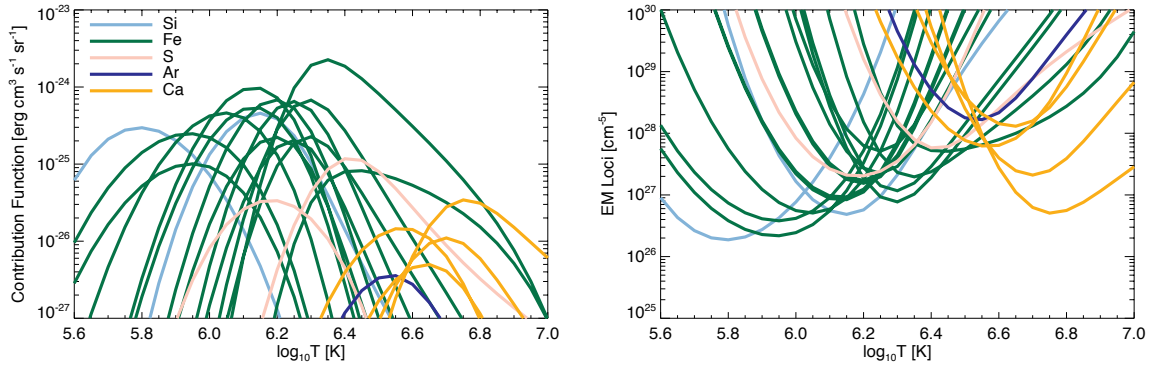


Figure 3.2: *Left*: Contribution functions for 22 spectral lines observed by *Hinode*/EIS, and described in Table 3.1 (cf. Warren *et al.*, 2012). Each element is colour coded by ion. *Right*: EM-loci curves for the same set of lines shown in Table 3.1, where  $I_\alpha$  are a set of observed intensities

the fluxes are accurately calculated with correct atomic physics and the lines are not blended. This method was first introduced by Strong (1979) (see Del Zanna & Mason, 2018), and this method has been used extensively in the literature (generally when only a few lines were available, e.g. Veck *et al.*, 1984; Jordan *et al.*, 1987; Landi *et al.*, 2002; Del Zanna *et al.*, 2002).

In addition to the EM-loci approach, other methods to measure the electron temperature exist and have been used throughout the literature. These include considering the intensity ratio of two emission lines (of the same ion) of different excitation energies. In this case, it can be shown (e.g. Del Zanna & Mason, 2018) that the ratio is temperature dependent if the thermal energy of the electrons is smaller than the excitation energies, and the electron temperature can also be extracted from ratios of lines of different ionisation stages of the same element.

To demonstrate the EM-loci approach, Table 3.1 contains 22 observed line intensities (ranging from  $\log_{10} T = 5.8 - 6.75$ ) and their uncertainties from an *Hinode*/EIS observation of NOAA AR 11259 (see Warren *et al.*, 2012). Figure 3.2 shows the contribution functions obtained from the CHIANTI atomic database under the assumption of coronal abundances (Feldman, 1992) and using the CHIANTI ionisation fractions (Dere *et al.*, 2009) for the 22 emission lines presented in Table 3.1. The contribution functions are plotted as a function of temperature, and the equivalent EM-loci curves are shown (*right*). From Figure 3.2 it is clear that this plasma is multi-thermal as no

Table 3.1. *Hinode*/EIS Observations of an Active Region Core (Warren *et al.*, 2012)

<i>Hinode</i> /EIS Emission Line	Wavelength [Å]	$\log_{10}T$ [K]	$I_{obs}$ [erg cm <sup>-2</sup> s <sup>-1</sup> sr <sup>-1</sup> ]	$\sigma_{I_{obs}}$ [erg cm <sup>-2</sup> s <sup>-1</sup> sr <sup>-1</sup> ]
Si VII	275.36	5.80	55.53	12.38
Fe IX	188.49	5.90	53.98	11.98
Fe IX	197.85	5.95	38.37	8.48
Fe X	184.54	6.05	234.89	51.87
Fe XI	180.40	6.15	807.94	178.26
Fe XI	118.28	6.15	494.16	108.76
S X	263.23	6.20	68.43	15.15
Si XI	258.37	6.15	221.05	48.74
Fe XII	192.39	6.20	342.98	75.48
Fe XII	195.12	6.20	1167.41	256.86
Fe XIII	202.04	6.25	1041.83	229.28
Fe XIII	203.83	6.25	1444.68	318.00
Fe XIV	264.79	6.30	520.71	114.61
Fe XIV	270.52	6.30	264.71	58.28
Fe XV	284.16	6.35	4429.94	974.72
S XIII	256.69	6.40	680.26	149.76
Fe XVI	262.97	6.45	418.98	92.24
Ar XIV	194.40	6.55	59.38	13.10
Ca XIV	193.87	6.55	90.15	19.87
Ca XV	200.97	6.65	64.86	14.40
Ca XVI	208.59	6.70	23.10	6.74
Ca XVII	192.85	6.75	17.41	4.83

common crossing point is observed. To demonstrate the case of an isothermal plasma, Figure 3.3 shows the case for the same set of contribution functions, where the line intensities have been synthesised from two temperature distributions represented by Dirac-delta functions (of a given  $T_c$ ,  $EM$ ).

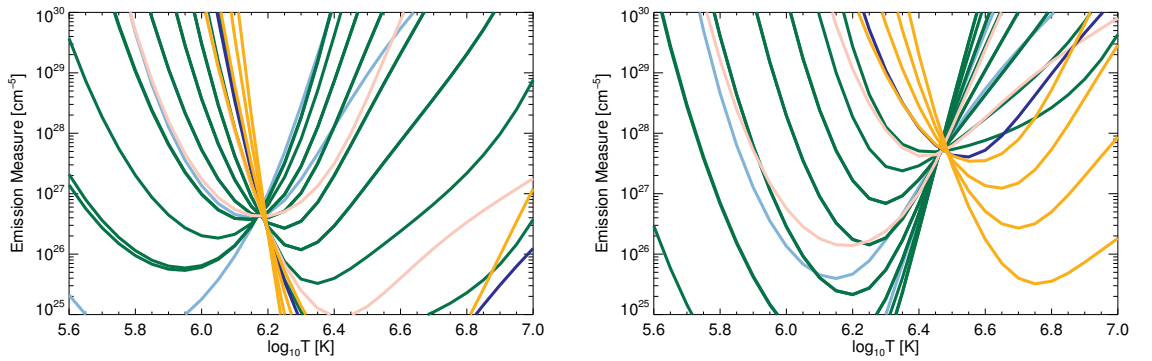


Figure 3.3: EM-loci curves for two synthesised isothermal plasmas. Each panel shows a different synthesised plasma defined as a Dirac-delta function of temperature  $T$ , and EM. In comparison to Figure 3.2, a common crossing point is observed for each example.

### 3.3 Difficulties in Reconstructing the DEM

In practice, all terms of Equation 3.21 are subject to errors and uncertainties. Not only are these errors observed in the directly observed quantities such as the line flux, but also in the atomic data, ion populations, and abundances. Blends of unresolved lines not considered in line flux measurements, and errors in instrument calibration also contribute to the systematic uncertainties.

From the contribution functions shown in Figure 3.2, if the uncertainties were assumed to be negligible,  $G(n_e, T)$  alone provides a limitation of the determination of the differential emission measure. It is clear that  $G(n_e, T)$  have a non-negligible width in temperature-space (with only slight dependence on the electron density), and if the number of lines were to be small (as in the case where *six* optically-thin *SDO/AIA* channels are used), then the DEM would be under-sampled, and even with a large number of lines, oversampling the temperature domain could occur. In this case different lines (sensitive to the same region of temperature-space) could lead to conflicting results (for a complete discussion see Phillips *et al.*, 2012).

An approach to find the best approximate solution is to find an equation that represents  $\xi(T)$  and minimises a loss function determined from observations and the predictions from the forward problem. Finding the DEM from Equation 3.21 can be

written as the least-squares problem

$$\left\| \frac{\mathbf{K}\xi(T) - \mathbf{g}}{\delta\mathbf{g}} \right\|_2^2 = \min, \quad (3.24)$$

where  $\|x\|_2$  is the Euclidian (L2) norm:  $\|x\|_2 = \sqrt{\sum_{i=1}^N x_i^2} = \sqrt{x_1^2 + x_2^2 + \dots + x_N^2}$ . Unfortunately, this does not have a unique solution, and additional constraints need to be implemented in order to provide a unique (and meaningful) solution. This can be done by adding linear constraints to the DEM (e.g. [Hannah & Kontar, 2012, § 3.4.1](#)), or indeed a solution can be found through forward fitting.

In order to constrain the DEM solutions further, a number of constraints grounded in the physics of the problem can be applied. For example, positivity of the DEM could be required (no negative emission measure will be observed), or an initial guess of the solution can be provided by the theoretical maxima given by the isothermal solutions (the EM-loci; [Figure 3.2](#)).

### 3.4 DEM Reconstruction Techniques

This chapter has introduced the concept of the differential emission measure (DEM), an ill-posed inverse problem. Within the literature there are a wide number of techniques available to reconstruct the DEM by inversion or forward fitting in order to limit to growth of uncertainties that comes about through inversion.

One of the long-standing methods to determine the DEM is the Metropolis-Hastings Markov Chain Monte Carlo (MCMC[M]) method introduced by [Kashyap & Drake \(1998, 2000\)](#) (§ 3.4.3) to search the large parameter space for a solution. More recently, [Weber \*et al.\*, 2004](#) represent the DEM as splines evenly spaced in  $\log_{10}T$ , § 3.4.2; [Hannah & Kontar \(2012\)](#) introduced the method of Tikhonov Regularisation (Regularised Inversion, § 3.4.1) which adds linear constraints to Equation 3.21; and [Cheung \*et al.\* \(2015\)](#) use the concept of sparsity to obtain a DEM solution that is faithfully represented by the least number of (pre-defined) basis functions (§ 3.4.4).

Alternate methods that are not discussed in detail this chapter, but should be mentioned include the forward fitting of multiple Gaussians, [Aschwanden & Boerner, 2011](#), power-laws (e.g. [Jordan, 1976](#)), or a combination ([Guennou \*et al.\*, 2013](#)), however the inherent issue with forward fitting techniques is that if the assumption on the form of

the DEM is inherently wrong, the results are then difficult to interpret.

The next sections will outline DEM codes used in this thesis, and present example DEM solutions for each method from spectroscopic and narrowband data (where possible).

### 3.4.1 Tikhonov Regularised Inversion (RI)

One approach is to perform Tikhonov regularisation (Tikhonov, 1963; Hannah & Kontar, 2012). This method<sup>2</sup>, adds linear constraints to the problem, and can therefore be interpreted as a *penalised* least squares problem. In this approach, starting with Equation 3.21, an additional term to represent the uncertainty on the observable is included outside the integral ( $+ \delta g_i$ ). Tikhonov regularisation solves the Lagrange multiplier problem:

$$\mathcal{L}(\mathbf{g}) \equiv \left\| \frac{\mathbf{K}\xi(T) - \mathbf{g}}{\delta \mathbf{g}} \right\|_2^2 + \lambda \|\mathbf{L}(\xi(T) - \xi_0(T))\|_2^2 = \min, \quad (3.25)$$

which is to say, we want to minimise  $\left\| \frac{\mathbf{K}\xi(T) - \mathbf{g}}{\delta \mathbf{g}} \right\|_2^2$  subject to  $\|\mathbf{L}(\xi(T) - \xi_0(T))\|_2^2 \leq \text{constant}$ , where  $\mathbf{L}$  is the constraint matrix,  $\lambda$  is the regularisation parameter, and  $\xi_0(T)$  is an initial guess of the DEM which can be *zero*. In this form,  $\|\mathbf{L}\xi(T)\|_2^2$  aims to reduce oscillations that are the result of noise amplification and  $\mathbf{L}$  controls the degree of regularisation. For example, we may wish to obtain a solution which minimises  $\xi(T)$  (which is to minimise the total EM required to obtain a solution), and in such a case,  $\mathbf{L}_0 \equiv \mathbf{L} = \mathbf{I}$  (the identity matrix). This is known as *zeroth-order regularisation*. We may also wish to minimise another measure such as  $\mathbf{L}_1\xi$ . Penalising  $\|\mathbf{L}_1\xi(T)\|_2$  will therefore favour a solution that is relatively flat ( $L_1$  is proportional to the first derivative of  $\xi$ ); similarly, as  $L_2$  is proportional to the second derivative of  $\xi$ , penalising  $\|\mathbf{L}_2\xi(T)\|_2$  will favour a smooth solution. We therefore refer to regularisation as zeroth-, first-, and second-order regularisation, respectively. Most importantly, unlike Equation 3.24, the solution to Equation 3.25 exists, and is unique.

This can be solved by taking the Generalised Singular Value Decomposition

<sup>2</sup>The code is available at <https://github.com/ianan/demreg>

$$\xi_\lambda(T) = \sum_{i=1}^M \frac{\phi_i^2}{\phi_i^2 + \lambda} \left( \frac{(\mathbf{g} \cdot \mathbf{u}_i) \mathbf{w}_i}{\gamma_i} + \frac{\lambda \xi_0(T)}{\gamma_i^2} \right), \quad (3.26)$$

with  $\phi_i = \gamma_i/\beta_i$ , (Hansen, 1992).  $\xi_\lambda(T)$  can be analytically obtained with the only variable being the regularisation parameter  $\lambda$ , using Morozov's discrepancy principle (Morozov, 1967):

$$\frac{1}{N} \left\| \frac{\mathbf{K} \xi_\lambda(T) - \mathbf{g}}{\delta \mathbf{g}} \right\|_2^2 = \alpha. \quad (3.27)$$

Here we define  $\alpha$  as a tweak parameter, which controls the  $\chi^2$  of the solution. We typically take  $\alpha = 1$  ( $\chi^2 \approx 1$ ), which allows  $\xi_\lambda(T)$  to be determined, and subsequently, Equation 3.25 can therefore be solved.

### 3.4.1.1 Error Estimation

Returning to the original equation for matrix formulation of the DEM (Equation 3.23), if we suppose that we know the true DEM,  $\xi_{true}(T)$ , then  $g = \mathbf{K} \xi_{true} + \delta g$ . The regularised solution is represented as  $\xi_\lambda(T) = \mathbf{R}_\lambda g$ , and it therefore follows that the estimated error on the DEM is,

$$\begin{aligned} \delta \xi &= \xi_\lambda - \xi_{true} \\ &= \mathbf{R}_\lambda g - \xi_{true} \\ &= \mathbf{R}_\lambda (\mathbf{K} \xi_{true} + \delta g) - \xi_{true} \\ &= (\mathbf{R}_\lambda \mathbf{K} - \mathbf{I}) \xi_{true} + \mathbf{R}_\lambda \delta g \end{aligned} \quad (3.28)$$

which is the result described in Hannah & Kontar (2012). Here, the first component represents the horizontal errors, and the second component represents the vertical errors.

From the equations for  $\xi_\lambda(T)$  and  $\xi_{true}(T)$  at the beginning of this section, it is clear that the temperature resolution is how much  $\mathbf{R}_\lambda \mathbf{K}$  differs from  $\mathbf{I}$ , the identity matrix. If this problem was well-posed,  $\mathbf{R}_\lambda \mathbf{K} \equiv \mathbf{I}$ , and  $\mathbf{R}_\lambda$  would be the inverse of  $\mathbf{K}$ . As a result,  $\mathbf{R}_\lambda \mathbf{K}$  is not the identity matrix, and the full-width at half maximum of  $\mathbf{R}_\lambda \mathbf{K}$  for a given temperature bin provides the temperature resolution.

### 3.4.1.2 Tikhonov Regularisation DEM Examples

Returning to the set of observations presented in Table 3.1, the emission measure distribution can be obtained<sup>3</sup>. For zeroth-order regularisation where the regularisation matrix,  $L$ , has been normalised by the EM-loci to constrain the solution, the emission measure distribution (EMD) is shown in Figure 3.4 for the same active region as used in Figure 3.2. To compute the solution shown in Figure 3.4, we have set  $\alpha = 1$ , positivity is enforced by choosing the smallest solution to Equation 3.27 (where  $\xi(T) > 0$ ), and an initial guess,  $\xi_0(T)$ , equal to the minimum of the EM-loci (See Figure 3.2) has been provided.

The output is the emission measure distribution (black line) with error bars in both temperature and emission measure overplotted in blue. From this Figure it is clear that the solution is below the EM-loci, and there are significant uncertainties at high-temperatures ( $\log_{10}T \gtrsim 6.7$ ), and also at low-temperatures ( $\log_{10}T \lesssim 5.9$ ). This behaviour is also clearly reflected in the  $\mathbf{R}_\lambda\mathbf{K}$  matrix (§ 3.4.1.1). Figure 3.5 shows the  $\mathbf{R}_\lambda\mathbf{K}$  matrix with the rows providing information on the temperature resolution. The  $\mathbf{R}_\lambda\mathbf{K}$  matrix is almost diagonal over  $\log_{10}T$ . As seen in Figure 3.4, there is deviation from the diagonal at both high and low temperatures, but this is expected as there is little constraint in this region (e.g. Warren *et al.*, 2012). Additional soft X-ray observations (such as those from *MaGIXS*, § 2.2.2), or hard X-ray observations (e.g. *NuSTAR*, Chapter 4, and as will be shown in Chapter 5), would be able to constrain the higher temperature component of the EMD.

It is important to note that without the positivity flag we obtain a solution that is oscillatory between positive and negative values. This is similar to the situation in Figure 17 in Hannah & Kontar (2012), and highlights a solution that is over-regularised (Craig, 1977; Bertero *et al.*, 1985).

In order to demonstrate the different orders of regularisation, Figure 3.6 compares the zeroth-order regularised solution (see Figure 3.4) to the first-, and second-order regularised solutions (as plotted in Figure 3.4). The corresponding  $\mathbf{R}_\lambda\mathbf{K}$  matrices for zeroth-, first-, and second-order regularisation are shown in Figure 3.7. Figure 3.6 shows the EMD solutions (as in Figure 3.4) for the zeroth-, first-, and second-order solutions (black, dark grey, and grey). While uncertainties are omitted for clarity (cf. Figure 3.4 for uncertainties on the zeroth-order solution), Figure 3.7 displays the respective  $\mathbf{R}_\lambda\mathbf{K}$

<sup>3</sup>using the IDL code located at <https://github.com/ianan/demreg>

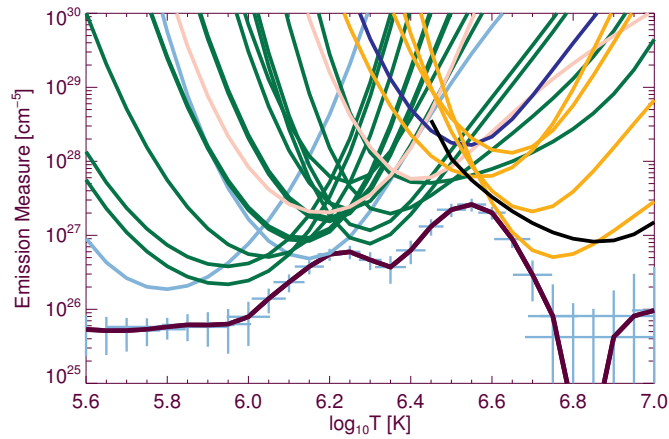


Figure 3.4: Emission measure distribution determined by Regularised Inversion for the 22 *Hinode*/EIS emission line observations outlined in Table 3.1 (see Warren *et al.*, 2012). The EM-loci are overplotted and provide a theoretical maximum of emission measure. The emission measure distribution (black line), where the error bars in both  $\log_{10}T$  and Emission Measure are plotted in blue.

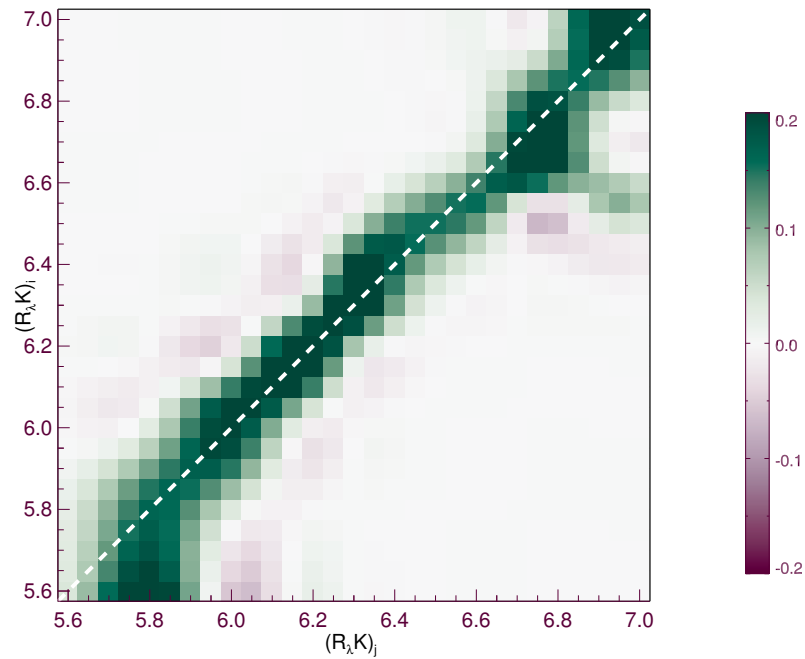


Figure 3.5:  $\mathbf{R}_\lambda \mathbf{K}$  matrix with each row providing the temperature resolution (for each temperature,  $T_j$ ).

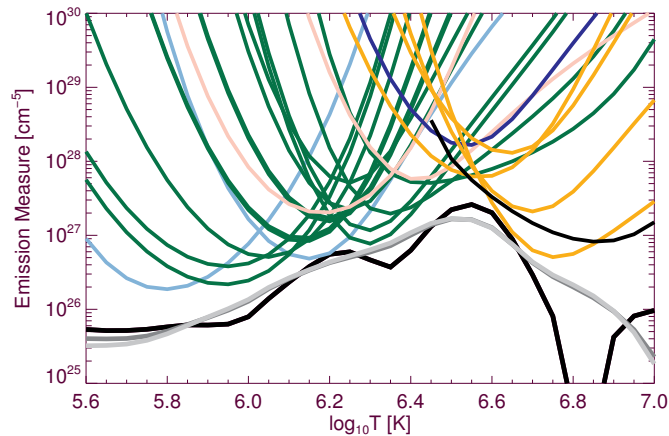


Figure 3.6: Emission measure distribution determined by Regularised Inversion for the 22 *Hinode*/EIS emission line observations outlined in Table 3.1 (see Warren *et al.*, 2012). The EM-loci are overplotted and provide a theoretical maximum of emission measure. The emission measure distribution for zeroth-order regularisation is shown (as in Figure 3.4, black line); first-, and second-order regularisation are shown in dark grey and grey, respectively.

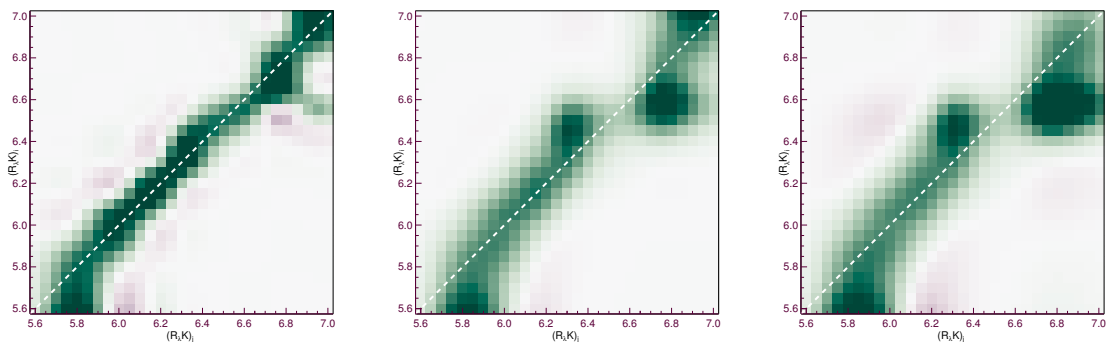


Figure 3.7:  $\mathbf{R}_\lambda \mathbf{K}$  matrices for the zeroth-, first-, and second-order solutions (*left to right*) for the EMDs shown in Figure 3.6. With increasing order, there is significant deviation from the diagonal with uncertainties generally increasing.

matrices for each solution. These are observed to increase in FWHM with higher-order, and above  $\log_{10} T \sim 6.7$  K there are significant uncertainties present in the second-order solution. With a higher order solution, we are forcing a “smooth”/flatter solution. This can result in more EM at high-, and low temperatures, blurring the  $\mathbf{R}_\lambda \mathbf{K}$  matrix (increasing uncertainties).

Finally to demonstrate DEM inversion with *SDO/AIA* data, we extracted the *SDO/AIA* intensities from the same region (at the same time) as those presented in Table 3.1. Using the *six* optically-thin *SDO/AIA* channels and *SDO/AIA* response functions, we are able to recover the equivalent *SDO/AIA* EMDs for zeroth-, first-, and second-order regularisation (Figure 3.8).

Figure 3.8 shows the three EMDs (zeroth, black; first, dark grey; second, grey), with the *SDO/AIA* EM-loci overplot. In addition to the *SDO/AIA* loci, Figure 3.8 shows the *Hinode/EIS* EM-loci for reference, as the EMD should also lie below the *Hinode/EIS* EM-loci (see § 3.2.2).

The  $\mathbf{R}_\lambda \mathbf{K}$  matrix is also shown in Figure 3.9 for zeroth-order regularisation only. As would be expected (due to the broad nature of the *SDO/AIA* temperature response functions), the EMD is constrained (to a comparable degree to spectroscopic observations) only over a small region of temperature space. This region, located at  $\log_{10} T = 6.1 - 6.5$ , is well-constrained by many filter channels.

Additionally, for the *SDO/AIA* EMD there is considerable amount of addition emission measure at  $\sim 10$  MK which is poorly constrained by *SDO/AIA*, and in order to constrain this emission measure further, additional observations are required (e.g. *Hinode/XRT*, and *NuSTAR*; see Chapter 5).

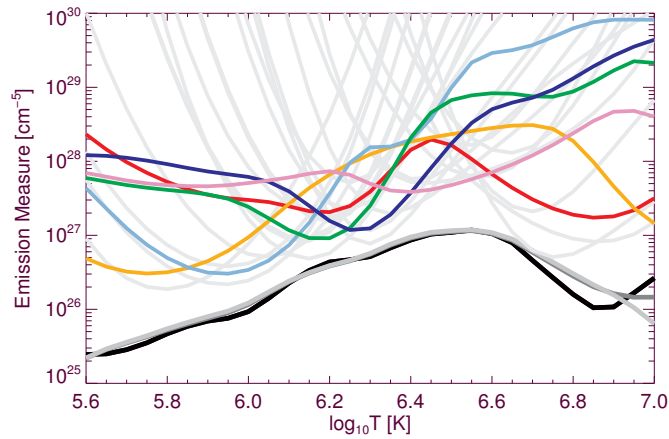


Figure 3.8: Emission measure distribution determined by Regularised Inversion for the *six* optically-thin EUV *SDO/AIA* observations. The *SDO/AIA* EM-loci are over-plotted in addition to the *Hinode/EIS* EM-loci and provide a theoretical maximum of emission measure. The emission measure distribution for zeroth-order regularisation is shown as in Figure 3.4 (black line); first-, and second-order regularisation are shown in dark grey and grey, respectively.

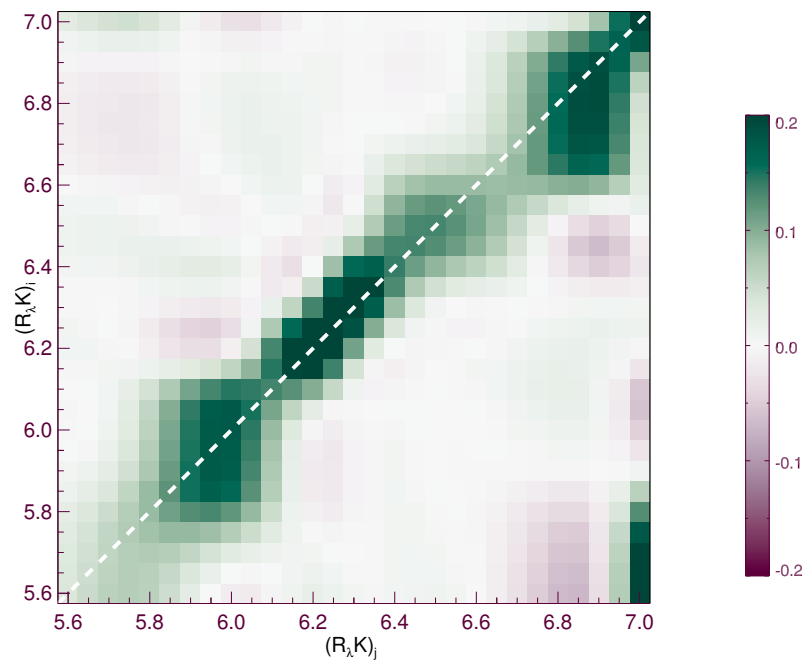


Figure 3.9:  $\mathbf{R}_\lambda \mathbf{K}$  matrix with each row providing the temperature resolution (for each temperature,  $T_j$ ). In comparison to Figure 3.5, the  $\mathbf{R}_\lambda \mathbf{K}$  matrix is similarly constrained over only a small subset of the temperature-space.

### 3.4.2 Iterative Least-Squares Approach

An iterative least-squares approach has been implemented by Golub *et al.* (2004); Weber *et al.* (2004) and is available as part of SSWIDL (`xrt_dem_iterative2.pro`<sup>4</sup>; XIT). XIT produces a least-squares fit to the observation with the DEM represented by a spline with knots spaced evenly in  $\log_{10}T$ .

In order to reconstruct a DEM for a set of observations, a (flat) starting DEM is assumed (see Figure 3.10), where the number of spline knots equals the number of input channels (with a maximum of seven spline knots). Synthetic fluxes from this flat DEM are generated, and then compared to the predicted observations in each filter. The optimal DEM is found by minimising  $\chi^2$  with the `mpfit` routines<sup>5</sup>. These use the non-linear least-squares method based on the FORTRAN MINPACK-1<sup>6</sup> routines.

Figure 3.10 (*top*) shows the output of a modified version of `xrt_dem_iterative2.pro` (to demonstrate the process of this method), from a flat DEM at iteration *zero* (light blue), to the final DEM (blue - black) with the *six* spline knots are denoted by filled circles. Figure 3.10 (*bottom*) shows  $\chi^2$  value as a function of iteration using the same colour table.

#### 3.4.2.1 Error Estimation

Uncertainties on the DEM can be calculated with Monte Carlo (MC) iterations: input data is perturbed by an amount randomly drawn from a Gaussian distribution with a standard deviation equal to the uncertainty in the observation. The routine described in § 3.4.2 is repeated for each MC iteration. Starting at a flat DEM, least-squares minimisation is performed and the collection of DEMs that are a result of MC iterations can then be assumed to represent uncertainty. It should be noted, that there is no guarantee that the  $\chi^2$  of the MC iterations is near the  $\chi^2$  of the original DEM solution. It is therefore advisable that for each MC iteration plotted, the  $\chi^2$  value is considered.

#### 3.4.2.2 Iterative Least-Squares DEM Examples

Figure 3.11 shows the *SDO/AIA* EMD obtained using the `xrt_dem_iterative2.pro` code, and was initially designed for *Hinode/XRT* observations. The *SDO/AIA* obser-

<sup>4</sup>[https://hesperia.gsfc.nasa.gov/ssw/hinode/xrt/idl/util/xrt\\_dem\\_iterative2.pro](https://hesperia.gsfc.nasa.gov/ssw/hinode/xrt/idl/util/xrt_dem_iterative2.pro)

<sup>5</sup><http://cow.physics.wisc.edu/~craigm/idl/idl.html>

<sup>6</sup><http://www.netlib.org/minpack/>

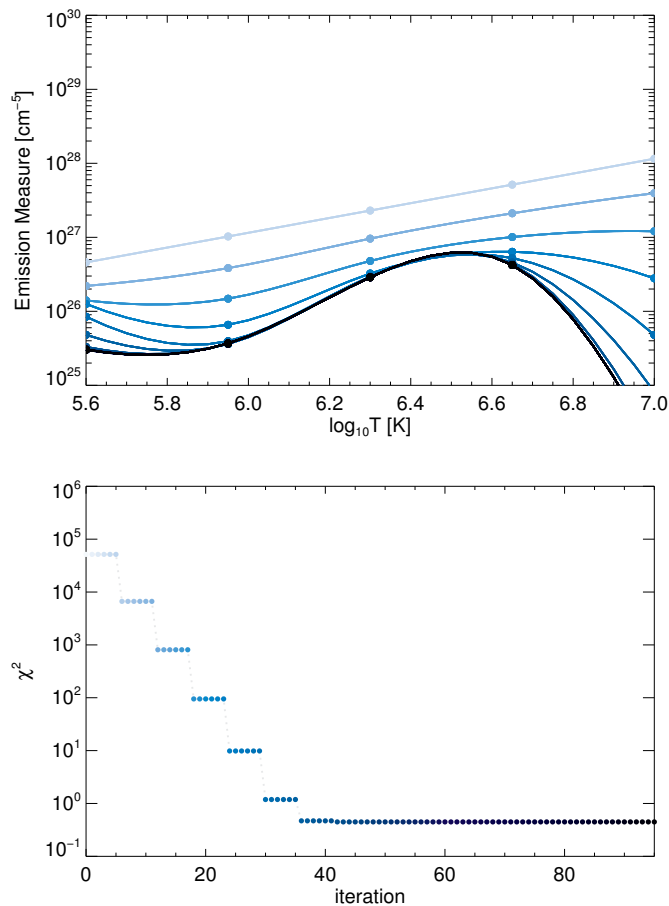


Figure 3.10: A single run of `xrt_dem_iterative2.pro`, using 6 channels of *SDO/AIA* observations. *Top*: iterative least-squares EMD for increasing iterations from a flat DEM, to the final form (light to dark blue). Six spline knots are highlighted as filled circles, evenly spaced in  $\log_{10}T$ . *Bottom*:  $\chi^2$  as a function of iteration. The colours of each iteration correspond to the same colours of the EMDs (*top*), and show a decrease in  $\chi^2$ .

vations were obtained for the same region as the *Hinode/EIS* observations in Table 3.1, and Figure 3.11 shows the EMD (first shown in Figure 3.10) as a dark blue line, with the addition of 300 MC iterations (overplotted as dashed lines in blue). These iterations are performed to understand the uncertainty on the DEM. As the DEM is calculated with spline knots evenly spaced in  $\log_{10}T$ , the DEMs are inherently smooth.

Furthermore, in order to compare to Figure 3.4, the `xrt_dem_iterative2.pro` code was slightly modified to accept the *Hinode/EIS* lines described in Table 3.1. In

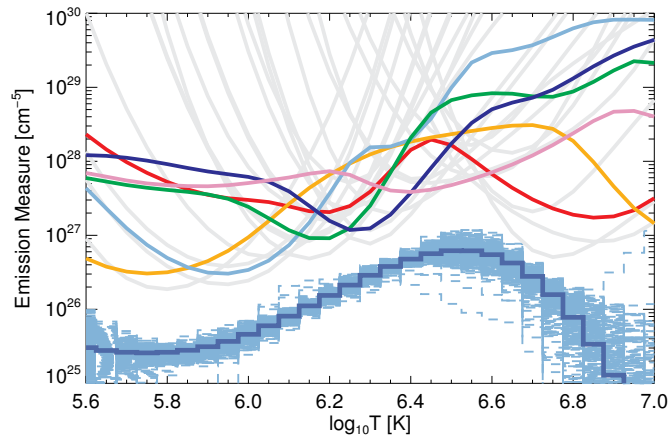


Figure 3.11: `xrt_dem_iterative2.pro` emission measure distribution for the *six* optically-thin *SDO/AIA* observations. The EMD shows the *SDO/AIA* EM-loci, and *Hinode/EIS* EM-loci (grey) for comparison. 300 MC iterations are overplotted in light blue, and provide an approximate error region.

this case (Figure 3.12), there are *seven* spline knots evenly spaced in  $\log_{10}T$ , and the DEM captures similar information to that from RI (Figure 3.4): two peaks, one high-temperature peak at  $\log_{10}T = 6.15$ , and another at approximately  $\log_{10}T = 6.55$ . A characteristic of spline interpolation is a large increase of emission measure as one approaches the extremities. Figure 3.13 shows the final EMD with 300 MC iterations. Here, a significant amount of emission measure is seen at  $\log_{10}T = 5.6$  in the original solution, and traces of this can be seen at  $\log_{10}T = 7.0$  in the (light blue) MC iterations.

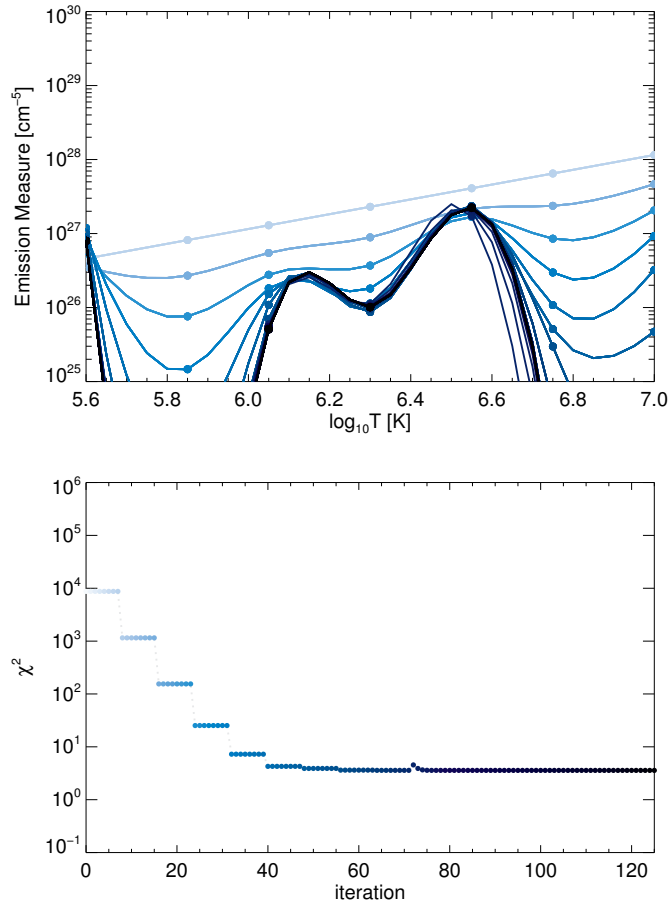


Figure 3.12: A single run of `xrt_dem_iterative2.pro`, using 22 channels of *Hinode*/EIS observations (Table 3.1). *Top*: iterative least-squares EMD for increasing iterations, from a flat DEM, to the final form (light to dark blue). Spline knots are highlighted as filled circles. *Bottom*:  $\chi^2$  as a function of iteration. The colours of each iteration correspond to the same colours of the EMD curve (*top*), and show a decrease in  $\chi^2$ .

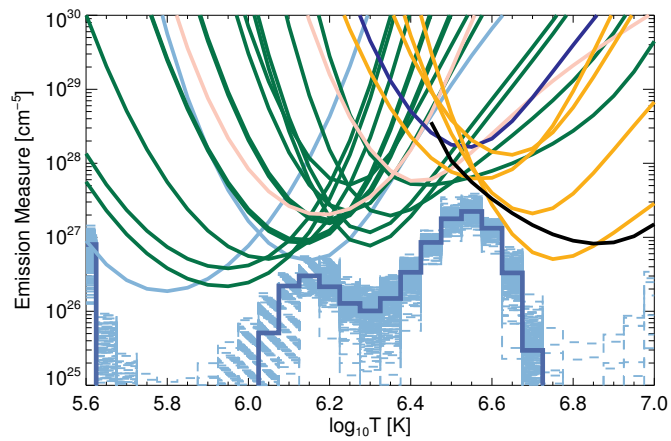


Figure 3.13: `xrt_dem_iterative2.pro` solution for the *Hinode*/EIS observations outlined in Table 3.1. The form of the EMD is similar to the RI EMD in Figure 3.4, and shows two peaks at similar temperatures, with the high-temperature peak at  $\log_{10}T = 6.55$ .

### 3.4.3 Markov-Chain Monte-Carlo MCMC[M]

The Metropolis-Hastings Markov-Chain Monte-Carlo, MCMC[M], algorithm of [Kashyap & Drake \(1998, 2000\)](#) is available as part of the `Package for the INterative Analysis of Line Emission (PINTofALE7)`. The MCMC[M] method is based on the Markov-Chain Monte Carlo process, with the aim of obtaining the most probable set of model parameters that describe the data by adopting a Bayesian approach.

Initially, a guess of the DEM solution is generated, and randomised adjustments are made in the set of parameters that define the initial DEM. One parameter is changed at a time, (depending only on the parameters at step  $t - 1$ ) in order to search the large parameter space for a small “volume” which accurately represents the data. For each step a new probability is calculated, and either accepted or rejected according to the Metropolis Algorithm ([Metropolis \*et al.\*, 1953](#)). While the MCMC[M] algorithm assumes no *a priori*, local smoothing is implemented based on the set of contribution functions, and the algorithm is computationally demanding.

Figure 3.14 shows the MCMC[M] EMD (black line) for the *Hinode*/EIS observations presented in Table 3.1, and the blue dotted lines represent 300 MC iterations.

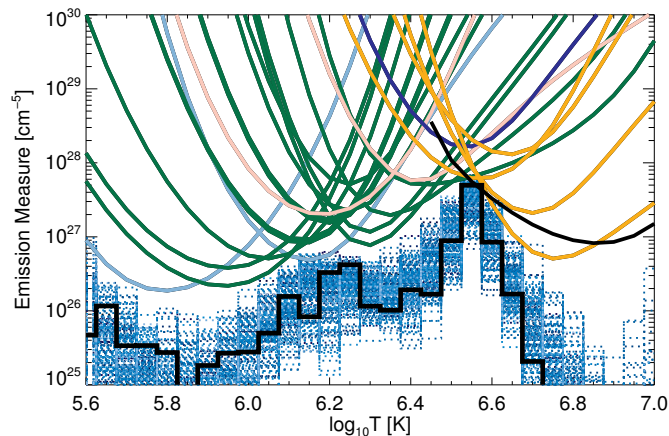


Figure 3.14: MCMC[M] emission measure distribution for the 22 *Hinode*/EIS observations shown in Table 3.1 (see [Warren \*et al.\*, 2012](#)), with EM-loci overplot. The blue dotted lines represent 300 MC iterations, and the black line indicates the iteration with the highest probability.

<sup>7</sup><http://hea-www.harvard.edu/PINTofALE/>

### 3.4.4 Basis Pursuit

In order to obtain a solution to a system of linear equations that is underdetermined we have seen that we must impose extra constraints. An alternative to Tikhonov Regularisation is to minimise the number of non-zero entries in order to obtain a sparse model—an ideal that is the basis of the field of compressed sensing. As has been discussed previously, the least-squares solution to this problem is to minimise the L2-norm. To enforce sparsity when solving this underdetermined system of linear equations, one can instead minimise the number of non-zero components. This method has been implemented by [Cheung \*et al.\* \(2015\)](#)<sup>8</sup>.

The matrix formulation of the integral in Equation 3.21 has been shown to be represented in the form,  $g = \mathbf{K}\xi$  (Equation 3.23), where  $g$  an  $m$ -tuple corresponding the measurements obtained by *SDO/AIA*;  $\mathbf{K}$  is an  $m \times n$  matrix representing the underlying physics, and  $\xi$  is the differential emission measure, an  $n$ -tuple. In order to represent the DEM as a set of basis functions, Equation 3.21 can be first represented as

$$g_i = \sum_{j=1}^n \mathbf{K}_{i,j} \mathbf{E} M_j, \quad (3.29)$$

and for this method, we can further represent the DEM as

$$\xi(\log_{10} T) = \sum_{k=1}^l b_k(\log_{10} T) x_k. \quad (3.30)$$

Here, we have rewritten the DEM in terms of a set of basis functions,  $b_{j,k}$ , with  $j = \log_{10} T$ , ( $k = 1, 2, \dots, l$ ), with quadrature coefficients  $x_k \geq 0$  ([Cheung \*et al.\*, 2015](#)). The final discretised version of the integral in Equation 3.21, as sums in  $\log_{10} T$ , is represented as

$$g_i = \sum_{j=1}^n \sum_{k=1}^l K_{i,j} B_{j,k} x_k \Delta \log_{10} T, \quad (3.31)$$

where as with previous examples,  $j = 1, \dots, n$  is the index of the temperature bin, and  $K_{i,j} = K_i(\log T_j)$  with dimensions  $m \times n$ . Important to the case here,  $B_{j,k} =$

<sup>8</sup>This code is available at [http://www.lmsal.com/~cheung/AIA/tutorial\\_dem/](http://www.lmsal.com/~cheung/AIA/tutorial_dem/).

$b_k(\log T_j)$  has dimensions  $n \times l$ , and the  $l$ -tuple,  $x$ , is the desired solution vector—the set of coefficients determined to represent the differential emission measure—with components  $x_k \Delta \log_{10} T$ , ( $k = 1, 2, \dots, l$ ). This is equivalent to  $g = \mathbf{K}\xi$ , and is denoted as  $g = \mathbf{D}x$  where the *dictionary matrix* is defined as  $\mathbf{D} \equiv \mathbf{K}\mathbf{B}$ , and  $\xi \equiv \mathbf{B}x$ .

#### 3.4.4.1 Basis Functions

From Equation 3.30, we have seen that the DEM is now represented in terms of basis functions. These basis functions can be defined by the user, however the basis functions described and validated for *SDO/AIA* inversions in Cheung *et al.* (2015) consist of Dirac-delta functions represented as

$$\begin{aligned} b_k^{Dirac}(\log T_j) &= 1, \text{ if } \log T_j = \log T_k, \\ &= 0, \text{ otherwise,} \end{aligned} \quad (3.32)$$

and Gaussians with widths  $a = \{0.1, 0.2, 0.6\}$ ,

$$\begin{aligned} \{b_k^a | k = 1, 2, \dots, n\}, \text{ where,} \\ b_k^a(\log T_j) &= e^{-\frac{(\log T_j - \log T_k)^2}{a^2}} \text{ if } |\log T_j - \log T_k| \leq 1.8a, \\ &= 0, \text{ otherwise.} \end{aligned} \quad (3.33)$$

Equation 3.33 describes Gaussians that are truncated for values of  $\log_{10} T_j$  outwith the temperature grid, and for values of  $|\log T_j - \log T_k| \leq 1.8a$ . We can then describe the basis matrix  $\mathbf{B}$  as

$$\mathbf{B} = (\mathbf{B}^{Dirac} | \mathbf{B}^{a=0.1} | \mathbf{B}^{a=0.2} | \mathbf{B}^{a=0.6}), \quad (3.34)$$

where for  $n$  temperature bins,  $\mathbf{B}$  has dimensions  $n \times 4n$  as  $\mathbf{B}$  is the concatenation of four different basis functions. As  $\mathbf{D} \equiv \mathbf{K}\mathbf{B}$ ,  $\mathbf{D}$  will have dimensions  $m \times 4n$ , and  $x$  will be a  $4n$ -tuple.

It is also important to note that with the choice of basis functions that are not normalised, if there are multiple solutions which produce an equal fit to the data, the method will favour the solution that consists of a single broad Gaussian rather than multiple narrower Gaussian (Cheung *et al.*, 2015).

While the aforementioned basis functions have been tested and validated for *SDO/AIA* data, recently, Su *et al.* (2018) demonstrated that this set of basis functions may over

predict X-ray fluxes as they inhibit a steep drop-off at high temperatures. [Su \*et al.\* \(2018\)](#) therefore recommend a set of basis functions that consist of Dirac-delta functions plus Gaussians with  $a = 0.1$ .

#### 3.4.4.2 The Method

In their papers, [Candès & Tao \(2006, 2007\)](#), show that this approach of sparsity for underdetermined linear systems often results in a better approximation to the real signal than least-squares. The sparsest solution is the solution to the optimisation problem

$$\text{minimise } \|x\|_0 \text{ subject to } \mathbf{D}x = g \quad (3.35)$$

where  $\|x\|_0$  is the L0 “norm” (the number of non-zero components, [Donoho, 2006](#)), and we recall that  $\mathbf{D} = \mathbf{K}\mathbf{B}$ . While this problem is extremely difficult to solve ([Cheung \*et al.\*, 2015](#)), [Candès & Tao \(2006\)](#) showed that an effective alternative is to solve the L1-problem. This is equivalent (or at least close) to the L0-norm. Fortunately, obtaining a solution to the L1-problem,

$$\text{minimise } \|x\|_1 \text{ subject to } \mathbf{D}x = g \quad (3.36)$$

is relatively easy as methods already exist to solve the linear program. In this case, the L1-norm is defined as

$$\|x\|_1 = \sum_{j=1}^n |x_j| = |x_1| + |x_2| + \dots + |x_n|. \quad (3.37)$$

As has been discussed in [Section 7.2.3](#), random errors on  $g$  may not satisfy  $g = \mathbf{D}x$ , and we also require a solution with values  $\geq 0$ . The convex objective function  $\|x\|_1$  therefore reduces to the linear form,  $\sum_j x_j$ . This can then be solved using the simplex algorithm ([Dantzig \*et al.\*, 1955](#)) which is designed to find optimal solutions to a such a problem where the objective function is linear and constraints are provided as inequalities. The method of [Cheung \*et al.\* \(2015\)](#) therefore solves the linear program that is represented as

$$\begin{aligned}
&\text{minimise } \sum_{j=1}^n x_j \text{ subject to:} \\
&\mathbf{D}x \leq g + \eta \\
&\mathbf{D}x \geq \max(g - \eta, 0) \\
&x \geq 0
\end{aligned} \tag{3.38}$$

where  $\eta$  is an  $m$ -tuple corresponding to the uncertainties on  $g$ , and there are two constraints on  $\mathbf{D}x$  attempt to limit the solution deviating from  $\mathbf{D}x = g$ .

This inversion problem in Equation 3.38 is an example of the *basis pursuit* optimisation principle. As described in [Chen \*et al.\* \(1998\)](#),

“Basis pursuit (BP) is a principle for decomposing a signal into an ‘optimal’ superposition of dictionary elements”.

This is to say that the optimal solution is the solution that minimises the L1-norm to find the most sparse representation of  $y$  from the overcomplete dictionary  $\mathbf{D}$ . In the simplex implementation of basis pursuit one finds an initial basis  $\mathbf{A}$  that consists of a number of columns of  $\mathbf{D}$ , for which  $\mathbf{A}^{-1}g$  is non-negative (see [Chen \*et al.\*, 2001](#)). This is iterated by swapping one term in the basis (from the dictionary) for one that is not included to improve the objective function. This continues until the optimal solution is reached.

Finally, as with the DEM reconstruction methods described by [Hannah & Kontar \(2012\)](#), and [Weber \*et al.\* \(2004\)](#), uncertainties in the vertical direction can be estimated with Monte Carlo iterations.

#### 3.4.4.3 Basis Pursuit DEM Examples

To demonstrate the output of the Basis Pursuit code, we first consider the case of DEM inversion using the set of basis functions described in [Cheung \*et al.\* \(2015\)](#). For this example, and in order to compare to the other methods in this Chapter we have modified the original code<sup>9</sup> that has been designed for *SDO/AIA* and *Hinode/XRT* data to allow input of spectroscopic line information (such as *Hinode/EIS* as described in Table 3.1).

<sup>9</sup>[http://www.lmsal.com/~cheung/AIA/tutorial\\_dem/](http://www.lmsal.com/~cheung/AIA/tutorial_dem/)

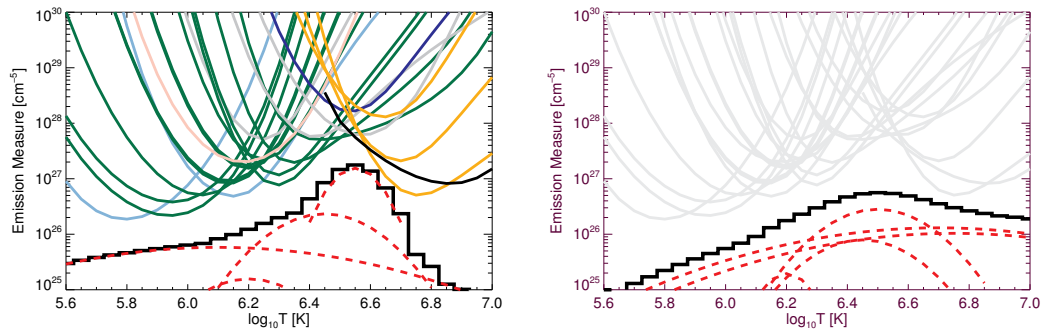


Figure 3.15: Basis Pursuit solution with a set of basis functions described by Dirac-delta functions and Gaussians with  $a = \{0.1, 0.2, 0.6\}$ . These are shown for *Hinode*/EIS observations (*left*), and the corresponding *SDO*/AIA observations (*right*).

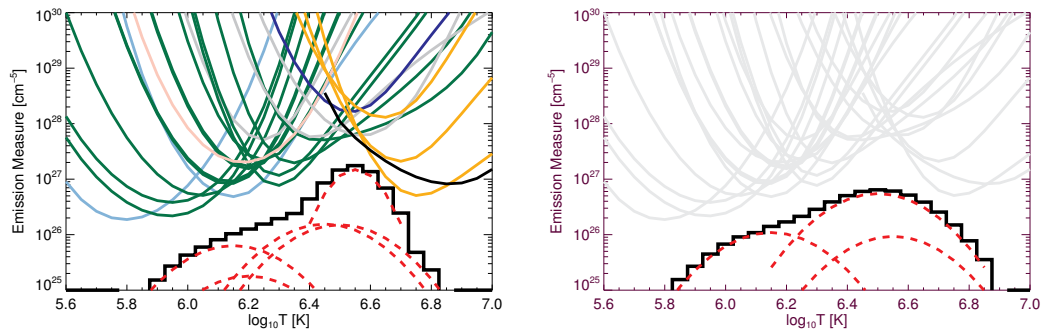


Figure 3.16: Basis Pursuit solution with a set of basis functions described by Dirac-delta functions and Gaussians with  $a = \{0.1, 0.2\}$ . These are shown for *Hinode*/EIS observations (*left*), and the corresponding *SDO*/AIA observations (*right*).

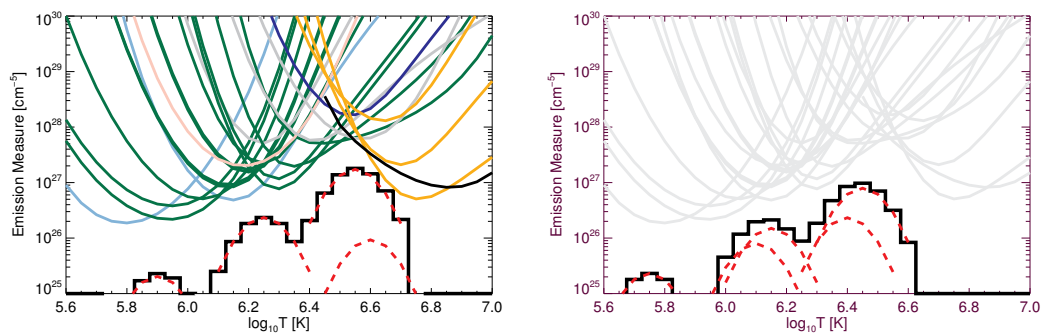


Figure 3.17: Basis Pursuit solution with a set of basis functions described as Dirac-delta functions and Gaussians with  $a = 0.1$ . These are shown for *Hinode*/EIS observations (*left*), and the corresponding *SDO*/AIA observations (*right*).

Figure 3.15 shows DEM reconstruction from the *Hinode*/EIS data described in Table 3.1, and *SDO*/AIA observations (*left, right*). The DEMs are reconstructed for both *Hinode*/EIS, and *SDO*/AIA observations using a set of Dirac-delta functions and Gaussians with widths,  $a = \{0.1, 0.2, 0.6\}$ . The *Hinode*/EIS DEM (Figure 3.15, *left*) is represented by five Gaussians with widths, and peak temperatures described as  $a = [0.1, 0.2, 0.2, 0.6, 0.6]$ , and  $\log_{10}T = [6.55, 6.20, 6.45, 6.10, 6.15]$ , respectively. Similarly, the *SDO*/AIA DEM (*right*) shares the same widths, but at values of  $\log_{10}T = [6.20, 6.45, 6.50, 6.70, 6.75]$ . Comparing the DEMs in Figure 3.15, it is clear that in this case the *SDO*/AIA DEM returns a solution with a significant amount of emission at 10 MK, which is not present in the DEM obtained from spectroscopic data and in many situations will over predict observations in higher energies (e.g. [Su et al., 2018](#)).

We next consider the case of DEM inversion using the set of basis functions described previously but without the Gaussian with  $a = 0.6$  as this is seen to overpredict the amount of high-temperature emission. Figure 3.17 shows DEM reconstruction from the data described in Table 3.1, and the synthesised *SDO*/AIA observations. In this case the solution obtained from *Hinode*/EIS and *SDO*/AIA with  $a = \{0.0, 0.1, 0.2\}$  closely resemble each other. The basis functions for the *Hinode*/EIS, and *SDO*/AIA DEMs are,  $a = [0.1, 0.2, 0.2, 0.2, 0.2]$ ,  $\log_{10}T = [6.55, 6.15, 6.20, 6.45, 6.50]$ ;  $a = [0.2, 0.2, 0.2, 0.2, 0.2]$ ,  $\log_{10}T = [5.7, 6.10, 6.15, 6.50, 6.55]$ .

Finally, we consider the case of DEM inversion using the set of basis functions described in [Su et al. \(2018\)](#). In this case, the DEM is reconstructed using a set of Dirac-delta functions and Gaussians with widths,  $a = 0.1$ , and shows a similar solution with both methods albeit shifted in the  $x$ -direction. The basis functions for the *Hinode*/EIS, and *SDO*/AIA DEMs are both represented by five Gaussians with  $a = 0.1$  and  $\log_{10}T = [5.90, 5.95, 6.25, 6.55, 6.60]$  and  $\log_{10}T = [5.75, 6.10, 6.15, 6.40, 6.45]$  respectively.

The dependence of the solution on the set of defined basis functions clearly indicates that the set of basis functions used to recover the DEM needs to be assessed. Here it was clear that a set of basis functions including a Gaussian with  $a = 0.6$  vastly overestimates the high-temperature component when compared to the equivalent temperature distribution derived from *Hinode*/EIS observations. [Su et al. \(2018\)](#) determined that

a set of basis functions consisting of Dirac-delta functions and Gaussians with  $a = 0.1$  will not over fit the X-ray data, however further investigation of these basis functions is required. Higher energy observations will allow the high-temperature component of the DEM to be further constrained, and this will allow the choice of basis functions to be further refined.

## 3.5 Summary

In this Chapter we have introduced the concept of differential emission measure inversion. As seen in Chapter 1, this is a widely used technique to understand the heating of the corona.

In Chapter 5 the differential emission measure will be constrained over an unprecedented range in temperature using *SDO/AIA*, *Hinode/XRT*, and *NuSTAR*. This is performed with the Tikhonov Regularisation code (§ 3.4.1), and the iterative least-squares approach (§ 3.4.2) as these codes are able to easily accept the input of all instruments.

In Chapter 7, the EM-weighted time series will be extracted from DEM inversion. Tikhonov Regularisation (§ 3.4.1) has a particular advantage in that it can provide both horizontal and vertical uncertainties. These uncertainties can be represented by the  $\mathbf{R}_\lambda \mathbf{K}$  matrix (e.g. Figure 3.5) in order to understand where the DEM is best constrained. Basis Pursuit (§ 3.4.4, published since the start of this work) is also considered.

# Chapter 4

## *NuSTAR* Hard X-ray Imaging Spectroscopy

The *Nuclear Spectroscopic Telescope Array* (*NuSTAR*) is a NASA SMall EXplorer (SMEX) mission that was launched in 2012 (Harrison *et al.*, 2013), and it is the first of its kind to take advantage of the recent technological advancement in the ability to directly focus photons  $> 10$  keV. The technological advancements in optics and solid-state detectors have only become possible in the last decade, and these allow *NuSTAR* to be significantly more sensitive than instruments such as *RHESSI* that use indirect imaging techniques to observe at these energies.

This chapter will provide an overview of the *NuSTAR* telescope, and an introduction to *NuSTAR* imaging and data processing. This chapter will also discuss the inherent limitations for heliophysics observations, along with the heliophysics science goals and results from the initial observations of the Sun.

### 4.1 Overview

The *NuSTAR* satellite was launched in to a low-Earth orbit in its stowed formation (Figure 4.1, *right*) in June 2012. Upon reaching orbit, the solar arrays were first deployed (Figure 4.1, *left*), followed by the mast many days later. The final configuration is shown in Figure 4.1 (*bottom*). Figure 4.1 shows two schematics of *NuSTAR* in the pre-, and deployed mast configurations in addition to a photograph in the stowed (launch) position. Additionally, Figure 4.2 shows photographs of the deployable mast,

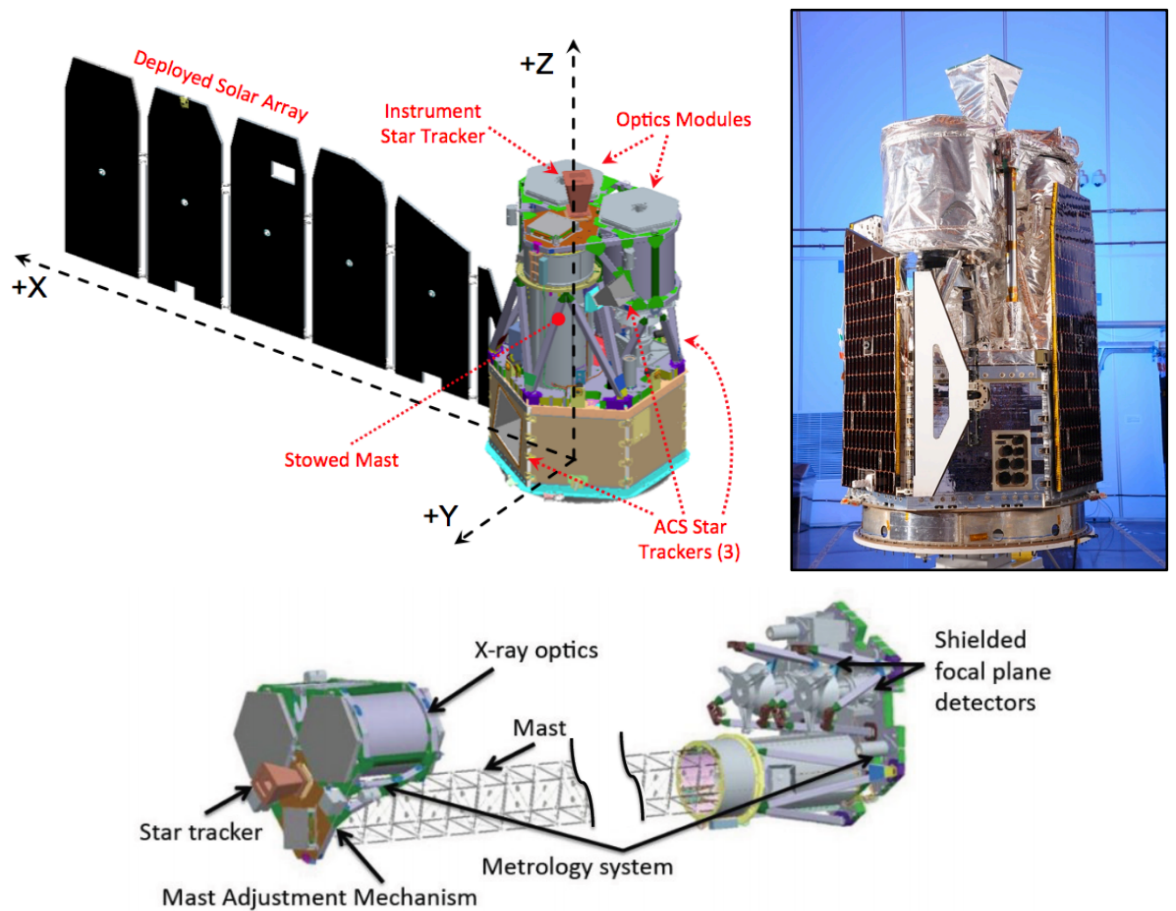


Figure 4.1: *Top Left:* A schematic of *NuSTAR* prior to mast deployment. *Top Right:* A photograph of the stowed configuration of *NuSTAR*. *Bottom:* A schematic of *NuSTAR* in the deployed position with the optics modules separated from the focal plane by the 10 m mast. These images are from the *NuSTAR* User’s Guide at the High Energy Astrophysics Science Archive Research Center (HEASARC).

one of the detector modules, and one of the optics modules.

*NuSTAR*’s two-year primary mission began in August 2012, and was aimed at addressing five primary astrophysics-related science objectives (Harrison *et al.*, 2013). After this initial period, *NuSTAR*’s extended mission opened to proposed observations through the guest observer programme (§ 4.4.2).

In terms of the instrumentation itself, *NuSTAR* consists of two *identical*, co-aligned telescopes (A, B) that each utilise focusing optics to directly image Hard X-rays (HXRs, 2.5 – 78 keV) on to the Focal Plane Modules (FPMA, FPMB)  $\sim 10$  m behind—each consisting of pixellated detectors totalling  $64 \times 64$  pixels. The *NuSTAR* field-of-view is

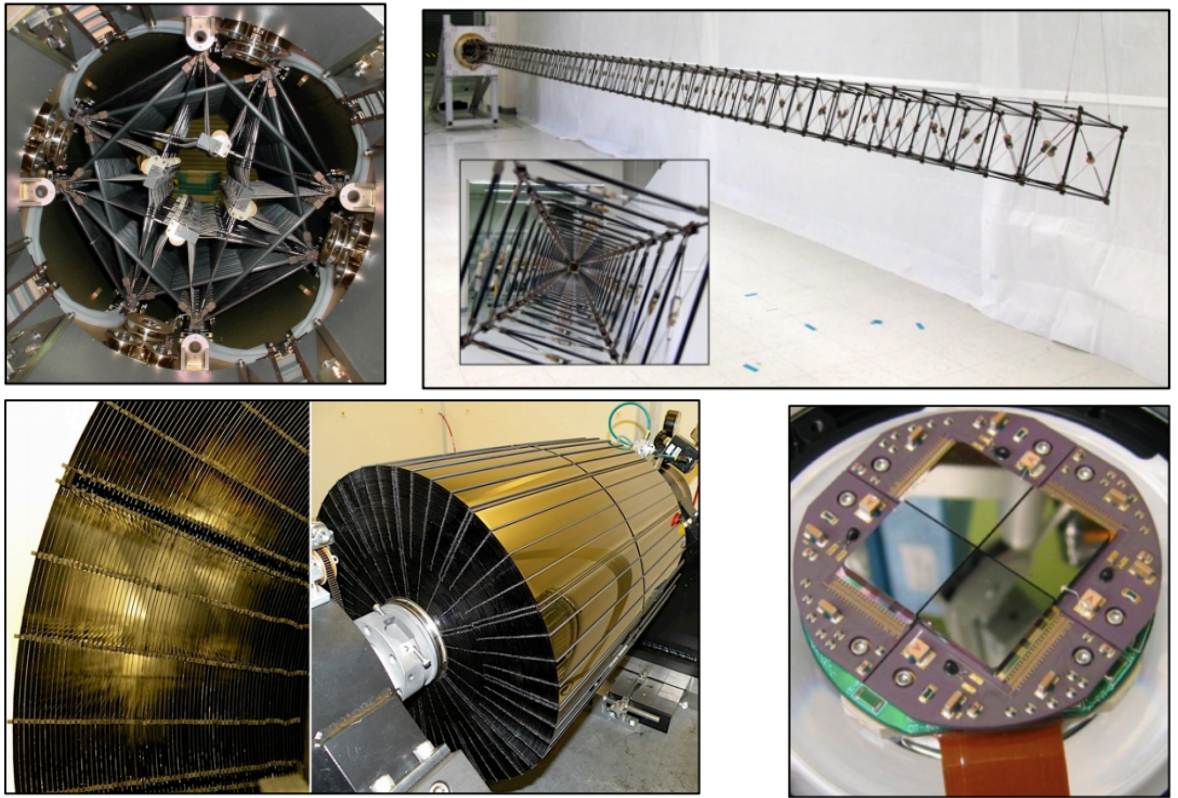


Figure 4.2: *Top Left, Top Right:* A photograph of *NuSTAR* mast in the stowed position and a photograph of deployed *NuSTAR* mast (cf. Figure 4.1). *Bottom Left:* Photographs of one of the optics modules consisting of 133 nested Wolter-I shells. *Bottom Right:* Photographs of one of the detector modules consisting of four  $32 \times 32$  pixel detectors crystals (each crystal measures  $2 \times 2$  cm). These images were extracted from the *NuSTAR* User’s Guide at the HEASARC

approximately  $12' \times 12'$  (Harrison *et al.*, 2013) and each telescope achieves an angular resolution of  $18''$  (which is dominated by the optics), and a half-power diameter of  $58''$  (Madsen *et al.* 2015). In terms of spectroscopy, *NuSTAR* has a useable energy range of between 2.5 and 78 keV (which is well calibrated above 3 keV, Grefenstette *et al.*, 2016) and the energy resolution of each telescope has a FWHM of 400 eV at 10 keV, which extends to 0.9 keV at 60 keV. There is a “dead-time” window of 2.5 ms between triggered counts (in which no additional counts are recorded, which results in a maximum throughput of  $400 \text{ counts s}^{-1}$  per telescope, § 4.2.2.1) and the readout time of the onboard electronics is only  $8 \mu\text{s}$  per event, which minimises pileup (§ 4.2.2.3). In

Table 4.1. Summary of *NuSTAR* & *RHESSI* Specifications

Specification	<i>NuSTAR</i>	<i>RHESSI</i>
Launch Date	2012	2002
Mission Duration	2012 – present	2002 – 2018
Imaging	Focussing Optics	RMCS <sup>a</sup>
Energy range [keV]	2.5 – 78	3 – 17000
field-of-view	12' × 12'	full Sun
Angular Resolution	18''	≥ 2.3''
FWHM	400 eV at 10 keV 0.9 keV at 60 keV	≲ 1 keV at 10 keV ~ 1 keV at 60 keV
Throughput [counts s <sup>-1</sup> ]	800 <sup>b</sup>	3 × 10 <sup>5</sup>
Effective Area [cm <sup>2</sup> ]	600	45.6

<sup>a</sup>Rotational Modulation Collimators

<sup>b</sup>400 counts s<sup>-1</sup> per module

comparison to *RHESSI*, in the range of solar flaring events (4 – 15 keV), *NuSTAR* has an average effective area over 10× greater, and a background four orders of magnitude lower (Grefenstette *et al.*, 2016, § 4.2.2). A summary of *NuSTAR* specifications in comparison to *RHESSI* is shown in Table 4.1.

## 4.2 *NuSTAR* Instrument

### 4.2.1 Focusing Optics

Mirrors are widely used to focus incoming light. The interaction of X-ray light with the matter it propagates through can be described by the complex index of refraction (Attwood, 2007):

$$n = 1 - \delta + i\beta. \quad (4.1)$$

Here,  $\delta$  describes the phase change and  $\beta$  accounts for absorption, and are both functions of wavelength ( $\lambda$ ), or photon energy. The real part of  $n$ ,  $1 - \delta$ , is exactly unity in a vacuum, and under such conditions, according to Snell's law, photons will undergo *total external reflection* at a grazing angle  $\theta_c$ <sup>1</sup>:

$$\cos(\theta_c) = 1 - \delta. \quad (4.2)$$

For X-rays, as  $\delta \ll 1$  the small angle approximation can be made<sup>2</sup>. The solution, the *critical angle for total external reflection of X-rays*, is therefore written as

$$\theta_c = \sqrt{2\delta}. \quad (4.3)$$

As  $\delta$  accounts for absorption,  $\delta$  is dependent on the material used for reflection. It is dependent on the atomic number  $Z$ , and is proportional to  $\lambda^2$ . For the case of heavy elements where  $Z/A \sim 0.5$  (the ratio of atomic number and weight), the critical angle (as thoroughly described in [Aschenbach, 1985](#)) can be estimated as

$$\theta_c = 5.6 \lambda \sqrt{\rho}, \quad (4.4)$$

or in terms of Energy ( $E$ , keV),

$$\theta_c = 6.9 \frac{\sqrt{\rho}}{E}, \quad (4.5)$$

where  $\theta_c$  is in units of arcminutes (');  $\lambda$  is in units of Å; and  $\rho$  is in units of  $g\ cm^{-3}$ .

For X-rays with a wavelength of a few Å, Equations 4.4, and 4.5 describe a critical angle of about  $1^\circ$ , so a grazing incidence design is required § 4.2.1.1. While these equations also explicitly demonstrate the superiority of heavy elements such as gold (Au,  $Z = 79$ ) or platinum (Pt,  $Z = 78$ ), these elements have their own absorption structures. Gold has an absorption structure at  $\sim 2.2$  keV ( $\sim 5.6$  Å, Figure 4.3), and platinum has an absorption structure at  $\sim 78$  keV ( $\sim 0.2$  Å). As will be discussed, it is ultimately this absorption structure at  $\sim 78$  keV that results in the upper-limit of the *NuSTAR* energy sensitivity. To demonstrate this, Figure 4.3 shows the optical constants and reflectance of gold (including the 2.2 keV absorption structure) over the energy range of 0.1 – 10 keV for a range of grazing angles.

<sup>1</sup>As in reality  $\beta$  is non-vanishing, the reflection is not total for  $\theta \leq \theta_c$ , and thus X-rays will be reflected at  $\theta > \theta_c$ .

<sup>2</sup> $\cos(\theta) = 1 - \frac{\theta^2}{2}$

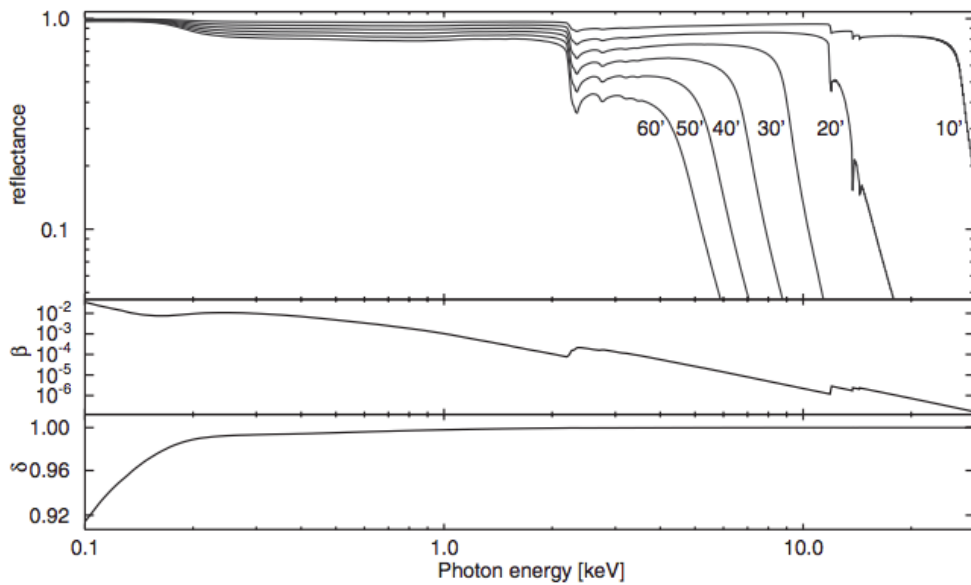


Figure 4.3: Optical constants ( $\delta$ ,  $\beta$ ) and reflectance of gold over the energy range 0.1 – 10 keV, for a set of grazing angles. The absorption structure at 5.6 Å ( $\sim 2.2$  keV) is evident. This Figure is reproduced from [Friedrich \(2008\)](#).

A way to enhance the reflection angles is to use multi-layer coated optics. Multi-layer coated optics are composed of a stack of thin, alternating layers of two different materials. The alternating layers typically consist of a dense and a light material, with the light material used as a spacer to introduce discontinuities in the refractive index. Reflectivity can be further enhanced across a range of hard X-ray wavelengths by varying the thickness throughout the stack, such that the period decreases with depth (depth-grading, [Christensen \*et al.\*, 1992](#); [Gorenstein, 2012](#)).

#### 4.2.1.1 Wolter-Type Telescopes

To image X-rays, [Wolter \(1952\)](#) proposed three configurations for two-mirror grazing incidence design. These three concepts are known as Wolter-I; Wolter-II; and Wolter-III, and each of these produces sharp images for on-, and off-axis objects<sup>3</sup>. Figure 4.4 shows the Wolter-I design that uses a parabolic and hyperbolic mirror configuration. With a prescription by [VanSpeybroeck & Chase \(1972\)](#) this configuration has become the most common configuration for X-ray telescopes as it can be nested to achieve large

<sup>3</sup>each satisfy the Abbe sine condition, [Abbe \(1881\)](#).

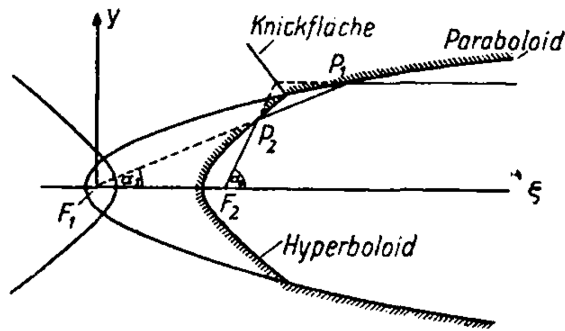


Figure 4.4: Wolter-I configuration consisting of a paraboloid and a hyperboloid, with the two reflection surfaces indicated as  $P_1$  and  $P_2$ , and the focal point as  $F_2$ . This Figure is reproduced from [Wolter \(1952\)](#).

effective areas.

Each shell of nested Wolter-I optics has a collecting area that is dependent on a thin projected circle with an area dependent on the mirror radius,  $r$ , and the length of the mirror element,  $l$ . For small angles this can be approximately represented as

$$\text{area} = \frac{1}{2}\pi r^2 \cdot \frac{l}{f} \quad (4.6)$$

where  $f$  is the focal length (see [Friedrich, 2008](#)). This area is significantly smaller than the mirror surface, and nesting many mirror shells can enlarge the collecting area and prevent direct light entering the optics, but also limit the field-of-view.

*NuSTAR* employs a conical approximation of the Wolter-I design ([Petre & Serlemitsos, 1985](#)), and each Optics Module (OMA, OMB) consists of 133 depth-graded multi-layer coated nested shells (see Figure 4.2 for a photograph of one of the optics modules). The 43 outer shells are multi-layer coated with W/Si, and the inner 90 are similarly coated with Pt/C to enhance reflectivity ([Madsen \*et al.\*, 2009](#); [Christensen \*et al.\*, 2011](#)). The sensitivity drop-off at  $\sim 78$  keV results directly from the Pt K absorption edge of the Pt/C multi-layer coating.

Each telescope achieves an angular resolution of  $18''$  (FWHM), which is dominated by the optics, and a half-power diameter of  $58''$  ([Madsen \*et al.\*, 2015](#)) which is characterised by a centrally sharp point spread function (PSF) with broad wings (see Figure 7 in the *NuSTAR* observatory guide and [Madsen \*et al.\*, 2015](#)).

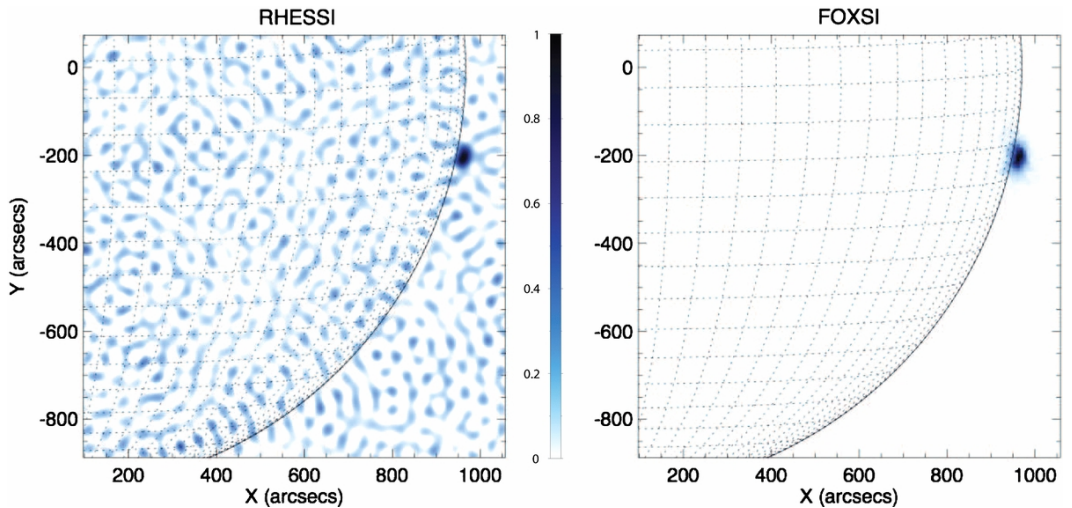


Figure 4.5: Direct comparison between the observation of a GOES B2.7-class microflare observed by *RHESSI* (left; with a field-of-view restricted to the *FOXSI* field-of-view,  $16.5' \times 16.5'$ ), and *FOXSI* (right, see § 2.3.1) during the first flight in 2012 (Krucker *et al.*, 2014). These images are plotted with the same colour scaling and reconstruction artifacts are present across the *RHESSI* image. This Figure is reproduced from Krucker *et al.* (2014).

In the range of solar flares (4–15 keV), the combination of both *NuSTAR* telescopes has an average effective area of  $600 \text{ cm}^2$ ; over ten times the equivalent for *RHESSI* ( $45.6 \text{ cm}^2$  for 8 *RHESSI* detector modules, Grefenstette *et al.*, 2016).

The advantage of using direct *vs.* indirect imaging is clearly shown in Figure 4.5. Figure 4.5 shows a comparison of a small flare (GOES B2.7) observed with both Rotational Modulation Collimators (RMCs) and Wolter-I focusing optics. For the indirect observations by *RHESSI* (Figure 4.5, left), reconstruction artefacts are clearly shown in addition to the B2.7-class microflare (located at  $[950'', -200'']$ ).

#### 4.2.1.2 Ghost-Rays & Stray Light

For a photon to be “focused” through the Wolter-I optics, two sequential reflections are required (Figure 4.4). However, with sources that are located off-axis, a well-known problem with Wolter-I optics is that it is still possible for a photon with only one single reflection in the optics to reach the detector plane (as can be seen in Figure 4.6). *Top to bottom*, Figure 4.6 shows the possible reflection geometries for a focused photon (double bounce), two geometries for singly reflected photons (on the primary or secondary

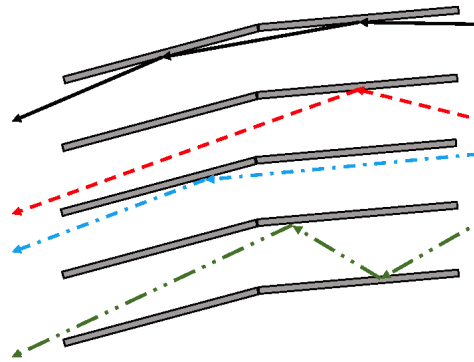


Figure 4.6: *Top to bottom*: double bounce (properly “focussed” X-ray); single bounce (upper); single bounce (lower); and back reflected photons through Wolter-I optics. This Figure is adapted from [Madsen \*et al.\* \(2017\)](#).

mirror respectively), and there is also the example of a back-reflection (Figure 4.6, *bottom*) which dominates at the largest off-axis angles as a result of nesting shells ([Madsen \*et al.\*, 2017](#)).

These single bounce photons shown in Figure 4.6 are known as “ghost-rays” ([Madsen \*et al.\*, 2015](#)), and are an inherent problem associated with *NuSTAR* solar observations. As the *NuSTAR* field-of-view is smaller than the solar disk, bright X-ray sources outside the *NuSTAR* field-of-view (between 3′ and 40′, see Figure 7, [Grefenstette \*et al.\*, 2016](#)) can provide a significant contribution of ghost-rays to observations. These ghost-ray sources produce distinct spatial patterns, and these can easily be identified in images, but without knowledge of the sources outside the field-of-view there is significant difficulty in applying a correction. Figure 4.7 shows three examples of mosaic observations of the solar disk when bright active regions were present. Each of these observations display clear indication of ghost-rays from two simple and one complex active region configuration. A simulation of the ghost-rays from the complex active region configuration has been taken from ([Grefenstette \*et al.\*, 2016](#)) and shown in Figure 4.8. For observations of the Sun, the ability for ghost-rays to be detected means that the best observations will be the result of observing the brightest region on disk, when there is little to no activity outwith the 12′ × 12′ field-of-view. For observational targets such as weakly flaring active regions this is difficult to achieve outwith solar minimum, and therefore, the best *NuSTAR* observations will come at that time.

For solar-dedicated instruments such as *FOXSI*, [Buitrago-Casas \*et al.\* \(2017\)](#) inves-

tigated methods for reducing ghost-rays reflecting through the *FOXSI* sounding rockets Wolter-I optics. [Buitrago-Casas \*et al.\* \(2017\)](#) address the problem with ray tracing simulations and by measuring the PSF of one of the *FOXSI* shells. They note that one of the easiest ways to reduce the number of ghost-rays is to reduce the gaps between nested Wolter-I mirrors. While *NuSTAR* has tightly packed mirrors which mitigate the problem, it does not eliminate the problem completely, and [Buitrago-Casas \*et al.\* \(2017\)](#) consider baffles, collimators, and absorbers to directly address the problem. For the *FOXSI-3* flight (September 2018), *FOXSI* was fitted with a honeycomb collimator that was designed to block off-axis rays at angles  $> 13'$  (See Figure 6, [Buitrago-Casas \*et al.\*, 2017](#)). Unfortunately during these observations there was very little activity, so observations were minimal.

In addition to ghost-rays, stray (X-ray) light can be detected from bright sources located  $3 - 6^\circ$  off-axis through an unbaffled part of the instrument ([Wik \*et al.\*, 2014](#)). These sources can be of solar origin, or even originate from the cosmic X-ray background (CXB).

### 4.2.2 Detectors

Each of the *NuSTAR* focal plane modules (FPMA, FPMB) has four detectors (see Figure 4.2) each consisting of Cadmium Zinc Telluride (CdZnTe) crystal which absorbs  $\sim 100\%$  of incident photons in the *NuSTAR* operational range ( $< 80$  keV, [Bhalerao, 2012](#)). Each detector consists of  $32 \times 32$  pixels that is formed by a segmented anode pattern, and each detector is separated by less than a pixel. Detector calibration is performed in-flight with a retractable radioactive source which emits X-ray lines in the range of  $6 - 105$  keV ([Kitaguchi \*et al.\*, 2011, 2014](#)).

For each HXR photon event detected, the  $x$  and  $y$  detector coordinates, the focal plane module and detector identifiers, along with timing information (accurate to  $\mu\text{s}$  time-scales) are sent to the central processor (for a detailed description of the readout scheme, see [Bhalerao, 2012](#)). From this information the energy can be calculated, a GRADE assigned (§ 4.2.2.2), and with pointing information sky co-ordinates can be recovered (§ 4.3).

The background of the *NuSTAR* detectors is  $8 \times 10^{-4}$  counts  $\text{s}^{-1}$  (cf. *RHESSI*'s  $54$  counts  $\text{s}^{-1}$ ; [Smith \*et al.\*, 2002](#)); [Grefenstette \*et al.\* \(2016\)](#) constructed a figure of

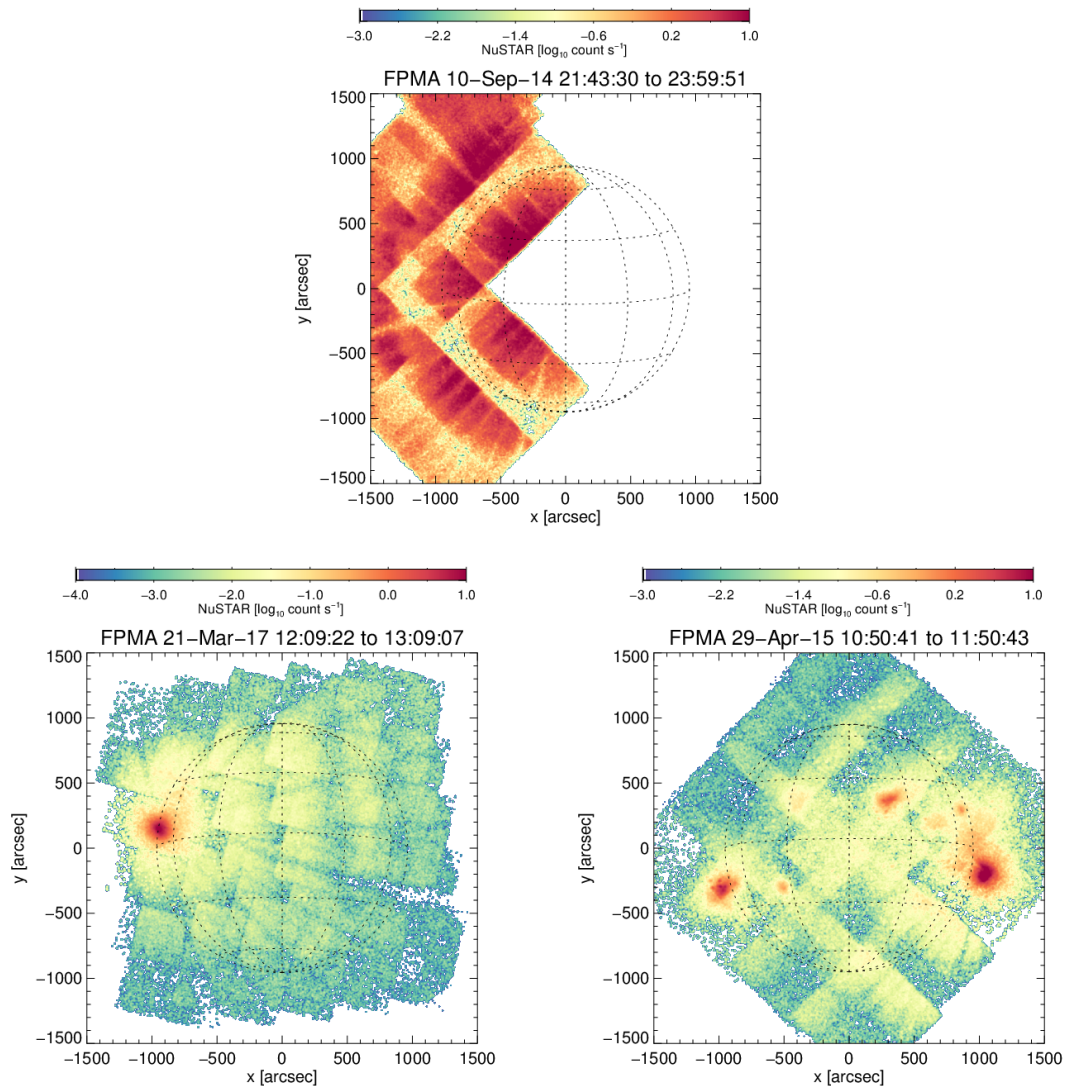


Figure 4.7: Three examples of *NuSTAR* observations that are the result of operating in the solar mosaic mode. These images show ghost-ray patterns, as observed by Focal Plane Module A (FPMA). *Top:* *NuSTAR* mosaic tiles during the first solar observations (initial engineering test) on 10th September 2014. Prior to these observations a GOES X-class flare was observed near disk center. The X-ray flux from this X-class event was so large that the disk center images were rejected by the on-board software (see Grefenstette *et al.*, 2016). *Bottom:* These images are from subsequent science observations. Both of these observations show ghost-ray patterns from a single (*left*) and complex (*right*, further simulated in Figure 4.8) active region configuration. These images are courtesy of Iain Hannah ([http://ianan.github.io/nsigh\\_all/](http://ianan.github.io/nsigh_all/)).

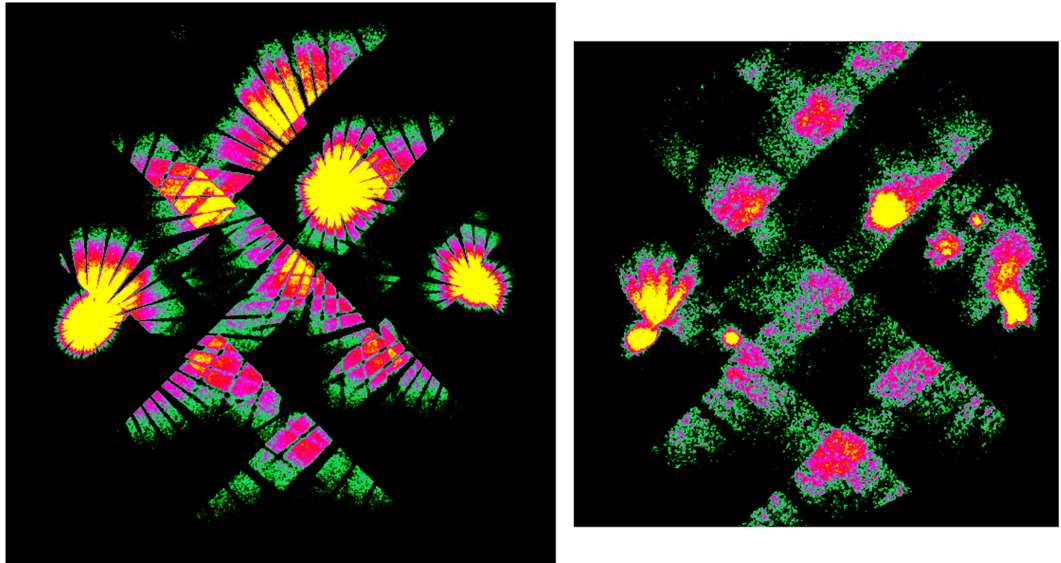


Figure 4.8: *Left*: Simulation of a ghost-ray pattern based on the active region configuration shown in Figure 4.7 (*bottom right*), and further shown over the same colour scaling in the right panel. *Right*: A solar mosaic observation of obtained on 29th April 2015 showing the three active region configuration and observed ghost-ray pattern. The three active regions result in a complex ghost-ray structure which is accurately reproduced in simulations. This Figure is from [Grefenstette \*et al.\* \(2016\)](#).

merit, and interpreted this to suggest that a solar flare at the background level in *NuSTAR* would be a million times fainter than for *RHESSI*.

#### 4.2.2.1 Detector & Electronics Throughput

One of the most significant limitations of using *NuSTAR* for heliophysics observations is the  $\tau = 2.5$  ms dead-time window after a photon trigger that is a result of the throughput of the onboard electronics to process the event. After each photon trigger there is a 2.5 ms window in which no other photons incident in the focal plane trigger a detection. The onboard electronics therefore limit the maximum throughput of  $400 \text{ counts s}^{-1} \text{ telescope}^{-1}$  (calculated as  $\tau^{-1}$ ). Importantly, at the start of this window there is an  $8 \mu\text{s}$  readout time during which pile-up can also occur (§ 4.2.2.3).

For most astrophysical sources the incident count rate at *NuSTAR* is smaller than the maximum throughput rate. However, even for modest activity on the Sun, the count rate on the focal plane can be hundreds of thousands of counts per second ([Grefenstette](#)

*et al.*, 2016). The maximum throughput of the electronics can dramatically diminish the hard X-ray sensitivity of *NuSTAR* if there are bright sources on disk. The high count rate leads to large dead-time windows, lost photons, and a limited dynamic range.

For example, the presence of very bright sources in the field-of-view leads the *NuSTAR* detectors to assume a problem, as was seen with the engineering tests on September 2014 when a large X-ray flare was observed a few hours prior to the start of the *NuSTAR* observations. Near the flare location the observations mimicked cosmic ray interactions (many photons co-temporally arriving at different spatial locations), such that these observations were vetoed by the electronics (Grefenstette *et al.*, 2016), which led to a 0% livetime. With more modest levels of activity from within the field-of-view—those equivalent to *GOES* B-class—leads to livetimes of a few percent, which increases to tens-of-percent for *GOES* A-class. With decreasing activity, an active region free, quiet Sun observation will result in livetimes of up to 100%.

For livetimes  $< 100\%$ , the effective exposure (calculated as the livetime fraction multiplied by the dwell time) is smaller than the dwell time, and these limited livetimes limit the spectral dynamic range as a steep drop-off to higher energies is expected. Furthermore, because of ghost-rays (§ 4.2.1.2), pointing *NuSTAR* to a quieter region of the Sun would lead to the brighter regions outside the field of view still being detected, and could dominate the limited throughput (See Figure 4.7). Ideal observations with *NuSTAR* will be obtained near solar minimum when there are minimal X-ray sources outside the field-of-view.

#### 4.2.2.2 GRADE

For those events that are recorded, each photon event is given a **GRADE**—an integer between 0 and 31. The **GRADE** is based on the morphology of triggered pixels within a  $3 \times 3$  grid centred on a pixel with the highest deposited energy. **GRADE** 0 indicates a single pixel hit, but higher grades mean the neighbouring pixels recorded a detection within the  $8 \mu\text{s}$  readout time. Figure 4.9 shows morphology of pixel interactions for the most common grades that are assigned. Grades 21 – 24 give the clearest example of a second photon during this time, instead of a single photon being detected across multiple pixels, and so can be used to help determine the amount of pileup, as will be discussed in § 4.2.2.3.

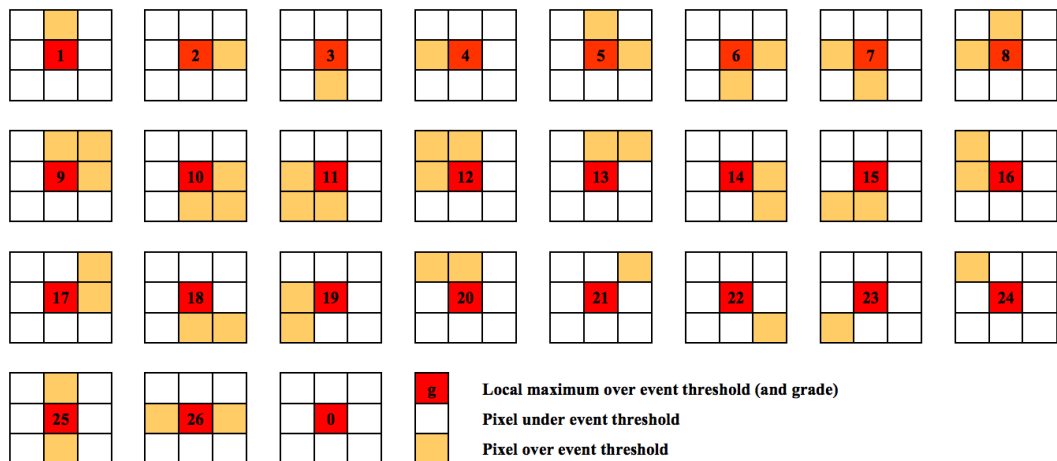


Figure 4.9: The  $3 \times 3$  pixel morphology of GRADEs 0 – 26. These images are extracted from the *NuSTAR* User’s Guide at the HEASARC.

#### 4.2.2.3 Pileup

With high (incident) count rates the effects of pileup on the observed spectra need to be considered. The term “pileup” (Datlowe, 1975) refers to the phenomena of two (or more) incident photons being read out as a single photon with an energy that is the sum of these photon energies. This generally occurs when photons are incident at a higher rate than the readout time. While pileup can still occur with pixellated detectors, it is less problematic than with previous methods of detection; for a discussion of pileup with *RHESSST*’s nine RMCs, see Smith *et al.* (2002). For *NuSTAR* observations, pileup can occur as the result of two scenarios (as discussed in Grefenstette *et al.*, 2016):

1. Two photons hit the same pixel and are assumed, by the on-board electronics, to be a single-pixel event.
2. Two photons hit adjacent pixels ( $\text{GRADE} > 0$ ; see § 4.2.2.2), are identified as a “split-pixel” event, and are combined in the post-processing.

In order to further understand the potential effects of pileup, specifically (1), on solar observations, Grefenstette *et al.* (2016) analysed the *NuSTAR* spectra of Scorpius X-1—a bright source with a steep thermal-type spectrum. During the observations with *NuSTAR*, Scorpius X-1 was observed to have count rates in its flaring state of over  $15000 \text{ counts s}^{-1}$  (cf. several hundred thousand counts per second for the Sun),

but these observations led [Grefenstette et al. \(2016\)](#) to conclude that one would expect  $< 0.05\%$  of events to be piled up in observations of the Sun.

In terms of case (2), the solution is straight forward to implement. As will be discussed in Chapter 5, events assigned with `GRADE > 0` are ignored.

### 4.2.3 Astrometric Alignment

Usually, where *NuSTAR* is pointing in the sky is determined by the instrument star tracker (Camera Head Unit 4, CHU 4), mounted on the optics bench (see Figure 4.1) in the direction of pointing. However, due to the bright Sun, this star tracker is unusable and *NuSTAR* solar observations are obtained using the spacecraft science mode (`SCIENCE_SC`, mode 06) ([Grefenstette et al., 2016](#)). The `SCIENCE_SC` mode uses combinations of the other orthogonal star trackers located on the spacecraft bus (CHUs 1 – 3) to determine the pointing of the spacecraft, and source of a photon on the sky.

The combination of CHUs 1-3 are automatically determined given the orbital position of the spacecraft and this varies over an observation. Although the pointing of the spacecraft is stable, the X-ray source location can be offset from its true location by up to about  $1'$ . This is why mode 6 is not *usually* recommended for imaging of astrophysical objects ([Walton et al., 2016](#)).

With solar observations there is no choice but to use this mode, but the true source locations can be found later by alignment to observations at other wavelengths, such as Soft X-rays from *Hinode*/XRT or EUV from *SDO*/AIA (as performed in [Wright et al., 2017](#), Chapter 5).

## 4.3 Data Processing

### 4.3.1 NuSTARDAS

The *NuSTAR* Data Analysis Software (NuSTARDAS<sup>4</sup>) as a part of HEASOFT is a collection of modules dedicated to process the *NuSTAR* data to a scientific data product that can consist of energy spectra, event files, images, exposure maps, light curves, and

---

<sup>4</sup>For more details see *NuSTAR* User's Guide at the HEASARC, <https://heasarc.gsfc.nasa.gov/docs/nustar/>

response files. The NuSTARDAS processing routine, `nupipeline`, allows the user to run the relevant processing routines on Level-1 data in order and is organised in to three stages, as follows:

1. **Data Calibration:** This stage uses the calibration database (CALDB) to calibrate the science event files. First, the relative alignment of the optics and focal plane modules (separated by the 10 m mast, Figures 4.1, 4.2) is realised using the laser meteorology system. Next, the attitude data obtained from the combinations of CHUs (§ 4.2.3) is processed, bad pixels and hot pixels are flagged, and a **GRADE** (§ 4.2.2.2) is calculated for each  $3 \times 3$  photon event. After energy and gain correction, an interaction depth threshold is applied, and the detector co-ordinates of each event are converted to sky co-ordinates (see Harp *et al.*, 2010, for details on the pointing reconstruction). The result of data calibration is a Level-1a event file: a fits file of a list of detected X-rays with a variety of properties (such as energy channel, position on detector, **GRADE**, etc.)
2. **Data Screening:** screens the calibrated event files (1) to account for attitude, orbital, and instrument parameters and event properties, returning Level 2 cleaned event files. This includes the removal of bad pixels, events with **GRADE**  $> 0$ , and data obtained during Earth occultation, slewing, and South Atlantic Anomaly passages, to name a few.
3. **Product Extraction:** The final stage is the calculation of high-level scientific products (e.g. energy spectra, response files, images, exposure maps). The energy spectra and response files for the chosen observation and configuration (e.g. time range, specific spatial region) can then be inputted to data analysis programs such as XSPEC (Arnaud, 1996) and OSPEX (Schwartz *et al.*, 2002) for X-ray spectral fitting.

An additional step for solar observations is the conversion of the co-ordinates from right ascension and declination (R.A./Dec.) to helioprojective co-ordinates using NASA’s Jet Propulsion Lab Horizons online ephemeris tool (Giorgini *et al.*, 1996) as described in (Grefenstette *et al.*, 2016). This processing of the eventlist files can be performed in Python or SSWIDL. These resulting eventlists can be spatially binned to produce images (again software in both Python and SSWIDL) so that they can be compared to solar observations at other wavelengths. These images can then be

further aligned with additional heliocentric observations such as those from *SDO/AIA*, and *Hinode/XRT*. The scripts to perform these transformations are available on the *NuSTAR* GitHub repository<sup>5</sup>.

## 4.4 Overview of *NuSTAR* Solar Science Goals, Observations, and Results

### 4.4.1 *NuSTAR* Solar Science Goals

The primary science goals of the *NuSTAR* heliophysics group are:

1. **Heating of the Solar Corona** – One of the main targets of the *NuSTAR* solar campaign are the smallest X-ray flares from within both active regions (e.g. [Hannah \*et al.\*, 2011](#)), and the quiet Sun ([Krucker \*et al.\*, 1997](#)). It is of interest to understand if there are high-temperature, and/or non-thermal particles present in these smallest events, and how these relate to larger flares, and contribute to coronal heating. In addition to targeting the smallest observable events, by investigating quiescent (apparently non-flaring) active regions and the quiet Sun, these *NuSTAR* observations seek to understand if emission is consistent with an ensemble of unresolved nanoflares. Due to the nature of these observations, they are obtained when there are few to no active regions on disk, and they are only weakly flaring (< GOES B-level).
2. **Particle Acceleration in Solar Flares** – In addition to the faint X-ray emission from small flares, *NuSTAR* can also be used to detect faint coronal emission from larger flares. X-rays from flares are dominated by the bright lower coronal/chromospheric footpoint and loop emission, but there should also be fainter emission from higher up in the corona—the source of the initial heating and particle acceleration—as well as the faint X-ray emission from outward heading material, such as from radio Type-II producing electrons or coronal mass ejections. These observations are limited to times when there are active regions producing larger flares and eruptions, but are located just behind the solar limb so that the bright lower atmosphere emission is blocked from *NuSTAR*'s view.

---

<sup>5</sup><http://www.github.com/nustar>

3. **Solar Axions** – A further potential source of weak solar X-rays are those from solar axions. Axions are a hypothetical weakly interacting particle, that is a postulated Dark Matter candidate (Peccei & Quinn, 1977). If they exist, axions would be created in the solar corona and convert to an X-ray of the same energy as the result of interacting with the magnetic field. The simulated Axion source from the Sun would be a solar core sized region, with a blackbody spectrum of the core temperature (Hudson *et al.*, 2012). These observations need to target the center of the solar disk, would ideally occur during solar minimum, and when there are no other bright sources or regions on disk.

#### 4.4.2 *NuSTAR* Solar Observations

An overview of *NuSTAR* solar observations is continually updated online<sup>6</sup>, and this section will summarise the *NuSTAR* observations and publications to date in the context of the solar science goals.

Solar observations with *NuSTAR* are usually obtained by triggering Guest Observer Target of Opportunity (GO/ToO) observations with time allocated through proposals submitted to the guest observer cycles. Previous ToO time was awarded for occulted flare studies (PI, Krucker), and since June 2018 there has been ToO time awarded for the study of weakly flaring active regions (PI, Glesener). In exceptional cases, unsolicited ToO requests can also be submitted through the *NuSTAR* ToO website, but result in significantly shorter observation times. In addition to ToO requests, *NuSTAR* has a number of “Legacy Surveys”<sup>7</sup>. For the Sun, there is currently a survey specifically designed to obtain full-disk mosaic observations to monitor the solar corona through solar minimum (approximately once every three months, starting in September 2018).

Depending on the science goal to be addressed (which directly relates to the level of activity), *NuSTAR* observations of the Sun have been obtained using a number of observational modes. To date there have been a handful of main modes for observing the Sun. These are:

- **Mosaic** – This mode allows full-Sun context observations to be obtained. As the *NuSTAR* field-of-view is a limited to  $12' \times 12'$ , in order to obtain full-disk HXR

---

<sup>6</sup>[http://ianan.github.io/nsigh\\_all/](http://ianan.github.io/nsigh_all/)

<sup>7</sup>[https://www.nustar.caltech.edu/page/legacy\\_surveys](https://www.nustar.caltech.edu/page/legacy_surveys)

observations *NuSTAR* performs multiple observations to complete a mosaic. Full-Sun mosaics are either obtained with *NuSTAR* oriented in a diagonal pattern so the detector gap is not aligned with active region bands (e.g. 29th April 2015), or in a square pattern when the Sun is quiet (e.g. 28th September 2018). These mosaics are scientifically interesting as they provide snapshots of the HXR Sun. This technique has been used in obtaining HXR observations on the 29th April, 2015 (Wright *et al.*, 2017); 1st September 2015; and 21st March 2017. The latest mosaic observation was obtained on the 28th September 2018 as part of the *NuSTAR* solar Legacy Survey, and these will be continued every three months through solar minimum.

- **Sit-and-Stare** – To address particle acceleration in solar flares, *NuSTAR* has obtained observations at the solar limb in order to observe high-coronal signatures associated with solar flares (**Limb Sit-and-Stare**). Similarly, there have been **Active Region & Quiet Sun Sit-and-Stare** observations in order to obtain temporal observations of weakly, and non-flaring regions of the Sun. These active region observations have been obtained in August 2017 and in 2018 during the coordinated observations with sounding rocket flights.
- **Drifting** – With a similar scientific reasoning to Limb sit-and-stare observations, by fixing the R.A./Dec. pointing of *NuSTAR*, *NuSTAR* appears to drift from the limb to higher altitudes. This technique has been used in obtaining HXR observations off the limb to higher altitudes and were obtained during the initial 2014 observations (e.g. 11th December 2014).

Each of these observations typically consists of a number of orbits (where an orbit consists of 1 hour observations with 30 minute eclipse). Furthermore, in order to make full use of the limited *NuSTAR* observation time, these observations are generally coordinated with other observatories such as *Hinode*, *IRIS* (De Pontieu *et al.*, 2014), *ALMA*, and also sounding rockets such as *FOXSI*, and *Hi-C*.

As of September 2018, *NuSTAR* has observed the Sun 15 times. The first four pointings (those obtained between September 2014 and April 2015) are summarised in Grefenstette *et al.* (2016), and these observations have resulted in numerous publications (Hannah *et al.*, 2016; Kuhar *et al.*, 2017; Wright *et al.*, 2017; Glesener *et al.*,

2017; Marsh *et al.*, 2017; Marsh *et al.*, 2018). This section will provide a chronological overview of the observations and results.

#### 4.4.2.1 September 10, 2014

The first observations from the *NuSTAR* heliophysics campaign were obtained on the 10th September 2014. These first observations were performed as an engineering test in order to ensure that observations of the Sun would not cause irreversible damage to the *NuSTAR* spacecraft and optics (Grefenstette *et al.*, 2016). These first observations lasted for two orbits: during the first orbit, *NuSTAR* performed observations in the mosaic mode § 4.4.2, and during the second orbit *NuSTAR* was aimed at the solar North pole.

As has been discussed in § 4.2.1.2, the observations from the first orbit show clear ghost-ray patterns due to a significant amount of high-temperature emission measure. This emission was present as the result of an X-class flare that had occurred in the disk-center active region a few hours prior. During these observations the observed count rate became so high that the behaviour mimicked cosmic ray interactions in the detector (Grefenstette *et al.*, 2016). As a result, these counts were rejected by the electronics, and the telescope recorded no data during these observations. While these observations were not scientifically valuable per se, these observations demonstrated that even in the most extreme conditions no irreversible damage was caused to the *NuSTAR* telescope.

#### 4.4.2.2 November 1, 2014

The first set of solar science observations were obtained on November 1, 2014. The observations were triggered to study high coronal sources above AR 12192 (Grefenstette *et al.*, 2016), and the observations were performed over four orbits. The first and last orbits targeted “quiet” portions of the solar disk, and the middle two orbits were aimed at the coronal sources on the West limb. The middle two orbits were observed with the pointing fixed in R.A./Dec. allowing the Sun to drift across the field-of-view. At the start of the orbit *NuSTAR* therefore observed the bright thermal emission from low altitudes, and fainter emission as the altitude increases.

There have been numerous papers that use these first science observations. The science addressed ranges from non-flaring active regions, to quiet Sun transient bright-

enings. These papers are presented here in order of publication:

[Hannah \*et al.\* \(2016\)](#) performed analysis on the first directly imaged, and spectrally resolved *NuSTAR* X-ray observations of five quiescent (non-flaring) active regions above 2 keV. These active regions were located on the West limb of the Sun. The analysis of these active regions was performed using the fourth orbit (as this was the most stable), and these observations had effective exposures (§ 4.2.2.1) of 3, and 11 s.

The *NuSTAR* X-ray images match the bright features seen in EUV and SXR, and additionally the active region spectra were well-fitted by isothermal models (Figure 4.10). Figure 4.10 shows the *NuSTAR* HXR spectra from FPMA/B for two disk regions (D1, D2), and three limb regions (L1, L2, L3) all well-fitted with isothermal models. [Hannah \*et al.\* \(2016\)](#) observed no emission above 5 MK. So instead, they were able to place upper-limits on the emission measure of a second thermal component (between 5 and 12 MK) down to an order of magnitude lower than previous limits obtained by *EUNIS* ([Brosius \*et al.\*, 2014](#)) and *SMM/FCS* ([Del Zanna & Mason, 2014](#)).

[Marsh \*et al.\* \(2017\)](#) performed imaging spectroscopy of the quiet Sun in search of transient brightenings, and placed the first *NuSTAR* limits on quiet Sun HXR transients. As with [Hannah \*et al.\* \(2016\)](#), [Marsh \*et al.\* \(2017\)](#) analysed data from the fourth orbit. In addition to the active regions observations presented in [Hannah \*et al.\* \(2016\)](#), this orbit also included two quiet-Sun pointings towards the North pole, where the second pointing had the lowest solar flux level of these observations. Using the observations from the second quiet Sun pointing, [Marsh \*et al.\* \(2017\)](#) performed a transient search over the full *NuSTAR* energy range and over a low energy band (2.5 – 4 keV) with timescales of 100 s. An example of a transient event is highlighted in Figure 4.11. Figure 4.11 shows three temporally adjacent observations (time progression is *left to right*) that have been summed over 100 s windows. The two cases shown are the original observations with no detection (*top*), and the bottom row shows the same observations but with the counts in the chosen pixel artificially increased to satisfy the 95% detection threshold. [Marsh \*et al.\* \(2017\)](#) were also able to set limits on brightenings in the 10 – 20 keV range for a set of timescales of 30, 60, 100 s. These limits were lower than previous active region microflares, but not lower than quiet Sun brightenings observed with *Yohkoh/SXT* ([Krucker \*et al.\*, 1997](#)). This was expected as these observations were

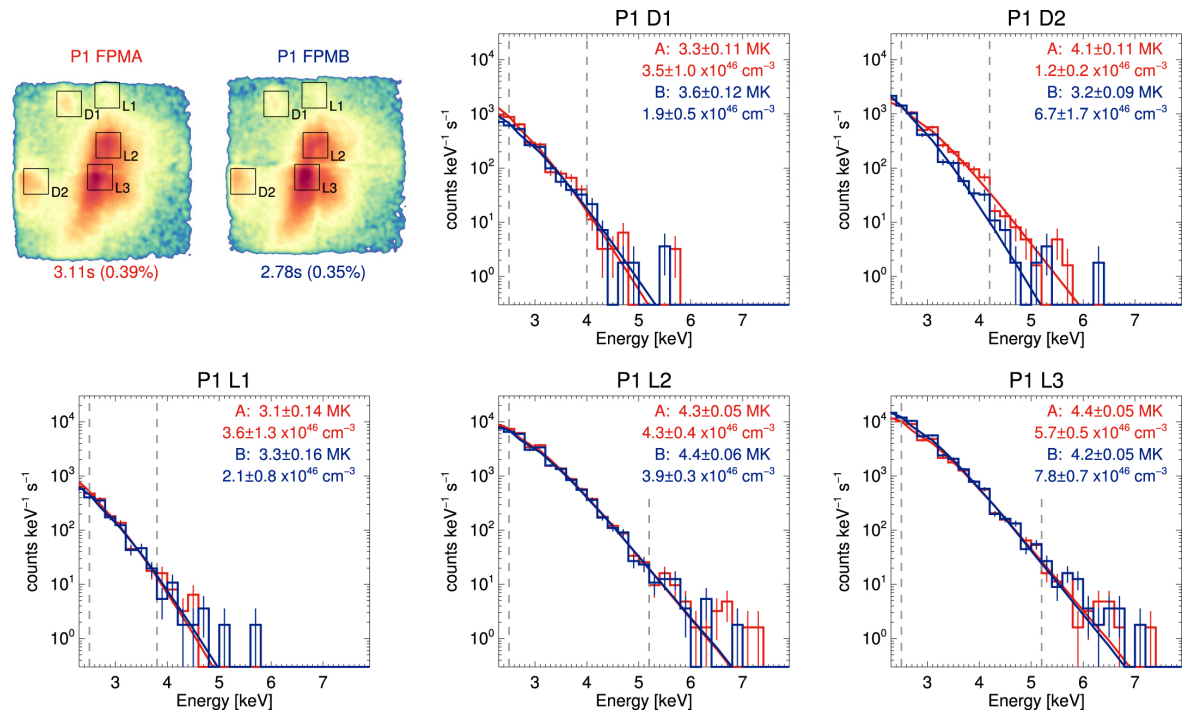


Figure 4.10: *NuSTAR* HXR spectra (FPMA/B) for two disk regions (D1, D2), and three limb regions (L1, L2, L3) each well-fitted with isothermal models. This Figure is from [Hannah \*et al.\* \(2016\)](#).

obtained at times with bright regions on disk, and future observations with higher live-times would provide lower detection limits.

#### 4.4.2.3 December 11, 2014

The third observations from the *NuSTAR* heliophysics campaign were obtained on December 11 2014. These observations were obtained to coincide with the *FOXSI-2* sounding rocket launch ([Christe \*et al.\*, 2016](#)). These observations targeted AR 12222 that was located on the West limb of the solar disk, and have produced two publications:

[Kuhar \*et al.\* \(2017\)](#) performed imaging spectroscopy on the post-flare loops observed above an occulted active region that not imageable by *RHESSI*. [Kuhar \*et al.\* \(2017\)](#) associated these observations with a solar flare that occurred 24 hours prior, and were the first observations of the EUV late phase of a solar flare observed with *NuSTAR*. With observations integrated over 25 minutes, [Kuhar \*et al.\* \(2017\)](#) were able to fit the

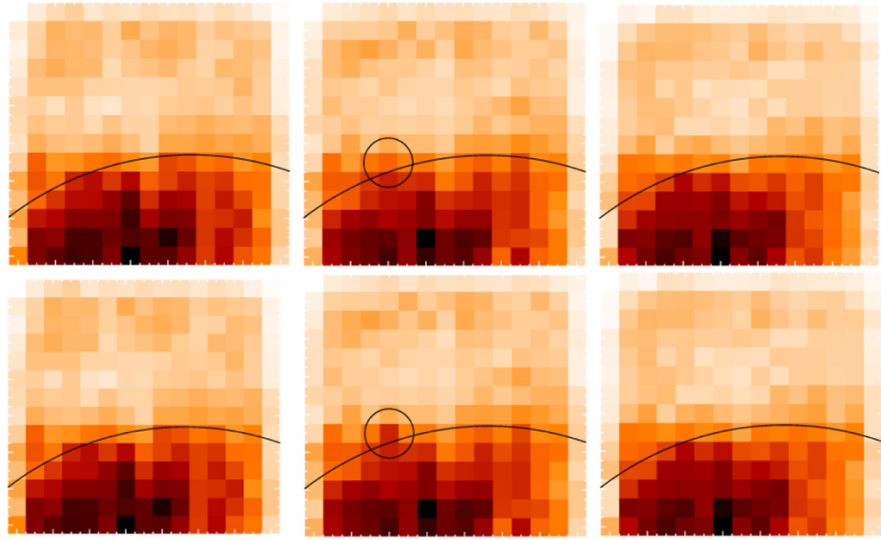


Figure 4.11: *Top*: An example of three successive (100 s averaged) *NuSTAR* observations of a  $60'' \times 60''$  region near the solar limb (black line), with a pixel highlighted by a black circle. *Bottom*: As above but with the highlighted pixel containing enough counts to reach the 95% detection threshold (Marsh *et al.*, 2017). This Figure is from Marsh *et al.* (2017).

spectrum with a single thermal component of 3.8 – 4.6 MK and emission measure in the range of  $(0.3 - 1.8) \times 10^{46} \text{ cm}^{-3}$ . Using the approach of Cargill *et al.* (1995) (with post-flare loop properties derived from *GOES*), Kuhar *et al.* (2017) deduce that for these loops must have formed and then cooled since the flare, and were estimated to have an energy content up to an order of magnitude larger than the one derived at the flare peak.

Marsh *et al.* (2018) used the coordinated *NuSTAR* and *FOXSI-2* observations to constrain physical properties of the nanoflares (e.g. heating amplitude,  $H_0$ ; duration,  $\tau$ ; and delay time,  $t_N$ , between events) with EBTEL hydrodynamic simulations. For the EBTEL simulations, Marsh *et al.* (2018) used a triangular heating function, with a heating amplitude  $H_0$ , and a width (event duration) of  $\tau$  seconds, in addition to a constant background heating rate. The EBTEL coronal DEMs were used to model the X-ray spectra which was then compared to observations from *NuSTAR* and *FOXSI-2*. For a number of parameter combinations Marsh *et al.* (2018) produced  $\chi^2$  intensity maps with 90% confidence regions to constrain a portion of parameter space that is

consistent with observations. For the (hotter) *FOXSI-2* observations, [Marsh \*et al.\* \(2018\)](#) find that the best fits occur with  $t_N > 900$  s, the heating amplitudes required to fit the *FOXSI-2* data are  $H_0 = 0.02 - 13 \text{ erg cm}^{-2} \text{ s}^{-1}$ , and that the fit quality is insensitive to nanoflare duration.

#### 4.4.2.4 April 25, 2015 & September 2, 2015

*NuSTAR* has also been used to investigate the smallest observable microflares in order to understand if the properties of flares scales from the largest to smallest events (e.g. [Hannah \*et al.\*, 2011](#)). There have been two publications on the observation of active region microflares, and both were determined to be equivalent to a GOES  $\sim$ A0.1-class event.

The first of these observations were obtained on 29th April 2015 and consisted of two full-Sun mosaics with additional Sun-center pointings (in search of an axion-like signal). These observations were also complemented by *Hinode*/XRT observations of the on-disk active region, AR 12333, and are described further in Chapter 5. In this work, [Wright \*et al.\* \(2017\)](#) performed imaging-spectroscopy of an on-disk microflaring active region, and further performed DEM analysis (Chapter 3) over an unprecedented temperature range using *SDO*/AIA, *Hinode*/XRT, and *NuSTAR*.

The second of these observations were obtained on 1st September 2015. These observations include a single full-disk mosaic and a limb sit-and-stare observation that lasted several orbits. During these limb observations a small microflare was observed [Glesener \*et al.\* \(2017\)](#). [Glesener \*et al.\* \(2017\)](#) performed time-dependent *NuSTAR* imaging spectroscopy over the duration of the microflare (see Figure 4.12). Figure 4.12 shows the hard X-ray evolution of a microflare observed on the (West) solar limb by [Glesener \*et al.\* \(2017\)](#) in the 2 – 4, and 4 – 8 keV ranges with FPMA. These observations have been summed in to one minute intervals, with the observed spectra of the microflare showing heating, but no non-thermal emission. During the flare evolution shown in Figure 4.12, the spectra for each time are fitted by single thermal models with temperatures of 5.2–8.4 MK, and emission measures of  $0.1 - 3 \times 10^{45} \text{ cm}^{-3}$ , in addition to a quiescent 3.9 MK,  $1 \times 10^{46} \text{ cm}^{-3}$  component. This leads to well-fitted spectra for all times, except during the second and third intervals in Figure 4.12.

This A0.1-class microflare reached a peak thermal energy of  $2.4 \times 10^{27} \text{ erg}$ , with higher energy hard X-rays peaking earlier which suggests impulsive energy release, and

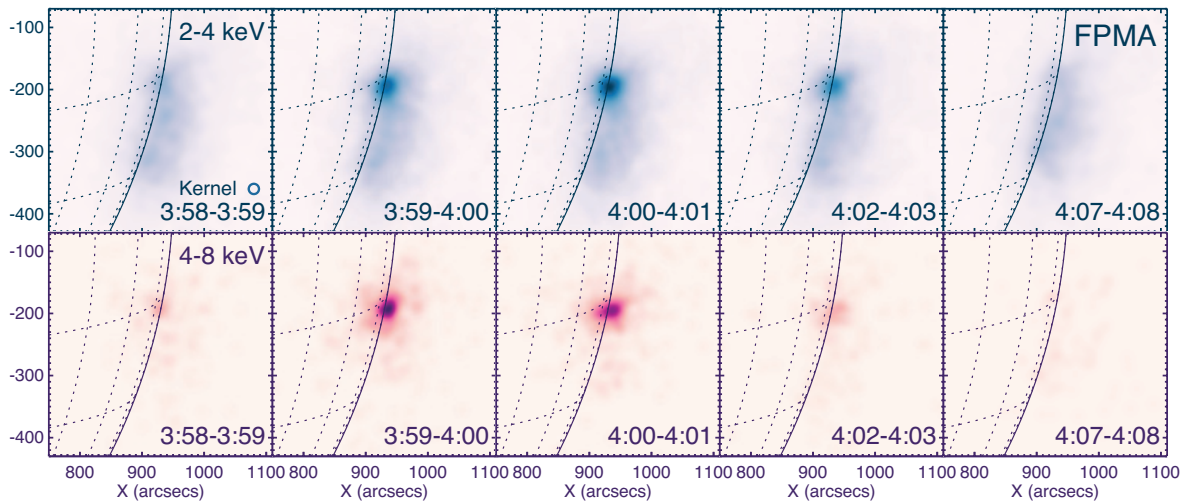


Figure 4.12: Time evolution of the 2 – 4, and 4 – 8 keV *NuSTAR* (FPMA) hard X-ray images summed in to five one minute bins. Adapted from [Glesener \*et al.\* \(2017\)](#).

all times are well-fitted by a single thermal model, except for the impulsive phase. No non-thermal emission was observed in this flare, which may be caused by the low livetime (1 – 2% over the observations) which limits the spectral dynamic range, which will be addressed in Chapter 5.

#### 4.4.2.5 Further Observations: 2016 - Present

As of September 2018, there have been 10 additional observations since 2016. These include observations obtained during the Great American Eclipse (21st August 2017) and observations with the *Hi-C* 2.1 (29th May 2018) and *FOXSI-3* (7th September 2018) sounding rockets.

From these more recent observations [Kuhar \*et al.\* \(2018\)](#) investigated X-ray flares in the quiet Sun. Using 1.5 hours of quiet Sun observations obtained on 2016 July 26 and 2017 March 21, [Kuhar \*et al.\* \(2018\)](#) performed the first imaging spectroscopy of three quiet Sun microflares. These three microflares are well fitted by temperatures of 3.2 – 4.1 MK, with emission measures in the range of  $(0.6 - 15) \times 10^{44} \text{ cm}^{-3}$ , with the estimated GOES classes being between A-0.001 and A-0.01. As with the *NuSTAR* active region microflares ([Wright \*et al.\*, 2017](#); [Glesener \*et al.\*, 2017](#)), no non-thermal emission was detected, however the thermal emission of these three events ranges from  $1.8 - 6.0 \times 10^{26} \text{ erg}$ . Using the method described in [Wright \*et al.\* \(2017\)](#) (Chapter 5),

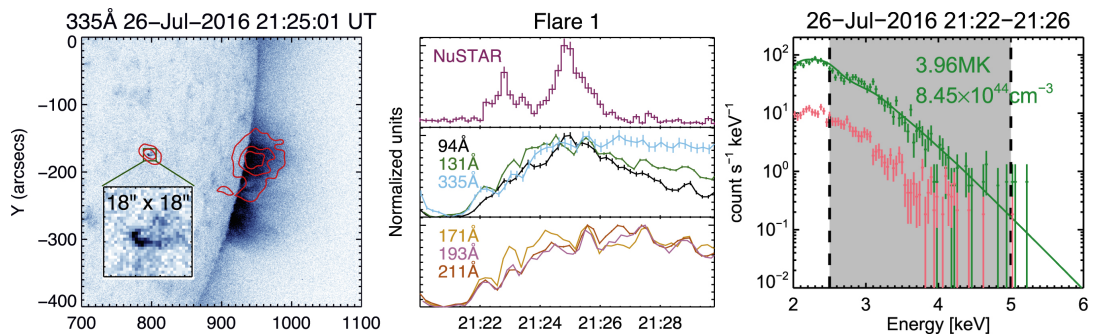


Figure 4.13: Overview of one of the three quiet Sun flares. *Left*:  $400'' \times 400''$  *SDO/AIA*  $335 \text{ \AA}$  image, with a zoomed in  $18'' \times 18''$  image of the quiet Sun flare with the 30%, 50%, and 70% *NuSTAR* contours overplotted. *Middle*: background-subtracted and normalised *SDO/AIA* plots of flux together with the *NuSTAR* integrated flux. *Right*: *NuSTAR* spectrum (FPMA, FPMB combined) for this flare (dark green), with the background spectrum shown in pink. The Temperature and Emission Measure values are calculated from a fit in the energy range  $2.5 - 5.0 \text{ keV}$ . This Figure is adapted from [Kuhar et al. \(2018\)](#).

[Kuhar et al. \(2018\)](#) set an upper limits on the non-thermal component to be  $\sim 5 \times 10^{26}$  erg, consistent with the thermal result. Figure 4.13 shows the observation, and evolution of one of these flares with time. Figure 4.13 shows the *SDO/AIA*  $335 \text{ \AA}$  observation for a  $400'' \times 400''$  region (*left*), along with the temporal behaviour of the *NuSTAR* flux and *SDO/AIA* channels (*middle*), and the *NuSTAR* spectrum (dark green) fit between  $2.5 - 5.0 \text{ keV}$  is also shown (*right*).

## 4.5 Summary

Even though *NuSTAR* is not optimised for solar observations, this chapter has shown, with the aid of several publications, that *NuSTAR* is highly capable of obtaining scientifically useful observations of the Sun. These observations have led to advances in knowledge of active regions, quiet Sun, and transient coronal events, and the next chapter will provide a detailed overview of the first *NuSTAR* microflare.

From these initial results it is clear that future observations from a solar-dedicated focusing optics hard X-ray instrument will further our understanding of heating and particle acceleration in the solar corona. *NuSTAR* observations of the Sun will continue

---

through solar minimum—which is increasingly important in a time when there is no dedicated solar hard X-ray instrument—in order to address the three science goals outlined in § 4.4.1. Importantly, the observations will also overlap with the *FOXSI* sounding rocket, and soft(er) X-ray observations from instruments such as *MinXSS-2* (Moore *et al.*, 2018) and *MaGIXS* (Kobayashi *et al.*, 2018), which together will help build a more complete understanding of high-temperature coronal emission.

# Chapter 5

## The First *NuSTAR* Microflare

*The work in this chapter has been published as part of Wright et al. (2017).*

This chapter will present *NuSTAR* imaging spectroscopy of the first microflare jointly observed with *Hinode*/XRT (Kosugi *et al.*, 2007; Golub *et al.*, 2007) and *SDO*/AIA (Pesnell *et al.*, 2012; Lemen *et al.*, 2012). This active region microflare occurred on 29th April 2015 at  $\sim 11:29$  UT, and shows heating of material to several million Kelvin which was observed in Soft X-rays (SXR) with *Hinode*/XRT, and was faintly visible in Extreme Ultraviolet (EUV) with *SDO*/AIA.

The observations used in this chapter were obtained during the fourth *NuSTAR* solar pointing in a coordinated observing campaign between *SDO*/AIA, *Hinode*/XRT, and *NuSTAR* to obtain the first full-Sun mosaic observations with *NuSTAR*. The press release image<sup>1</sup> is presented in Figure 5.1, and this image is one of the five highlights from *NuSTAR*'s first five years in space<sup>2</sup>. Figure 5.1 shows the Sun over a wide range of wavelengths, from EUV (*SDO*/AIA, 171 Å, 193 Å), to SXR (*Hinode*/XRT), and HXR (*NuSTAR*, 2 – 6 keV, blue). As *NuSTAR* observes a limited field-of-view (Chapter 4), the *NuSTAR* observations obtained during these observations were obtained in its mosaic mode (§ 4.4.2). This means that the on-disk microflaring active region was only observed at four times throughout the observation. Coincidentally, these will be shown to coincide with the pre-flare, impulsive, decay, and post-flare phases.

In this chapter, § 5.1 and § 5.2 will present the *SDO*/AIA, *Hinode*/XRT, and *NuSTAR* overviews for this microflare, and § 5.3 will present the analysis of *NuSTAR* data

---

<sup>1</sup><https://www.nasa.gov/jpl/pia19821/nustar-stares-at-the-sun>

<sup>2</sup><https://www.jpl.nasa.gov/news/news.php?feature=6872>

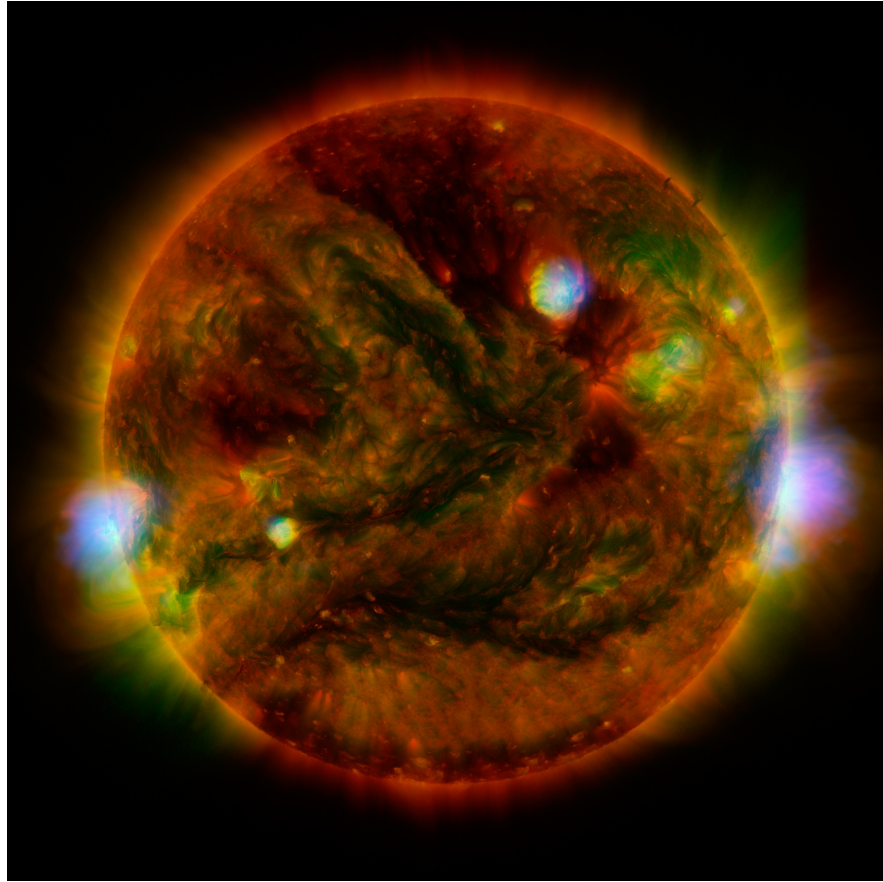


Figure 5.1: Combined *NuSTAR* 2 – 6 keV (blue), *SDO/AIA* (171 Å, red; 193 Å, yellow), *Hinode/XRT* (green) observations of the Sun on 29th April 2015. This press release image is available at <https://www.nasa.gov/jpl/pia19821/nustar-stares-at-the-sun>.

to derive thermal properties of this event. In addition to this approach, § 5.4.2 presents DEM analysis, constraining the emission measure over an unprecedented temperature range. The thermal energetics from DEM analysis are also derived. Finally, as the *NuSTAR* spectrum is purely thermal, in § 5.5 upper-limits on the possible non-thermal bremsstrahlung emission are calculated.

## 5.1 *SDO/AIA* and *Hinode/XRT* Event Overview

The microflare observed by *NuSTAR* within NOAA AR 12333 occurred during a time when there were two brighter active regions on the disk, as can be seen in Figure 5.2. Figure 5.2 shows the *SDO/AIA* Fe XVIII conditions during the microflare (*middle*), and

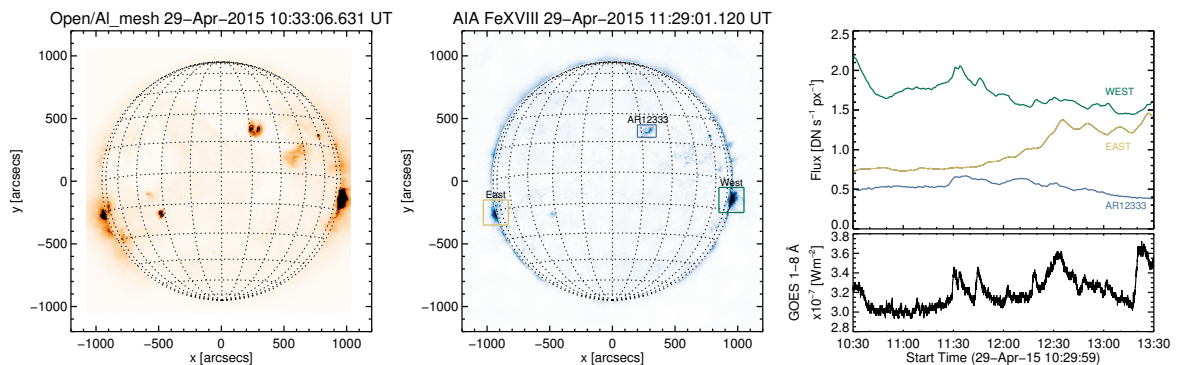


Figure 5.2: Overview of the *SDO/AIA* 94 Å Fe XVIII conditions during the times of the *NuSTAR* observations, and *Hinode/XRT* prior to the AR 12333 microflare onset. *Left*: full-disk image from *Hinode/XRT* one hour prior to the microflare onset. *Middle*: full-disk *SDO/AIA* 94 Å Fe XVIII image at the peak of the microflare impulsive phase with the ARs indicated. The *SDO/AIA* 94 Å Fe XVIII light curves from these three regions are shown in comparison to the full-disk *GOES* 1-8 Å SXR flux (*right*). All of the regions are producing several microflares during these times, but those from AR 12333 are hidden in the *GOES* light curve as those from the two limb regions are brighter.

a *Hinode/XRT* image (Al-mesh, *left*) one hour prior. Additionally shown (*right*) are three hours of Fe XVIII fluxes for the three regions that correspond to active regions (and the majority of high energy emission). This is shown in comparison to the spatially-integrated *GOES* 1 – 8 Å observations, and describe the individual contributions to the *GOES* 1 – 8 Å flux. In these observations it was the limb active regions that were producing microflares that dominate the *GOES* 1 – 8 Å SXR light curve.

The Fe XVIII line contribution to the *SDO/AIA* 94 Å channel peaks at  $\log_{10} T = 6.85$  K ( $\sim 7$  MK), and can be recovered using a combination of the *SDO/AIA* channels (Reale *et al.*, 2011; Warren *et al.*, 2012; Testa & Reale, 2012; Del Zanna, 2013). Here we use the approach of Del Zanna (2013),

$$F(\text{Fe XVIII}) \approx F(94 \text{ \AA}) - \frac{F(211 \text{ \AA})}{120} - \frac{F(171 \text{ \AA})}{450}, \quad (5.1)$$

where  $F(\text{Fe XVIII})$  is the Fe XVIII flux [ $\text{DN s}^{-1} \text{ px}^{-1}$ ] and  $F(94 \text{ \AA})$ ,  $F(171 \text{ \AA})$ ,  $F(211 \text{ \AA})$ , are the equivalent fluxes in the *SDO/AIA* 94 Å, 171 Å, and 211 Å channels. Equation 5.1 was empirically derived by Del Zanna (2013) using a linear combination of the

171 Å, and 211 Å channels. This was performed as the 211 Å emission is used as a proxy for the Fe XIV line, and the 171 Å channel is used to roughly estimate the weaker contributions from Fe VIII, Fe IX, and Fe X lines which all contribute to the 94 Å temperature response function. By utilising *Hinode/EIS* observations of an active region core, [Del Zanna \(2013\)](#) performed DEM inversion (with 12 Iron lines) and were able to estimate the Fe XVIII contribution in the *SDO/AIA* 94 Å channel. This was performed by subtracting all known contributions to the *SDO/AIA* 94 Å count rates where the Fe VIII–Fe XIV contributions can be accurately estimated by *Hinode/EIS*.

*Hinode/XRT* observed AR 12333 in a high cadence mode ( $\sim 2 - 3$  minutes), cycling through five different filter channels centred on this region. Full-disk synoptic images were obtained before and after this observation mode (Figure 5.2). Figure 5.3 shows the main loops of the region rapidly brightening, indicating that energy is being released to heat these loops. This is apparent in the SXR channels from *Hinode/XRT* and *SDO/AIA* 94 Å Fe XVIII, but not the cooler EUV channels from *SDO/AIA*, so we conclude that the heating is to mostly above 3 MK. For the  $95'' \times 45''$  loop region shown in Figure 5.3 we produce the time profile of the microflares in each of these SXR and EUV channels, shown in Figure 5.4. Figure 5.4 shows the *Hinode/XRT* and *SDO/AIA* time profiles with the *NuSTAR* observations of the active region highlighted by black dashed lines. These light curves have been obtained after processing via the instrument preparation routines, de-rotation of the solar disk (to  $\sim 11:29$  UT), and manual alignment of *Hinode/XRT* Be-Thin to the  $1''$  down-sampled *SDO/AIA* 94 Å Fe XVIII data. Here we again see that the microflare activity is only occurring in the channels sensitive to the hottest material, i.e. the SXR ones from *Hinode/XRT* and *SDO/AIA* 94 Å Fe XVIII. This activity is in the form of three distinctive peaks with the first, and largest, impulsively starting at  $\sim 11:29$  UT. This is clear in the SXR (with the exception of the low signal-to-noise *Hinode/XRT* Be-Thick channel), and *SDO/AIA* 94 Å Fe XVIII lightcurves, all showing similar time profiles.

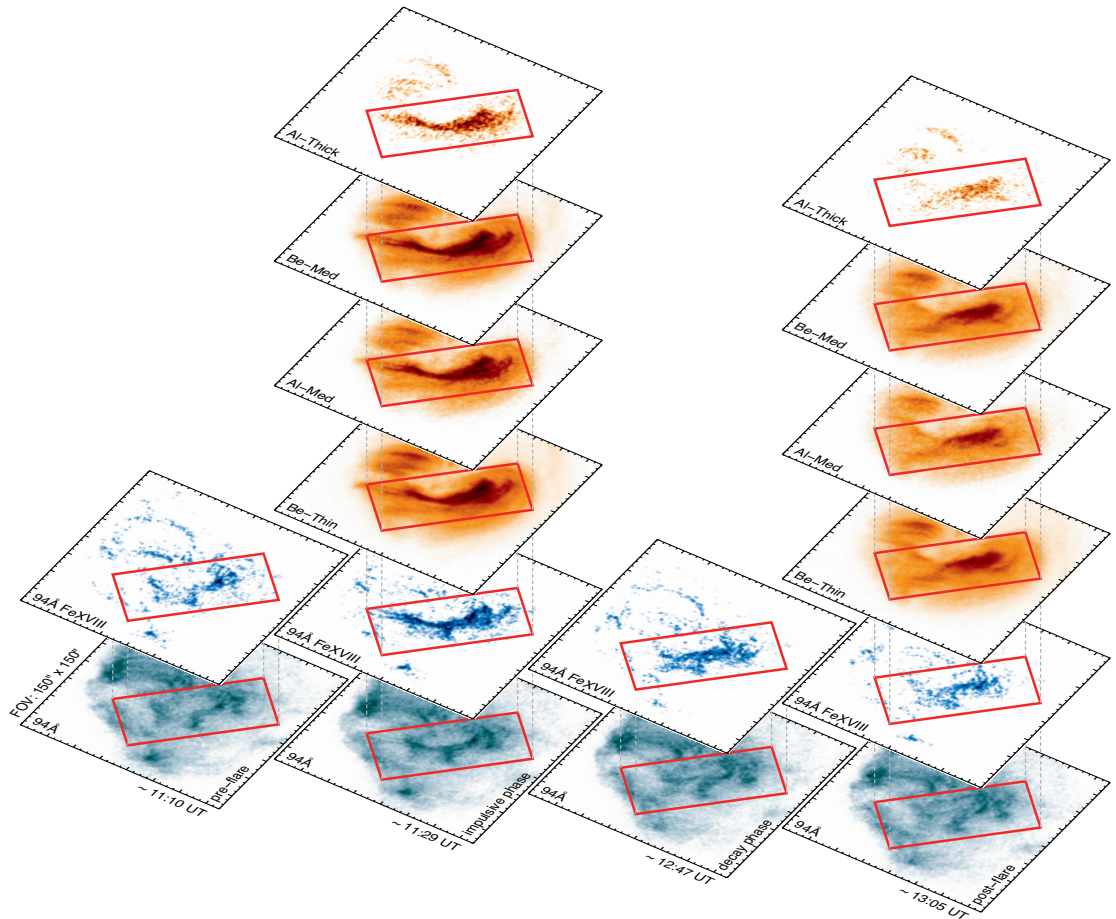


Figure 5.3: Comparison of AR 12333 from *SDO*/AIA and *Hinode*/XRT at the times of *NuSTAR* observations (pre-flare,  $\sim 11:10$  UT; impulsive phase,  $\sim 11:29$  UT; decay phase,  $\sim 12:47$  UT; and post-flare,  $\sim 13:05$  UT). Each image is  $150'' \times 150''$  and is centered on  $[275'', 400'']$ . The loop region ( $95'' \times 45''$ ) used for the light curves and DEM analysis is overplotted as a red rectangle. The loop region is faintly observable in *SDO*/AIA  $94 \text{ \AA}$  with the structure well-recovered in the *SDO*/AIA  $94 \text{ \AA}$  Fe XVIII and SXR channels.

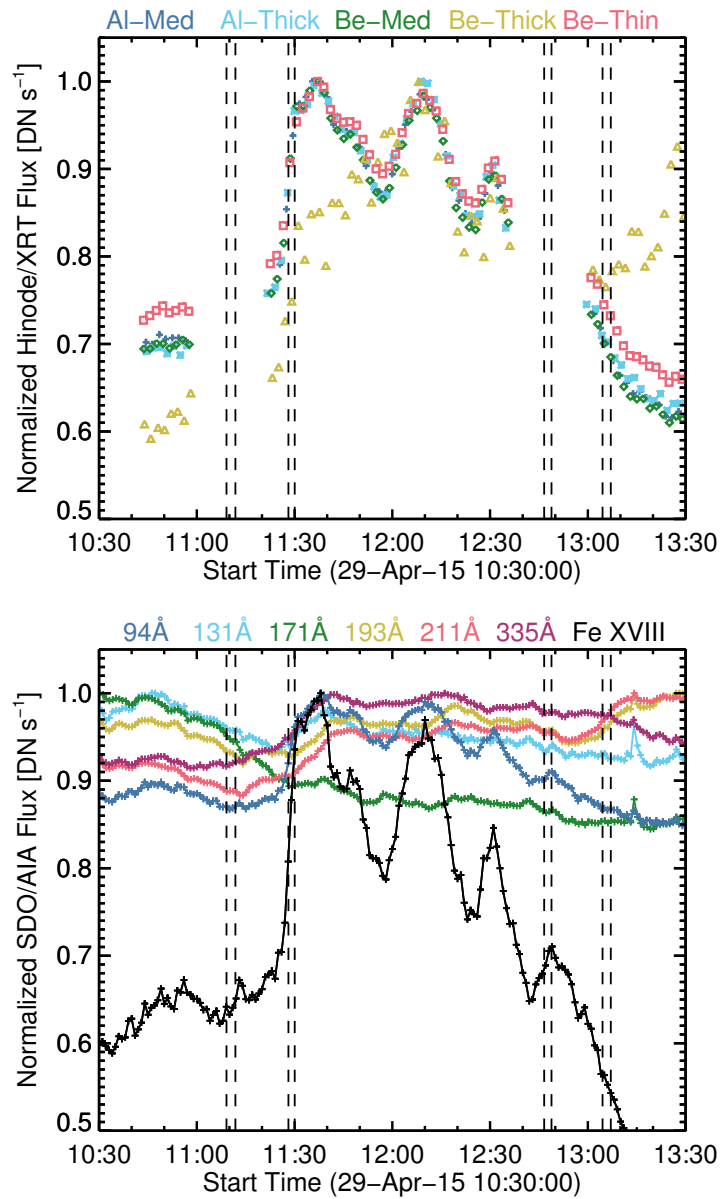


Figure 5.4: Time profiles of the different *Hinode/XRT* (*top*) and *SDO/AIA* (*bottom*) channels from the loop region of AR 12333 shown in Figure 5.3. The vertical bars indicate the four time periods of the *NuSTAR* observation of the same region. The gaps in the *Hinode/XRT* light curves are due to incomplete coverage.

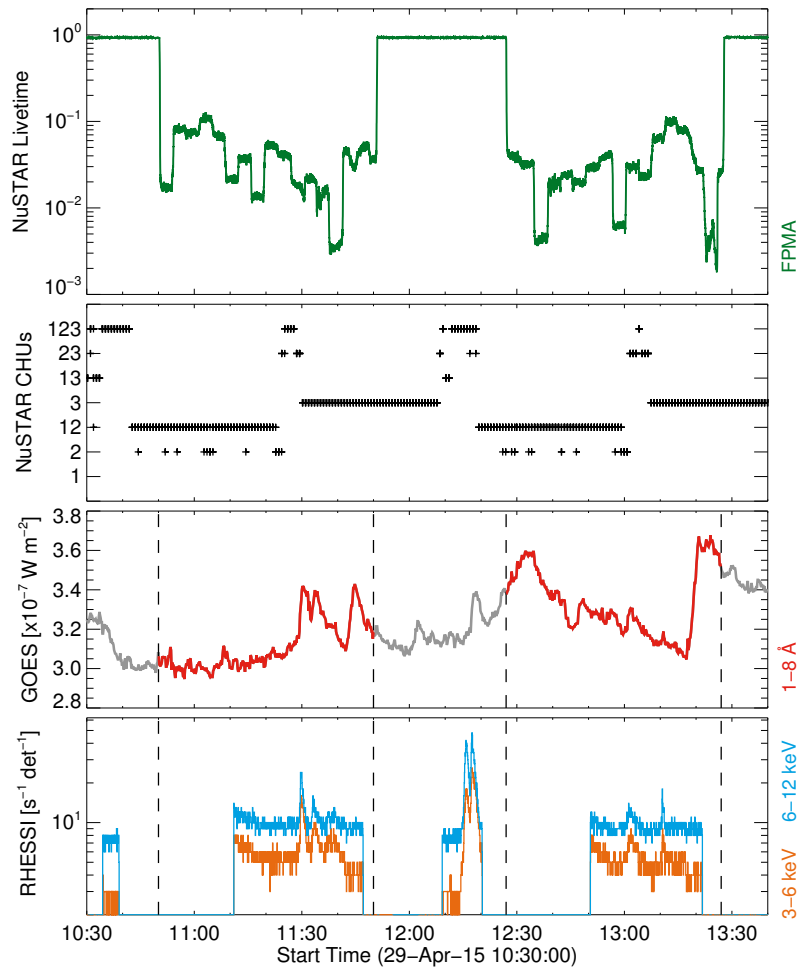


Figure 5.5: *Top to bottom*: *NuSTAR* (FPMA) livetime over the three-hour observation window, with two; CHU combination over the observation window; GOES 1 – 8 Å flux, with vertical dashed lines indicating the two orbits (10:50–11:50 UT and 12:27–13:27 UT) where the GOES 1 – 8 Å flux is highlighted red; and RHESSI counts  $\text{s}^{-1}$  per detector, 3 – 6 keV (orange), 6 – 12 keV (blue). This Figure is from the *NuSTAR* quick-look observations at [http://ianan.github.io/nsigh\\_all/](http://ianan.github.io/nsigh_all/).

## 5.2 *NuSTAR* Event Overview

The observations reported here consist of two orbits of observations (each consisting of approximately an hour of observations, and a 30 minute eclipse) covering 10:50–11:50 UT and 12:27–13:27 UT (see [Grefenstette et al., 2016](#)). Figure 5.5 shows the *NuSTAR* livetime (for FPMA); CHU combination; GOES 1 – 8 Å flux; and *RHESSI* counts over

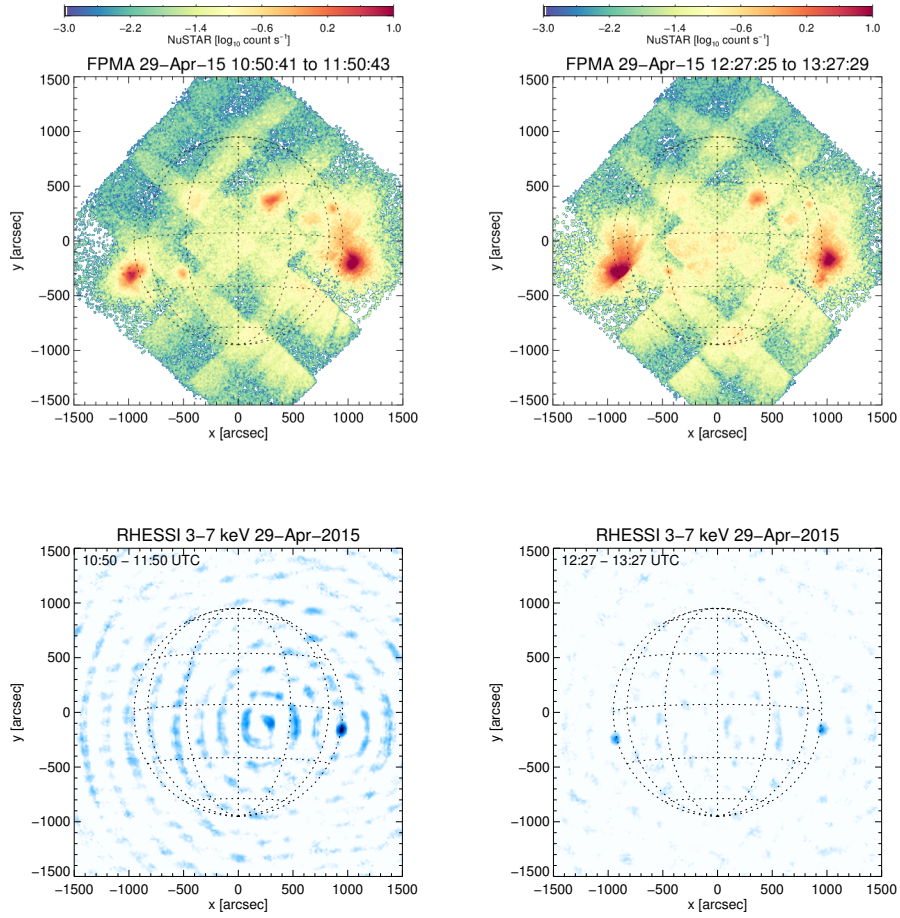


Figure 5.6: *Top*: *NuSTAR* mosaics between 10:50–11:50 UT (*left*), and 12:27–13:27 (*right*), displaying three active regions (one at either limb, and one on disk), along with ghost-ray signatures (§ 4.2.1.2). *Bottom*: Reconstructed images at similar times from *RHESSI*. For 10:50–11:50 UT, the *RHESSI* observations show only the brightest active region, and for 12:27–13:27 UT both limb active regions are observed. At both times, *RHESSI* observations do not show the on-disk active region analysed within this chapter.

3 – 6, and 6 – 12 keV for the 3.5 hours of observations, with the two orbits highlighted in the *GOES* observations (red).

Figure 5.6 (*top*) shows these two mosaic observations obtained by one of the *NuSTAR* (telescope A) over these orbits. For these observations, *NuSTAR* completed a full disk mosaic observation in each orbit consisting of 17 different pointings: the field-of-view requires 16 different pointings to cover the whole Sun, with some overlaps

between each mosaic tile, followed by an additional disk centre pointing (see Figure 4 Grefenstette *et al.*, 2016). In addition to the two *NuSTAR* mosaics, Figure 5.6 (*bottom*) shows the equivalent images for the *RHESSI* observations over the same time, where the *RHESSI* observations have been reconstructed using the CLEAN algorithm (Högbom, 1974).

These mosaic observations resulted in *NuSTAR* observing AR 12333 four times, each lasting for a few minutes. These times are shown in Figure 5.4. These data were processed using the *NuSTAR* Data Analysis software v1.6.0 and *NuSTAR* CALDB 20160502<sup>3</sup>, which produces an event list for each pointing. We use only single-pixel (“Grade 0”) events (Grefenstette *et al.*, 2016), to minimize the effects of pile-up. Figure 5.7 shows the resulting *NuSTAR* 2.5 – 4.5 keV image for each of the four pointings and these images are a combination of both FPMA and FPMB with  $\sim 7''$  Gaussian smoothing as the pixel size is less than the full width at half maximum (FWHM) of the optics.

### 5.3 *NuSTAR* Data Analysis

Two of these pointings, the first and last, caught the whole active region but the other two only caught the lower part as they were observed at the edge of the detector, however this is the location of the heated loops during the microflares in Figure 5.3. During some of the observations there was a change in the combination of Camera Head Units (CHUs)—star trackers used to provide pointing information. In such instances we used the time range that gave the longest continuous CHU combination (see Figure 5.5), instead of the whole duration. For each CHU combination, a different shift to match the *SDO/AIA* 94 Å Fe XVIII map at that time was required, however all were within the expected 1' offset (Grefenstette *et al.*, 2016). The alignment was straightforward for the *NuSTAR* maps which caught the whole region but for those with a partial observation (the second and third pointings) emission from another region (slightly to the South-West of AR 12333) was used for the alignment. The resulting overlap of the aligned *Hinode/XRT* and *NuSTAR* images to *SDO/AIA* 94 Å Fe XVIII are shown in Figure 5.8 and these images are assumed to be aligned to within 5". Figure 5.8 shows the four *NuSTAR* 2.5 – 4.5 keV maps (*left to right, top to bottom*) for the four observations

<sup>3</sup><http://heasarc.gsfc.nasa.gov/docs/NuSTAR/analysis/>

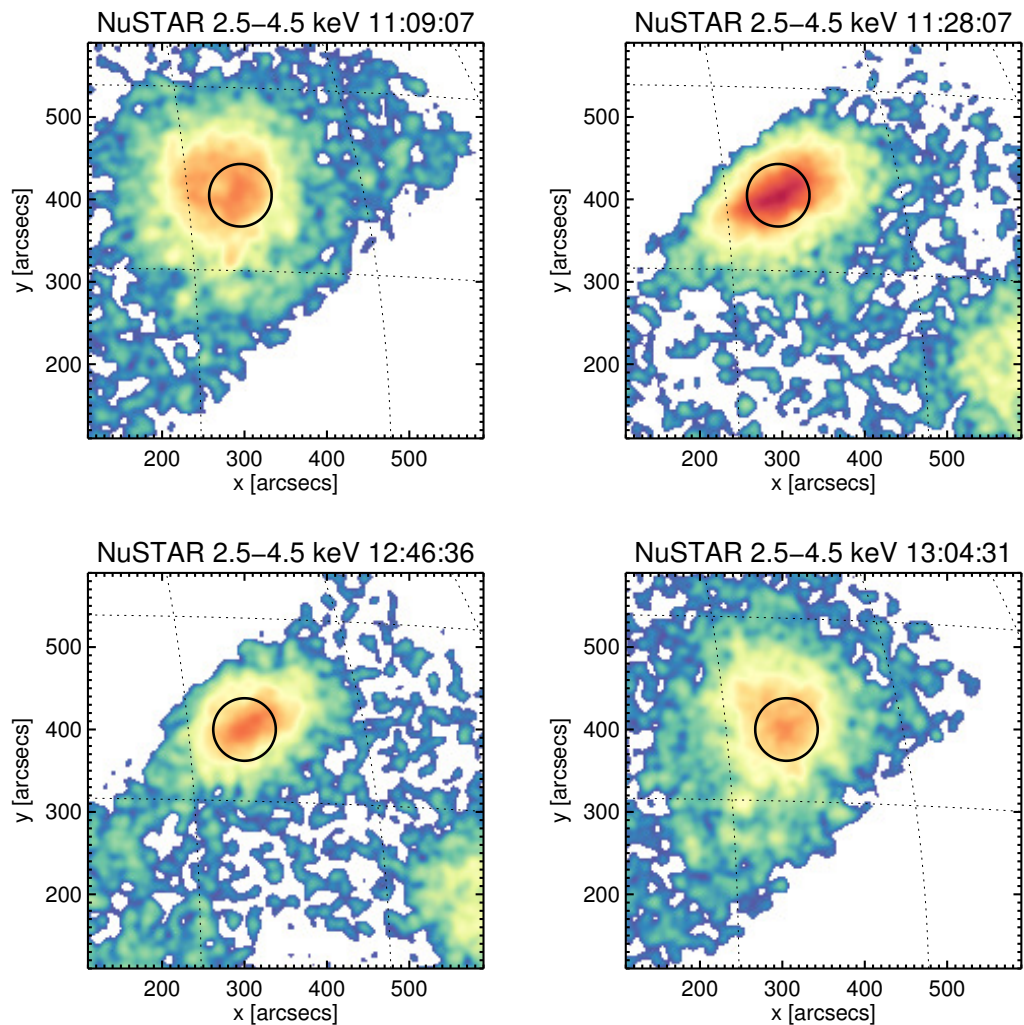


Figure 5.7: *NuSTAR* 2.5–4.5 keV maps for the four time intervals it observed AR 12333. These maps have been shifted to match the position of the *SDO/AIA* 94 Å Fe XVIII maps, shown in Figure 5.8. The black circles indicate the regions chosen for spectral fitting, shown in Figure 5.9. Note that the same colour scaling is used in all these maps.

(plotted over the same colour scale), including the circular region used for spectral fitting. The *NuSTAR* maps in Figure 5.7 reveal a similar pattern to the heating seen in EUV and SXR with *SDO/AIA* and *Hinode/XRT*: emission from the whole region before the microflare, with loops in the bottom right brightening as material is heated during the microflare, before fading as the material cools.

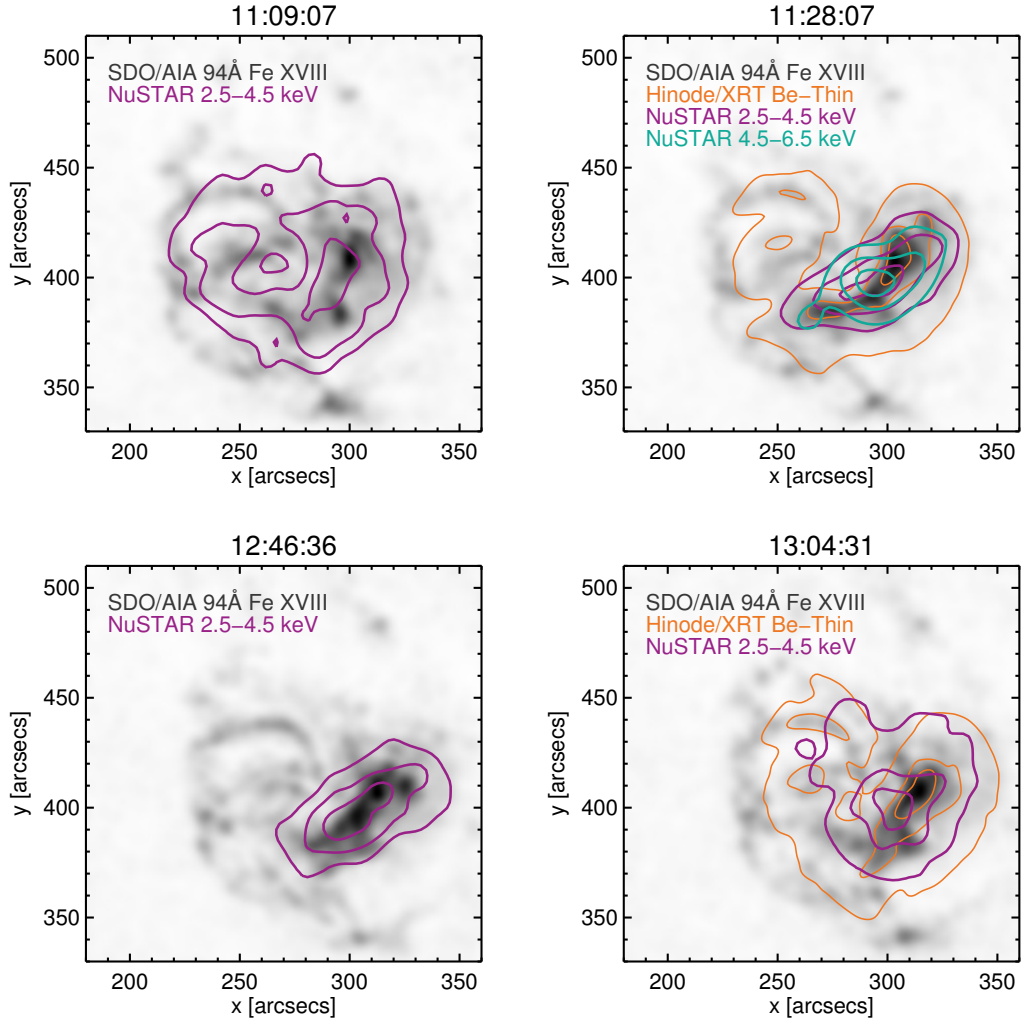


Figure 5.8: *SDO/AIA* 94 Å Fe XVIII maps overlotted with shifted contours from *Hinode/XRT* (20%, 50%, 80%; orange), and *NuSTAR* 2.5 – 4.5 keV and 4.5 – 6.5 keV emission (50%, 70%, 90%; purple, turquoise). A constant offset correction was required for *Hinode/XRT* but a different one was determined for each *NuSTAR* pointing. For the two time intervals where *NuSTAR* only observed part of the active region (middle two panels), the alignment was done using the full map and to other features on the disk.

### 5.3.1 *NuSTAR* Spectral Fitting

For each of the *NuSTAR* pointings we chose a region at the same location, and of the same area, as those used in the *SDO/AIA* and *Hinode/XRT* analysis, to produce

spectra of the microflare heating. These are circular as the *NuSTAR* software can only calculate the response files for such regions, but do cover the flaring loop region (rectangular box, Figure 5.3), and are shown in Figure 5.7. The spectra and *NuSTAR* response files were obtained using the *NuSTAR* Data Analysis software v1.6.0. These were then fitted using the XSPEC (Arnaud, 1996) software<sup>4</sup>, which simultaneously fits the spectra from each telescope module (FPMA and FPMB) instead of just adding the data sets. We also use XSPEC as it allows us to find the best-fit solution using Cash statistics (Cash, 1979) which is based on the Poisson distribution rather than using  $\chi^2$  (which assumes a Gaussian distribution). While for large number of counts the Poisson distribution tends to a Gaussian (and the Cash statistic tends to  $\chi^2$ ), the use of the Cash statistic particularly helps for the few counts at higher temperatures.

We fitted the spectra with a single thermal model, using the APEC model with solar coronal abundances (Feldman *et al.*, 1992), and the fit results are shown in Figure 5.9. For the first and fourth *NuSTAR* pointings, before and after the microflares, the spectra are well fitted by this single thermal model showing similar temperatures and emission measures (3.3 MK and  $6.3 \times 10^{46} \text{ cm}^{-3}$ , then 3.2 MK and  $7.0 \times 10^{46} \text{ cm}^{-3}$ ). Above 5 keV there are very few counts and this is due to a combination of the low livetime of the observations (164 s and 152 s dwell time with about 2% livetime fraction resulting in effective exposures of around 3.5 s) and the high likelihood that the emission from this region peaked at this temperature before falling off very sharply at higher temperatures. These temperatures are similar to the quiescent ARs previously studied by *NuSTAR* (Hannah *et al.*, 2016), although those regions were brighter and more numerous in the field-of-view, resulting in an order-of-magnitude worse livetime. The low livetime has the effect of limiting the spectral dynamic range, putting most of detected counts at the lower energy range, and no background or source counts at higher energies (Hannah *et al.*, 2016; Grefenstette *et al.*, 2016).

The two *NuSTAR* spectra from during the microflare, the second (impulsive phase) and third (decay phase, weaker peak) both show counts above 5 keV and produce higher temperature fits (5.1 MK and 3.5 MK). This is expected as there should be heating during the microflare, but neither fit matches the observed spectrum well, particularly during the impulsive phase. This shows that there is additional hot material during these times that a single-component thermal model cannot accurately charac-

---

<sup>4</sup><https://heasarc.gsfc.nasa.gov/xanadu/xspec/>

terise. For the spectrum during the impulsive phase, the second *NuSTAR* pointing, we tried adding additional thermal components to the fit, shown in Figure 5.10. We started by adding in a second thermal component fixed with the parameters from the pre-microflare spectrum, found from the first *NuSTAR* pointing (left spectrum in Figure 5.9), to represent the background emission. We did this as *NuSTAR*'s pointing changed during these two times (changing the part of the detector observing the region, and hence instrumental response) so we could not simply subtract the data from this pre-flare background time. The other thermal model component was allowed to vary and produced a slightly better fit to the higher energies and a higher temperature (5.6 MK). However this model still misses out counts at higher energies.

We therefore tried another fit where the two thermal models were both allowed to vary and this is shown in the right of Figure 5.10. Here there is a substantially better fit to the data over the whole energy range, fitting a model of 4.1 MK and 10.0 MK. The hotter model does seem to match the bump in emission between 6 and 7 keV, which at these temperatures would be due to line emission from the Fe K-Shell transition (Phillips, 2004). Although this model better matches the data, it produces substantial uncertainties, particularly in the emission measure. This is because it is fitting the few counts at higher energies which have a poor signal to noise. It should be noted that for the thermal model the temperature and emission measure are correlated and so the upper uncertainty on the temperature relates to the lower uncertainty on the emission measure, and vice versa. Therefore this uncertainty range covers a narrow diagonal region of parameter space, which we include later in Figure 5.14. These fits do however seem to indicate that emission from material up to 10 MK is present in this microflare and that the *NuSTAR* spectrum in this case is observing purely thermal emission. A non-thermal component could still be present, but the likely weak emission, combined with *NuSTAR*'s low livetime (limiting the spectral dynamic range), leaves this component hidden. Upper-limits to this possible non-thermal emission are calculated in § 5.5.2.

From these spectral fits we estimated the *GOES* 1–8 Å flux<sup>5</sup> to be  $5.3 \times 10^{-9} \text{ Wm}^{-2}$  for the impulsive phase, and  $4.0 \times 10^{-9} \text{ Wm}^{-2}$  for the pre-flare time. This means that the background subtracted *GOES* class for the impulsive phase is equivalent to  $\sim$ A0.1 and would be slightly larger during the subsequent peak emission time.

<sup>5</sup>[https://hesperia.gsfc.nasa.gov/ssw/gen/idl/synoptic/goes/goes\\_flux49.pro](https://hesperia.gsfc.nasa.gov/ssw/gen/idl/synoptic/goes/goes_flux49.pro)

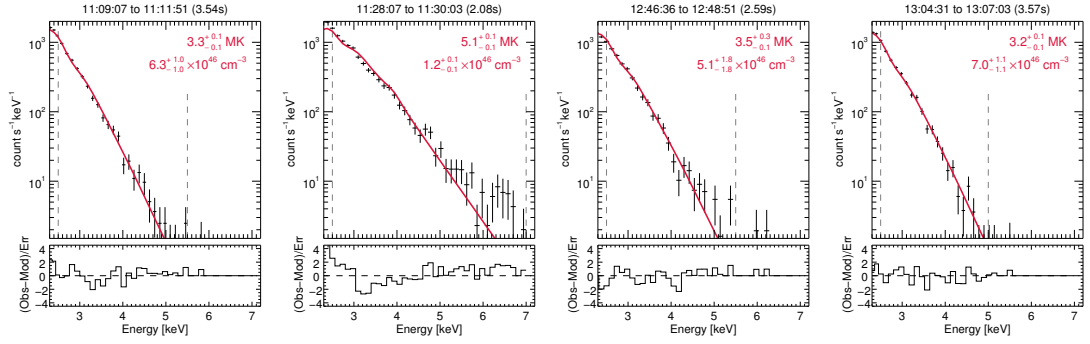


Figure 5.9: *NuSTAR* spectra for the regions shown in Figure 5.8, at different stages of flare evolution with time, increasing from *left to right*, and correspond the pre-flare, impulsive, post-flare, and decay phases. The black data points show the combined data from FPMA and FPMB, and the red line shows the best fit thermal model. Note that the fit was performed to the data simultaneously and is only combined for plotting. The bottom panels show the residuals and the dashed vertical grey lines indicate the energy range over which the fit was performed (starting from the minimal usable energy of 2.5 keV up where there are still substantial counts). The quoted uncertainties are with 90% confidence. The data shown here have been re-binned from  $\Delta\epsilon = 0.04$  for clarity.

## 5.4 Multi-thermal Microflare Emission

The *NuSTAR* spectrum during the impulsive phase of the microflare clearly shows that there is a range of heated material, so to get a comprehensive view of this multi-thermal emission we recovered the differential emission measure (DEM) by combining the observations from *NuSTAR*, *Hinode/XRT*, and *SDO/AIA*. This is the first time these instruments have been used together to obtain a DEM.

### 5.4.1 Comparison of *NuSTAR*, *Hinode/XRT* & *SDO/AIA*

To check the compatibility of the *NuSTAR*, *Hinode/XRT*, and *SDO/AIA* observations we compared the observed fluxes from *Hinode/XRT*, and *SDO/AIA* to synthetic fluxes obtained from the *NuSTAR* thermal fits. For the *NuSTAR* two thermal fit (Figure 5.10, right panel) we multiplied the emission measures by the *SDO/AIA* and *Hinode/XRT* temperature response functions at the corresponding temperatures, and then added the two fluxes together to get a value for each filter channel.

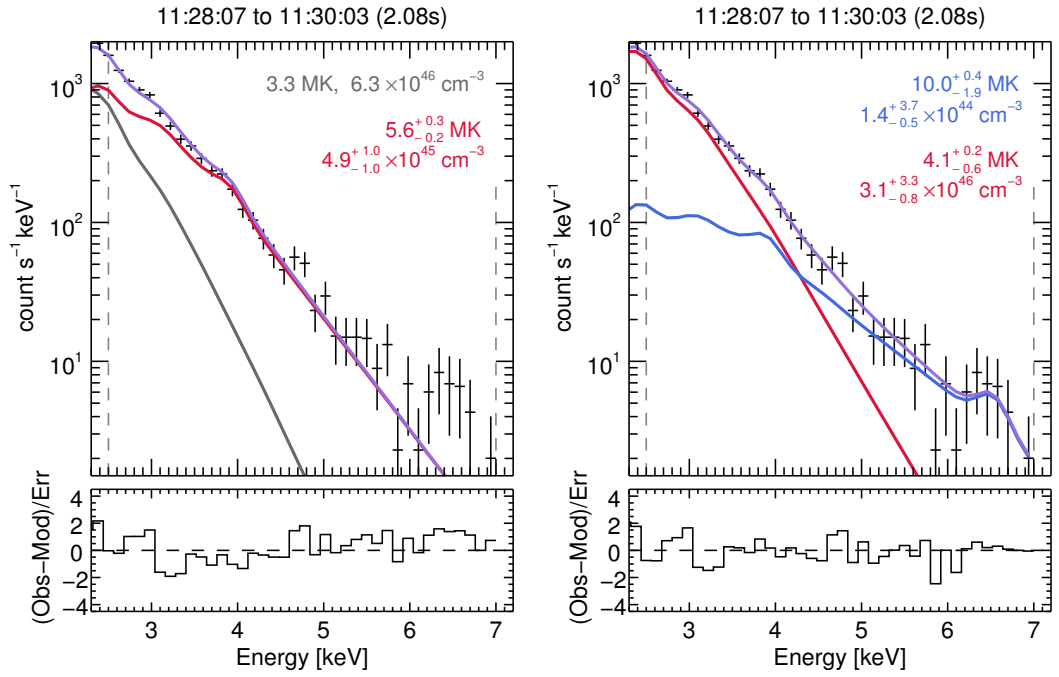


Figure 5.10: Additional model fits to the *NuSTAR* spectrum for the impulsive phase of the microflare. *Left*: model of two thermals, one fixed using the parameters from the pre-flare observation (grey line), the second one (red) fitted. *Right*: Model fitting two thermals. In both cases the total model is shown by the purple line and the black data points show the combined data from FPMA and FPMB. Note that the fit was performed to the data simultaneously and is only combined for plotting here. The quoted uncertainties are 90% confidence levels.

The *Hinode*/XRT temperature response functions were created using `xrt_flux.pro` with a CHIANTI 7.1.3 (Dere *et al.*, 1997; Landi *et al.*, 2013) spectrum (`xrt_flux713.pro`<sup>6</sup>) with coronal abundances (Feldman *et al.*, 1992), and the latest filter calibrations that account for the time-dependent contamination layer present on the CCD (Narukage *et al.*, 2014). The *SDO*/AIA temperature response functions are version six (v6; using CHIANTI 7.1.3) and obtained using `aia_get_response.pro` with the ‘chiantifix’, ‘eve\_norm’, and ‘timedepend\_date’ flags. The comparison of the observed and synthetic fluxes are shown in Figure 5.11.

We found that the *SDO*/AIA 94 Å Fe XVIII synthetic flux is near the observed value, as expected, however there is a consistent discrepancy for *Hinode*/XRT. The

<sup>6</sup>[http://solar.physics.montana.edu/takeda/xrt\\_response/xrt\\_resp\\_ch713\\_newcal.html](http://solar.physics.montana.edu/takeda/xrt_response/xrt_resp_ch713_newcal.html)

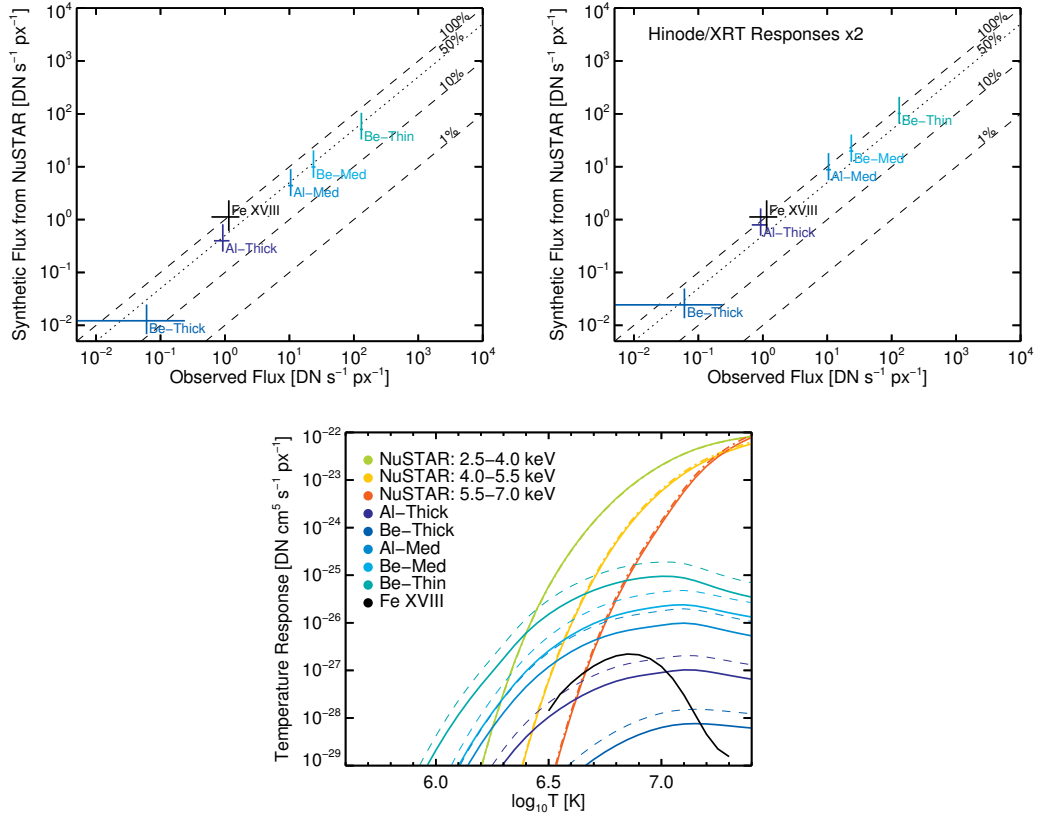


Figure 5.11: *Top*: Comparison of *Hinode*/XRT and *SDO*/AIA 94 Å Fe XVIII fluxes during the microflare’s impulsive phase, to the synthetic values obtained from the *NuSTAR* spectral fit. *Bottom*: The temperature response functions for *NuSTAR* (FPMA, solid; FPMB, dot-dash) for the region shown in Figure 5.7 (panel 2), *SDO*/AIA 94 Å Fe XVIII (solid black), and *Hinode*/XRT (original, solid;  $\times 2$ , dashed). This has been done using the standard *Hinode*/XRT responses (*top left*) and then multiplying them by a factor of two (*top right*) which gives values closer to the observed fluxes.

observed fluxes should match the synthetic fluxes from the *NuSTAR* spectral fits as they are sensitive to the same temperature range. Other authors have found similar discrepancies (Testa *et al.*, 2011; Cheung *et al.*, 2015; Schmelz *et al.*, 2015) and there is the suggestion that the *Hinode*/XRT temperature response functions are too small by a factor of  $\sim 2 - 3$  (see Schmelz *et al.*, 2015). We have therefore multiplied the *Hinode*/XRT temperature response functions by a factor of two (Figure 5.11, *top right*) and find a closer match to the synthetic values derived from the *NuSTAR* spectral fits. The main effect of these larger temperature response functions is that it requires there

to be weaker emission at higher temperatures to obtain the same *Hinode*/XRT flux.

### 5.4.2 Differential Emission Measure

As discussed in Chapter 3, recovering the line-of-sight DEM,  $\xi(T_j)$ , involves solving the ill-posed inverse problem,  $g_i = \mathbf{K}_{i,j}\xi(T)$ , where  $g_i$  [DN s<sup>-1</sup> px<sup>-1</sup>] is the observable, and  $\mathbf{K}_{i,j}$  is the temperature response function for the *i*th filter channel, and the *j*th temperature bin. Chapter 3 described a number of methods available in order to recover the temperature distribution.

In this chapter we use the regularised inversion (RI) approach (Hannah & Kontar, 2012, § 3.4.1), and the forward-fitting `xrt_dem_iterative2.pro` approach (XIT, Golub *et al.*, 2004; Weber *et al.*, 2004, § 3.4.2).

For the DEM analysis we calculated the uncertainties on the *Hinode*/XRT and *SDO*/AIA data. The non-statistical photometric uncertainties for *Hinode*/XRT were calculated from `xrt_prep.pro` (Kobelski *et al.*, 2014), and photon statistics calculated from `xrt_cvfact.pro`<sup>7</sup> (Narukage *et al.*, 2011, 2014). The uncertainties on the *SDO*/AIA data were computed with `aia_bp_estimate_error.pro` (Boerner *et al.*, 2012), and an additional 5% systematic uncertainty was added in quadrature to both the *Hinode*/XRT and *SDO*/AIA data account for uncertainties in the temperature response functions. The *Hinode*/XRT and *SDO*/AIA data and uncertainties have been linearly interpolated to a common time-step, and averaged over the *NuSTAR* observational duration. The uncertainty for the *NuSTAR* values in specific energy bands were determined as a combination of the photon shot noise and a systematic factor (of 5%) to account for the cross-calibration between *NuSTAR*'s two telescope modules (FPMA and FPMB). The *NuSTAR* temperature response functions, for each energy range and telescope module (shown in Figure 5.11) were calculated using the instrumental response matrix for the regions shown in Figure 5.7.

The resulting DEMs obtained for the impulsive phase are shown in Figure 5.12 (*left*) with the quality of the recovered DEM solution shown as residuals between the input, and recovered fluxes (*right*). XIT is used with the addition of 300 MC iterations where outlier XIT MC solutions have been omitted. We have used all available filters with the exception of *Hinode*/XRT Be-Thick due to large uncertainties that are the result of a lack of counts (Figure 5.4), and *SDO*/AIA 335 Å due to the observed long-term

<sup>7</sup>updated from CHIANTI 6.0.1 to CHIANTI 7.1.3 as part of this work

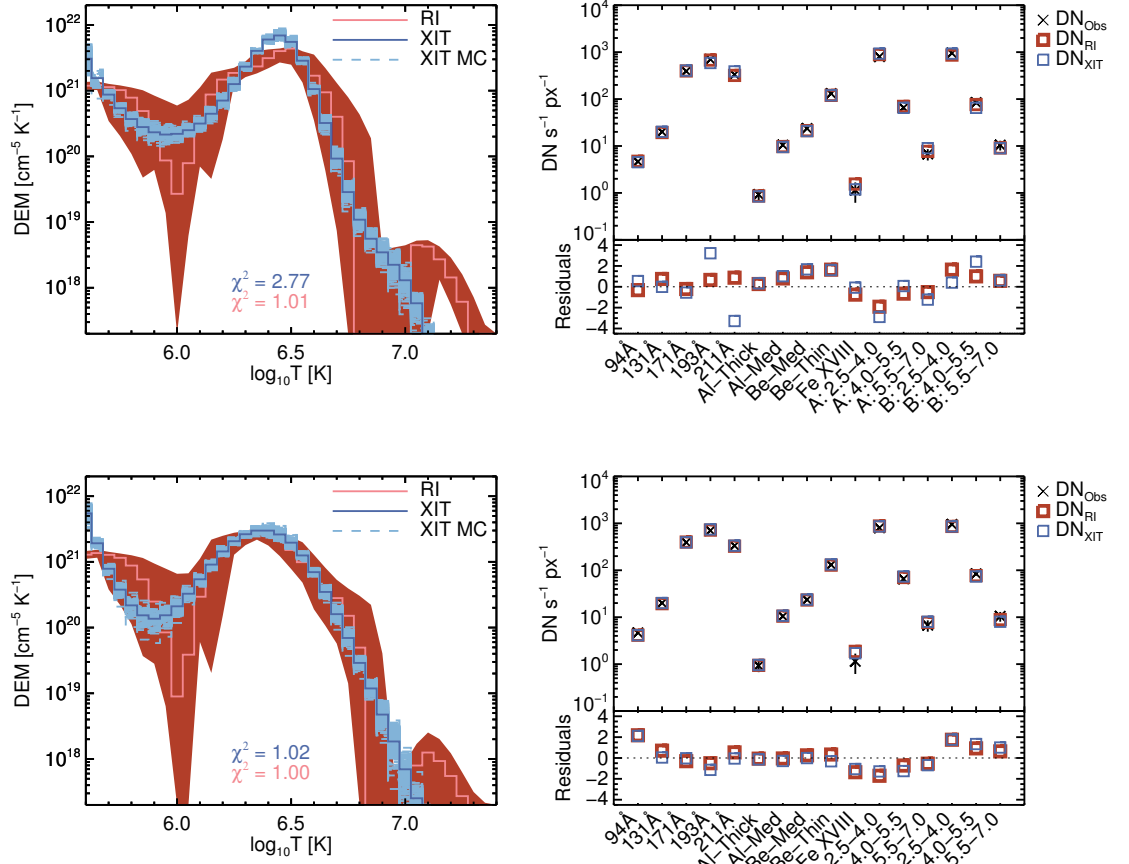


Figure 5.12: *Left*: DEMs obtained during the impulsive phase of the microflare using *SDO/AIA*, *Hinode/XRT* and *NuSTAR* data. *Right*: Residuals of the DEMs in data-space. The pink DEM (red error region) was obtained using the RI, and the blue (with 300 sky blue MC iterations) from XIT. The DEMs were calculated using both the standard *Hinode/XRT* temperature responses (*top*) as well as those multiplied by a factor of two (*bottom*).

drop in sensitivity (see Figure 1 Boerner *et al.*, 2014). The standard *Hinode/XRT* responses (Figure 5.12, *top*) lead to disagreement between the two methods for DEM recovery, notably at the peak, and at higher temperatures ( $\chi_{XIT}^2 = 2.77$ ,  $\chi_{RI}^2 = 1.01$ ). Using the *Hinode/XRT* responses multiplied by a factor of two results in the methods having much better agreement ( $\chi_{XIT}^2 = 1.02$ ,  $\chi_{RI}^2 = 1.00$ ), and the DEM solutions result in smaller residuals, specifically in the *Hinode/XRT* filters. These final DEMs (Figure 5.12, *bottom*) show a peak at  $\sim 3$  MK, and little material above 10 MK.

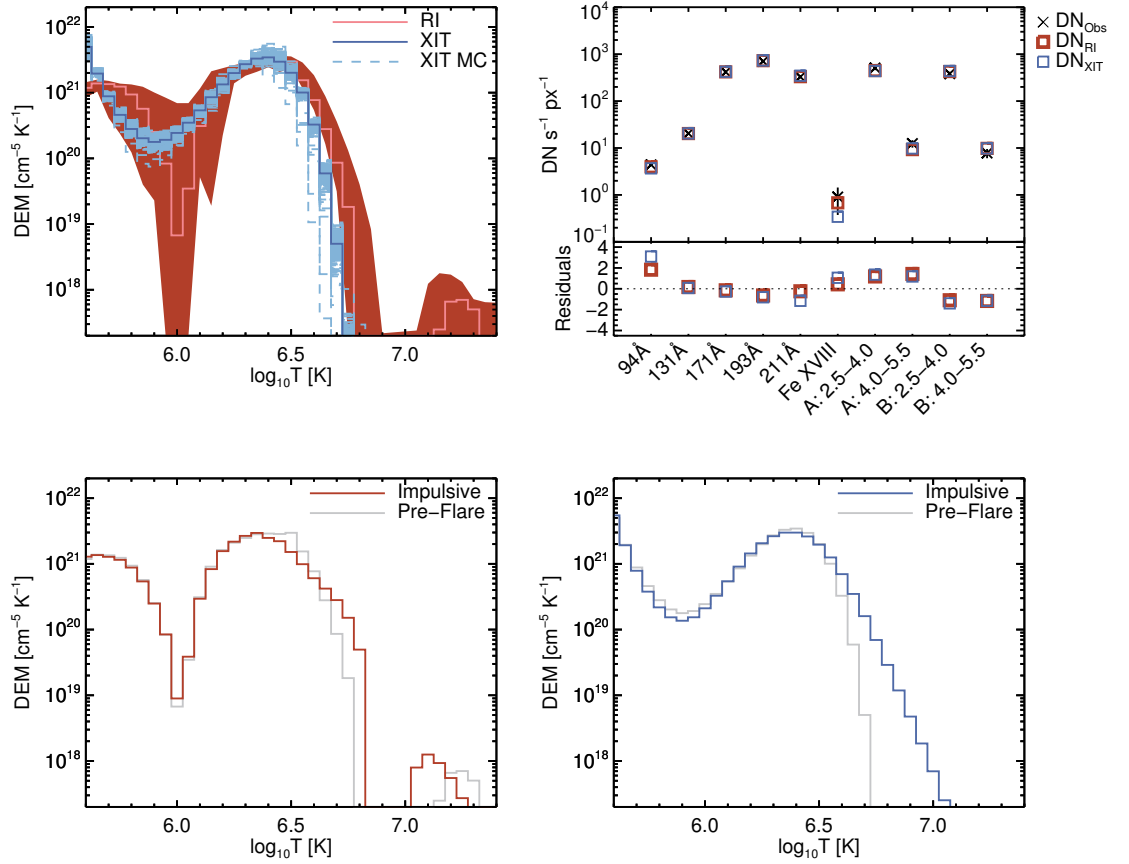


Figure 5.13: *Top Left*: DEM obtained from the pre-flare phase ( $\sim 11:10$  UT) using *SDO/AIA*, and *NuSTAR* data. (*top right* Residuals of the DEMs in data-space. *Bottom*: The RI (*left*) and XIT (*right*) pre-flare DEMs shown in comparison to the impulsive-phase DEMs (Figure 5.12, *bottom row*). The pre-flare DEMs peak at similar temperatures, and fall off more steeply than the impulsive-phase DEMs. The increase in the DEMs is due to the heating during the microflare.

To understand how much of this material has been heated out of the background during the microflare we performed DEM analysis for the pre-flare *NuSTAR* time ( $\sim 11:10$  UT). There is no *Hinode/XRT* data for this time so we determined the DEM using *NuSTAR* and *SDO/AIA* data. The DEMs for the pre-flare observations are shown in Figure 5.13. These DEMs for each method peak at a similar temperature ( $\sim 3$  MK), and fall off very sharply to  $\sim 5$  MK. During the microflare there is a clear addition of material up to 10 MK (Figure 5.13, *bottom*).

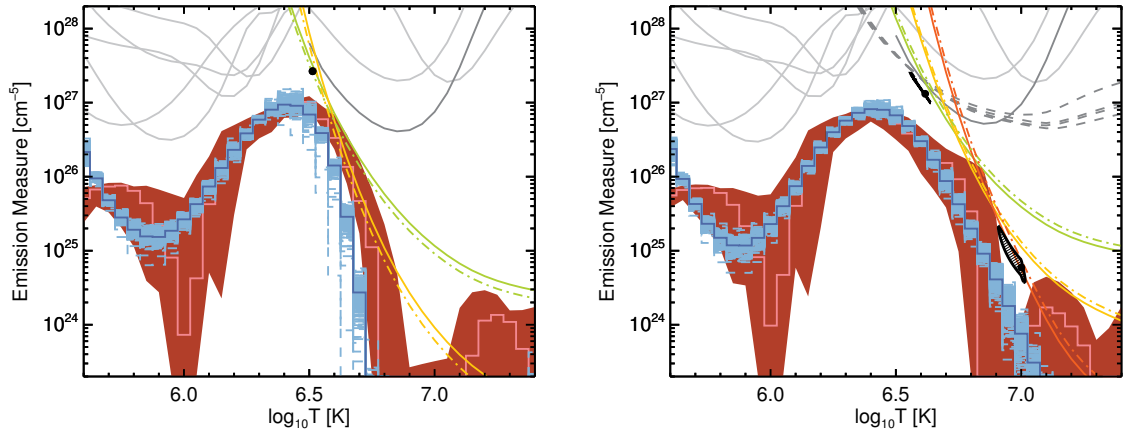


Figure 5.14: Emission measure distribution obtained from the pre-flare (*left*) using *SDO/AIA*, and *NuSTAR* data, and the impulsive phase of the microflare (*right*) using *SDO/AIA*, *Hinode/XRT* and *NuSTAR* data with the *Hinode/XRT* responses multiplied by a factor of two. The EM loci curves for *NuSTAR* are shown in the same colours as in Figure 5.11; the *SDO/AIA* loci are plotted in grey, with 94 Å Fe XVIII in dark grey; and *Hinode/XRT* loci are overplotted as dark grey dashed lines. The thermal fits from Figures 5.9 and 5.10 are plotted as filled circles (black) with shaded 90% confidence contours.

We also represent the DEMs as the emission measure distributions (EMDs;  $\xi(T)dT$ ) which allows us to compare the DEM results to the *NuSTAR* spectral fits, shown in Figure 5.14. Here we have also overplotted the EM loci curves,  $EM_i = g_i/K_i$ , which are the upper-limits of emission based on an isothermal model, with the true solution lying below all of the EM loci curves. The *NuSTAR* thermal model fits are the isothermal (in the pre-flare phase) or two thermal (impulsive phase) fits to the multi-thermal plasma distribution, and so represent an approximation of the temperature distribution and emission measure. These models produce the expected higher emission measure values compared to the EMD, and are consistent with the EM loci curves. It should be noted that in the RI solutions there is an additional, high-temperature component at  $\sim 10$  MK. This component is an artefact of inversion and has significant uncertainties in both temperature and emission measure; as the true solution should lie below the EM loci curves, this additional high-temperature component is not real and is a non-diagonal region of the  $\mathbf{R}_\lambda \mathbf{K}$  matrix (see § 3.4.1.1).

## 5.5 Microflare Energetics

### 5.5.1 Thermal Energy

For an isothermal plasma at a temperature  $T$  and emission measure  $EM$ , the thermal energy is calculated as

$$U_{T_I} = 3k_B T \sqrt{EM f V} \quad [\text{erg}] \quad (5.2)$$

where  $k_B$  is the Boltzmann constant,  $f$ , the filling factor, and  $V$ , the plasma volume (e.g. [Hannah \*et al.\*, 2008](#)). Using the two thermal fit (Figure 5.10, *right*) we calculated the thermal energy during the impulsive phase, finding  $U_{T_I} = 0.9 \times 10^{28}$  erg ( $t_I = 116$  s). Here the equivalent loop volume,  $V_E = fV$ , was calculated as a volume of a cylinder enclosing only the flaring loop with length,  $L \sim 50''$ , and diameter,  $d \sim 6''$ . This thermal energy includes both the microflare and background emission. We found the pre-flare energy (using fit parameters; Figure 5.9, *left*) as  $U_{T_{I_0}} = 0.9 \times 10^{28}$  erg (and  $t_{I_0} = 164$ s). The resulting heating power during the microflare from the thermal fits to the *NuSTAR* spectra is then  $P_{T_{I_F}} = U_{T_I}/t_I - U_{T_{I_0}}/t_{I_0} = 2.5 \times 10^{25}$  erg  $s^{-1}$ .

The thermal energy can also be estimated for a multi-thermal plasma using

$$U_T = 3k_B V_E^{1/2} \frac{\int_T T \xi_V(T) dT}{\sqrt{\int_T \xi_V(T) dT}} \quad [\text{erg}] \quad (5.3)$$

as described in [Inglis & Christe \(2014\)](#), with the filling factor,  $f = 1$ , and  $\xi_V(T) = n^2 dV/dT$  in units of  $\text{cm}^{-3} \text{K}^{-1}$ . For the RI and XIT DEM solutions we find values of  $U_{T_{RI}} = 1.1 \times 10^{28}$  erg, and  $U_{T_{XIT}} = 1.2 \times 10^{28}$  erg during the impulsive phase of the microflare. The pre-flare thermal energies we find  $U_{T_{RI_0}} = 1.2 \times 10^{28}$  erg, and  $U_{T_{XIT_0}} = 1.2 \times 10^{28}$  erg, and this then gives values of the heating power during the impulsive phase of the microflare as  $P_{T_{RI_F}} = 2.3 \times 10^{25}$  erg  $s^{-1}$ , and  $P_{T_{XIT_F}} = 3.0 \times 10^{25}$  erg  $s^{-1}$ . All of these approaches give a similar value for the heating, about  $2.5 \times 10^{25}$  erg  $s^{-1}$ , over the microflare's impulsive period, and a summary of these values with uncertainties are given in Table 5.1. It should be noted that these values are lower limits as the estimates neglect losses during heating.

From the analysis of 25,705 *RHESSI* events, (Table 1 [Hannah \*et al.\*, 2008](#)) microflare thermal energies were found to range from  $U_T = 10^{26-30}$  erg (5% – 95% range; from

Table 5.1. Summary of Thermal Energies of NOAA AR 12333

Method	$U_{T_0}^a$ [ $\times 10^{28}$ erg]	$U_T^b$ [ $\times 10^{28}$ erg]	$P_{TF}$ [ $\times 10^{25}$ erg s $^{-1}$ ]
<i>NuSTAR</i> fit	$0.9_{-0.1}^{+0.1}$	$0.9_{-0.2}^{+0.6}$	$2.5_{-1.6}^{+5.4}$
RI	$1.2_{-0.1}^{+0.1}$	$1.1_{-0.1}^{+0.1}$	$2.3_{-1.0}^{+0.9}$
XIT	$1.2_{-0.1}^{+0.1}$	$1.2_{-0.1}^{+0.1}$	$3.0_{-0.7}^{+0.6}$

Note. — The uncertainties on the energies and power derived from the *NuSTAR* fit are  $2.7\sigma$  (90% confidence), and those from RI/XIT are  $1\sigma$ .

<sup>a</sup>164s observation

<sup>b</sup>116s observation

a 16s observation). This is equivalent to  $P_T = 6.3 \times 10^{24-28}$  erg s $^{-1}$ , and therefore the thermal power from our *NuSTAR* microflare is in the lower range of *RHESSI* observations. This is as expected as *NuSTAR* should be able to observe well beyond *RHESSI*'s sensitivity limit to small microflares.

### 5.5.2 *NuSTAR* Non-Thermal Limits

As the *NuSTAR* spectrum in Figure 5.10 is well fitted by a purely thermal model we can therefore find the upper-limits of the possible non-thermal emission. This approach allows us to determine whether the accelerated electrons could power the observed heating in this microflare. We used the thick-target model (Brown, 1971) of a power-law electron distribution above a low-energy cut-off  $E_c$  [keV] given by

$$F(E > E_c) \propto E^{-\delta} \quad (5.4)$$

where  $\delta$  is the power-law index, and the power in this non-thermal distribution is given by

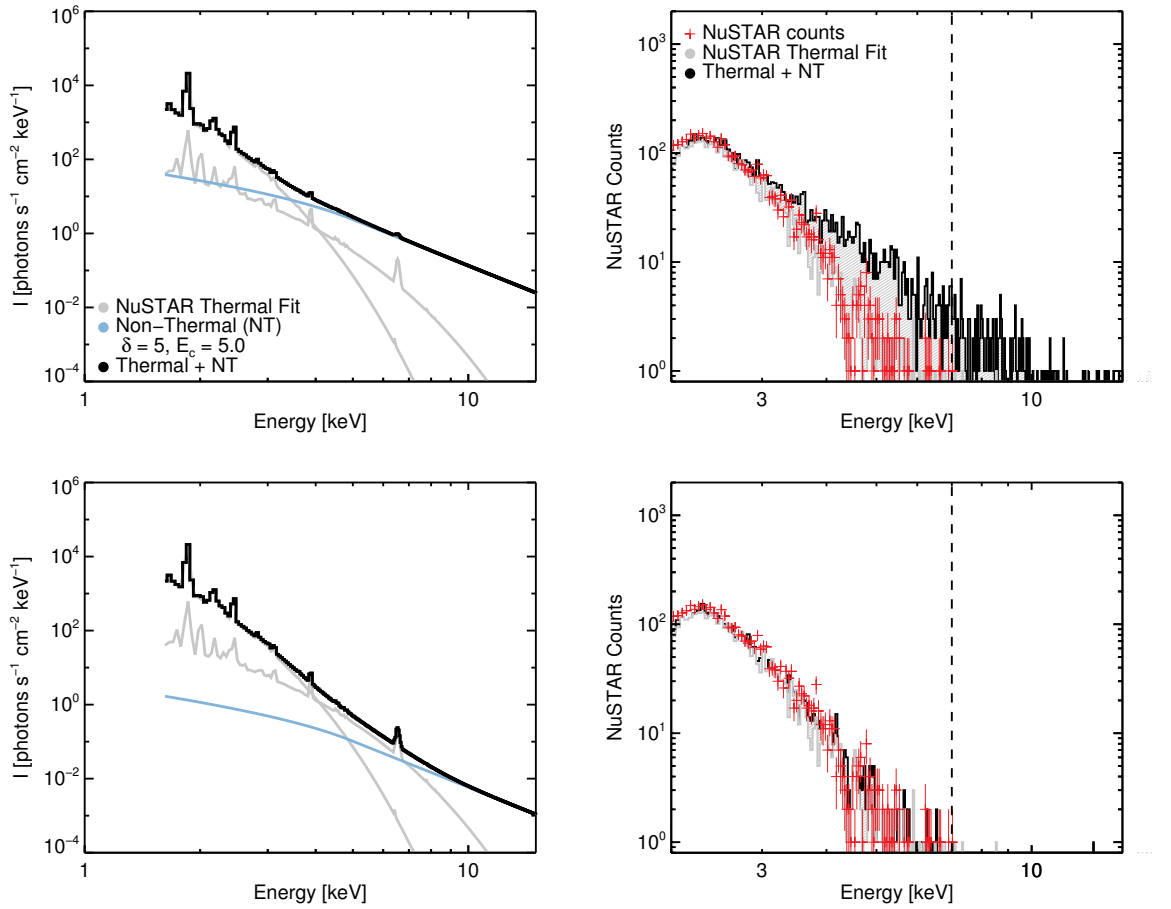


Figure 5.15: X-ray flux spectrum for a large value of non-thermal electron flux ( $N_N$ ), and the upper-limit that is consistent with a null detection in the *NuSTAR* spectrum for for  $\delta = 5$ , and  $E_c = 5$  (*top left, bottom left*). The respective *NuSTAR* count spectra are shown (*right*), where the original *NuSTAR* spectrum is shown in red; the thermal model, grey; and the thermal plus non-thermal model (*black*). The grey hatched region indicates the additional counts due to the non-thermal component.

$$P_N(> E_c) = 1.6 \times 10^{-9} \frac{\delta - 1}{\delta - 2} N_N E_c \quad [\text{erg s}^{-1}] \quad (5.5)$$

where  $N_N$  is the non-thermal electron flux [electrons  $\text{s}^{-1}$ ].

We determined the upper-limits on  $N_N$  (and  $P_N$ ) for a set of  $\delta$  ( $\delta = 5, 7, 9$ ), and  $E_c$  consistent with a null detection in the *NuSTAR* spectrum. We performed this by iteratively reducing the model electron flux  $N_N$  until there were less than 4 counts  $> 7$  keV, consistent with a null detection to  $2\sigma$  (Gehrels, 1986). We also ensured the

number of counts  $\leq 7$  keV are within the counting statistics of the observed counts. For each iteration we generated the X-ray spectrum for the two-component fitted thermal model (Figure 5.10, *right*) and added to this the non-thermal X-ray spectrum for our chosen  $\delta$ ,  $E_c$ , and  $N_N$ , calculated using `f_thick2.pro`<sup>8</sup> (see Holman *et al.*, 2011). This was then folded through the *NuSTAR* response to generate a synthetic spectrum using a Monte Carlo approach. The general process is that one can produce a cumulative distribution function (CDF) from the modelled spectrum and a synthetic *NuSTAR* spectrum can be generated by randomly sampling from the CDF (as performed in Hannah *et al.*, 2016).

An example of this iterative procedure is shown in Figure 5.15 for  $\delta = 5$ , and  $E_c = 5$ . Starting with a large value of non-thermal electron flux,  $N_N$ , Figure 5.15 (*top, left*) shows X-ray flux spectrum ( $I(\epsilon)$ ) as a function of energy for the original two-component *NuSTAR* fit (grey, cf. Figure 5.10, *right*) with the addition of a non-thermal component (sky blue). The *NuSTAR* count spectrum (red) along with the synthetic spectrum for the two-component thermal model (grey), and for the thermal and non-thermal model (black) were then calculated (*right*). The contribution from the non-thermal component alone is indicated by a grey hatched region.  $N_N$  is iteratively reduced until there are less than 4 counts  $> 7$  keV, and the number of counts  $\leq 7$  keV is within counting statistics of the original spectrum (as shown in Figure 5.15, *bottom*). The upper-limit of power in this non-thermal distribution can then be calculated (Equation 5.5).

The upper-limits for  $E_c = 5 - 14$ , and  $\delta = 5, 7, 9$  are shown in Figure 5.16 along with the three estimates of the thermal power for the background-subtracted flare,  $P_{T_{IF}}$  (“NuSTAR Fit”, black),  $P_{T_{RIF}}$  (pink), and  $P_{T_{XITF}}$  (blue). For a flatter spectrum of  $\delta = 5$  barely any of the upper-limits are consistent with the required heating power. With a steeper spectrum,  $\delta \geq 7$ , a cut-off  $E_c \lesssim 7$  keV is consistent with the heating requirement. These steep spectra indicate that the bulk of the non-thermal emission would need to be at energies close to the low energy cut-off to be consistent with the observed *NuSTAR* spectrum. If we instead consider some of the counts in the 6 – 7 keV range to be non-thermal (e.g. the excess above thermal model in the left panel in Figure 5.10) then we would obtain higher non-thermal power, about a factor of 0.5 larger. However this would only substantially affect the steep non-thermal spectra ( $\delta \geq 7$ ) as flatter models would be inconsistent with the data below 7 keV.

<sup>8</sup>[https://hesperia.gsfc.nasa.gov/ssw/packages/xray/idl/f\\_thick2.pro](https://hesperia.gsfc.nasa.gov/ssw/packages/xray/idl/f_thick2.pro)

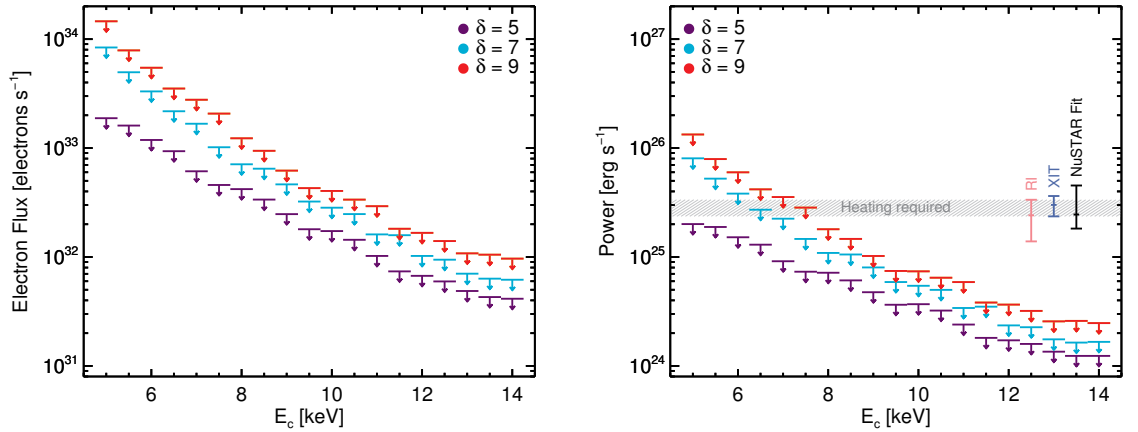


Figure 5.16: Non-thermal upper-limits as a function of  $E_c$  and  $\delta$  plotted in terms of non-thermal electron flux,  $N_N$  (*left*), and non-thermal power,  $P_N$  (*right*). The three estimates for the thermal power:  $P_{T_{IF}}$ , black;  $P_{T_{RLF}}$ , pink; and  $P_{T_{XITF}}$ , blue, are plotted with  $1\sigma$  uncertainties. The grey shaded region represents the required heating power, consistent with all three estimates.

We can again compare the microflare studied here to non-thermal energetics derived from *RHESSI* microflare statistics. [Hannah \*et al.\* \(2008\)](#) report non-thermal parameters of  $\delta = 4 - 10$ ,  $E_c = 9 - 16$  keV, and the non-thermal power ranges from  $P_N(\geq E_c) = 10^{25-28}$  erg s $^{-1}$ . The largest upper-limits *NuSTAR* produces for this microflare are again at the edge of *RHESSI*'s sensitivity. In a previous study of nanoflare heating [Testa \*et al.\* \(2014\)](#) investigated the evolution of chromospheric and transition region plasma from *IRIS* observations using RADYN nanoflare simulations. This is one of the few non-thermal nanoflare studies and they reported that heating occurred on time-scales of  $\lesssim 30$ s characterised by a total energy  $\lesssim 10^{25}$  erg, and  $E_c \sim 10$  keV. The simulated electron beam parameters in this *IRIS* event are consistent with the *NuSTAR* derived parameters, but in a range insufficient to power the heating in our microflare.

## 5.6 Discussion and Conclusions

This chapter has presented the first joint observations of a microflaring active region with *NuSTAR*, *Hinode*/XRT, and *SDO*/AIA that were published as [Wright \*et al.\* \(2017\)](#). During the impulsive start, the *NuSTAR* spectrum shows emission up to 10 MK, indicating that even in this  $\sim A0.1$  microflare substantial heating can occur. This

high temperature emission is confirmed with DEMs using *NuSTAR*, *Hinode*/XRT, and *SDO*/AIA data. These instruments crucially overlap in temperature sensitivity, with *NuSTAR* able to constrain and characterise the high temperature emission which is often difficult for other instruments to do alone.

Importantly, in this event we find the *Hinode*/XRT temperature response functions are a factor of two too small, suggesting that *Hinode*/XRT would normally overestimate the contribution from high temperature plasma in this microflare. There is currently ongoing work with combined *Hinode*/XRT, and *MinXSS* observations (Moore *et al.*, 2018; Moore, 2019) in order to investigate this further.

Overall for this event we find the instantaneous thermal energy during the microflare to be  $\sim 10^{28}$  erg; once the pre-flare has been subtracted this equates to a heating rate of  $\sim 2.5 \times 10^{25}$  erg s<sup>-1</sup> during the impulsive phase of this microflare. This is comparable to some of the smallest events observed with *RHESSI*, although *RHESSI* did not see this microflare as its indirect imaging was dominated by the brighter active regions elsewhere on the disk (see Figure 5.5).

Although no non-thermal emission was detected in this microflare, upper-limits were placed on the possible non-thermal component. A steep ( $\delta \geq 7$ ) power-law down to at least 7 keV would be required to be able to power the heating in this microflare. This is still consistent with this small microflare being physically similar to larger microflares and flares, but this would only be confirmed if *NuSTAR* detected non-thermal emission. To achieve this, future *NuSTAR* observations need to be made with a higher effective exposure time.

Since these observations, Glesener *et al.* (2017) has presented *NuSTAR* observations of an active region microflare observed on 1st September 2015, which was also estimated to be an A0.1-class event with a peak thermal energy of  $2.4 \times 10^{27}$  erg. As with the microflare presented in this chapter, Glesener *et al.* (2017) did not detect a non-thermal component, but observed qualities similar to larger hard X-ray events. For example, impulsive energy release followed by a gradual thermal response (and even more gradual at higher altitudes) was observed. Furthermore, the temporal evolution of that microflare also shows that higher energy hard X-rays peak earlier, a high-energy excess during the impulsive phase was observed, indicating heating via non-thermal electrons or (faint) hotter plasma.

More recently, there have also been a number of newer active regions microflares.

---

These events have higher livetimes (e.g. [Hannah \*et al.\*, 2018](#), obtained a 3s effective observation from a one-minute observation) and there have been indications of possible non-thermal emission ([Hannah & Glesener, 2019](#)).

# Chapter 6

## EUV Time Series Analysis

*This chapter utilises 12 hours of processed SDO/AIA data (at 30 s cadence), and EBTEL simulations that were provided by Nicholeen Viall (NASA Goddard Space Flight Center). The original observations were published in Viall & Klimchuk (2012), and the simulations were presented and discussed in Viall & Klimchuk (2013, 2015, 2016).*

At the time of writing, SDO/AIA has provided over eight years of high-resolution (0.6";  $4096 \times 4096$  px), high-cadence ( $\sim 12$  s) data in six optically-thin EUV channels. The result is an immensely rich data set for the study of active region heating; it is therefore unfortunate that only a few studies exist that have attempted to perform time series analysis of the pixel-level data to understand the coronal heating mechanism.

This chapter will first introduce time-lag analysis (Viall & Klimchuk, 2011, 2012), a method for deducing the temporal offset of two channels of the same spatial region but at different peak temperatures. Time-lag analysis will be introduced on EUV data from the multi-thermal channels of SDO/AIA (§ 6.2). Starting with a pixel of diffuse emission, and the seven channel pairs that were studied in Viall & Klimchuk (2012), this work will then be extended to three additional pixels that correspond to different active region features. This chapter will also introduce time-lag analysis on the 94 Å (Fe XVIII) – 335 Å channel pair, where the hotter Fe XVIII contribution (7 MK) from SDO/AIA 94 Å channel has been isolated using the empirical method of Del Zanna (2013). Finally, time-lag analysis will be performed on the  $250 \times 250$  pixel region in order to create time-lag maps. Time-lag analysis will also be performed on simulated data in order to further understand the time-lag signatures seen in the

observed *SDO/AIA* data.

Following on from this chapter, in order to extract signatures that would otherwise be masked by the multi-thermal nature of EUV observations, Chapter 7 will present time-lag analysis on the temperature distribution itself.

## 6.1 Time-Lag Analysis: *SDO/AIA*

The cooling of discrete coronal loops is seen observationally in the EUV as light curves from cooler spectral lines (or filter channels) peak progressively later in time. This well-known behaviour can be interpreted as the result of nanoflare heating (§ 1.3): individual strands in the coronal loop are impulsively heated, and as the loop cools they are sequentially visible in cooler channels. The delay (the temporal offset) between two light-curves at different temperatures can therefore describe the time-scale of this cooling.

The *time-lag* between two EUV light curves ( $x, y$ ) can be obtained by calculating the cross-correlation ( $\star$ ) as a function of temporal offset, and locating the offset at which the cross-correlation value peaks,  $\arg \max((x \star y)(t))$ . For positive and negative offsets, the following equations represent the cross-correlation value  $P$ , as a function of offset,  $L$ :

$$P(L) = \frac{\sum_{k=0}^{N-|L|-1} (x_{k+|L|} - \bar{x})(y_k - \bar{y})}{\sqrt{\sum_{k=0}^{N-1} (x_k - \bar{x})^2 \sum_{k=0}^{N-1} (y_k - \bar{y})^2}}, \text{ For } L < 0 \quad (6.1)$$

$$P(L) = \frac{\sum_{k=0}^{N-L-1} (x_k - \bar{x})(y_{k+L} - \bar{y})}{\sqrt{\sum_{k=0}^{N-1} (x_k - \bar{x})^2 \sum_{k=0}^{N-1} (y_k - \bar{y})^2}}, \text{ For } L \geq 0 \quad (6.2)$$

In these Equations,  $x$  and  $y$  are two normalised time series in order of peak temperature ( $T_{peak}^x > T_{peak}^y$ ), each consisting of  $N$  data points. Practically, this time-lag analysis can be implemented using the IDL cross-correlation routine `c_correlate.pro`<sup>1</sup>. In terms of *SDO/AIA* data, the cross-correlation is computed from the time series of a single pixel in a desired channel, and the same pixel in another channel with a peak temperature sensitivity that is cooler. In the literature this is computed for a set of offsets extending up to  $\pm 2$  hours for a 24 hour time series (Viall & Klimchuk, 2012). While uncertainties on the input data are not handled in time-lag analysis, this could

<sup>1</sup>[http://www.harrisgeospatial.com/docs/c\\_correlate.html](http://www.harrisgeospatial.com/docs/c_correlate.html)

be addressed in the future by performing Monte Carlo simulations: new time series could be generated by perturbing the original data at each time-step by an amount that is randomly drawn from a Gaussian distribution with the standard deviation equal to the uncertainty of the data at that time step. This would result in new time series and the distribution of cross-correlation values as a function of offset could be studied.

Nevertheless, time-lag analysis is a powerful tool for constraining coronal heating as the response of a coronal loop to an impulsive energy release is well-understood (e.g. [Cargill, 1994](#); [Cargill \*et al.\*, 1995](#); [Cargill & Klimchuk, 2004](#)). As a basic overview, for a loop in hydrostatic equilibrium that is heated sufficiently quickly that radiation and thermal conduction do not have time to immediately balance the supplied energy, this excess heat raises the temperature of the loop, inducing a heat flux toward the lower atmosphere. At the point at which the conduction is able to match the heating rate the plasma begins to cool, and the loop is known as “under-dense” compared to hydrostatic equilibrium.

During the cooling, conduction is initially more efficient (see [Cargill \*et al.\*, 1995](#), for derivations of the conductive and radiative cooling time-scales), and as the energy lost by radiation is proportional to the density, the transition region (and chromosphere) are more efficient at radiating away this energy that has been conducted downward from the corona. If the radiative losses of the transition region cannot keep up the excess energy heats the chromosphere which results in chromospheric evaporation. The filling of coronal loops increases the density which leads to radiative cooling becoming more efficient, lowering the temperature further, which in turn reduces chromospheric evaporation.

This cooling leads to the downward conductive flux being balanced by radiative losses in the transition region, and chromospheric evaporation stops. Here, radiation and conduction are as efficient, and this results in an “over-dense” loop due to the chromospheric evaporation; the cooling finally leads to the plasma falling back down the loop, and radiative cooling is much more efficient than conduction: the radiative cooling phase. The loop will return to its equilibrium temperature and density as long as the physical mechanism for which supported the initial hydrostatic equilibrium still exists.

Importantly, while such behaviour of the heating and cooling of coronal loops has been observed in numerous studies of warm coronal loops—those observed at temper-

atures of about 1MK—these loops only contribute a small enhancement (10 – 30% brighter) over the apparent uniform background emission. Furthermore, it is difficult to know how representative a single loop is, and how well the background has been subtracted—especially when line-of-sight geometries are considered—and if there is any bias from the instrument itself. It is also important to note that the majority of active region emission is both in between, and underneath these loops. This “background” emission is known as diffuse emission, and constitutes 60% – 90% of the total active region emission (Del Zanna & Mason, 2003; Viall & Klimchuk, 2011). Clearly, one important question is if the diffuse emission may in fact be composed of multiple loops, perhaps overlapping or fading, which renders them indistinguishable, or perhaps the mechanism is fundamentally different from that which heats loops.

In order to investigate both the loop, and diffuse emission, Viall & Klimchuk (2011) analysed three sets of *SDO/AIA* light curves extracted from locations within NOAA AR 11082 obtained from the six coronal EUV channels of *SDO/AIA* data. These locations consisted of two loop locations, and one location of diffuse emission. Within the region of diffuse emission Viall & Klimchuk (2011) observe a similar pattern of cooling to that of distinguishable loops: behaviour that can be described by nanoflare storm heating (and not steady heating). Significantly, they observe that the behaviour of the diffuse emission is consistent with a storm of nanoflares, suggesting that diffuse emission may be the result of the same physical mechanism that forms identifiable loops.

## 6.2 Time-Lag Analysis of an Active Region: Example Pixel Time-lags

To further the work of Viall & Klimchuk (2011), Viall & Klimchuk (2012) analysed 24 hours of *SDO/AIA* EUV data of NOAA AR 11082 on 19 June 2010 ( $450 \times 450$  px).

The level-1.5 *SDO/AIA* observations of NOAA AR 11082 (located near disk centre) have been de-rotated, and the channels co-aligned, so that the active region emission is observed by the same pixels throughout the 24 hour period (see Viall & Klimchuk, 2012). The rotation performed by Viall & Klimchuk (2012) was made under the assumption that the active region rotates with a single rotation rate of 300 s per *SDO/AIA* pixel ( $0.6''$  Snodgrass, 1983); the data were rotated to the first image in the

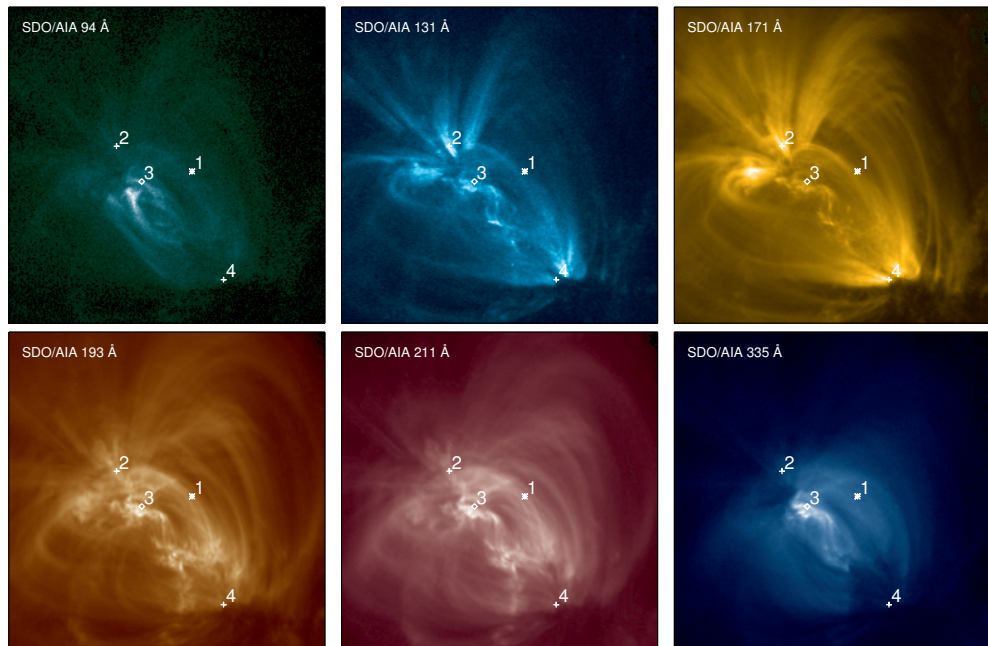


Figure 6.1: NOAA AR 11082 in six *SDO/AIA* channels. From *left to right, top to bottom*, these channels are 94 Å, 131 Å, 171 Å, 193 Å, 211 Å, 335 Å. Four pixels are highlighted in each of the *SDO/AIA* images. A pixel of diffuse emission is represented by an asterisk (1); a pixel in a fan loop is highlighted by a cross (2); a pixel in the core of the active region is highlighted by a diamond (3); and finally, a pixel at the footpoint of a fan loop is highlighted by a cross (4).

time series, and the fractional pixel rotation was also accounted for [Viall & Klimchuk \(2012\)](#).

For each pixel, in each *SDO/AIA* channel, a set of 24 hour light curves have been created, and split into two consecutive 12-hour, and 12 consecutive two-hour windows. Finally, these data were linearly interpolated into a common 30 s time-step. The *SDO/AIA* data for a single time in the 24 hour observations of NOAA AR 11082 is displayed in Figure 6.1. Figure 6.1 shows NOAA AR 11082 in six *SDO/AIA* channels on a linear scale. A pixel of diffuse emission that is described in the following section (similar in location to the pixel used and analysed in [Viall & Klimchuk, 2012](#)) is highlighted by a white asterisk (1, § 6.2.2). In addition to this diffuse emission pixel, the analysis for this chapter is expanded to a set of three additional pixels that were not individually studied in [Viall & Klimchuk \(2012\)](#). These are a pixel of a fan loop emission, highlighted by a white cross (2, § 6.2.3); a pixel of core emission that is

highlighted by a white diamond (3, § 6.2.4); and a pixel at a loop footpoint, highlighted by a white cross (4, § 6.2.5).

### 6.2.1 *SDO/AIA* Temperature Response Functions

Prior to both performing and interpreting the results of time-lag analysis, it is important to understand the temperature response functions of the *SDO/AIA* channels.

Figure 6.2 shows both the normalised and  $\log_{10}$ -scaled temperature response functions (over the range  $\log_{10}T = 5.0 - 7.5$ ) in order to highlight both the peak sensitivities, and the multi-thermal nature of these temperature response functions. Figure 6.2 clearly shows the varying forms of these response functions. 171 Å, 193 Å, and 211 Å are relatively narrow with single peaks (*top*), while others are multi-thermal and are double peaked at both high and low temperatures (e.g 131 Å; 94 Å). Notably, the 335 Å channel is comparatively broad, and while 335 Å peaks at 0.2 MK, this lower temperature peak is due to transition region emission (Del Zanna *et al.*, 2011). We therefore associate the coronal emission in 335 Å to the 2.5 MK peak, as will be justified later. From these temperature response functions it is therefore clear that this multi-thermal nature needs to be considered when interpreting the results of time-lag analysis in the following sections.

With that considered, for the seven sets of channel pairs introduced in Viall & Klimchuk (2012), Figure 6.3 visualises the positive time-lags between these seven channel pairs by using arrows to connect the peaks of the first and second channels temperature response functions that were seen in Figure 6.2 (recall the definition:  $T_{peak}^x > T_{peak}^y$ ). The *seven* channel pairs are plotted where the solid lines indicate the approximate temperature jump that would be associated with a positive time-lag. Considering the multi-thermal nature of these light curves (see, Figure 6.2), while the definition assumes that  $T_{peak}^x > T_{peak}^y$ , 94 Å is strongly bimodal (with peaks at approximately 7 MK,  $T_{hot}^{94}$ , and 1.6 MK,  $T_{cool}^{94}$ , see Figure 6.2). This channel can therefore be observed as either hotter or cooler than other channels (a negative time-lag does not indicate heating). Figure 6.3 therefore includes a solid line to indicate the positive time-lag (7 → 1.6 MK;  $T_{hot}^{94} \rightarrow T_{hot}^{335}$ ), an additional dashed line is included to indicate a negative time-lag (2.5 → 1.6 MK;  $T_{hot}^{335} \rightarrow T_{cool}^{94}$ ) for the 94 Å – 335 Å pair.

Section 6.2.2 will first analyse the pixel of diffuse emission, which is similar to the pixel analysed in Viall & Klimchuk (2012). Similar analysis to that conducted in Viall

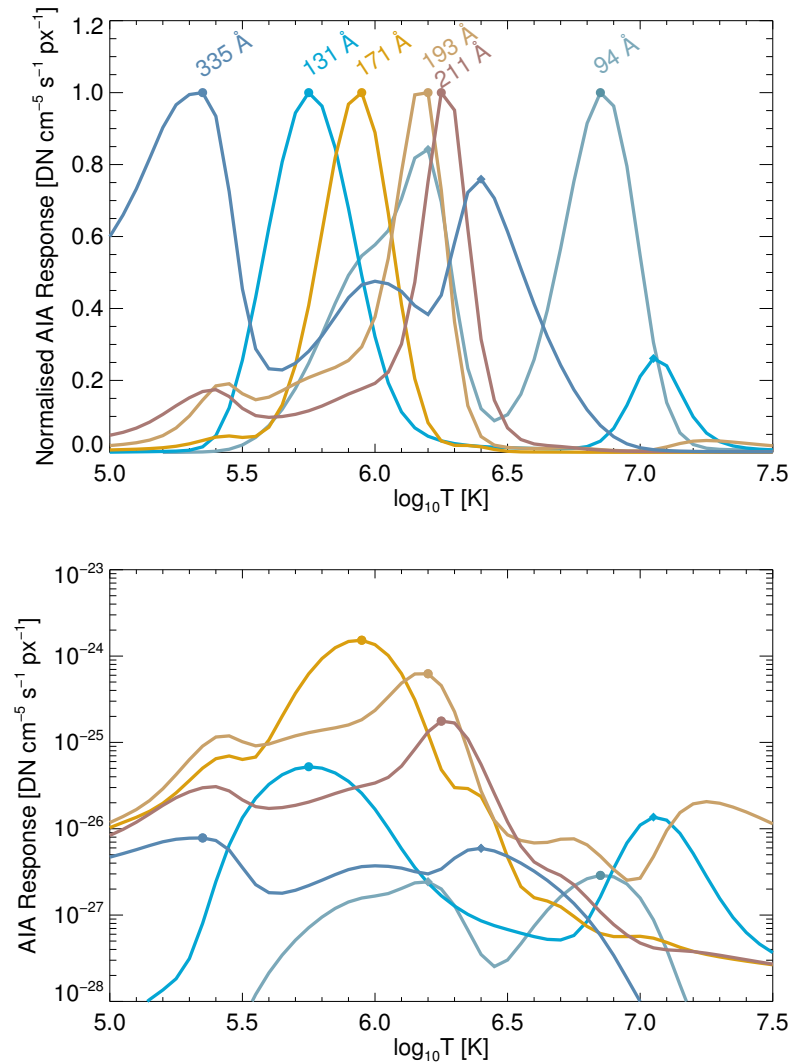


Figure 6.2: *SDO/AIA* temperature response functions for the six coronal (EUV) channels. The temperature response functions are shown here as both normalised (*top*), and plotted on a  $\log_{10}$ -scale (*bottom*) to highlight both the peak temperature sensitivity and the multi-thermal nature of these response functions. The peak of each temperature response function is plotted as a filled circle, and the secondary peaks of *SDO/AIA* 94 Å, 131 Å, and 335 Å are overplotted as filled diamonds.

& Klimchuk (2012) will be introduced on this pixel, and the following sections (§ 6.2.3 – 6.2.5) will repeat this same analysis on additional pixels from this  $250 \times 250$  pixel region.

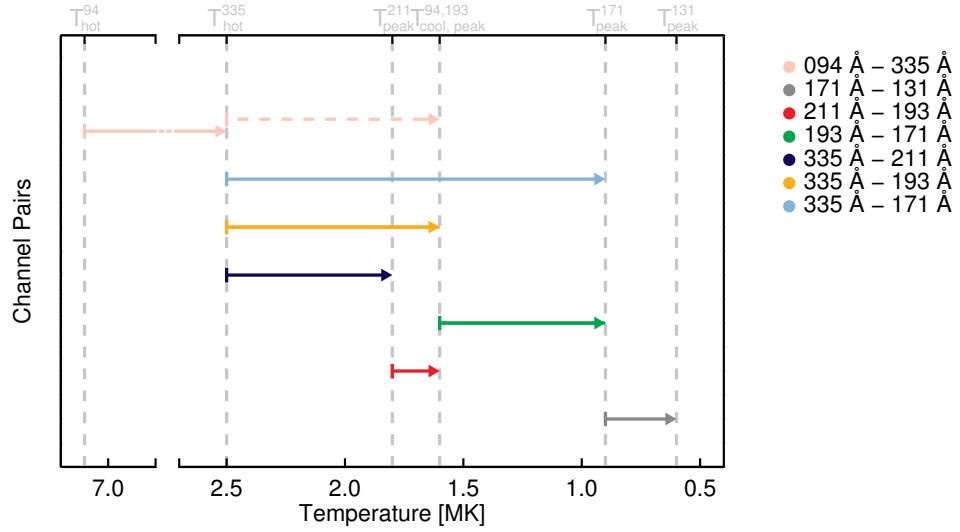


Figure 6.3: Visualisation of positive time-lags (solid lines) in temperature for the seven channel pairs described in Viall & Klimchuk (2012). Due to the strong bimodal nature of *SDO/AIA* 94 Å (7, 1.6 MK), the 94 Å – 335 Å may be positive or negative. The dashed pink line therefore indicates the positive time-lag where 335 Å precedes 94 Å.

### 6.2.2 Diffuse Emission, Pixel 1, Viall & Klimchuk (2012)

For the pixel of diffuse emission highlighted in Figure 6.1 (Pixel 1), the light curves for the six optically-thin EUV channels of *SDO/AIA* are shown in Figure 6.4. Furthermore, the cross-correlation value as a function of offset for the seven channel pairs used in Viall & Klimchuk (2012) (those shown in Figure 6.3) are shown in Figure 6.5.

Figure 6.4 shows the normalised light curves for two hours of observation of a pixel of diffuse emission offset in intensity to avoid overlap of the light curves. From top to bottom, the light curves are ordered in peak temperature: 94 Å, 335 Å, 211 Å, 193 Å, 171 Å, 131 Å. By eye it is clear that the intensity rises and falls in each of these channels over the shaded grey region investigated by Viall & Klimchuk (2012). In the two hour period investigated by Viall & Klimchuk (2012), 335 Å ( $\sim 2.5$  MK) peaks first (at  $\sim 2000$  s), followed by 211 Å ( $\sim 1.8$  MK),  $\sim 3000$  s; 193 Å ( $\sim 1.6$  MK),  $\sim 3300$  s; 94 Å ( $\sim 7$  and  $\sim 1.6$  MK),  $\sim 3600$  s, and then 171 Å and 131 Å ( $\sim 0.9$ ,  $\sim 0.6$  MK) at  $\sim 4000$  s. Furthermore, a similar pattern is also seen near the beginning and end of this two hour time series.

Figure 6.5 shows the cross-correlation value as a function of offset between pairs of

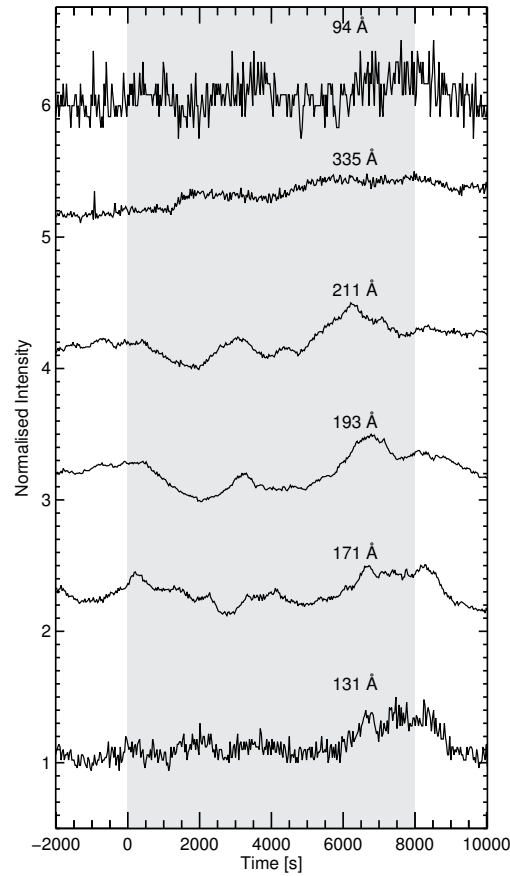


Figure 6.4: Light curves of a pixel of diffuse emission. These light curves correspond to 94 Å, 131 Å, 171 Å, 193 Å, 211 Å, and 335 Å (*top to bottom*). The light curves are plotted over the two-hour duration studied by [Viall & Klimchuk \(2012\)](#) (indicated by a grey region), and used for time-lag analysis. For context, an additional  $\pm 2000$  s is included.

light curves shown in Figure 6.4, where the time-lag (the value of peak cross-correlation) is represented by a filled circle, and the time resolution of the data and time-lag values are 30 s. As discussed, the cross-correlation is determined for a set of temporal offsets. The offset describes the shift of the second light curve with respect to the first; a positive offset describes a situation where the second light curve followed the first. As discussed in Figure 6.3, 94 Å can behave as a hotter or cooler channel. Under the definition of  $T_{peak}^x > T_{peak}^y$ , while 94 Å is defined as a hotter channel, a *negative* time-lag would indicate that the observed coronal plasma is concentrated at the secondary

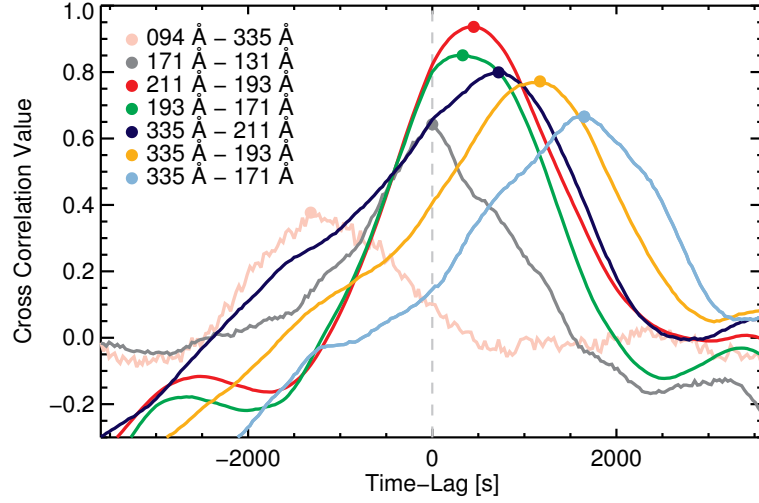


Figure 6.5: Cross-correlation value as a function of temporal offset for the seven pairs of light curves (highlighted in Figure 6.3) for a pixel of diffuse emission (Pixel 1). A positive time-lag indicates that the second channel in the pair lags the first, and a negative time-lag indicates that the first channels lags the second (e.g. for the  $94 \text{ \AA} - 335 \text{ \AA}$  pair,  $94 \text{ \AA}$  lags  $335 \text{ \AA}$ ). For each channel pair, the filled circle represents the observed time-lag which is defined as the value at which the cross-correlation value is maximum.

peak ( $\sim 1.6 \text{ MK}$ ;  $T_{\text{cool}}^{94}$ ), and  $94 \text{ \AA}$  is therefore behaving as a cooler channel.

For the channel pairs of  $211 \text{ \AA} - 193 \text{ \AA}$  ( $1.8 \text{ MK} - 1.6 \text{ MK}$ ) and  $335 \text{ \AA} - 171 \text{ \AA}$  ( $2.5 \text{ MK} - 0.9 \text{ MK}$ ), the peak cross-correlation values are at  $\sim 500 \text{ s}$ , and  $\sim 1600 \text{ s}$ , and are reached when the second channel in each pair follows the first by  $\sim 500 \text{ s}$ , and  $\sim 1600 \text{ s}$ , respectively. Importantly, these channels pairs (with the smallest and largest time-lags) have the smallest and largest offsets in temperature. Furthermore, it is clear that the lag between channels progressively increases with larger offset in temperature and this is highly indicative (and expected) of cooling plasma, e.g.  $335 \text{ \AA} - 211 \text{ \AA}$ , ( $2.5 \text{ MK} - 1.8 \text{ MK}$ );  $335 \text{ \AA} - 193 \text{ \AA}$ , ( $2.5 \text{ MK} - 1.6 \text{ MK}$ );  $335 \text{ \AA} - 171 \text{ \AA}$ , ( $2.5 \text{ MK} - 0.9 \text{ MK}$ ). This confirms that the time series of *SDO/AIA*  $335 \text{ \AA}$  is the result of coronal emission at temperatures around the secondary (coronal) peak in the response function ( $\sim 2.5 \text{ MK}$ ;  $T_{\text{hot}}^{335}$ ). It is also important that in the case of this diffuse emission pixel, the  $94 \text{ \AA} - 335 \text{ \AA}$  pair indicates that material located at the cooler component of  $94 \text{ \AA}$  channel is responsible for the observed time series. This is consistent with weaker heating (see

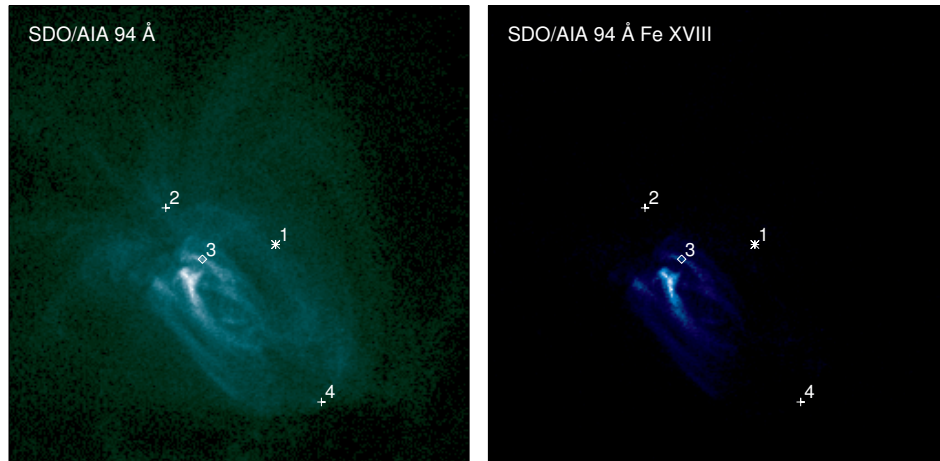


Figure 6.6: NOAA AR 11082 shown in the *SDO/AIA* 94 Å channel (*left*), and with the high-temperature Fe XVIII component of the *SDO/AIA* 94 Å channel isolated (*right*). The *SDO/AIA* 94 Å (Fe XVIII) image (*right*) shows that at this time-step there are a few loops within the centre of the active region that have been heated to  $\sim 7$  MK, while the majority of the *SDO/AIA* 94 Å emission is from plasma at cooler temperatures. As with Figure 6.1, the four pixels investigated in this section are also highlighted.

Viall & Klimchuk, 2011) where the majority of plasma is not heated to the Fe XVIII peak in *SDO/AIA* 94 Å. As can be seen in Figure 6.2, 131 Å is also peaked at  $\sim 13$  MK and therefore a negative time-lag in the 171 Å – 131 Å pair would indicate cooling from 13 MK down to 0.9 MK. As seen in Viall & Klimchuk (2012), and later in Figure 6.23, the majority of time-lags for 171 Å – 131 Å are *zero*, and there are very few cases of negative time-lags observed in this channel pair. This indicates that the emission observed in 131 Å is at  $\sim 0.6$  MK the majority of the time.

As has been discussed, there are various methods for isolating components of the *SDO/AIA* channels. In particular, Fe XVIII emission can be isolated from the 94 Å channel as described earlier (see Equation 5.1). By isolating the Fe XVIII component of the *SDO/AIA* 94 Å channel at every pixel in the images presented in Figure 6.1, it is possible to produce a synthetic *SDO/AIA* 94 Å (Fe XVIII) map. This *SDO/AIA* 94 Å Fe XVIII map, together with the *SDO/AIA* 94 Å map is shown in Figure 6.6. Figure 6.6 shows the same *SDO/AIA* 94 Å map as in Figure 6.1, and in comparison, also shows the *SDO/AIA* 94 Å (Fe XVIII) map where only a few (hot) core loops are visible. As with Figure 6.1, the four pixels that are analysed in this chapter are also highlighted. For the pixel of diffuse emission it is clear from Figure 6.6 that there is

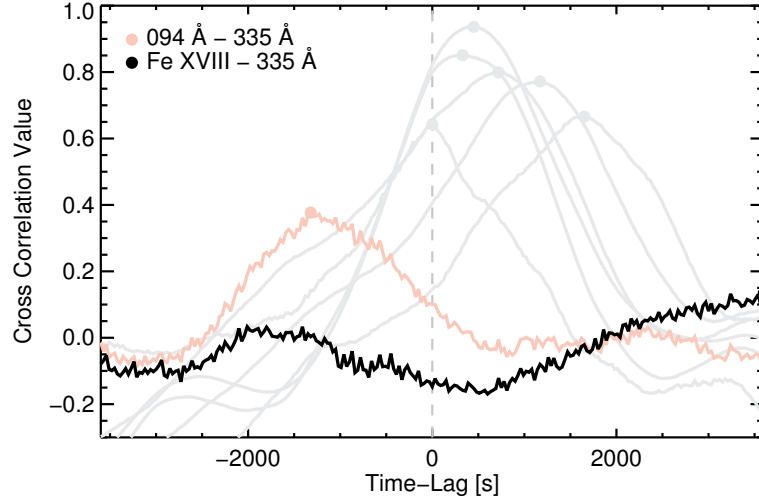


Figure 6.7: Cross-correlation value as a function of temporal offset between two pairs of channels:  $94 \text{ \AA} - 335 \text{ \AA}$  and  $94 \text{ \AA} (\text{Fe XVIII}) - 335 \text{ \AA}$  (first introduced in this thesis), where the Fe XVIII component of the *SDO/AIA*  $94 \text{ \AA}$  time series has been isolated. In addition to these two channel pairs, the six additional channel pairs from Figure 6.5 overplotted in grey. As with Figure 6.5, a negative time-lag for the  $94 \text{ \AA} - 335 \text{ \AA}$  channel pair indicates that  $335 \text{ \AA}$  brightens before  $94 \text{ \AA}$ , and is thought to be behaving as a cool channel. This is confirmed by the  $94 \text{ \AA} (\text{Fe XVIII}) - 335 \text{ \AA}$  channel pair that shows no clear correlation), and indicates that little to no material is being heated to the Fe XVIII peak of *SDO/AIA*  $94 \text{ \AA}$ .

no observed Fe XVIII emission at this time step.

In comparison to Figure 6.5, Figure 6.7 shows the cross-correlation values as in Figure 6.5 but with the addition of the  $94 \text{ \AA} (\text{Fe XVIII}) - 335 \text{ \AA}$  channel pair. By isolating the  $94 \text{ \AA}$  Fe XVIII component it is possible to confirm that the negative  $94 \text{ \AA} - 335 \text{ \AA}$  time-lag indicates there is little emission at  $7 \text{ MK}$  as there is no obvious correlation (cross correlation value  $< 0.2$ , see Viall & Klimchuk, 2012) between the  $94 \text{ \AA} (\text{Fe XVIII}) - 335 \text{ \AA}$  pair, as would be expected if cooling was happening between these temperatures. This, combined with Figure 6.5 also indicates that in this pixel the plasma was heated to  $\sim 2.5 \text{ MK}$  ( $T_{\text{peak}}^{335 \text{ \AA}}$ ) and cools to  $< 1 \text{ MK}$ . It should be noted here that the cross-correlation value of  $0.2$  was arbitrarily chosen by Viall & Klimchuk (2012) however, we have also chosen this value based upon the distribution of cross-correlation values in the  $94 \text{ \AA} (\text{Fe XVIII}) - 335 \text{ \AA}$  histogram (see later Figure, Figure 6.19, right). A

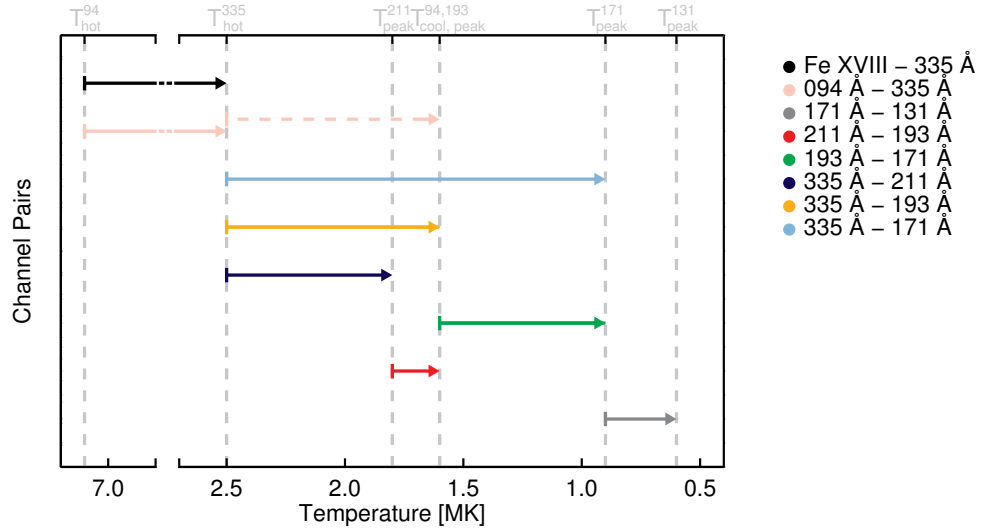


Figure 6.8: Visualisation of time-lags (as in Figure 6.3), including the addition of the 94 Å (Fe XVIII) – 335 Å channel pair that was first introduced in this thesis (7 → 2.5 MK, black). This removes the ambiguity of the 94 Å – 335 Å channel pair that can be positive (7 → 2.5 MK) or negative (2.5 → 1.6 MK).

more robust approach in order to understand the significance of the cross-correlation values for two time series could be obtained by generating a set of time series with similar power spectra to the data, and performing time-lag analysis on these data in order to understand the distribution of cross-correlation values that could be obtained through chance.

Figure 6.3 can now be updated to include this new 94 Å (Fe XVIII) – 335 Å pair. Figure 6.8 visualises positive time-lags (shown as solid lines) and the addition of the negative 94 Å – 335 Å time-lag which indicates that observed emission in the 94 Å channel is from material at the secondary,  $\sim 1.6$  MK, 94 Å peak. The inclusion of the 94 Å (Fe XVIII) – 335 Å pair (in addition to the seven pairs introduced by Viall & Klimchuk, 2012) allows us to highlight where cooling is observed from the hottest material.

### 6.2.3 Active Region Fan Loop, Pixel 2

In addition to the pixel of diffuse emission investigated by [Viall & Klimchuk \(2012\)](#) (§ 6.2.2), we have investigated a number of additional pixels in this image that are associated with other active region features. Figure 6.9 shows the same light curves as in Figure 6.4, for the pixel of active region fan loop emission highlighted by a cross (2) in Figure 6.1.

Figure 6.9 shows the normalised light curves for the same two hours of observation

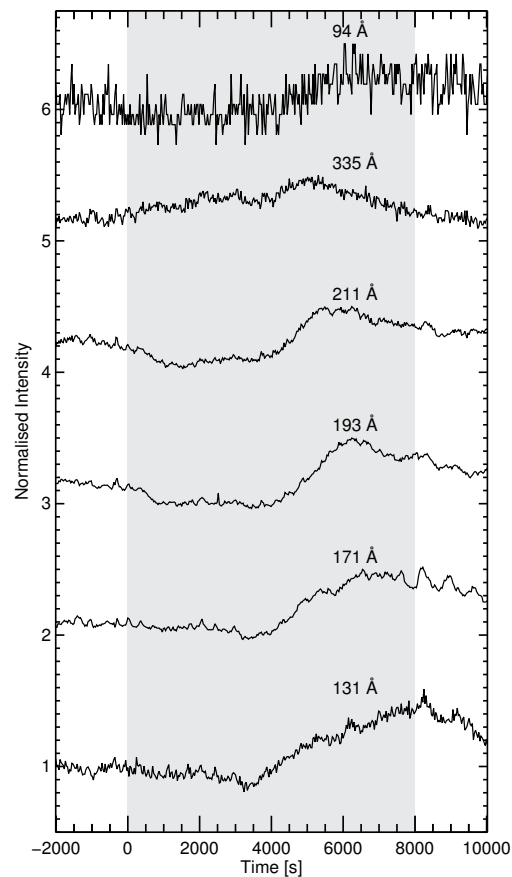


Figure 6.9: Light curves of a pixel of fan loop emission corresponding to 94 Å, 131 Å, 171 Å, 193 Å, 211 Å, and 335 Å (*top to bottom*). The light curves are plotted over the the same two-hour duration that was used for the pixel of diffuse emission [Viall & Klimchuk \(2012\)](#) (indicated by a grey region). For context, an additional  $\pm 2000$  s is included.

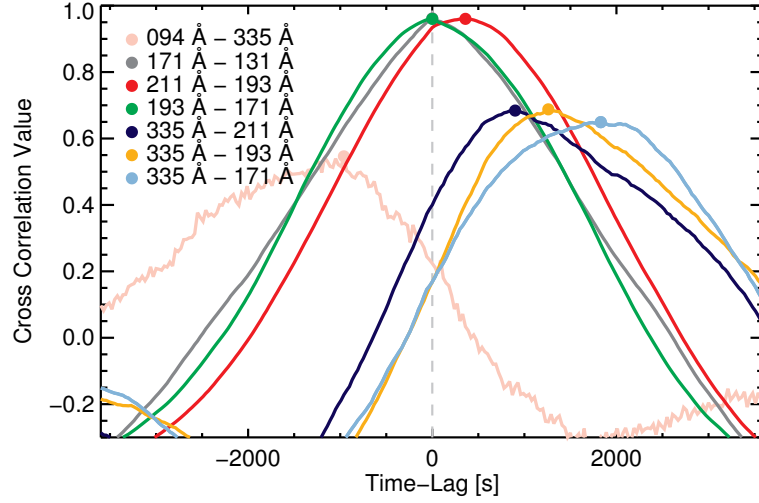


Figure 6.10: Cross-correlation value as a function of temporal offset between seven pairs of light curves for a pixel of fan loop emission. A positive time-lag indicates that the second channel in the pair lags the first, and a negative time-lag indicates that the first channels lags the second (e.g. for the 94 Å - 335 Å pair, 94 Å lags 335 Å). For each channel pair, the filled circle represents the observed time-lag which is defined as the value at which the cross-correlation value is maximum.

that were analysed for a pixel of diffuse emission, and are offset in intensity to avoid overlap of the light curves. From top to bottom, the light curves are once again: 94 Å, 335 Å, 211 Å, 193 Å, 171 Å, 131 Å. In this pixel, for the same two hour period as in the previous section, 335 Å ( $\sim 2.5$  MK) peaks first (at  $\sim 5000$  s), followed by 211 Å ( $\sim 1.8$  MK),  $\sim 5300$  s; 193 Å ( $\sim 1.6$  MK),  $\sim 6000$  s; 94 Å ( $\sim 7$ , and  $\sim 1.6$  MK),  $\sim 6250$  s; and then 171 Å and 131 Å ( $\sim 0.9$ ,  $\sim 0.6$  MK) at  $\sim 6500$  s. This order results in a similar set of time-lags as in Figure 6.5. In contrast to Figure 6.5, Figure 6.10 shows that the 171 Å - 131 Å (0.9 - 0.6 MK) channel has a *zero* time-lag in this pixel. It should be noted that in Figure 6.9, the 131 Å channel peaks near the edge of the 8000 s time series which could affect the time-lag value. By extending the time series to the full 12,000 s (shown in Figure 6.9) we can perform time-lag analysis again, and this reveals that the cross-correlation value is still peaked when the temporal offset is equal to *zero*; the *zero* time-lag is therefore not an effect of a finite (truncated) time series, and that emission in both channels is assumed to be from an overlapping temperature range.

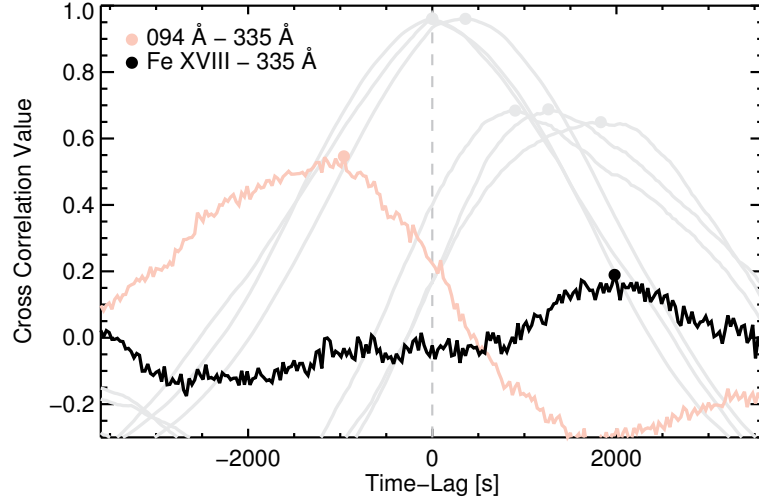


Figure 6.11: Cross-correlation value as a function of temporal offset between two pairs of channels:  $94 \text{ \AA} - 335 \text{ \AA}$ , and  $94 \text{ \AA} (\text{Fe XVIII}) - 335 \text{ \AA}$ , where the Fe XVIII component of the *SDO/AIA*  $94 \text{ \AA}$  time series has been isolated. In addition to these two channel pairs, the six additional channel pairs from Figure 6.10 overplotted in grey. As with Figure 6.10, a negative time-lag for the  $94 \text{ \AA} - 335 \text{ \AA}$  channel pair indicates that  $335 \text{ \AA}$  brightens before  $94 \text{ \AA}$ , and is thought to be behaving as a cool channel. This is again confirmed by  $94 \text{ \AA} (\text{Fe XVIII}) - 335 \text{ \AA}$  channel pair that displays a small positive correlation ( $\sim 0.2$  at  $2000 \text{ s}$ ), and may indicate that some material is being heated to the Fe XVIII peak of *SDO/AIA*  $94 \text{ \AA}$ , however the emission in the *SDO/AIA*  $94 \text{ \AA}$  channel is dominated by cooler emission.

Again, for the  $94 \text{ \AA} - 335 \text{ \AA}$  pair, a negative time-lag is observed. As with Figure 6.7, we can once again perform cross-correlation with the isolated Fe XVIII component of the *SDO/AIA*  $94 \text{ \AA}$  channel. The cross-correlation value as a function of offset for both  $94 \text{ \AA} - 335 \text{ \AA}$  ( $7, 1.6 - 2.5 \text{ MK}$ ) and for  $94 \text{ \AA} (\text{Fe XVIII}) - 335 \text{ \AA}$  ( $7 - 2.5 \text{ MK}$ ) are shown in Figure 6.11. Figure 6.11 shows the cross-correlation value as a function of offset for the  $94 \text{ \AA} - 335 \text{ \AA}$  and  $94 \text{ \AA} (\text{Fe XVIII}) - 335 \text{ \AA}$  channel pairs, and a slight correlation between  $94 \text{ \AA} (\text{Fe XVIII}) - 335 \text{ \AA}$  is observed at  $\sim 2000 \text{ s}$ , which falls off at offsets either side. As noted with the diffuse emission pixel, following the lead of Viall & Klimchuk (2012), the cross-correlation value is not greatly significant at values  $< 0.2$ , and this suggests that there is some emission at  $7 \text{ MK}$ , but the majority is at cooler temperatures.

### 6.2.4 Active Region Core/Loop Pixel, Pixel 3

Similarly, the same analysis can be performed for the active region core emission. Again, Figure 6.12 shows the light curves as in Figure 6.4, and Figure 6.13 shows the cross-correlation value as a function of offset (as in Figure 6.5) for the pixel of active region core emission highlighted by a diamond (3) in Figure 6.1.

For this pixel, during the time series, clear loop heating is observed (see Figure 6.12). This pixel is shown for the same two hour period as in the previous two sections

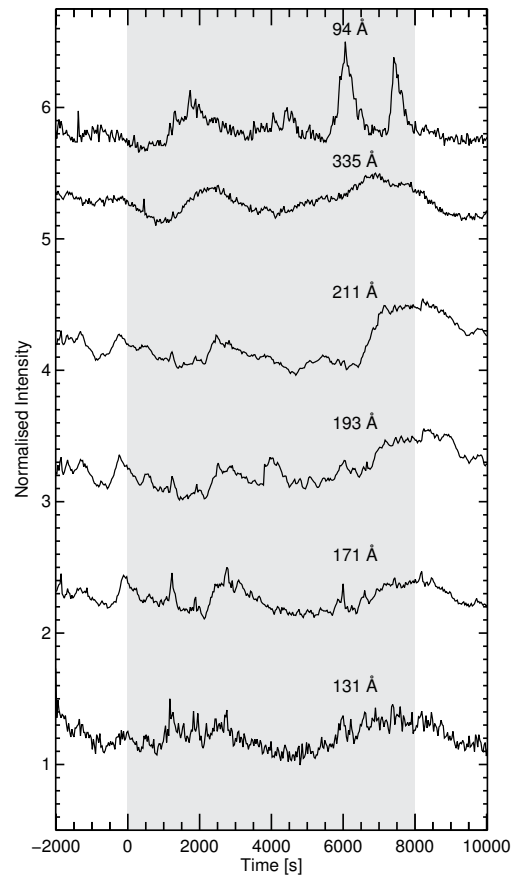


Figure 6.12: Light curves of a pixel of active region core/loop emission corresponding to 94 Å, 131 Å, 171 Å, 193 Å, 211 Å, and 335 Å (*top to bottom*). The light curves are plotted over the two-hour duration studied by [Viall & Klimchuk \(2012\)](#) (indicated by a grey region), and used for time-lag analysis. For context, an additional  $\pm 2000$  s is included.

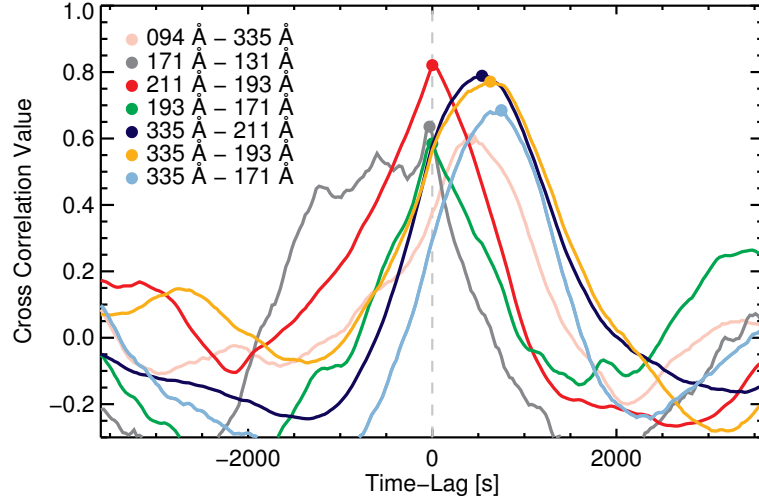


Figure 6.13: Cross-correlation value as a function of temporal offset between seven pairs of light curves for a pixel of active region core emission. A positive time-lag indicates that the second channel in the pair lags the first, and a negative time-lag indicates that the first channels lags the second. For each channel pair, the filled circle represents the observed time-lag which is defined as the value at which the cross-correlation value is maximum. Here, 335 Å lags 94 Å.

and in this case 94 Å (7, 1.6 MK) peaks first at  $\sim 1600$  s, followed by 335 Å (2.5 MK) at  $\sim 2250$  s; 211 Å and 193 Å (1.8 MK, 1.6 MK) at  $\sim 2500$  s; and 171 Å and 131 Å (0.9 MK, 0.6 MK) at  $\sim 2750$  s. This order results in a similar set of time-lags as in Figure 6.5. In contrast to Figure 6.5, both 171 Å – 131 Å (0.9 – 0.6 MK) and 211 Å – 193 Å (1.8 – 1.6 MK) have *zero* time-lags in this pixel, and 94 Å peaks first (indicating material  $> 2.5$  MK, and up to 7 MK).

Crucially, it is the behaviour of the 94 Å channel that is interesting. In this case, for the 94 Å – 335 Å pair, there is a *positive* time-lag (335 Å lags 94 Å), and pixel is clearly observable in the Fe XVIII image (Figure 6.6), where this image has been reconstructed from three *SDO/AIA* images to recover a synthetic Fe XVIII map. The cross-correlation values as a function of offset for both 94 Å – 335 Å and for 94 Å (Fe XVIII) – 335 Å are shown in Figure 6.14. There is a significant correlation ( $\sim 0.55$ ) for the 94 Å (Fe XVIII) – 335 Å pair that is observed at  $\sim 500$  s, which is nearly identical in both time-lag and cross-correlation value to the 94 Å – 335 Å time-lag which falls off sharply with larger offsets. This behaviour strongly indicates that there is emission at 7 MK, which cools

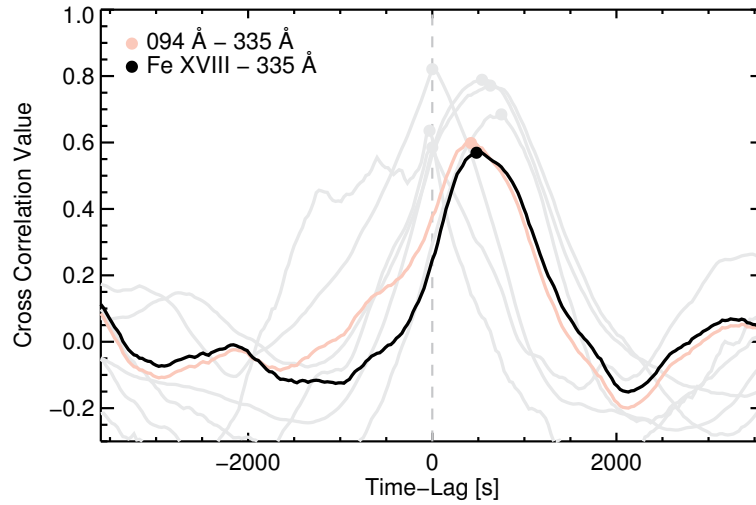


Figure 6.14: Cross-correlation value as a function of temporal offset between two pairs of channels:  $94 \text{ \AA} - 335 \text{ \AA}$ , and  $94 \text{ \AA} (\text{Fe XVIII}) - 335 \text{ \AA}$ , where the Fe XVIII component of the *SDO/AIA*  $94 \text{ \AA}$  time series has been isolated. In addition to these two channel pairs, the six additional channel pairs from Figure 6.13 overplotted in grey. As with Figure 6.13, a positive time-lag for the  $94 \text{ \AA} - 335 \text{ \AA}$  channel pair indicates that  $94 \text{ \AA}$  brightens before  $335 \text{ \AA}$ , and is thought to be behaving as a hot channel. This is again confirmed by  $94 \text{ \AA} (\text{Fe XVIII}) - 335 \text{ \AA}$  channel pair that displays a significant positive correlation ( $\sim 0.55$  at  $500 \text{ s}$ ; similar to the  $94 \text{ \AA} - 335 \text{ \AA}$  channel pair), and this strongly indicates material is being heated to the Fe XVIII peak of *SDO/AIA*  $94 \text{ \AA}$ , and this channel is dominated by emission from plasma at  $\sim 7 \text{ MK}$ .

to  $< 2 \text{ MK}$ , and that the majority of emission observed by *SDO/AIA*  $94 \text{ \AA}$  is at this temperature. Finally, while in this case *SDO/AIA*  $94 \text{ \AA}$  is acting as a hot channel, we observe that the majority of channel pairs report similar behaviour to previous pixels.

### 6.2.5 Loop Footpoint, Pixel 4

The fourth, and final pixel we discuss here is that of a fan loop footpoint, which is represented as a cross (4) in Figure 6.1. Again, as with the last three sections, Figure 6.15 shows the same information as in Figures 6.4. Here, all six light curves shown in Figure 6.15 appear to have similar, in-phase, behaviour. Regardless of *SDO/AIA* channel, in the two hour period that has been investigated here, all channels peak at the same time. This is clearly seen (by-eye) in Figure 6.15 where variations between channels

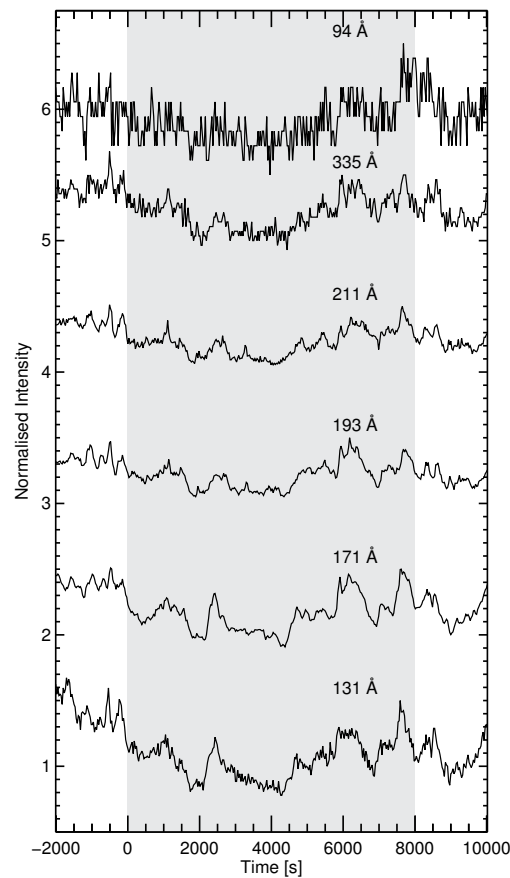


Figure 6.15: Light curves of a pixel of fan loop footpoint emission corresponding to 94 Å, 131 Å, 171 Å, 193 Å, 211 Å, and 335 Å (*top to bottom*). The light curves are plotted over the two-hour duration studied by [Viall & Klimchuk \(2012\)](#) (indicated by a grey region), and used for time-lag analysis. For context, an additional  $\pm 2000$  s is included.

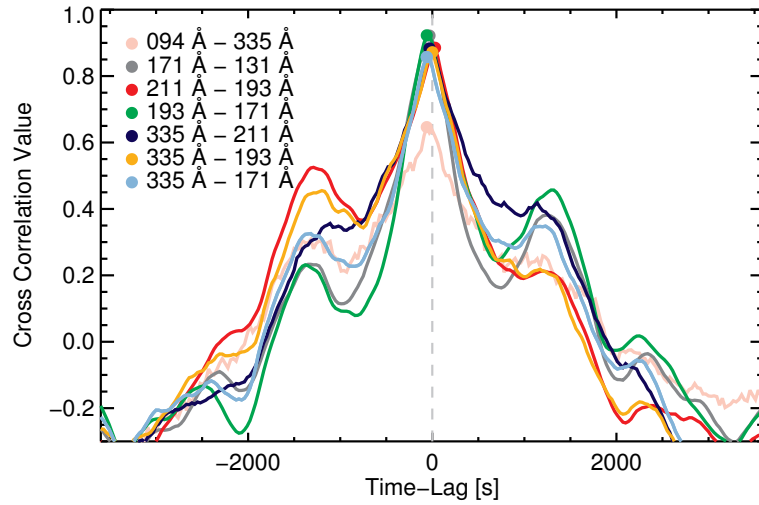


Figure 6.16: Cross-correlation value as a function of temporal offset between seven pairs of light curves for a pixel of fan loop footpoint emission. A positive time-lag indicates that the second channel in the pair lags the first, and a negative time-lag indicates that the first channels lags the second. For each channel pair, the filled circle represents the observed time-lag which is defined as the value at which the cross-correlation value is maximum, and here, each channel pair displays a *zero* time-lag with a strong cross-correlation value ( $> 0.6$ ), which indicates that the light curves are in phase.

are in phase, and is clearly shown when plotting cross-correlation value as a function of offset (Figure 6.16). In Figure 6.16 all pairs of channels have peak cross-correlation values at  $\sim 0$  s, with cross-correlation values  $> 0.6$  that fall off rapidly at larger values of offset. This suggests that the *zero* time-lags are significant.

### 6.2.6 Summary

So far, this chapter has introduced time-lag analysis (Viall & Klimchuk, 2011, 2012), and this has been performed on a set of four pixels in the  $250 \times 250$  pixel region studied by Viall & Klimchuk (2012). Starting with a pixel similar to the pixel of diffuse emission studied by Viall & Klimchuk (2012), this chapter performed similar analysis to that presented in Viall & Klimchuk (2012), before performing the same analysis on an additional set of pixels. As has been described throughout this chapter, each pixel (which relates to a different active region structure) has shown slightly different

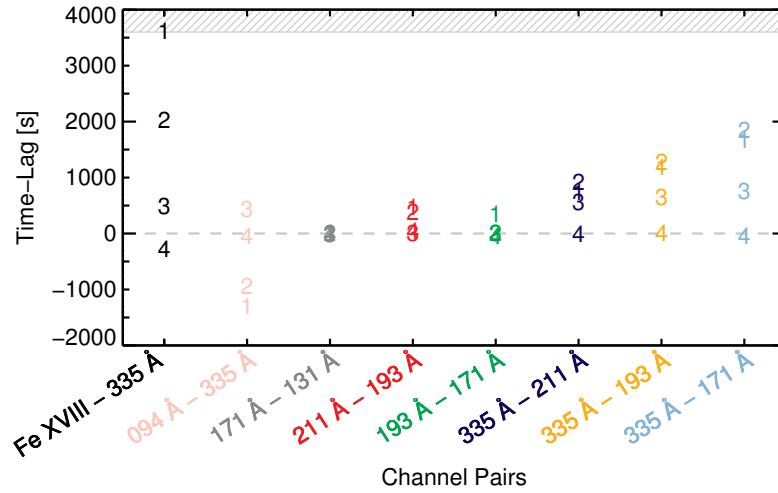


Figure 6.17: Summary of time-lags for each channel pair for the seven channel pairs defined by Viall & Klimchuk (2012), and the additional 94 Å (Fe XVIII) – 335 Å channel pair. The Time-lag is shown between  $-2000$  s, and  $4000$  s, where the maximum time-lag can only be  $3600$  s. *Left to Right*, these channel pairs are 94 Å (Fe XVIII) – 335 Å, black; 94 Å – 335 Å, pink; 171 Å – 131 Å, grey; 211 Å – 193 Å, red; 335 Å – 211 Å, dark blue; 335 Å – 193 Å, yellow; and 335 Å – 171 Å, sky blue. The respective time-lags for each pixel are highlighted by the corresponding pixel number (1 – 4).

behaviour in temperature, some of which can arise as artefacts of the truncated time series.

This chapter has for the first time introduced time-lag analysis on the isolated Fe XVIII component of the *SDO/AIA* 94 Å time series. This direct approach clarifies that the *SDO/AIA* 94 Å channel behaves as both a hot and cool channel, and that this leads the 94 Å – 335 Å pair to report time-lags as both *positive* and *negative*; behaviour is confirmed by studying the *SDO/AIA* 94 Å (Fe XVIII) – 335 Å channel pair.

Figure 6.17 summarises the time-lags observed in the previous four pixels. Figure 6.17 shows the *SDO/AIA* 94 Å (Fe XVIII) – 335 Å channel pair, and the same seven channel pairs that were first introduced in Viall & Klimchuk (2012). The time-lag observed for each pixel is represented by the respective pixel number (1 – 4) and this Figure highlights the increasing offset for the 335 Å – 211 Å, 335 Å – 193 Å, 335 Å – 171 Å pairs, for Pixels 1, 2, and 3, which indicates plasma cooling from  $\sim 2.5$  MK.

## 6.3 Time-Lag Analysis of an Active Region: Time-Lag Maps

In order to understand the global behaviour within the active region, time-lag analysis can be applied to the whole active region for the same sets of channels. By applying the time-lag analysis technique to each pixel and extracting the peak of the cross-correlation value (shown as a filled circle in Figure 6.5, for example), time-lag maps can be generated (e.g. Viall & Klimchuk, 2012). As the plasma is optically thin, the time-lags in each individual pixel will likely be the combination of multiple structures along the line-of-sight all of which may have different properties and heating frequencies. The extracted time-lag extracted in each pixel is therefore the combination of these processes.

First we discuss the  $94 \text{ \AA} - 335 \text{ \AA}$  (7, 1.6–2.5 MK; introduced by Viall & Klimchuk, 2012), and  $94 \text{ \AA}$  (Fe XVIII) –  $335 \text{ \AA}$  (7 – 2.5 MK; introduced in this thesis) channel pairs for the same time period as shown in the previous sections. Figure 6.18 shows the time-lag maps for the  $94 \text{ \AA} - 335 \text{ \AA}$ , and  $94 \text{ \AA}$  (Fe XVIII) –  $335 \text{ \AA}$  channel pairs, plotted on the same (linear) scale. To keep consistent with the literature, *positive* time-lags represented as reds, oranges, and yellows; *zero* time-lags are olive green; and *negative* time-lags are represented by blues, greens, and blacks.

Starting with the  $94 \text{ \AA} - 335 \text{ \AA}$  channel pair, we are able to see that the core of the active region has generally positive time-lags ( $94 \text{ \AA}$  precedes  $335 \text{ \AA}$ ), while in general, the map displays *negative* time-lags, as seen for Pixels 1 and 2 (§ 6.2.2 - § 6.2.3). To emphasise this point, Figure 6.19 shows the corresponding time-lag and cross-correlation histograms which indicate the majority of pixels have *negative* time-lags ( $\sim 37000$ ), *positive* time-lags ( $\sim 25000$ ), with a few *zero* time-lags ( $\sim 2000$ ), and the majority of these time-lags are at cross-correlation values of  $< 0.2$ . The behaviour observed in Figure 6.18 (*left*) suggests that heating in the core of the active region is dominated by strong nanoflares, while outside the core, weaker nanoflares dominate. The pattern of time-lag signatures seen for the  $94 \text{ \AA} - 335 \text{ \AA}$  channel pair suggests that only the core of the active region is heated to  $\sim 7$  MK, and this can be further confirmed by the  $94 \text{ \AA}$  (Fe XVIII) –  $335 \text{ \AA}$  time-lag map (Figure 6.18, *right*), which displays cooling from the  $94 \text{ \AA}$  Fe XVIII peak in the core of the active region. As with the  $94 \text{ \AA} - 335 \text{ \AA}$  channel pair, Figure 6.19 (*right*) shows the time-lag and cross-

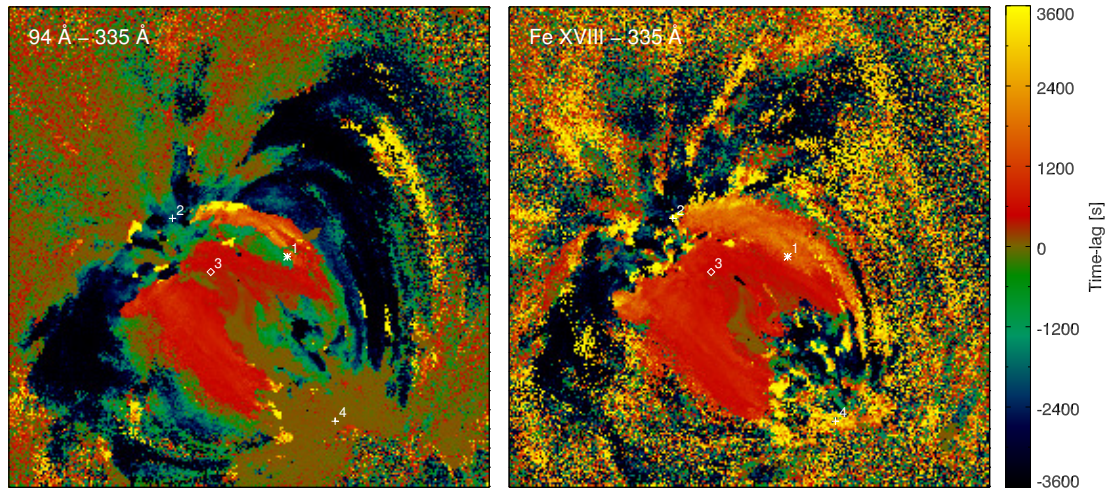


Figure 6.18: Time-lag maps for the  $94 \text{ \AA} - 335 \text{ \AA}$  (*left*) and  $94 \text{ \AA}$  (Fe XVIII) –  $335 \text{ \AA}$  channel pairs (*right*). The colour bar shows the time-lag in seconds with both time-lag maps plot on the same scale. The four pixels that have been analysed in the previous sections are also highlighted.

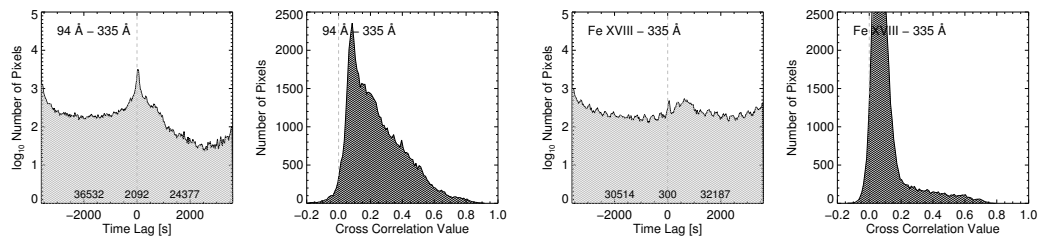


Figure 6.19: Time-lag and Cross-correlation histograms for the *SDO/AIA*  $94 \text{ \AA} - 335 \text{ \AA}$  channel pair (*left*), and the  $94 \text{ \AA}$  (Fe XVIII) –  $335 \text{ \AA}$  channel pair (*right*). Here the time-lag histograms are summed in to *positive*, *zero*, and *negative* time-lags and these numbers are indicated respectively.

correlation histograms for the  $94 \text{ \AA}$  (Fe XVIII) –  $335 \text{ \AA}$  pair, which indicates there is a similar number of *positive* and *negative* time-lags, and very few ( $\sim 300$ ) *zero* time-lags, although a significant number of these time-lags have low cross-correlation values and time-lag values outside the core appear as noise.

It should be noted that the time-lag maps shown in Figure 6.18 do not discriminate based on an active region structure or cross-correlation value (shown in Figure 6.19). It is therefore of interest to understand the how the cross-correlation value influences these plots. Figure 6.20 shows two maps of cross-correlation value for the time-lag

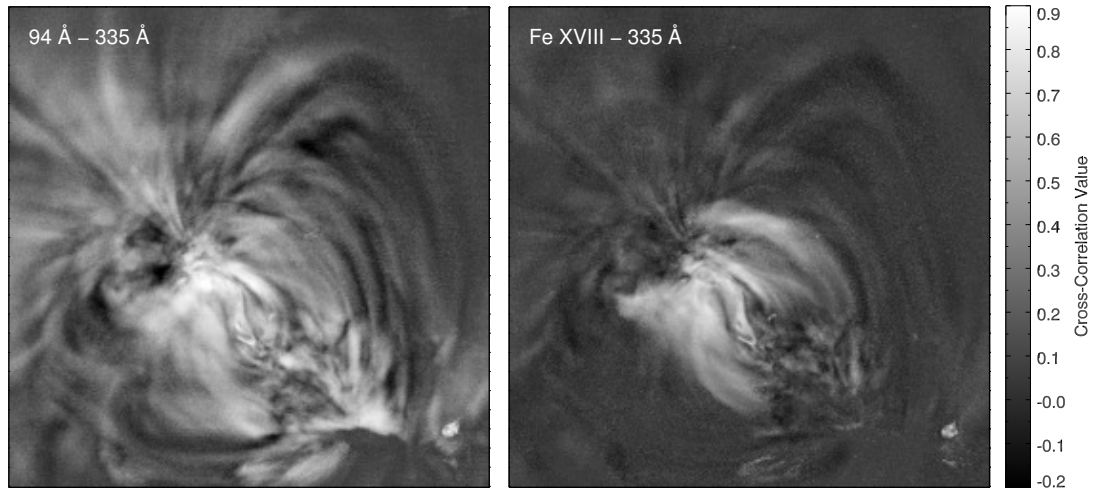


Figure 6.20: Cross-Correlation maps for the  $94 \text{ \AA} - 335 \text{ \AA}$  (*left*) and  $94 \text{ \AA}$  (Fe XVIII) –  $335 \text{ \AA}$  channel pairs (*right*), linearly scaled between  $-0.2$  and  $0.9$ . For the  $94 \text{ \AA} - 335 \text{ \AA}$  channel pair, the majority of high cross-correlation values are located within the core of the active region where positive time-lags are observed. As expected, this behaviour is amplified with the  $94 \text{ \AA}$  (Fe XVIII) –  $335 \text{ \AA}$  pair. In this case, the core of the active region has a significantly higher cross-correlation values than the rest of the active region, as this is where there material has been heated to the  $\sim 7 \text{ MK}$  Fe XVIII peak of *SDO/AIA*  $94 \text{ \AA}$ .

maps presented in Figure 6.18. The cross-correlation maps indicate that the largest cross-correlation values are observed in the core of the active region (light grey – white), and this trend is emphasised when one considers the  $94 \text{ \AA}$  (Fe XVIII) –  $335 \text{ \AA}$  pair. In this case, in contrary to the  $94 \text{ \AA} - 335 \text{ \AA}$  pair, for a large cross-correlation value to be present there must be emission at  $\sim 7 \text{ MK}$ ; emission that is generally confined to active region cores (and hot loops), e.g. Warren *et al.* (2012).

If one is to again assume that a significant value of cross-correlation is  $\sim 0.2$ , then time-lag maps can be restricted to values of  $> 0.2$ , as performed in Viall & Klimchuk (2012). Figure 6.21 shows the time-lag maps (as in Figure 6.18) for cross-correlation values of  $> 0.2$ . For the  $94 \text{ \AA} - 335 \text{ \AA}$  channel pair the time-lag is approximately equally distributed between *positive* and *negative* time-lags (Figure 6.22), while for the  $94 \text{ \AA}$  (Fe XVIII) –  $335 \text{ \AA}$  pair the vast majority of pixels that have cross-correlation values  $> 0.2$  are positive, as would be expected, and are located within the active region core.

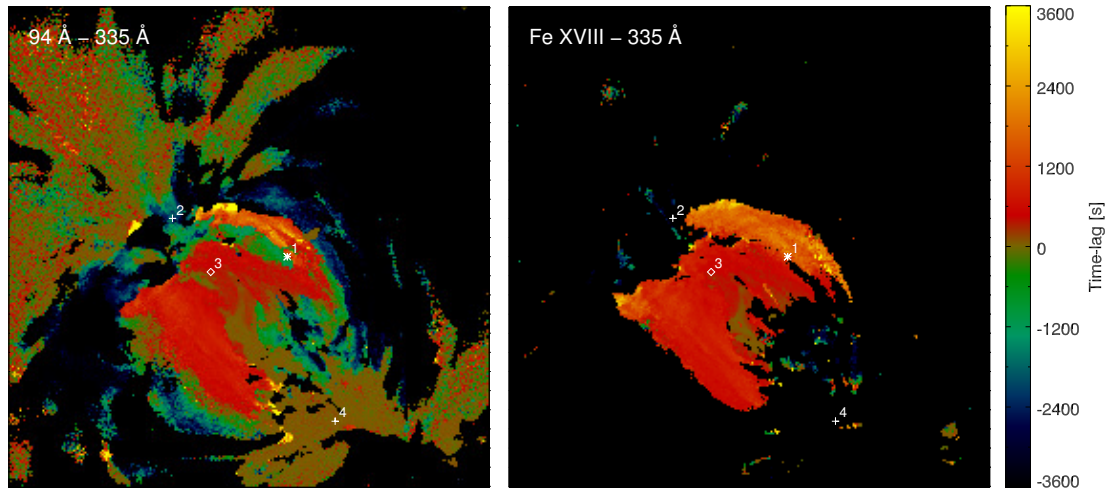


Figure 6.21: Time-lag maps for the  $94 \text{ \AA} - 335 \text{ \AA}$  (*left*) and  $94 \text{ \AA}$  (Fe XVIII) –  $335 \text{ \AA}$  channel pairs (*right*) where the cross-correlation value is  $> 0.2$ . This Figure is plot on the same scale as Figure 6.18, and highlights that cooling from the  $\sim 7 \text{ MK}$  Fe XVIII peak of *SDO/AIA*  $94 \text{ \AA}$  is observed only within the active region core.

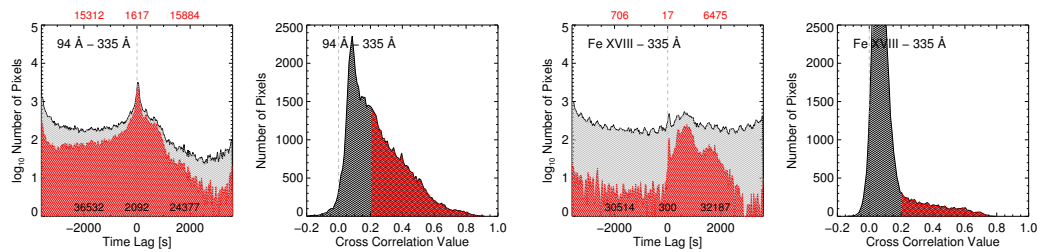


Figure 6.22: Time-lag and Cross-correlation histograms for the *SDO/AIA*  $94 \text{ \AA} - 335 \text{ \AA}$  channel pair (*left*), and the  $94 \text{ \AA}$  (Fe XVIII) –  $335 \text{ \AA}$  channel pair (*right*). Both the time-lag histograms for all pixels, and those with cross-correlation values  $> 0.2$  are shown (black, red). Each histogram is summed in to *positive*, *zero*, and *negative* time-lags and these numbers are indicated in the same colour. Additionally, the cross-correlation histograms are shaded red in the region where the cross-correlation  $> 0.2$ .

Figure 6.22 shows the same time-lag and cross-correlation value histograms as in Figure 6.19. These plots include the addition of a red time-lag histogram indicating the time-lag histogram for cross-correlation values  $> 0.2$ . Here it is clear that for the  $94 \text{ \AA} - 335 \text{ \AA}$  pair there is still an equal distribution between *positive* and *negative* time-lags with significant correlations, however with the  $94 \text{ \AA}$  (Fe XVIII) –  $335 \text{ \AA}$  pair there are very few ( $\sim 700$ ) time-lags that are *negative*.

### 6.3.1 Further *SDO/AIA* Channel Pairs

In addition to the  $94 \text{ \AA} - 335 \text{ \AA}$ , and the  $94 \text{ \AA} (\text{Fe XVIII}) - 335 \text{ \AA}$  pair, Figure 6.23 shows a further six time-lag maps for the same channel pairs studied for the individual pixels. From top to bottom, left to right, these channel pairs are  $335 \text{ \AA} - 211 \text{ \AA}$  ( $2.5 - 1.8 \text{ MK}$ ),  $335 \text{ \AA} - 193 \text{ \AA}$  ( $2.5 - 1.6 \text{ MK}$ ),  $335 \text{ \AA} - 171 \text{ \AA}$  ( $2.5 - 0.9 \text{ MK}$ ),  $211 \text{ \AA} - 193 \text{ \AA}$  ( $1.8 - 1.6 \text{ MK}$ ),  $193 \text{ \AA} - 171 \text{ \AA}$  ( $1.6 - 0.9 \text{ MK}$ ),  $171 \text{ \AA} - 131 \text{ \AA}$  ( $0.9 - 0.6 \text{ MK}$ ). In addition, Figure 6.24 and Figure 6.25 show the corresponding time-lag histograms, and cross-correlation histograms as shown previously.

For the  $335 \text{ \AA} - 211 \text{ \AA}$ ,  $335 \text{ \AA} - 193 \text{ \AA}$ ,  $335 \text{ \AA} - 171 \text{ \AA}$  channel pairs in Figure 6.23 (*top*), these maps are dominated by *positive* time-lags (which is confirmed by the time-lag histograms in Figure 6.24). This indicates that the  $335 \text{ \AA}$  channel precedes  $211 \text{ \AA}$ ,  $193 \text{ \AA}$ , and  $171 \text{ \AA}$ . These channel pairs (which have increasingly larger jumps in temperature, see Figure 6.3) follow the same signatures as we have seen for Pixels 1, 2, and 3 (§ 6.2.2, 6.2.3, 6.2.4): the time-lags are mostly *positive* (some *zero* time-lags are seen, as for Pixel 4, § 6.2.5) and the time-lags are observed to increase as the temperature gap between the peaks of the channels increases. As is shown in Figure 6.23, there is again a clear tendency for the time-lag value to increase from the active region core, and these maps indicate that plasma is heated to at least  $2.5 \text{ MK}$ , and cools to  $\sim 1.6 \text{ MK}$ . As Viall & Klimchuk (2012) note in their work, these *zero* time-lags are spatially related to locations of moss, and fan loops.

From left to right, the bottom panels of Figure 6.23 show the  $211 \text{ \AA} - 193 \text{ \AA}$ ,  $193 \text{ \AA} - 171 \text{ \AA}$ ,  $171 \text{ \AA} - 131 \text{ \AA}$  channel pairs. Considering the  $211 \text{ \AA} - 193 \text{ \AA}$  channel pair (Figure 6.23, *bottom left*), the majority of time-lag values are *positive* or *zero* with *very few* pixels showing *negative* time-lags. There is a clear tendency for the time-lag value to increase from the active region core. Interestingly for this channel pair the cross-correlation histogram is peaked at  $\sim 0.9$ , indicating these time series are highly correlated (Figure 6.25). For the  $193 \text{ \AA} - 171 \text{ \AA}$  channel pair, Figure 6.23, (*bottom middle*) shows similar time-lag signatures to the set of  $335 \text{ \AA}$  pairs shown above, with *zero* time-lags are observed in regions of moss, and the time-lag values become increasingly positive (red – yellow) with distance from the active region core. Finally, as with the single pixel examples in Figure 6.5 and Figure 6.10, the  $171 \text{ \AA} - 131 \text{ \AA}$  channel pair (Figure 6.23, *bottom right*) shows that *zero* time-lags dominate, and comparatively, very few *positive* or *negative* pixels exist. This indicates that these

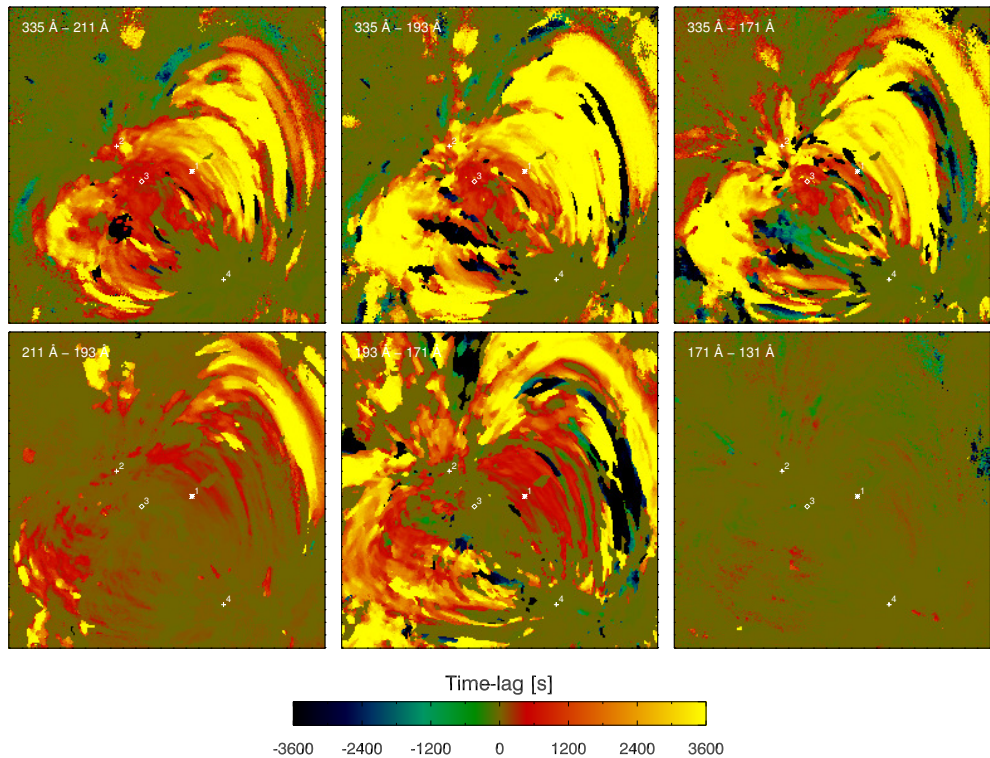


Figure 6.23: Time-lag maps for six sets of channel pairs. *Top to bottom, left to right:* 335 Å – 211 Å, 335 Å – 193 Å, 335 Å – 171 Å, 211 Å – 193 Å, 211 Å – 171 Å, 193 Å – 171 Å. The colour bar shows the time-lag in seconds (plotted on a linear scale), and the four pixels that have been analysed in the previous sections are also highlighted.

channels may be observing plasma of similar temperature, behaviour that was observed for all individual pixels previously.

Finally, for these time-lag maps the time-lag values are consistent with the relevant cooling timescales for loops (see [Cargill \*et al.\*, 1995](#)), however some edge effects associated with time-lag analysis do exist (see [Figure 6.24](#) at  $\pm 3600$  s).

### 6.3.2 Discussion

As shown both here, and in [Viall & Klimchuk \(2012\)](#), widespread cooling is observed within the active region. This is generally true with the exception of both moss and fan structures, and includes pixels where there are both discernible, and indiscernible loops (e.g. diffuse emission). It is clear from the 94 Å – 335 Å pair, the 94 Å channel behaves as both a hot, and cool channel which is the result of material being heated

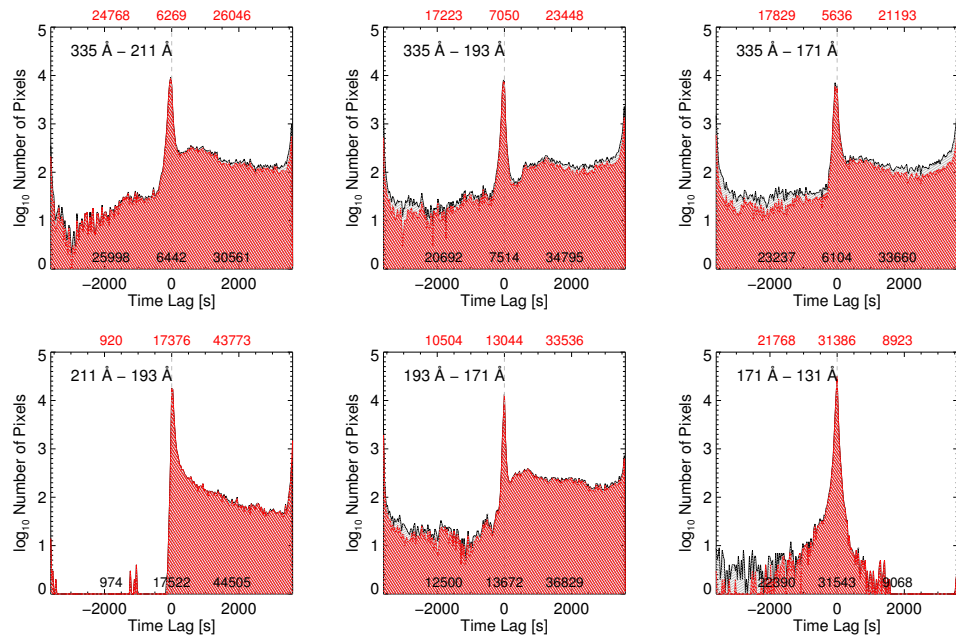


Figure 6.24: Time-lag histograms for the six sets of channel pairs shown in Figure 6.23. Each plot shows the time-lag histogram for all pixels (black, grey hatched region), and those for the pixels where the cross-correlation value is  $> 0.2$  (red). Each histogram is summed as *positive*, *zero*, and *negative*, and these are highlighted in black and red.

to different temperatures. By isolating the Fe XVIII component of *SDO/AIA* 94 Å and performing time-lag analysis on *SDO/AIA* 94 Å (Fe XVIII) – 335 Å channel pair extracts information about the hottest material observed by *SDO/AIA*. As has been seen in Figure 6.21, the hottest material is confined to the core of the active region, as expected.

In the next section we provide an overview results of coronal and transition region EBTEL simulations of diffuse emission within NOAA AR 11082 (Viall & Klimchuk, 2013). As with the previous sections, the light curves and time-lags will be presented for the same sets of channels.

## 6.4 Testing with Model Time Series

### 6.4.1 EBTEL Diffuse Emission Simulation: Corona

The results of time-lag analysis applied to the diffuse emission pixel in § 6.2.2 are consistent with a single impulsively heated flux tube, and/or by a collection of flux

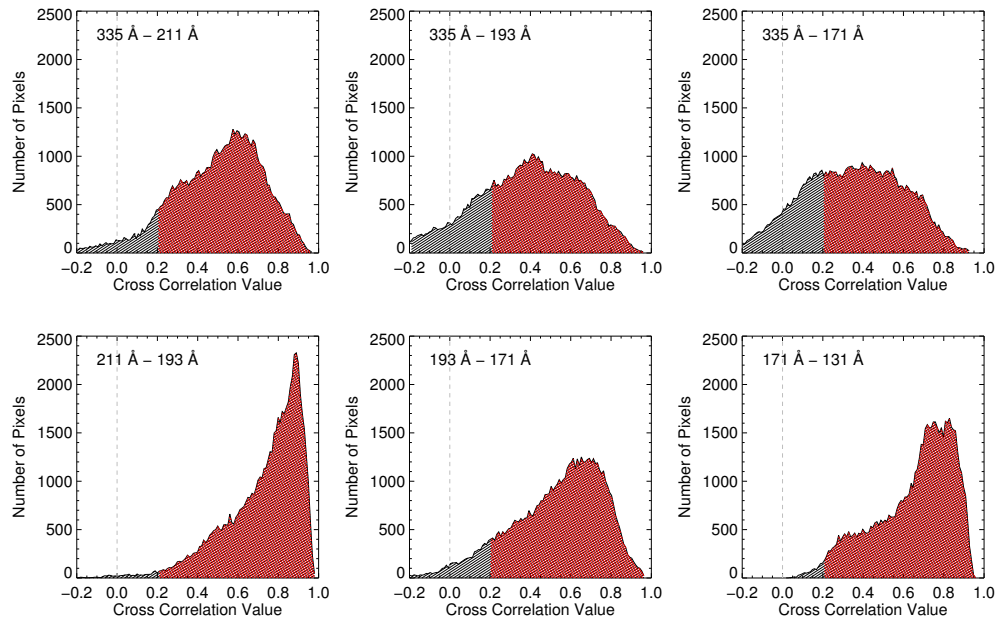


Figure 6.25: Cross-correlation histograms for the six sets of channel pairs shown in Figure 6.23. Each plot shows the cross-correlation histogram (binned at a resolution of 0.01) for all pixels in the  $250 \times 250$  region between  $-0.2$  and  $1.0$ . Values of cross-correlation  $> 0.2$  are highlighted in red.

tubes that behave as collective, e.g. a “nanoflare storm” (Viall & Klimchuk, 2012). For diffuse emission in the core of an active region, this may be a collection of multiple structures which are uncorrelated, which together makes them indistinguishable.

To further understand this scenario, and the results of time-lag analysis on the pixel of diffuse emission in NOAA AR 11082 (Pixel 1, § 6.2.2), Viall & Klimchuk (2013) modelled the full line-of-sight coronal emission (as would be observed with *SDO/AIA* in a single pixel), with the Enthalpy-Based Thermal Evolution of Loops (EBTEL, Klimchuk *et al.*, 2008; Cargill *et al.*, 2012, § 1.3.1).

In the original paper, Viall & Klimchuk (2013) use the EBTEL DEM( $T, t$ ) to synthesise *SDO/AIA* observations, which are then used for time-lag analysis. In this chapter, the EBTEL DEMs, which have been obtained at *one* second cadence between  $\log_{10}T = 4.0 - 8.5$  MK (and  $\Delta\log_{10}T = 0.01$ ) are folded through the *SDO/AIA* temperature response functions that have been limited to  $\log_{10}T = 5.6 - 7.0$  MK. This is performed in order to allow for comparisons to DEMs obtained through inversion methods where it is common to recover the DEM over a limited temperature range due to the limited

temperature sensitivity of the *SDO*/AIA channels. While there is sensitivity outwith this temperature range in the *SDO*/AIA filter channels, these regions of temperature space are poorly constrained and we assume that in observations there is little contribution from these temperatures. The implications of determining the DEM over a restricted temperature range (for actual observations) where the underlying distribution is unknown can result in emission from hotter or cooler material being assumed to be the result of material within the temperature range. By synthesising *SDO*/AIA counts from a DEM that is similarly limited in temperature-space allows us to assess the ability for DEM inversion to recover the input data.

#### 6.4.1.1 Simulation Setup, Viall & Klimchuk (2013, 2015)

In order to investigate the diffuse emission analysed in Viall & Klimchuk (2012) (Pixel 1, § 6.2.2), Viall & Klimchuk (2013, 2015) built a library consisting of 1000 impulsively heated EBTEL simulations consistent with low-frequency nanoflares.

These simulations have strand half-lengths ranging  $3 - 10.6 \times 10^9$  cm, consistent with what is expected through the active region core of NOAA AR 11082. The nanoflare magnitude chosen by Viall & Klimchuk (2013) was dependent on  $1/L^2$  (Mandrini *et al.*, 2000). For a set loop length, 10 nanoflare magnitudes were possible (1 – 5 times the smallest), and there were five possible durations between 50 and 250 s (Viall & Klimchuk (2013)).

Viall & Klimchuk (2013) assumed stochasticity by choosing a random number of these simulations to begin every second (at the time resolution of the simulations). The final light curves are obtained by adding together the individual simulation DEMs.

With the EBTEL simulations, the simulated *SDO*/AIA light curves are recovered by folding  $\text{DEM}(T,t)$  through the *SDO*/AIA temperature response functions that have defined over  $\log_{10}T = 5.6 - 7.0$  MK. As a result of the limited *SDO*/AIA temperature coverage, both the *SDO*/AIA light curves, and time-lags will vary slightly from those presented in Viall & Klimchuk (2013) (cf. Figure 1 and Figure 2, Viall & Klimchuk, 2013).

Figure 6.26 shows the normalised simulated *SDO*/AIA intensity (*top*), and the corresponding cross-correlation values as a function of offset for seven channel pairs. As observed here, and noted in Viall & Klimchuk (2013), these light curves have a much smaller intensity variation than a background-subtracted light curve of a coronal

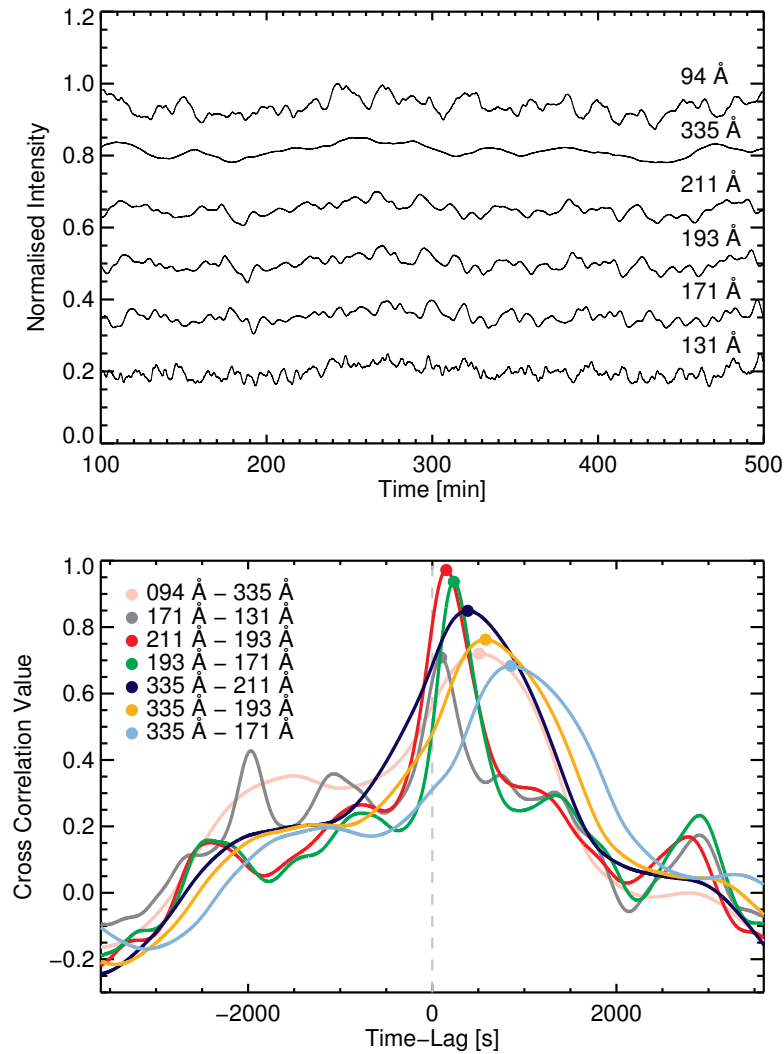


Figure 6.26: *Top*: Light curves synthesised from the coronal EBTEL simulation of diffuse emission. These light curves correspond to 94 Å, 131 Å, 171 Å, 193 Å, 211 Å, and 335 Å (*top to bottom*), and are plotted over  $\sim 8$  hours. *Bottom*: Cross-correlation values as a function of offset time between a pair of light curves simulated from EBTEL coronal DEMs for the same sets of channels as shown in Figure 6.5.

loop. From top to bottom these light curves are 94 Å, 335 Å, 211 Å, 193 Å, 171 Å, 131 Å. Figure 6.26 (*bottom*) shows the cross-correlation value as a function of temporal offset for the same pairs of channels, where as in previous sections (cf. Figure 6.5), the maximum offset has been defined as  $\pm 3600$  s. As in Figure 6.5 the time-lags are represented by filled circles where the cross-correlation value is maximum.

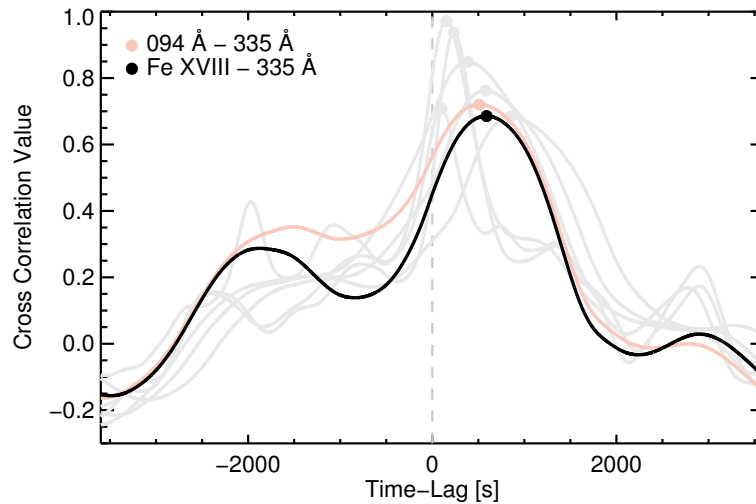


Figure 6.27: Cross-correlation value as a function of temporal offset between two pairs of channels:  $94 \text{ \AA} - 335 \text{ \AA}$ ; and  $94 \text{ \AA} (\text{Fe XVIII}) - 335 \text{ \AA}$ , where the Fe XVIII component of the *SDO/AIA*  $94 \text{ \AA}$  time series has been isolated. In addition to these two channel pairs, the six additional channel pairs from Figure 6.26 overplotted in grey.

In comparison to those in Figure 6.5, Figure 6.26 is consistent in that it shows that  $211 \text{ \AA} - 193 \text{ \AA}$  ( $1.8 - 1.6 \text{ MK}$ ) and  $193 \text{ \AA} - 171 \text{ \AA}$  ( $1.6 - 0.9 \text{ MK}$ ) have very short time-lags (albeit the order is reversed in this simulation), and  $335 \text{ \AA} - 171 \text{ \AA}$  ( $2.5 - 0.9 \text{ MK}$ ) has the longest time-lag, where the  $335 \text{ \AA} - 211 \text{ \AA}$  ( $2.5 - 1.8 \text{ MK}$ ),  $335 \text{ \AA} - 193 \text{ \AA}$  ( $2.5 - 1.6 \text{ MK}$ ),  $335 \text{ \AA} - 171 \text{ \AA}$  pairs have increasingly larger time-lags. Contrary to Figure 6.5, in this simulated case the  $94 \text{ \AA} - 335 \text{ \AA}$  ( $7, 1.6 - 2.5 \text{ MK}$ ) pair exhibits a positive time-lag consistent with material at temperatures of  $\sim 7 \text{ MK}$ . As in the previous sections, the Fe XVIII component of the  $94 \text{ \AA}$  channel can be isolated. Figure 6.27 shows cross-correlation value as a function of offset for  $94 \text{ \AA} - 335 \text{ \AA}$  and  $94 \text{ \AA} (\text{Fe XVIII}) - 335 \text{ \AA}$ . Here, the  $94 \text{ \AA} (\text{Fe XVIII}) - 335 \text{ \AA}$  pair has a longer time-lag than the  $94 \text{ \AA} - 335 \text{ \AA}$  pair (as was also seen in Pixel 3, where  $94 \text{ \AA} - 335 \text{ \AA}$  had a positive time-lag), and this is consistent with material being heated to  $\sim 7 \text{ MK}$ .

While these simulations do not necessarily agree with the pixel of diffuse emission presented in Viall & Klimchuk (2012), importantly, as with the results from time-lag analysis, these simulations are consistent with cooling plasma, and this simulation shows that the time-lag signatures of plasma are observed even when the heating events are completely uncorrelated. These simulations are also important for later chapters

as for each time-step EBTEL provides the temperature distribution, DEM(T) (Chapter 3).

### 6.4.2 EBTEL Diffuse Emission Simulation: Transition Region Response

The definition of the transition region provided in Klimchuk *et al.* (2008); Cargill *et al.* (2012), (introduced by Vesecky *et al.*, 1979) defines the top of the transition region as the location where thermal conduction changes from an energy source to an energy sink (see Viall & Klimchuk, 2015), in contrary to the temperature definition ( $\sim 1$  MK). Under this definition, the transition region can be hotter than 1 MK, and all *SDO/AIA* channels can image both coronal and transition region material. EBTEL does not model the spatial structure of the transition region, but instead computes the DEM over the transition region temperature interval (Equation 30, Klimchuk *et al.*, 2008). This is implemented by deriving the DEM for *strong evaporation*, *static equilibrium*, and *strong condensation*. By combining each of these limiting cases into a single form the DEM can then be represented as a single expression as in Equation A13 in Klimchuk *et al.* (2008). This single expression then reduces to each individual case under the relevant limits.

As the corona and transition region are inherently coupled (thermal conduction, mass exchange), Viall & Klimchuk (2013) studied time-lag analysis for both the coronal and transition region response to a coronal nanoflare. As with Figure 6.26, Figure 6.28 shows the *SDO/AIA* light curves, and the cross-correlation values for same set of seven channel pairs, but here these are simulated from the transition region DEMs. In contrast to the coronal time-lags seen in the previous section (where the time-lags ranged from  $\sim 100$  s to  $\sim 1000$  s), the time-lags in Figure 6.28 are *zero* or near *zero* values. This suggests that only the amplitude of the DEM changes as the flux tube evolves, there is no observable dependence on temperature (all temperatures respond in unison Viall & Klimchuk, 2015), and transition region emission is observed in *all* *SDO/AIA* channels.

As was seen for the fan loop footpoint (Pixel 4, § 6.2.5), the light curves are clearly in phase in Figure 6.28, and this is further emphasised with cross-correlation plot as a function of offset. The result time-lag analysis is that all channel pairs are highly correlated at time-lag = *zero*.

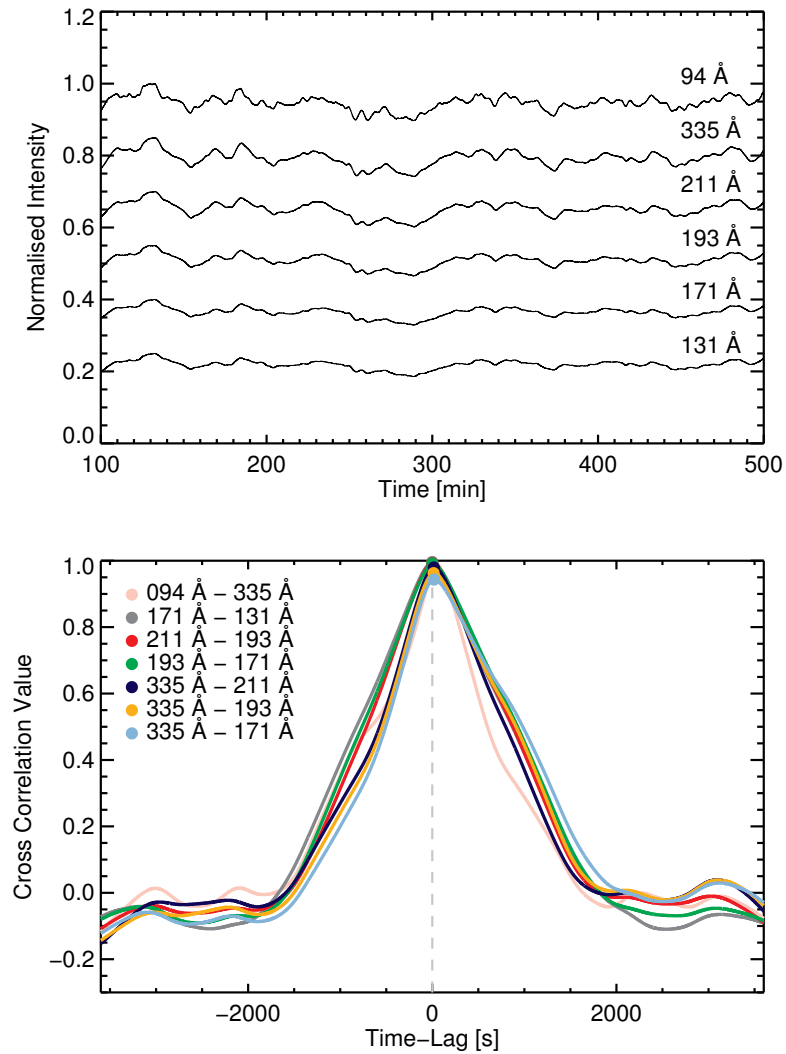


Figure 6.28: *Top*: Light curves synthesised from the coronal EBTEL simulation of diffuse emission. These light curves correspond to 94 Å, 131 Å, 171 Å, 193 Å, 211 Å, and 335 Å (*top to bottom*), and are plotted over a  $\sim 8$  hours. *Bottom*: Cross-correlation values as a function of offset time between a pair of light curves simulated from EBTEL transition region DEMs (*top*) for the same sets of channels as shown in Figure 6.5.

#### 6.4.2.1 Further Mechanisms for Zero Time-lags: In-Phase Time Series

The results of these simulations are in agreement with the observed behaviour for the fan loop footpoint (Pixel 4, § 6.2.5). These results can be interpreted as time-lags equal to *zero* being associated with the transition region response to (impulsive) nanoflare heating where the line-of-sight intersects with the transition region, although, as Viall

& Klimchuk (2016) note, other possibilities do exist including the presence of static plasma along the line-of-sight, or the plasma not fully cooling before being reheated (Bradshaw & Viall, 2016). In the latter case, this would be seen as plasma cooling in to, but not through the peak sensitivities of the channels. Furthermore, zero time-lags could be the result plasma moving along the loop, which would also be observable as doppler shifts in *Hinode*/EIS observations.

Most interestingly with respect to the next chapter, Uritsky *et al.* (2013) detected plasma motion in the regions of fan loops in the periphery of NOAA AR 11082 (Chapter 6; in the region of Pixel 2). The process of an oscillating fan loop moving in and out of a given pixel location would be able to reproduce a *zero SDO/AIA* time-lag. Finally, if the plasma is isothermal over the temperature range where both channels are sensitive, the light curves may evolve in unison (as was seen for the *SDO/AIA* 171 Å – 131 Å channel pair, for example). For a complete discussion see Viall & Klimchuk (2016).

### 6.4.3 Steady Heating

Viall & Klimchuk (2013) also simulated steady heating by assuming photon noise on top of a set of steady light curves. Practically, this was simulated by extracting the observed count rates of a chosen pixel and adding Poisson noise.

As with both the observed data and EBTEL simulations described previously, the light curves and cross-correlation values of this “steady heating” can be computed. These light curves and the cross-correlation are shown in Figure 6.29, and are as described in Viall & Klimchuk (2013). Figure 6.29 shows 25000 s of steady heating, where the channels, and their mean intensities are: 94 Å, 12 counts s<sup>-1</sup>; 131 Å, 49 counts s<sup>-1</sup>; 171 Å, 950 counts s<sup>-1</sup>; 193 Å, 2481 counts s<sup>-1</sup>; 211 Å, 1000 counts s<sup>-1</sup>; 335 Å, 136 counts s<sup>-1</sup>.

Figure 6.29 shows the light curves with Poisson noise (*top*), and the cross-correlation value as a function of offset (*bottom*). The cross-correlation value as a function of offset, appears as noise for the seven sets of channels that have been used. The result of this analysis is that the time-lags for these channel pairs are random and have extremely low values, with no discernible peaks. As Viall & Klimchuk (2016) note it is therefore a misconception that steady emission would result in a *zero* time-lag (e.g. Lionello *et al.*, 2016).

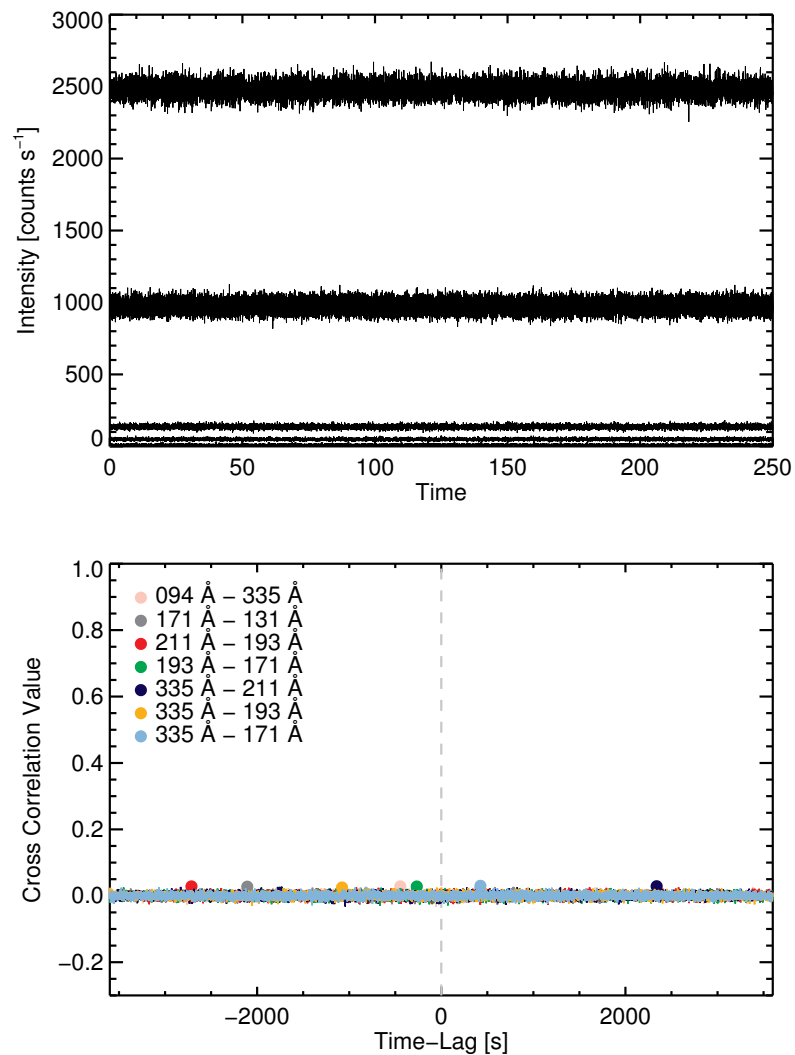


Figure 6.29: Light curves (*top*) and Cross-Correlation value as a function of temporal-offset (*bottom*) between synthetic “steady” light curves generated from mean intensities and a Poisson noise component. For each of the seven channel pairs, the cross-correlation value is consistently low ( $\leq 0.03$ ), with no clear increase in cross-correlation value over time. These steady light curves have various time-lag values that are not consistent with cooling (e.g. Figure 6.27).

## 6.5 Summary

This chapter has introduced time-lag analysis (Viall & Klimchuk, 2011, 2012) on a set of four pixels in the  $250 \times 250$  pixel region (centred on NOAA AR 11082), chosen to

include a pixel of diffuse emission (Pixel 1, similar in location to the pixel analysed in Viall & Klimchuk, 2012), and three additional pixels corresponding to an active region fan loop (Pixel 2), an active region core/loop (Pixel 3), and a pixel of fan loop footpoint emission (Pixel 4). This chapter first performed time-lag analysis on the pixel of diffuse emission before performing the same analysis on the additional three pixels. As discussed in this chapter, each pixel showed slightly different behaviour in temperature (See, Figure 6.17).

This chapter has, for the first time, introduced time-lag analysis on the isolated Fe XVIII component of the *SDO*/AIA 94 Å time series. This direct approach clarifies that the *SDO*/AIA 94 Å channel behaves as both a hot and cool channel, and that this leads the 94 Å – 335 Å pair to report both *positive* and *negative* time-lags; behaviour is confirmed by studying the *SDO*/AIA 94 Å (Fe XVIII) – 335 Å channel pair.

After studying the four individual pixels, time-lag maps were presented. Starting with the 94 Å – 335 Å, and 94 Å (Fe XVIII) – 335 Å channel pairs, it was clear that the 94 Å (Fe XVIII) – 335 Å time-lag map isolated cooling (from  $\sim 7$  MK; *positive* time-lags) observed in the core of the active region, while the 94 Å – 335 Å pair displayed both *positive* and *negative* time-lags. The remaining six channel pairs (that were presented in Viall & Klimchuk, 2012) were also presented, demonstrating widespread cooling.

In order to understand the results of time-lag analysis, Viall & Klimchuk (2013, 2015) performed EBTEL simulations of low-frequency nanoflare heating. These simulations were presented (as in Viall & Klimchuk, 2013, 2015) in preparation for analysis in Chapter 7, and from the coronal simulations a similar pattern of cooling (to that seen in EUV observations) was extracted. While these simulations did not agree (in terms of peak temperature) with the diffuse emission pixel earlier in the chapter, similar cooling patterns were observed. Furthermore, as EBTEL provides both the coronal and transition region DEMs for every time-step, this allows the transition region response to nanoflare heating to be studied. From the transition region DEMs, all time-lags were reported to be *zero*, and therefore Viall & Klimchuk (2015) associate in-phase behaviour (such as that seen in Pixel 4) to the transition region response to nanoflare heating, however this is one of many explanations for in-phase time series. Finally, we present the “steady heating” time series (first presented in Viall & Klimchuk, 2013) which were simulated by adding Poisson noise to a steady light curve. These time series resulted in random time-lag values at insignificant cross-correlation values ( $\leq 0.03$ ), indicating

that such heating is not responsible for the observed behaviour.

# Chapter 7

## EM Time Series Analysis

Following on from the work outlined previously in Viall & Klimchuk (2011, 2012, 2013, 2015, 2016) the same time-lag method could be applied to spectroscopic observations, or even be performed on the underlying temperature distribution itself. As the *SDO/AIA* response functions are multi-thermal, the true time-lag signature may be masked, and by recovering the time-lag from the evolution of the temperature distribution we attempt to recover the *true* time-lag signature.

As has been shown in Chapter 3, there are a number of methods available to recover the differential emission measure (DEM) with *SDO/AIA* data. Performing time-lag analysis on time series extracted from the DEM should allow us to study how the temperature distribution along the line-of-sight changes, rather than assuming that the variability observed in the *SDO/AIA* channels is from plasma at the peak temperature of the respective temperature response functions. As was seen for *SDO/AIA* 335 Å and 94 Å this is not always the case, and further interpretation is required.

Starting from the work outlined in Chapter 6, this chapter will first return to NOAA AR 11082 and the four previously discussed pixels using DEM( $T,t$ ) maps (where DEM( $T,t$ ) includes reference to an additional temporal component that is present for this analysis). These DEM( $T,t$ ) maps have been re-binned from 28 to six temperature bins chosen to coincide with the peak temperature response functions of *SDO/AIA* (within the temperature range where the DEM is recovered). The results of this analysis will be compared to those obtained from the *SDO/AIA* data alone in order to understand to what extent the time-lag signature is masked by the multi-thermal nature of *SDO/AIA* temperature response functions.

This chapter will also present time-lag analysis performed on both the observed and synthesised *SDO/AIA* EUV light curves from DEM( $T,t$ ) inversion. Large discrepancies between the temporal behaviour of the cross-correlation coefficient from the observed and synthesised *SDO/AIA* light curves will highlight areas where the DEM( $T,t$ ) inversion was poor over time, and when presented as time-lag maps, this method introduces a simple quality check on the inversion: if the DEM( $T,t$ ) can not return the original data then the quality of the DEM( $T,t$ ) at temperatures near that peak of the *SDO/AIA* channel have to be questioned.

Finally, this chapter will also present analysis of EUV light curves obtained from the EBTEL coronal and transition region simulations (§ 6.4). These will be presented for a number of reasons. Firstly, these simulations will allow the direct comparison of EM time-lag analysis, and *SDO/AIA* time-lag analysis simulated from the same underlying temperature distribution. Secondly, with the “ground-truth” DEM from EBTEL, these simulations provide an insight in to how well DEM inversion recovers the “ground-truth”. Finally, by combining the EBTEL simulations, EBTEL-synthesised *SDO/AIA* observations, the DEM( $T,t$ ) (through inversion), and DEM( $T,t$ )-synthesised *SDO/AIA* observations, it will be possible to understand how well DEM inversion captures the variability of the underlying DEM, but also recovers the original *SDO/AIA* observations.

## 7.1 Active Region DEM

Starting from the set of six observations shown in Figure 6.1, DEM maps were created for each pixel ( $250 \times 250$ ) and each time-step in the 12-hour time series (1440 time-steps; 30 s cadence). These DEM maps were initially calculated between  $\log_{10}T = 5.6 - 7.0$  K at a resolution of  $\Delta \log_{10}T = 0.05$ , and the DEM maps have been subsequently re-binned in to six temperature bins that have been chosen to correspond to the peak sensitivities of the *SDO/AIA* channels over  $\log_{10}T = 5.6 - 7.0$  K (Figure 7.1). This is done in order to provide a comparison to the original *SDO/AIA* time-lags, and this additionally increases the signal to noise. Figure 7.1 shows the normalised and  $\log_{10}$ -scaled temperature response functions for the six optically-thin *SDO/AIA* filter channels. The six temperature bins (**A** – **F**) were chosen to approximately correspond to the peaks of the *SDO/AIA* temperature response functions (within the limitations

of the  $\Delta\log_{10}T = 0.05$  binning). The boundaries between two temperature bins were chosen to correspond to locations in temperature where the normalised temperature response functions are equal. The final choice of temperature bins are highlighted in alternating shades of grey. These temperature bins are approximately: **A**, 131 Å,  $\log_{10}T = 5.6 - 5.8$  K; **B**, 171 Å,  $\log_{10}T = 5.8 - 6.1$  K; **C**, 193 Å,  $\log_{10}T = 6.1 - 6.2$  K; **D**, 211 Å,  $\log_{10}T = 6.2 - 6.3$  K; **E**, 335 Å,  $\log_{10}T = 6.3 - 6.7$  K; **F**, 94 Å,  $\log_{10}T = 6.7 - 7.0$  K, and are the basis of EM time series.

The *SDO/AIA* observations as initially presented in Figure 6.1 are shown in Figure 7.2, and the corresponding DEM (temperature) maps obtained with the regularised inversion code (Hannah & Kontar, 2012, § 3.4.1) are shown in Figure 7.3. Presenting the original *SDO/AIA* observations together with the six DEM maps chosen at temperatures that coincide with the peak temperature response functions (Figure 7.2, Figure 7.3) demonstrates how the features observed in *SDO/AIA* observations are generally reconstructed by the equivalent DEM bins. This highlights that the majority of emission observed in these channels is consistent with plasma at temperatures near the peak of the temperature response functions. By taking the DEM( $T$ ) ( $\log_{10}T = 5.6 - 7.0$ ,  $\Delta\log_{10}T = 0.05$ ) for every pixel and rebinning the temperature distribution in to six temperature bins (**A** - **F**) generates six temperature maps as in Figure 7.3. Performing this for every time step,  $t$ , returns the time series in temperature for every pixel: *the EM time series*.

Importantly, black pixels in the DEM maps represent solutions of the DEM where the DEM in that temperature bin is  $\leq 0$ . The majority of these are confined to locations outwith the active region core, however there are notably a few such values near Pixel 3 in temperature bin **B** (*top, middle*). This behaviour is not however limited to regularised inversion, and similar features appear when performing identical DEM inversion with Basis Pursuit (Cheung *et al.*, 2015), as will be discussed in § 7.3.2.

### 7.1.1 EM (Temperature) Time-lags

Before considering individual pixels in the next section, Figure 7.4 shows the original *SDO/AIA* time-lag map for the 193 Å – 171 Å channel pair (*left*), and the EM time-lag map (for the equivalent **B** - **C** channel pair), *right*. In this Figure, all pixels where a single  $\leq 0$  value was observed in one of DEM bins **B** and **C** (those that correspond to the 193 Å – 171 Å channel pair; cf. Figure 7.2) in the 12-hour time series are

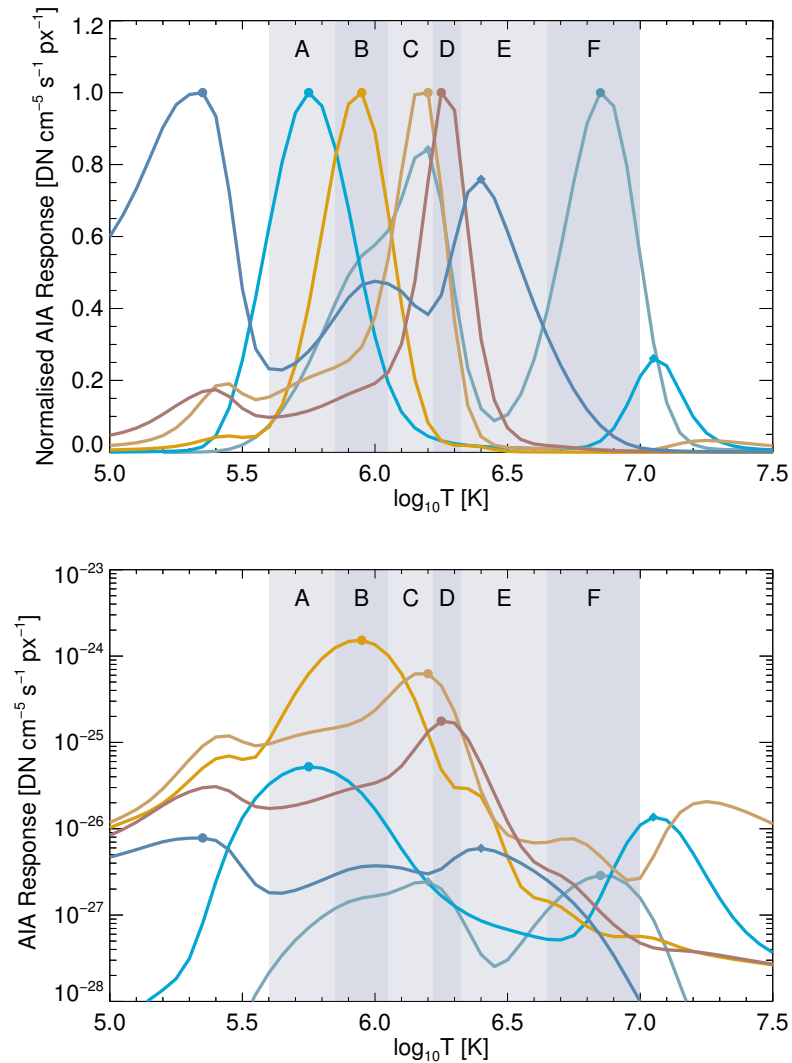


Figure 7.1: *SDO/AIA* temperature response functions for the six coronal (EUV) channels shown in Figure 6.2. The temperature response functions are shown here as both normalised (*top*), and plotted on a  $\log_{10}$ -scale (*bottom*) to highlight both the peak temperature sensitivity and the multi-thermal nature of these response functions. The six temperature bins corresponding to the peaks of each channel are additionally highlighted as **A** – **F**.

automatically removed from this analysis, and are shown as a red hatched region (in both panels). This is a precautionary step taken to eliminate the possibility of the presence of co-temporal *zeros* which would either lead to in-phase EM light curves (and in-phase synthesised *SDO/AIA* time series), or out-of-phase *zeros* that could lead

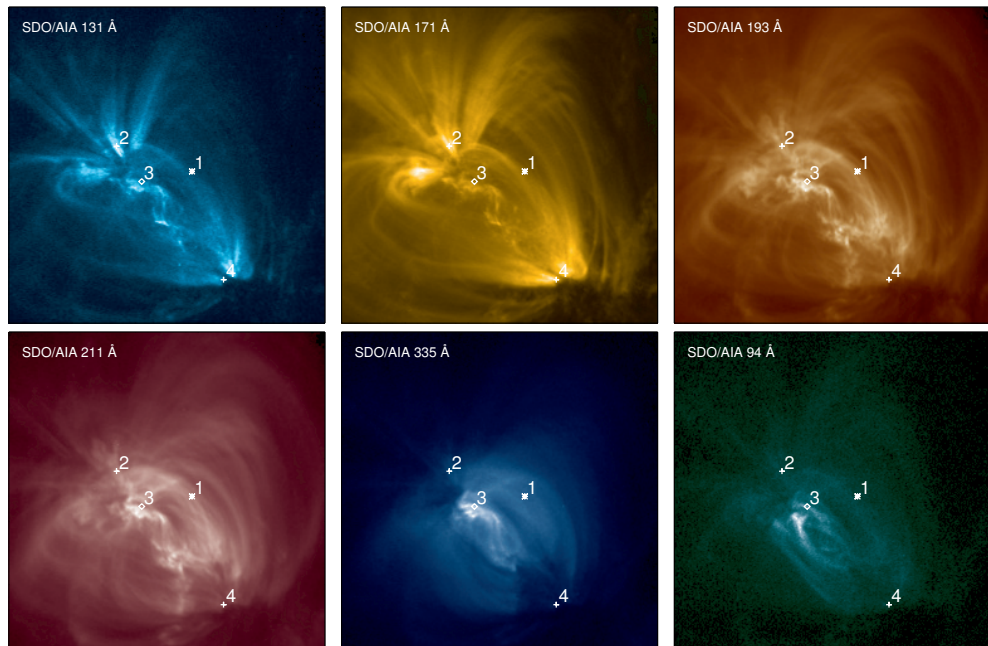


Figure 7.2: NOAA AR 11082 in six *SDO/AIA* channels displayed in order of temperature bins (**A** – **F**). From *left to right, top to bottom*, these channels are 131 Å, 171 Å, 193 Å, 211 Å, 335 Å, 94 Å.

to (false) non-*zero* time-lag signatures. In practice it may be reasonable to interpolate over these *zeros* (as will be discussed for Pixel 4 in § 7.1.5), but these pixels are generally excluded as they tend to not interfere with the analysis of the four pixels in this chapter. With these regions excluded there are a number of noticeable similarities and differences between the *SDO/AIA* time-lag and the EM time-lags. Firstly, where the *SDO/AIA* time-lag values are not equal to *zero*, EM time-lag analysis generally reports a similar time-lag indicating that the *SDO/AIA* time-lags are the result of plasma cooling from  $T_{peak}^{193} - T_{peak}^{171}$ . Secondly, EM time-lag analysis appears to assign non-*zero* time-lags to a large number of the *zero* values (shown as olive green), and this will be discussed later. Furthermore, it is also not clear how well the  $DEM(T,t)$  used to generate the EM time-lags can recover the input data for 171 Å, and 193 Å, and therefore later Figures will include the *SDO/AIA* (observed and DEM-synthesised) time-lag maps in comparison to the EM time-lag maps. These are shown because if the  $DEM(T,t)$  cannot recover the original time series then the  $DEM(T,t)$  will not be representative of the underlying thermal behaviour.

For Figure 7.4, this choice of *SDO/AIA* filter channels was made as both 171 Å and

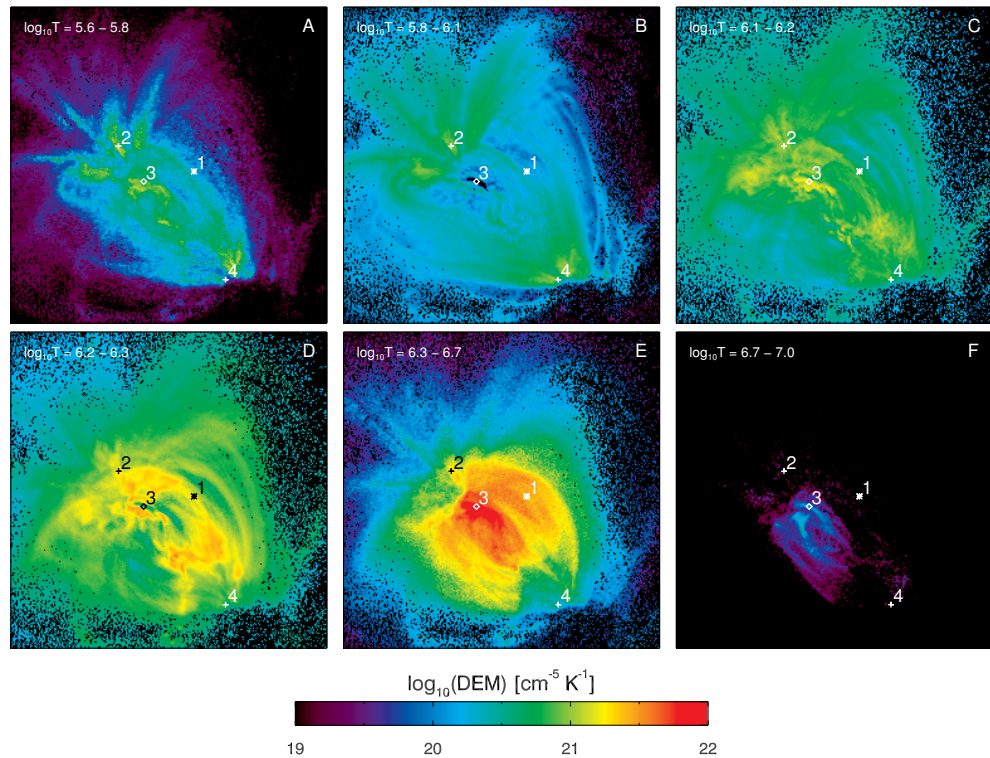


Figure 7.3: Regularised Inversion DEM (temperature) maps re-binned from 28 temperature bins in to six temperature bins chosen to coincide with the peak temperature response functions of the *SDO/AIA* response functions: **A**,  $131 \text{ \AA}$ ,  $\log_{10}T = 5.6 - 5.8$  K; **B**,  $171 \text{ \AA}$ ,  $\log_{10}T = 5.8 - 6.1$  K; **C**,  $193 \text{ \AA}$ ,  $\log_{10}T = 6.1 - 6.2$  K; **D**,  $211 \text{ \AA}$ ,  $\log_{10}T = 6.2 - 6.3$  K; **E**,  $335 \text{ \AA}$ ,  $\log_{10}T = 6.3 - 6.7$  K; **F**,  $94 \text{ \AA}$ ,  $\log_{10}T = 6.7 - 7.0$  K.

$193 \text{ \AA}$  are relatively isothermal channels with temperature peaks separated by  $\log_{10}T$   $0.4 - 0.5$  K (cf. Figure 7.1). Additionally, Figure 6.23 shows a wide range of time-lag values at a variety of cross-correlation values which allows us to test on a wide variety of situations.

As has been shown earlier in Chapter 3 (Figure 3.5), this temperature range is also well constrained according to the  $\mathbf{R}_\lambda \mathbf{K}$  matrix. It is therefore expected that the results from EM time-lag analysis, and *SDO/AIA* time-lag analysis would lead to similar results, which simplifies the initial investigation presented here.

The following sections will analyse the four pixels described in Chapter 6 in order to further investigate the results of EM time-lag analysis for this channel pair. An initial discussion of these first results will follow, and a brief overview of further work

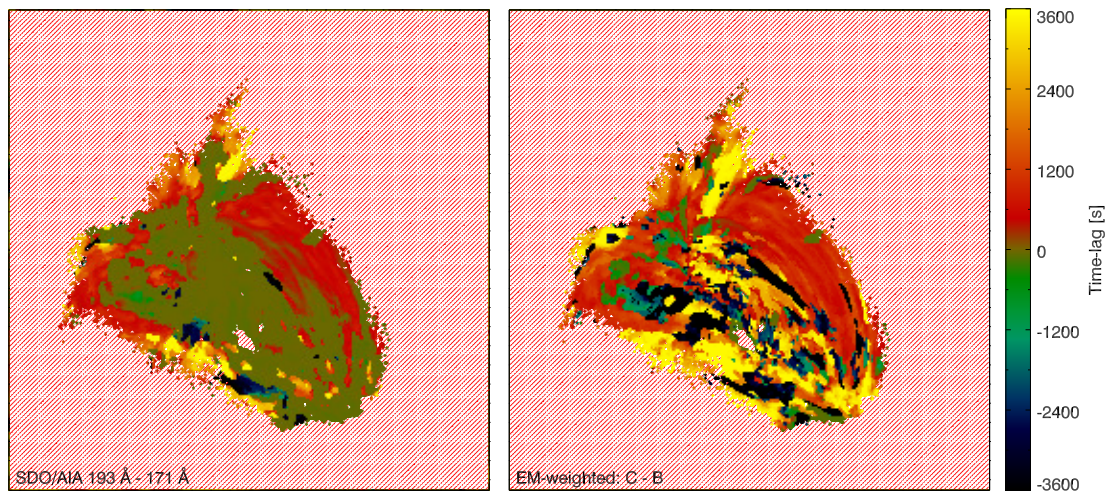


Figure 7.4: *SDO/AIA* time-lag maps for  $193 \text{ \AA} - 171 \text{ \AA}$  (*left*), and the EM time-lag map for the corresponding **B** - **C** channel pair (*right*). The red shaded region excludes pixels where the DEM in both temperature bins (**B**, **C**, those that are located at the peak of the  $171 \text{ \AA}$ , and  $193 \text{ \AA}$  temperature response functions) were equal to *zero* at  $\geq 1$  time-steps. These pixels are excluded as *zeros* in the time series can introduce false in-phase or time-lag signatures.

will be presented.

### 7.1.2 Diffuse Emission Pixel; Pixel 1

For the diffuse pixel described in § 6.2.2 (Pixel 1), Figure 7.5 (*left*) shows the EUV *SDO/AIA* light curves for this pixel as shown previously in Figure 6.4 (black), with the addition of the DEM( $T,t$ )-synthesised *SDO/AIA* light curves overplotted in red. The light curves, as in Figure 6.4, have been offset in intensity to avoid overlap. From *top to bottom*, the light curves in Figure 7.5 are 94 Å; 335 Å; 211 Å; 193 Å; 171 Å; and 131 Å, and it is clear that the variability is generally well-preserved through DEM inversion. This statement rings particularly true for 171 Å, 193 Å, and 211 Å which are inferred from a well-constrained region of temperature-space (see Figure 3.5). The same statement could be extended to 131 Å, although while the general trends are preserved, DEM( $T,t$ ) is unable to fully preserve all variability, especially over short time-scales. For the 94 Å, and 335 Å light curves, the DEM( $T,t$ ) provides noise suppression and amplification. For the former channel, the combination of low count rates, and the bi-modal nature of *SDO/AIA* 94 Å temperature response function leads to the high-temperature component of the DEM being poorly constrained, and results in the synthesised 94 Å intensity values to have significant values of uncertainty. Furthermore, due to the broad temperature response function of 335 Å, perfect reconstruction (without needing to consider uncertainties propagated from DEM analysis) of the original *SDO/AIA* time series would heavily rely on the DEM( $T,t$ ) being well-constrained (over both  $T$  and  $t$ ). To provide context to the rest of this chapter, Figure 7.5 (*right*) plots the equivalent EM time series for temperature bins **A** - **F**. As discussed for Figure 7.3, for each time-step the DEM was re-binning in to six temperature bins **A** - **F** chosen to coincide with the peaks of the *SDO/AIA* temperature response functions over the temperature range used for DEM inversion. These six time series are the EM time series and represent variability in temperature. In this Figure, similar variability exists in both the *SDO/AIA* and EM time series, which is generally expected as the majority of emission for a given *SDO/AIA* channel is likely to be from plasma at the peak of the temperature response function, however, we are interested in understanding if the time-lags between temperature bins is different to the time-lags from the *SDO/AIA* channels.

The quality at which the original light curves can be reconstructed can be interpreted as an indicator of the quality of the DEM( $T,t$ ) inversion: if for a given set of *SDO/AIA* observations DEM( $T,t$ ) cannot reproduce those same observations (with-

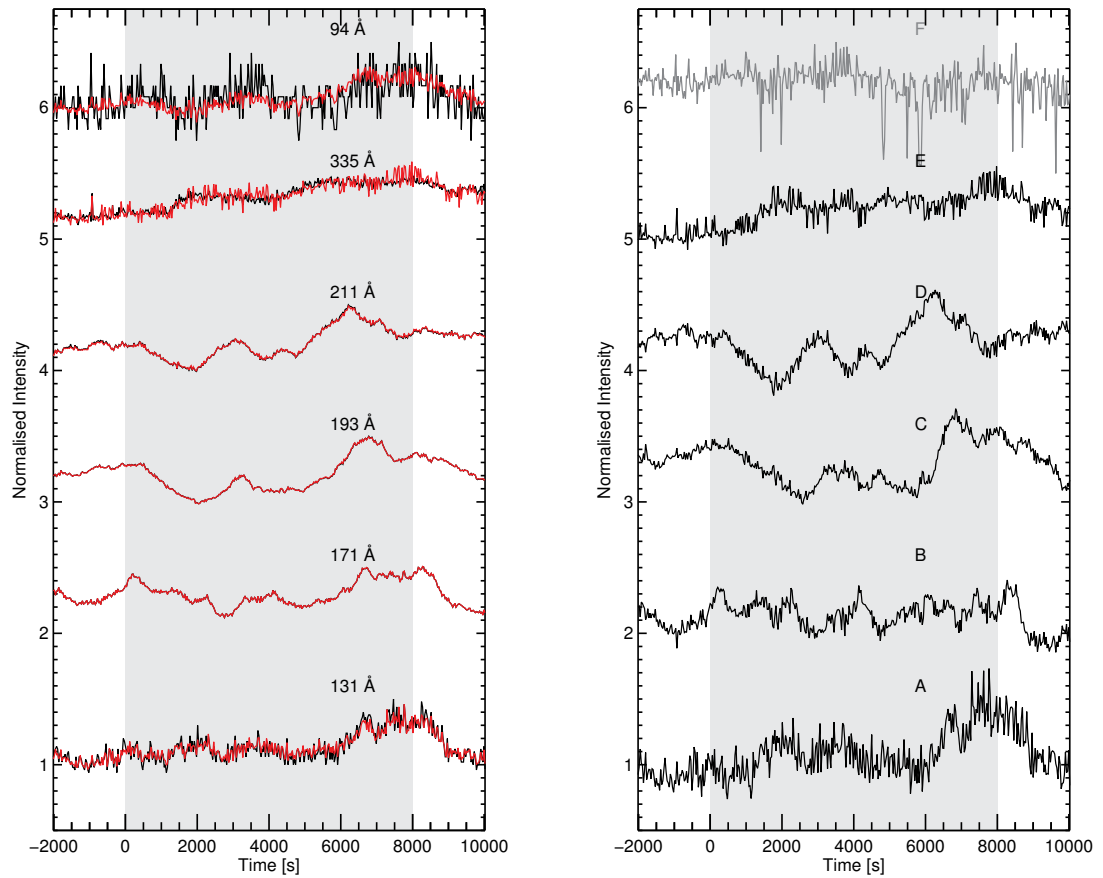


Figure 7.5: *Left*: Light curves of a pixel of diffuse emission (Pixel 1; § 6.2.2). Top to Bottom these light curves are 94 Å; 335 Å; 211 Å; 193 Å; 171 Å; and 131 Å, where the original light curves (as in Figure 6.4) are shown in black, and the synthesised *SDO/AIA* observations from DEM( $T,t$ ) inversion are shown in red. The two-hour region used from time-lag and EM temperature analysis is shaded grey, and includes an additional  $\pm 2000$  s for context. *Right*: As *left*, but for the EM time series. These are plotted alphabetically from *bottom to top* in order to coincide with the equivalent *SDO/AIA* time series (*left*). The corresponding temperature range that each letter corresponds to (in comparison to *SDO/AIA* channels) can be found in Figure 7.1. Additionally, the temperature bin **F**, which corresponds to the  $\sim 7$  MK peak of 94 Å is scaled alternatively between 0 and 1 due to the large range of values.

out considering uncertainties propagated from DEM inversion), then the quality of the DEM( $T,t$ ) reconstruction in that region of temperature space has to be questioned,

and the EM time-lag would be uninterpretable. This is especially true when the DEMs and observations are used without uncertainties, as in the case of time-lag analysis. From Figure 7.5 the *SDO/AIA* variability is generally best preserved in 171 Å, 193 Å, and 211 Å, which is expected as the DEM is well-constrained over this temperature range.

An additional quality check for DEM(T,t) reconstruction can be visualised by plotting the cross-correlation value as a function of temporal offset for both the original *SDO/AIA* observations, as well as those synthesised from DEM(T,t) inversion (those plotted in red in Figure 7.5). Figure 7.6 (top) therefore shows the cross-correlation value for the same set of channels as shown in Figure 6.5. Here, the cross-correlation value as a function of offset for the original *SDO/AIA* observations are plotted with solid lines (and filled circles representing the time-lags), and similarly, cross-correlation value as a function of offset is plotted for the synthesised *SDO/AIA* observations are shown as dotted lines, with the time-lag value represented as a filled diamond of the same colour.

In Figure 7.6 (top) it is clear that for the 211 Å – 193 Å (1.8 – 1.6 MK), 193 Å – 171 Å (1.6–0.9 MK), and 171 Å – 131 Å (0.9–0.6 MK) pairs, the observed (*SDO/AIA*) time-lags—those obtained from *SDO/AIA* observations—are nearly identical to the time-lags obtained after performing DEM(T,t) inversion, and synthesising *SDO/AIA* observations. While for the 171 Å – 131 Å pair the behaviour is similar, and the cross-correlation peaks at the same value of offset for both the observed and synthesised *SDO/AIA* observations, there are differences which are highlighted when plotting cross-correlation value as a function of temporal-offset. For the other channels that are plotted in this Figure, the 335 Å – 211 Å (2.5 – 1.8 MK), 335 Å – 193 Å (2.5 – 1.6 MK), and 335 Å – 171 Å (2.5 – 0.9 MK) pairs the time-lag is located at similar values of offset, however the cross-correlation is much lower. This is likely an artefact that is the result of noise being injected in to the synthesised *SDO/AIA* 335 Å time series, as the three (previously discussed) channel pairs that include combinations of 131 Å, 171 Å, and 193 Å are well reconstructed. Similarly, for the 94 Å – 335 Å pair, the cross-correlation over time is significantly different. A sharp peak is observed at a time-lag of *zero* and this appears to indicate that there is an additional noise component that contributes to both time series, and leads them to be in-phase.

In addition to the observed and DEM-synthesised *SDO/AIA* time-lags, Figure 7.6

(*bottom*) shows the time-lags for EM channel pairs that correspond to the three *SDO/AIA* channel pairs that were well recovered in the top panel of Figure 7.6. These channel pairs are **B - A**, **D - C**, **C - B**, and correspond to  $171 \text{ \AA} - 131 \text{ \AA}$ ,  $211 \text{ \AA} - 193 \text{ \AA}$ , and  $193 \text{ \AA} - 171 \text{ \AA}$ . EM time series are calculated by performing DEM inversion and re-binning in to six temperature bins (**A - F**, see Figure 7.3). By performing this at every time-step, this returns a time series in temperature (weighted by the Emission Measure). For EM time-lag analysis, the **D - C** pair is highly correlated ( $> 0.8$ ) which sharply falls off at larger offsets. This indicates that this time-lag is significant. Comparing this to the  $211 \text{ \AA} - 193 \text{ \AA}$  channel pair, there is a slight positive shift observed in the time-lag (which will be investigated later). For the other EM channel pairs the cross-correlation as a value of offset is relatively low ( $< 0.3$ ) and these two channel pairs are not significantly peaked at a single value and this suggests that these EM time series are not significantly correlated, however the **C - B** pair reports a time-lag similar to *SDO/AIA* time-lag analysis.

By simply comparing time-lags for the original *SDO/AIA* observations and those synthesised from DEM( $T,t$ ) inversion, Figure 7.6 demonstrates that this provides a quick indication of the quality of DEM( $T,t$ ) inversion. Importantly however, the method of comparing time-lags (when plotted as time-lag maps) for the original and synthesised observations does not take the value of cross-correlation for the time-lag in to consideration. The cross-correlation value could be low, and not significant compared to the cross-correlation value at other offsets (as for two of the EM channel pairs in Figure 7.6, *bottom*). From the behaviour observed in Figures 7.5 and Figure 7.6 the rest of this chapter will concentrate on the  $193 \text{ \AA} - 171 \text{ \AA}$  pair and the corresponding (**C - B**) EM channel pair to understand if *SDO/AIA* time-lag analysis is masking the true time-lag signature. Furthermore, this region is observed (in Figure 6.23) to have a variety of *SDO/AIA* time-lag values, over a large range of cross-correlation values. This allows us to compare EM time-lag analysis over a large variety of possible situations.

Figure 7.7 shows the observed *SDO/AIA*  $193 \text{ \AA} - 171 \text{ \AA}$  time-lag map including a rectangular  $100 \times 50$  pixel cutout chosen to encompass the pixel of diffuse emission and similar neighbouring pixels to understand how well DEM inversion can recover the underlying DEM of the *SDO/AIA* data, and by concentrating on a region this allows a more general interpretation of the results to be made. As discussed in § 6.3.1, this Figure (now shown on an alternative colour table) shows that the majority of the

pixels display *positive* time-lags (shown as yellows, and greens); followed by time-lags of *zero*, white; and few *negative* time lags (shown in shades of blue). This behaviour indicates that 193 Å precedes 171 Å and is an indicator material cooling from  $\sim 2.5 \rightarrow \sim 1.6$  MK.

For the rectangular cutout around the diffuse emission pixel, that is shown in Figure 7.7, Figure 7.8 shows the time-lag maps for 193 Å – 171 Å for *SDO/AIA* (*left*), EM time-lag analysis (*middle*), and for the DEM-synthesised 193 Å – 171 Å channel pair (*right*). Figure 7.8 shows that the time-lags observed from the original *SDO/AIA* data (*left*), and the synthesised *SDO/AIA* data (*right*) are nearly identical throughout this region. As seen in Figure 7.6, this provides a good indication of the quality of DEM(T,t) reconstruction (DEM(T,t) can recover the observed data) and provides some reassurance that the EM temperature bins at these temperatures are reliable. There are however a number of differences between these two *SDO/AIA* time-lag maps. The first is the presence of *zero* time-lags along the top edge (solar North West) of this cutout region for the DEM(T,t)-synthesised *SDO/AIA* observations (Figure 7.8, *right*). In comparison, the original *SDO/AIA* observations (*left*) consist of mainly *positive* and *zero* time-lag values in that portion of the image.

In order to understand these discrepancies between the observed and DEM-synthesised *SDO/AIA* observations, Figure 7.9 shows these same time-lag maps (as in Figure 7.8), but excluding pixels where DEM(T,t) inversion returns at least one *zero* in both temperature bins (**B**, **C**; those chosen to coincide with the peak of the 171 Å, and 193 Å temperature response functions) during the 12 hours of observation. The presence of co-existing *zeros* in these time series, either co-temporally, or offset in time can lead to false time-lags. It is therefore only the pixels where both the observed, and synthesised time-lags agree that EM time-lag analysis can be easily interpreted. Supplementary to Figure 7.8, Figure 7.9 therefore excludes the regions where there are *zero* values in both temperature bins, and this leads to better agreement between the observed and synthesised time-lags.

Figure 7.9 shows the same information as Figure 7.8 with the locations of *zeros* in both EM time series hatched in red. The middle panel in Figure 7.9 shows the EM time-lag map for the rectangular region in addition to the observed and synthesised *SDO/AIA* 193 Å – 171 Å time-lags. This EM time-lag map provides similar time-lag values where the *SDO/AIA* time-lag map is non-*zero*, and EM time-lag analysis

appears to assign non-zero time-lags to the *zeros* that were reported by *SDO/AIA* time-lag analysis within this rectangular region. These values in EM time-lag analysis are not dissimilar to adjacent non-*zero* values from *SDO/AIA* time-lag analysis which may suggest that the *zero* time-lags observed by Viall & Klimchuk (2012) are the result of the true time-lag signature being masked by the *SDO/AIA* response (but in general, the *SDO/AIA* and EM time-lags agree as one would expect).

Furthermore, in Figure 7.9 (and also seen in Figure 7.8), all three panels contain a ( $8 \times 12$  pixel) region of *zero* time-lags near the centre of the image, which is highlighted here by a black contour that was extracted from the EM time-lag map (*middle*). Interestingly, this region of *zero* time-lags is not assigned non-zero values during EM time-lag analysis indicating that this region is the result of in-phase time series (*SDO/AIA* and EM).

To further investigate the presence of this region of *zero* time-lags, Figure 7.10 shows the observations of the rectangular cutout for the beginning of the two-hour time series (shown in Figure 7.5;  $t = 0$  s). These are shown for both *SDO/AIA* 171 Å, and 193 Å (those channels used to create the *SDO/AIA* time-lag maps in Figure 7.8, and Figure 7.9), including the contour highlighting this region (as in Figure 7.9). From these images a clear co-temporal brightening is observed in this region (brightening in 171 Å and 193 Å in-phase), and this behaviour is further highlighted in Figure 7.11.

Figure 7.11 (*left*) shows the *SDO/AIA* time series as in Figure 7.5 where the original *SDO/AIA* observations are plot in black, and the DEM-synthesised observations are overplotted in red. The cross-correlation value as a function of offset is shown for the three channel pairs that were well recovered for Pixel 1 (*top right*), and for the equivalent EM pairs (*bottom right*), as was described in Figure 7.6. Figure 7.11 (*left*) shows that the brightening is observed in all channels at  $t \sim 0$  s, and this behaviour is generally well recovered through DEM inversion for all channels. The time-lags for the observed and DEM-synthesised *SDO/AIA* channel pairs are therefore in good agreement (solid and dotted, Figure 7.11, *top right*). As discussed in § 6.4.2, a *zero* time-lag is assumed to be the transition region response to heating and from these observations it is clear that this region is associated with a transition region brightening where each channel responding in phase. Importantly, the in-phase nature of these light curves is well-preserved through DEM(T,t) inversion (the DEM(T) bins rise and fall in-phase over time, as seen in Figure 7.11, *bottom right*).

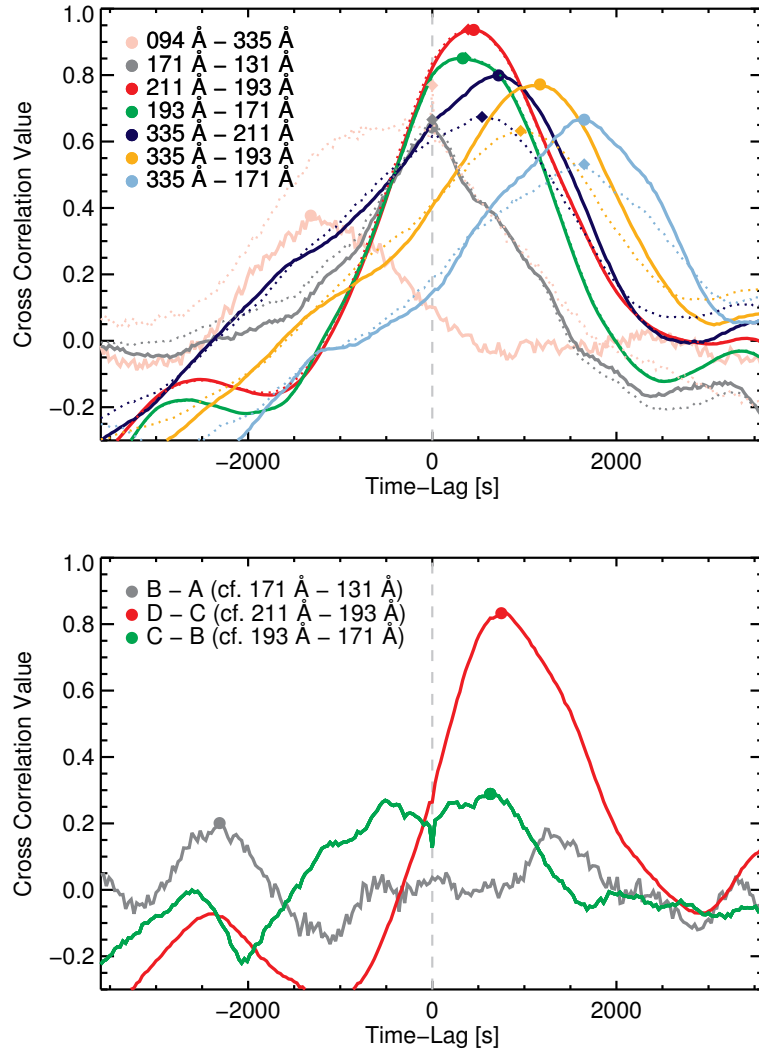


Figure 7.6: *Top*: Cross-correlation value as a function of temporal offset between the same seven channel pairs shown in Figure 6.5. The original cross-correlation value as a function of offset from Figure 6.5 (those for the *SDO/AIA* data) are shown as solid lines, and the cross-correlation value as a function of offset for the DEM-synthesised *SDO/AIA* observations from DEM( $T,t$ ) inversion are shown as dotted lines. As in previous Figures, a positive time-lag indicates that the second channel pair lags the first, and a negative time-lag indicates the first channel lags the second. For each channel pair the time-lag is defined as the point at which the cross-correlation value is maximum. *Bottom*: As *top* but for the respective EM temperature bins that correspond to the peak temperature response functions where the time-lags are well-recovered from DEM inversion (dotted and solid lines agree, *top*).

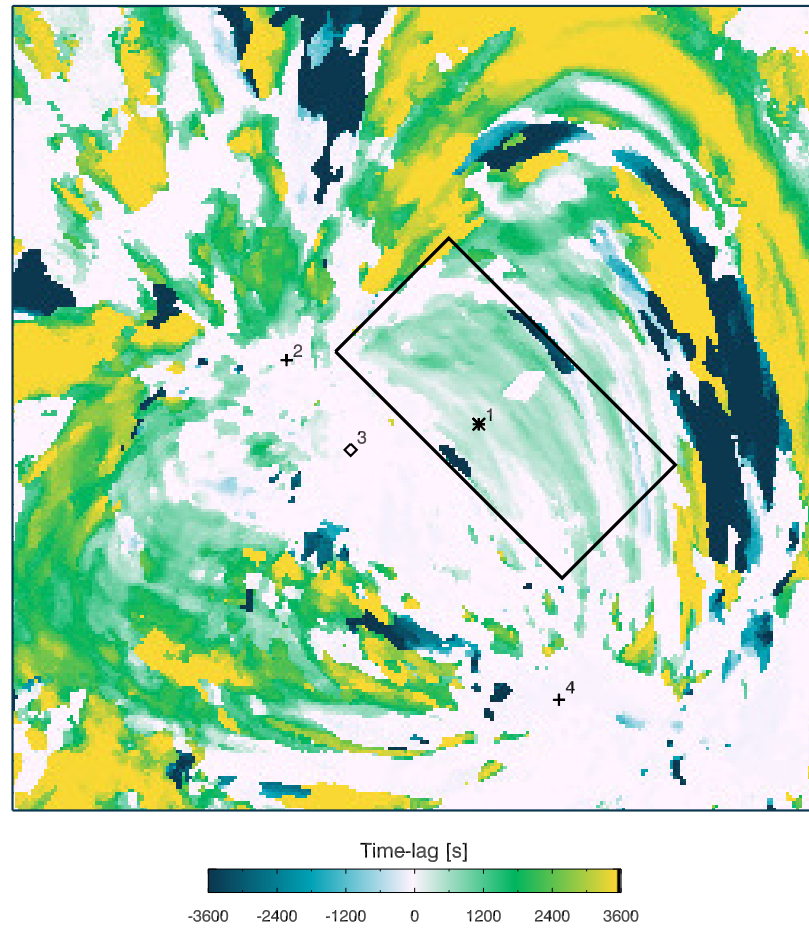


Figure 7.7:  $250 \times 250$  pixel time-lag map for the observed *SDO/AIA*  $193 \text{ \AA} - 171 \text{ \AA}$  channel pair with the four pixels highlighted, as in Figure 6.23, but plotted on alternative colour table. The rectangular cutout region that encompasses the pixel of diffuse emission is presented in later Figures.

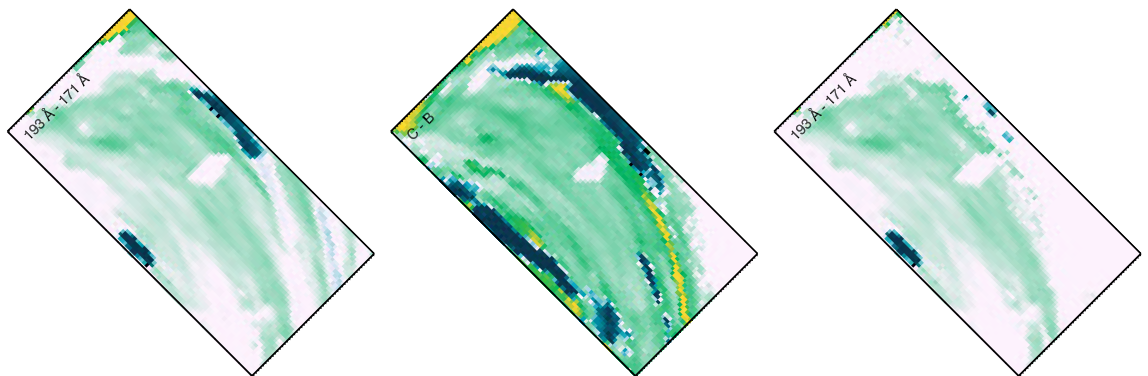


Figure 7.8: Time-lag maps for the observed  $193 \text{ \AA} - 171 \text{ \AA}$  channel pair, the corresponding EM channel pair (**C - B**), and the  $193 \text{ \AA} - 171 \text{ \AA}$  channel pair recovered through DEM inversion are shown *left to right*. There are shown for the  $100 \times 50$  pixel cutout chosen to include the the pixel of diffuse emission studied in § 6.2.2 (and [Viall & Klimchuk, 2012](#)) for all pixels regardless of quality. Regions where the observed and DEM-synthesised *SDO/AIA* time-lags agree indicate locations where the DEM inversion is reliable, and the EM time-lags are interpretable.

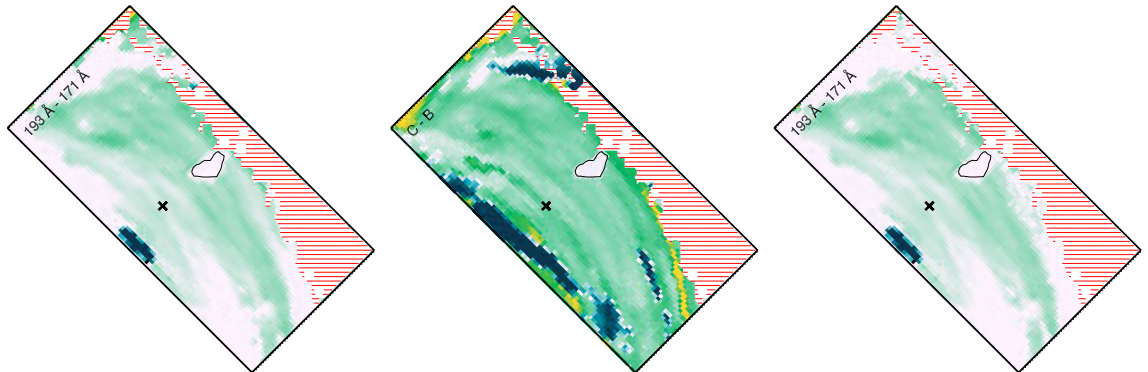


Figure 7.9: Time-lag analysis for the observed  $193 \text{ \AA} - 171 \text{ \AA}$  channel pair, the corresponding EM channel pair (**C - B**), and the  $193 \text{ \AA} - 171 \text{ \AA}$  channel pair recovered through DEM inversion (*left to right*). These are shown for the  $100 \times 50$  pixel cutout chosen to include the the pixel of diffuse emission studied in § 6.2.2 (and similar to that analysed in Viall & Klimchuk, 2012), as shown in Figure 7.8. This Figure includes a red hatched region indicating where at least one DEM bin in each time series used for EM time-lag analysis (middle panel) were found to be *zero*, and includes a contour around the persistent  $8 \times 12$  pixel region where time-lags are *zero*, extracted from the EM time-lag map.

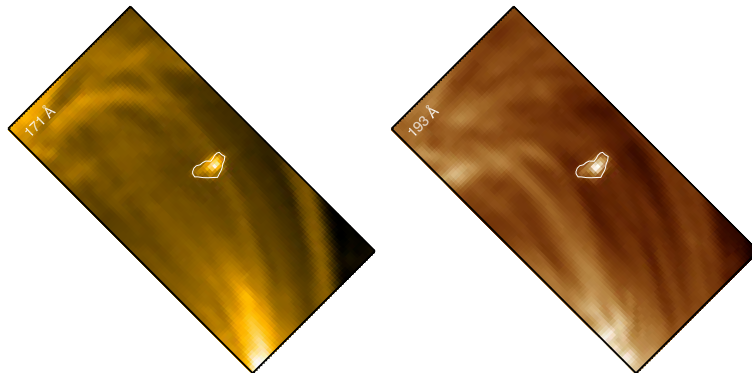


Figure 7.10: *SDO/AIA* observations at the start of the two-hour time series for the rectangular cutout region (shown in Figure 7.7) for  $171 \text{ \AA}$  (*left*), and  $193 \text{ \AA}$  (*right*). A co-temporal (in-phase) brightening is observed in a region that is spatially consistent with the region of *zero* time-lag in Figure 7.8, and Figure 7.9.

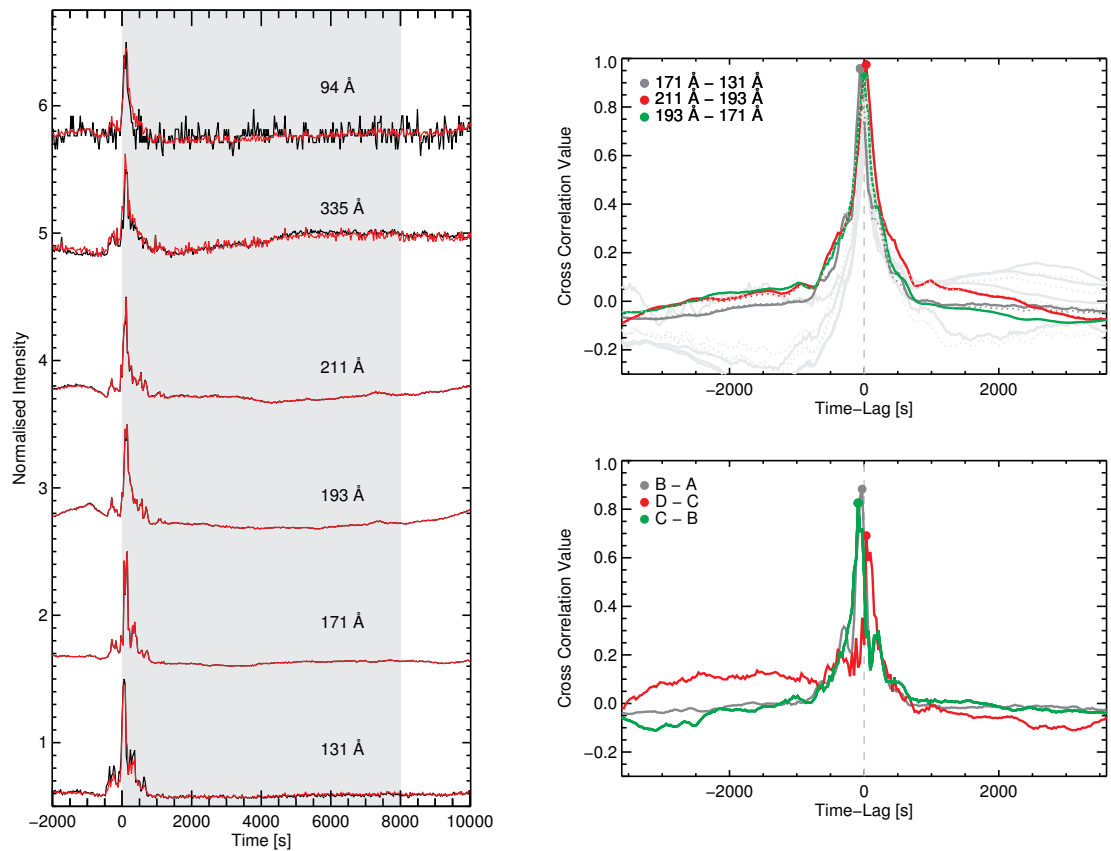


Figure 7.11: *Left*: Light curves of a pixel from the  $8 \times 12$  pixel region that is seen to have *zero* time-lags in both *SDO/AIA* and EM time-lag maps (Figure 7.9). The observed *SDO/AIA* data is shown in black, and the DEM-synthesised *SDO/AIA* time series are overplotted in red. *Top Right*: Cross-correlation value as a function of offset for the three channel pairs that are well-reconstructed in Figure 7.6. This is plotted for the observed *SDO/AIA* data (solid lines, filled circle representing the time-lag), and the DEM-synthesised *SDO/AIA* data (dotted lines, filled diamond representing the time-lag). *Bottom Right*: Cross-correlation value as a function of offset for the EM time series that correspond to the *SDO/AIA* channel pairs (*top right*). For these three channel pairs the *zero* time-lags seen in *SDO/AIA* time-lag analysis *top right* are reproduced in EM time-lag analysis *bottom right*.

### 7.1.3 Active Region Fan Loop; Pixel 2

As for the the diffuse pixel described in the previous section, this section concentrates on the pixel of fan loop emission (Pixel 2, § 6.2.3).

Figure 7.12 shows the *SDO/AIA* light curves (black) with the addition of the DEM(T,t)-synthesised *SDO/AIA* light curves overplotted in red. These light curves, as in previous Figures, have been offset in intensity to avoid overlap of the light curves, and from top to bottom these light curves are 94 Å; 335 Å; 211 Å; 193 Å; 171 Å; and 131 Å. From this Figure it is clear that the variability is well-preserved through DEM(T,t) inversion with the same qualities as previously shown for Pixel 1: 171 Å, 193 Å, and 211 Å are generally well-reconstructed, while 131 Å, 94 Å, and 335 Å preserved the general variability, however there are differences on short-timescales. For this pixel the recovery of 335 Å is significantly worse. While there is general agreement between the original and synthesised observations over the 12,000 s shown in Figure 7.12, between 500 – 3500 s, DEM(T,t) inversion does not preserve the long-scale variability, and from 6000 s onwards, the two time series start diverging. The difference between these light curves should lead to a difference in cross-correlation value over time for the 335 Å time-lag pairs (335 Å – 211 Å (2.5 – 1.8 MK), 335 Å – 193 Å (2.5 – 1.6 MK), 335 Å – 171 Å (2.5 – 0.9 MK), where the second channels in these pairs are observed to be well recovered through DEM(T,t) inversion.

Figure 7.13 shows the cross-correlation for the same set of channels as shown in Figure 6.10. Again, the cross-correlation value as a function of offset for the observed *SDO/AIA* channel pairs are solid lines (filled circles represent the time-lag), and the same information is plotted for the DEM-synthesised *SDO/AIA* observations as dotted lines (filled diamond representing the time-lag). As expected from Figure 7.12, Figure 7.13 (top) shows that the observed and synthesised *SDO/AIA* 211 Å – 193 Å (1.8 – 1.6 MK), 193 Å – 171 Å (1.6 – 0.9 MK), 171 Å – 131 Å (0.9 – 0.6 MK) channel pairs strongly agree, as was observed for the pixel of diffuse emission. The 335 Å channel pairs (335 Å – 211 Å, 335 Å – 193 Å, and 335 Å – 171 Å) vary significantly as was hypothesised earlier. This behaviour directly highlights that the reconstruction of the *SDO/AIA* 335 Å time series was poor. For the 335 Å – 171 Å channel pair in particular, disregarding the cross-correlation value (which is not highlighted when presenting time-lag maps), the offset between the original *SDO/AIA* observa-

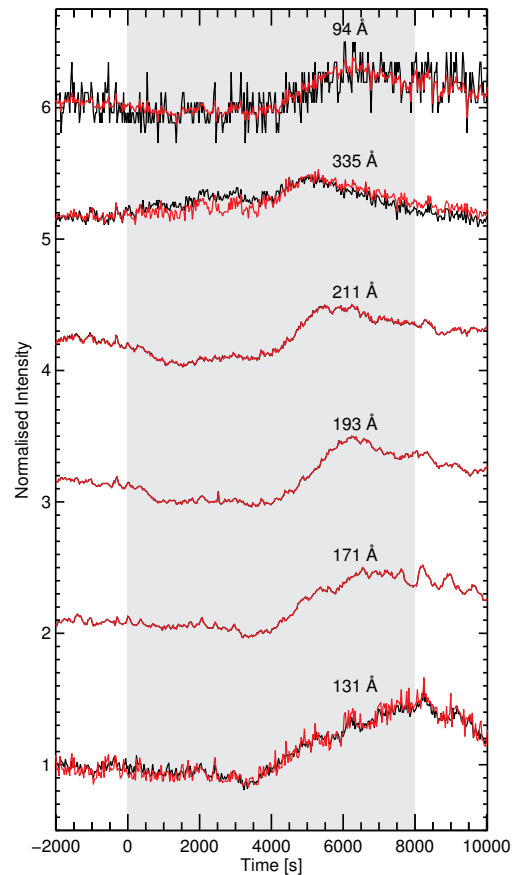


Figure 7.12: Light curves of a pixel of fan loop emission (Pixel 2; § 6.2.3). Top to Bottom these light curves are 94 Å; 335 Å; 211 Å; 193 Å; 171 Å; and 131 Å, where the original light curves (as in Figure 6.9) are shown in black, with the synthesised *SDO/AIA* observations from DEM( $T,t$ ) inversion are shown red. The two-hour region studied earlier is shaded grey with the additional  $\pm 2000$  s.

tions and DEM( $T,t$ )-synthesised *SDO/AIA* observations is  $-1000$  s. Such an offset would be clearly discernible when time-lag maps are plotted. This Figure therefore reinforces how performing cross-correlation on the observed and synthesised data can quickly highlight where DEM( $T,t$ ) reconstruction is particularly poor.

Additionally, for the three well-recovered channel pairs in Figure 7.13 (*top*), Figure 7.13 (*bottom*) shows the corresponding plot for the EM pairs. Here, all three channels are highly correlated (cross-correlation value  $> 0.7$ ), with values to larger offsets dropping rapidly. This again suggests that these values are significant. The

time-lag values for the **B - A**, and **C - B** pairs peak at  $\sim 0$  s, as with their *SDO/AIA* counterparts, and as in Figure 7.6, the **D - C** channel pair peaks at a slightly more positive offset than the *SDO/AIA* 211 Å – 193 Å channel pair. The behaviour observed between the *SDO/AIA* channels is replicated by the EM time series, indicating that the observed cooling in *SDO/AIA* corresponds to material cooling from plasma at the peak of the *SDO/AIA* temperature response functions.

Figure 7.14 shows the observed *SDO/AIA* 193 Å – 171 Å time-lag map as plotted in Figure 7.7 where, in this case, there is the addition of a rectangular region surrounding the pixel of fan loop emission. Here, the majority of pixels are once again indicative of cooling (*positive* time-lags) with some *zero*, and very few *negative* time-lags. The time-lag maps generated for the *SDO/AIA* 193 Å – 171 Å channel pair, EM time-lag analysis (**C - B**), and reconstructed *SDO/AIA* 193 Å – 171 Å channel pairs are shown in Figure 7.15 for the rectangular cutout region shown in Figure 7.14.

Figure 7.15 shows the *SDO/AIA*, EM, and DEM-synthesised *SDO/AIA* time-lag maps (*top to bottom*) for the 193 Å – 171 Å channel pair (and the equivalent **C - B** pair). Figure 7.15 (*left*) shows the results for all pixels of emission while the right-hand side displays the same time-lag maps with pixels where both EM time series have at least one *zero* value have been removed (red hatched region). Additionally, Figure 7.15 (*right*) highlights the pixel of fan loop emission (Pixel 2, cross), and a loop-like structure in all three panels. This loop-like structure has been extracted from the EM time-lag maps (*middle*), and will be compared to *SDO/AIA* observations in Figure 7.16. For the time-lag maps shown in Figure 7.15 (*right*), and as was seen for the pixel of diffuse emission (Pixel 1) the time-lags for *SDO/AIA* (observed and synthesised, *top*, *bottom*) are nearly identical. The major differences between the observed and synthesised *SDO/AIA* time-lags is the agreement with increasing distance from the active region core. Comparing the time-lags where only the original *SDO/AIA* time-lags are reconstructed through DEM inversion (*right*), the EM time-lag again appears to assign non-zero values to the majority of the *zero* time-lags that are reported by *SDO/AIA* time-lag analysis (*top*). In particular, for EM time-lag analysis, the *zero* time-lags are only confined to regions where loops are visually observed to brighten, which includes the region appearing to trace out fan loop structure (*right*, black contour).

For additional context to these time-lag maps, and to investigate the region that traces out a fan loop, Figure 7.16 shows the *SDO/AIA* observations for 171 Å and

193 Å over the same region as in Figure 7.15. Figure 7.16 shows this same rectangular region at three times during the observations used for time-lag analysis. These times are at the beginning and end of the 12-hour observations (*top*, *bottom*; time-step = 0, 1439), and at an observation near the middle of the 2-hour time series (*middle*;  $t \approx 4000$  s in Figure 7.12). The loop region co-spatially corresponds to a loop that observed to brighten in both 171 Å and 193 Å at the end of the 12-hour time series (time-step = 1439; *bottom*). While EM time-lag analysis appears to assign non-zero values to the vast majority of pixels that displayed *zero* time-lags that are reported in *SDO/AIA* time-lag maps, there are regions where there are *zero* values in both EM time-lag maps and *SDO/AIA* time-lag maps that correspond to clear brightenings.

From the EM time-lags, the regions of *zero* time-lag are in locations where in-phase brightening was observed, and these appear to be consistent with the idea that they arise from the transition region response to heating. However, the ubiquitous presence of *zero* time-lags in *SDO/AIA* time-lag maps (as observed by Viall & Klimchuk, 2012) may not be exclusively indicative of this process, and it is important to note that for pixels where the observed *SDO/AIA* time-lag analysis leads to *zero* time-lags, EM time-lag analysis is not necessarily *zero*. As discussed in § 6.4.2, while *zero* time-lags observed from *SDO/AIA* time-lag analysis can be related to the transition region response to a coronal nanoflare, Uritsky *et al.* (2013) observed propagating disturbances along the fan loops shown here. If the loops were to move in and out of a pixel region, this would result in in-phase behaviour in the *SDO/AIA* time series, and this could be the reason for the large fraction of *zero* time-lags observed from *SDO/AIA* time-lag analysis.

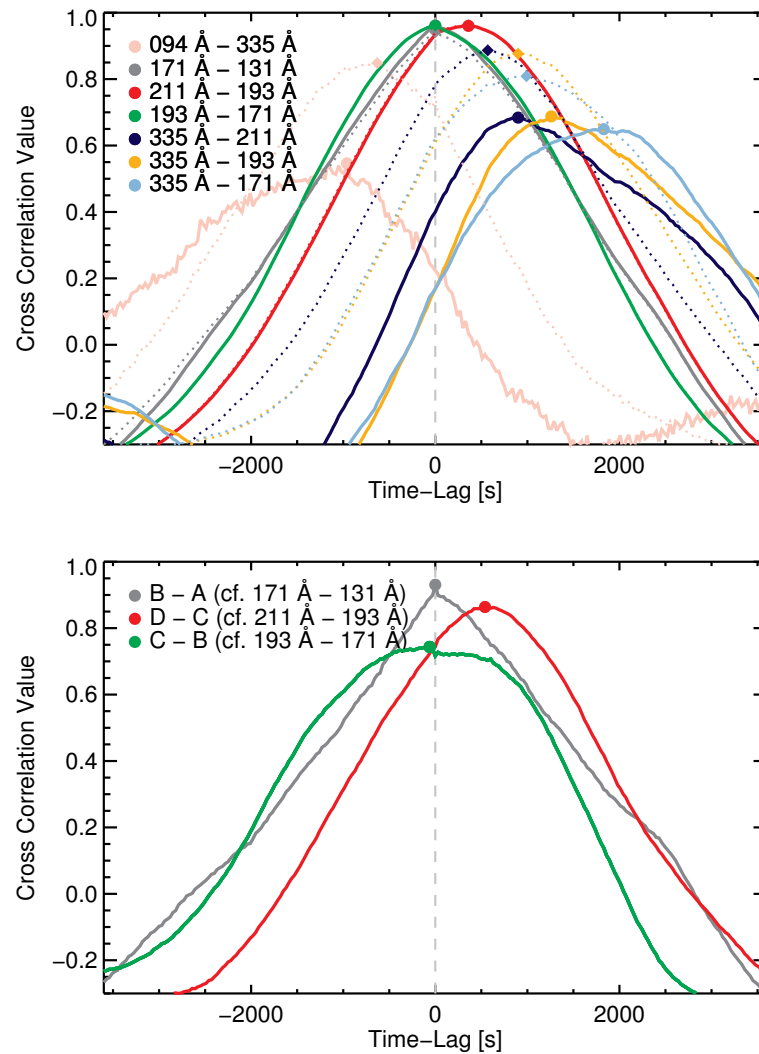


Figure 7.13: Top: Cross-correlation value as a function of temporal offset between the same seven channel pairs shown in Figure 6.10. The original cross-correlation value as a function of offset from Figure 6.5 (those for the *SDO/AIA* data) are shown as solid lines, and the cross-correlation value as a function of offset for the DEM-synthesised *SDO/AIA* observations are shown as dotted lines. As in previous Figures, a positive time-lag indicates that the second channel pair lags the first, and a negative time-lag indicates the first channel lags the second. For each channel pair the time-lag is defined as the point at which the cross-correlation value is maximum. Bottom: As *top* but for the respective EM temperature bins that correspond to the peak temperature response functions where the time-lags are well-recovered from DEM inversion (dotted and solid lines agree, *top*).

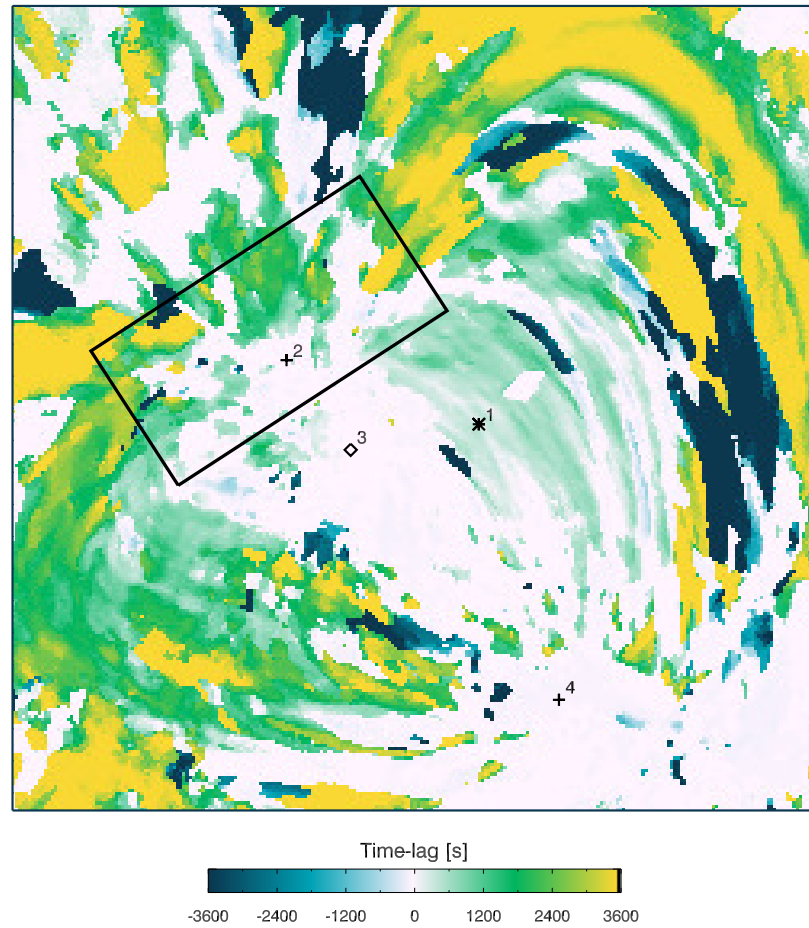


Figure 7.14:  $250 \times 250$  pixel time-lag map for the observed *SDO/AIA*  $193 \text{ \AA} - 171 \text{ \AA}$  channel pair with the four pixels of emission highlighted, as in Figure 6.23 The rectangular cutout region that encompasses the pixel of fan loop emission is presented in later Figures within this section.

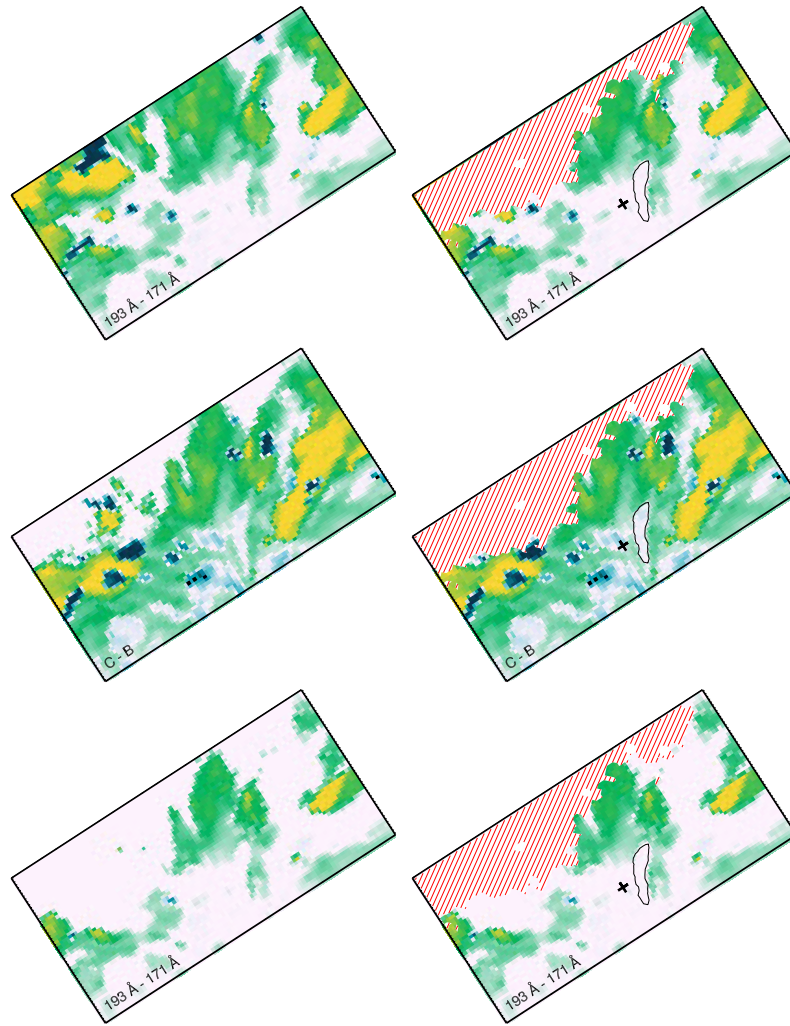


Figure 7.15: Time-lag analysis for the observed  $193 \text{ \AA} - 171 \text{ \AA}$  channel pair, the corresponding EM channel pairs (**C - B**), and the  $193 \text{ \AA} - 171 \text{ \AA}$  channel pair recovered through DEM inversion are shown *top to bottom*. These are shown for the  $100 \times 50$  pixel cutout chosen to include on the pixel of fan loop emission. These time-lag maps are shown with and without a region of *zero* time-lags, highlighted by a red hatched region (*left, right*), that are the result of co-temporal zeros within the EM time series, and these maps have an additional loop-like region (extracted from the EM time-lag map) overplotted (*right*). Regions where the observed and DEM-synthesised *SDO/AIA* time-lags agree indicate locations where the DEM inversion is reliable, and the EM time-lags are interpretable.

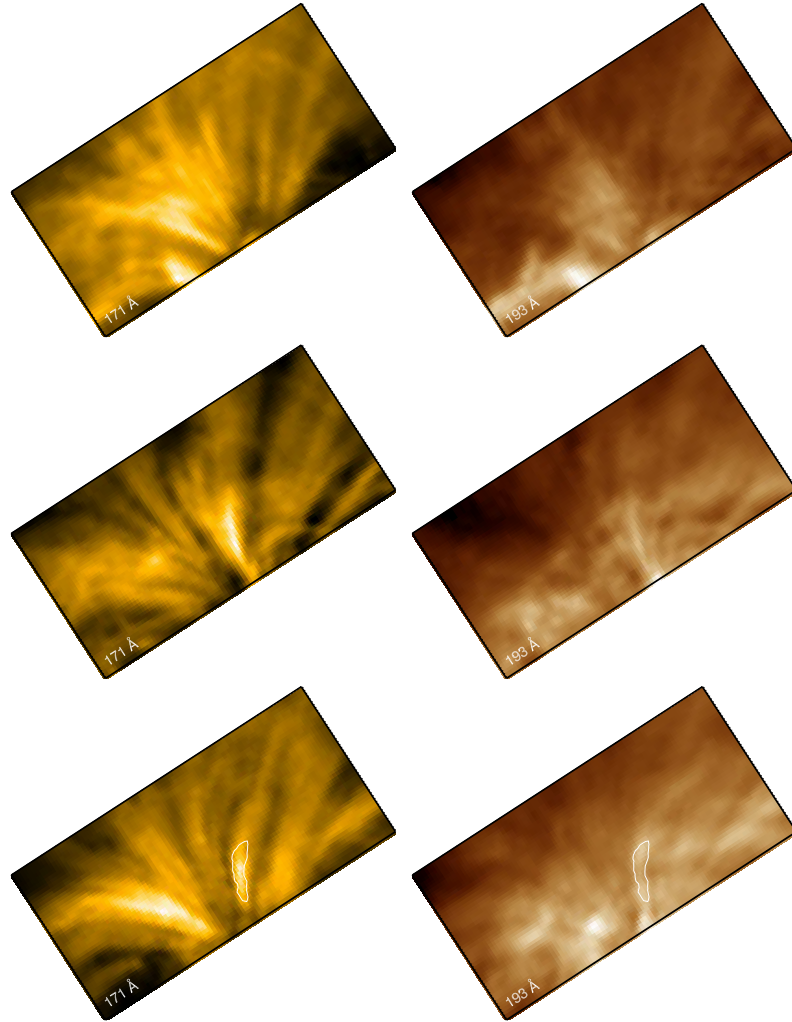


Figure 7.16: *SDO/AIA* observations of the rectangular region chosen to encompass the pixel of fan loop emission, for 171 Å, and 193 Å, at the beginning and end of the 12-hour observations (time-step = 0, *top*; 1439, *bottom*), and an additional image (*middle*) at  $t = 4000$  s (see Figure 7.12). The bottom panel includes the contour shown in Figure 7.15 where *SDO/AIA* and EM time-lag analysis highlighted pixels of *zero*. This contour coincides with, and traces out a brightening fan loop at the end of the 12 hour time series.

### 7.1.4 Active Region Core/Loop; Pixel 3

For the active region core/loop pixel (Pixel 3, § 6.2.4), Figure 7.17 shows the original *SDO*/AIA light curves (black) together with the DEM(T,t)-synthesised *SDO*/AIA light curves (red). As with Figure 7.5 and Figure 7.12, the 211 Å, 193 Å, and 171 Å time series are well-preserved through DEM(T,t) inversion. For 131 Å, 335 Å, and 94 Å similar behaviour to Pixels 1 and 2 is observed: 131 Å is well-recovered on most time-scales apart from the shortest time-scales, and 335 Å includes additional noise (and is poorly recovered near 6000 s). For the 94 Å channel, this channel appears to be dominated by Fe XVIII emission (Figure 6.6) which is calculated through the empirical method of Del Zanna (2013) (Equation 5.1). While DEM(T,t) inversion preserves the general variability, there are a number of noticeable differences across all time-scales which is expected as there is little constraint in this region of temperature space from *SDO*/AIA observations alone.

As before, Figure 7.18 shows the same cross-correlation plot for the seven channel pairs that have been used throughout this chapter. Here it is clear that for the 211 Å – 193 Å (1.8 – 1.6 MK), and 193 Å – 171 Å (1.6 – 0.9 MK) channel pairs the cross-correlation over time is well-preserved, as has been seen throughout this chapter. Good recovery of 335 Å, leads the 335 Å – 211 Å (2.5–1.8 MK), 335 Å – 193 Å (2.5–1.6 MK), 335 Å – 171 Å (2.5–0.9 MK) channel pairs to be reconstructed relatively well compared to the previous pixels. For the 171 Å – 131 Å (0.9 – 0.6 MK) pair cross-correlation value as a function of time (and the time-lag itself) is not well preserved. For the original 171 Å – 131 Å pair, the cross-correlation value was not sharply peaked with cross-correlation values falling off at increasing values of offset, and the cross-correlation of values of offset over the range –1500 – 0 s are fairly similar. The introduction of noise (through DEM inversion) to the synthesised 131 Å time series led the synthesised 171 Å – 131 Å pair to amplify a particular feature in the original time series that was the source of the secondary cross-correlation peak ( $\sim -600$  s). This noise leads the synthesised 171 Å – 131 Å channel pair to have a cross-correlation value at  $\sim -600$  s that is marginally larger than the cross-correlation value at the original time-lag offset of *zero*. The difference between these two channels noticeable in time-lag maps, however, this particular situation highlight how concentrating on specific time-lag values (and not performing interpretation of the observed trends over multiple pixels) can be misleading. In addition to time-lag maps not discriminating based upon

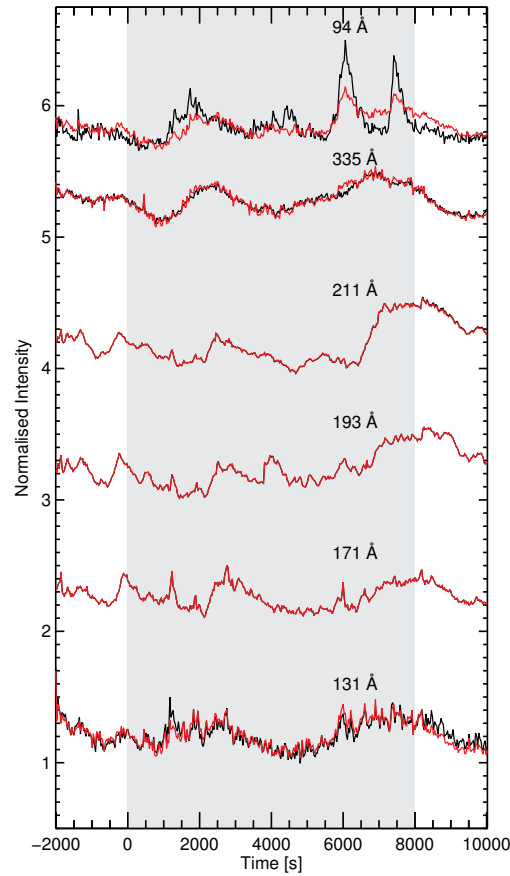


Figure 7.17: Light curves of a pixel of active region core emission (Pixel 3; § 6.2.4) corresponding to 94 Å; 335 Å; 211 Å; 193 Å; 171 Å; and 131 Å, where the original light curves (as in Figure 6.12) are shown in black, and the synthesised *SDO/AIA* observations from DEM( $T,t$ ) inversion are shown in red. The two-hour region used from time-lag and EM temperature analysis is shaded grey, and includes an additional  $\pm 2000$  s for context.

cross-correlation value, it is also not clear how significant the cross-correlation value is compared to other values of offset.

Figure 7.18 (*bottom*) also shows the cross-correlation value as a function of offset for the three channel pairs that are well recovered (Figure 7.18, *top*). These channel pairs (as with Pixel 1, and Pixel 2) are **B - A**, **D - C**, and **C - B** and these are equivalent to 171 Å – 131 Å, 211 Å – 193 Å, and 193 Å – 171 Å. For EM time-lag analysis **B - A** is peaked with a cross-correlation value of  $\sim 0.4$ , however, this channel pair *does not*

return the original *SDO/AIA* time-lag (Figure 7.18, *top*) and therefore it is difficult to make conclusions about this EM time-lag. The other two channel pairs recover the *SDO/AIA* data much better, but are peaked near the edge of the time series which could be physical, or an edge effect due to the finite length of the data.

Figure 7.19 shows the *SDO/AIA* 193 Å – 171 Å time lag map, including a rectangular region that encompasses the active region core pixel. It should be noted that this region overlaps the regions presented in Pixel 1 and Pixel 2. For reference the two rectangular regions used earlier are hatched in grey. In the region where there is no overlap, the majority of pixels exhibit *zero* time-lags for the *SDO/AIA* 193 Å – 171 Å channel pair, with very few *positive* or *negative* time-lags. The time-lag maps for the observed *SDO/AIA* 193 Å – 171 Å channel pair, EM time-lag analysis (**C** – **B**), and synthesised *SDO/AIA* 193 Å – 171 Å pair are shown in Figure 7.20 for this same rectangular region.

Figure 7.20 presents the *SDO/AIA* 193 Å – 171 Å time-lag map, *top*; the EM time-lag map, **C** – **B**, *middle*; and the synthesised *SDO/AIA* 193 Å – 171 Å time-lag map, *bottom*. Figure 7.20 (*left*) shows these maps as obtained, and Figure 7.20 (*right*) includes the active region core pixel (Pixel 4, black diamond), the fan loop pixel (Pixel 2) as a black cross, and as there are no pixels where the DEM reports a value of  $\leq 0$  in both temperature bins **B**, and **C**, the regions used for the analysis of Pixels 1 and 2 are overplotted as a grey hatched region.

Outwith this grey hatched region, while EM time-lag analysis assigned non-zero values to some *SDO/AIA zero* time-lags, there are a significant number of extreme time-lag values (dark blue, bright yellow) within the core of the active region. These extreme values represent maximum positive or negative time-lags (e.g. **C** - **B** in Figure 7.18, *bottom*).

The abundance of these extreme values suggests that there is no significant correlation between the EM time series in the majority of core pixels (similarly to the behaviour seen in Figure 7.18 for the same channel pair).

Regardless of the number of extreme time-lags co-spatially located where the original *SDO/AIA* time-lags are *zero*, the original *SDO/AIA* time-lag maps nearly identical to the *SDO/AIA* time-lag maps synthesised from DEM(T,t) inversion. This does suggest that the DEM(T,t) is able to reconstruct the observed *SDO/AIA* time series, but perhaps the assumptions of the DEM no longer hold in the core of the active region, or

that the  $\text{DEM}(T,t)$  just does not represent the evolution of the underlying temperature distribution. Further investigation of these extreme values is needed.

For completeness, for the rectangular region shown in Figure 7.19 and Figure 7.20, Figure 7.21 shows the same region displayed in *SDO/AIA* 171 Å *left*, and 193 Å *right*, for the same three time-steps as shown in Pixel 2: time-step = 0, 1439 (beginning and end of the 12 hour time series, *top*, *bottom*), and also an image in the middle of the 2 hour time series ( $t \approx 4000$  s, *middle*).

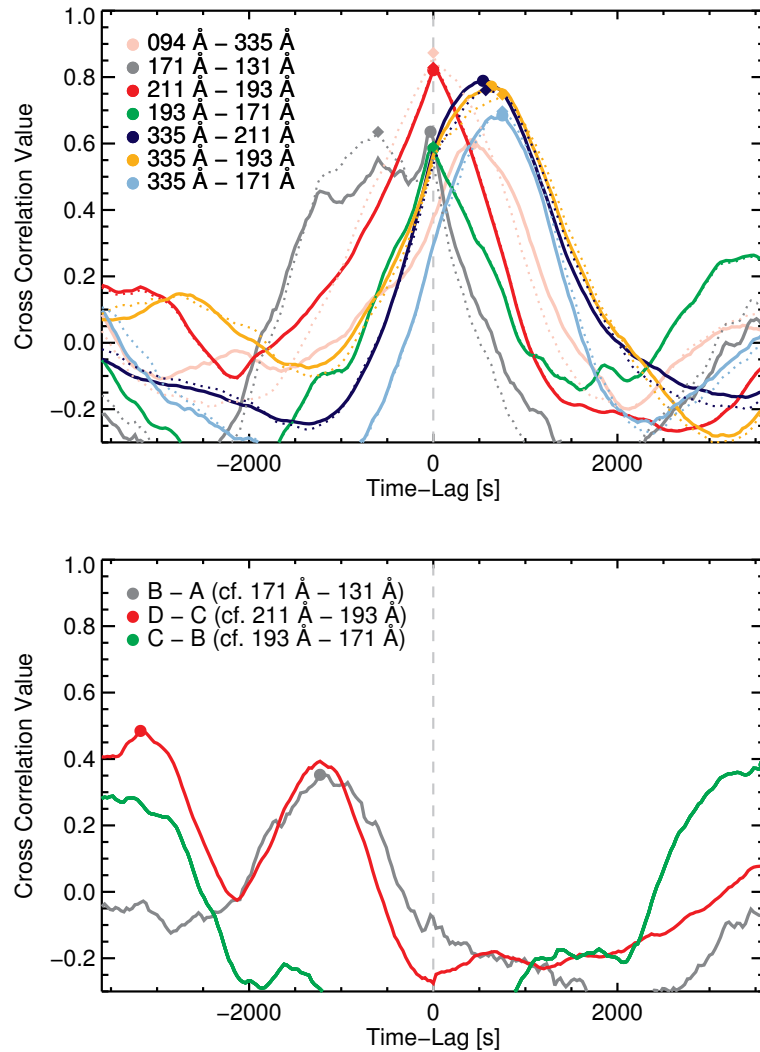


Figure 7.18: Top: Cross-correlation value as a function of temporal offset between the same seven channel pairs shown in Figure 6.13. The original cross-correlation value as a function of offset from Figure 6.5 (those for the *SDO/AIA* data) are shown as solid lines, and the cross-correlation value as a function of offset for the DEM-synthesised *SDO/AIA* observations are shown as dotted lines. As in previous Figures, a positive time-lag indicates that the second channel pair lags the first, and a negative time-lag indicates the first channel lags the second. For each channel pair the time-lag is defined as the point at which the cross-correlation value is maximum. Bottom: As *top* but for the respective EM temperature bins that correspond to the peak temperature response functions where the time-lags are well-recovered from DEM inversion (dotted and solid lines agree, *top*).

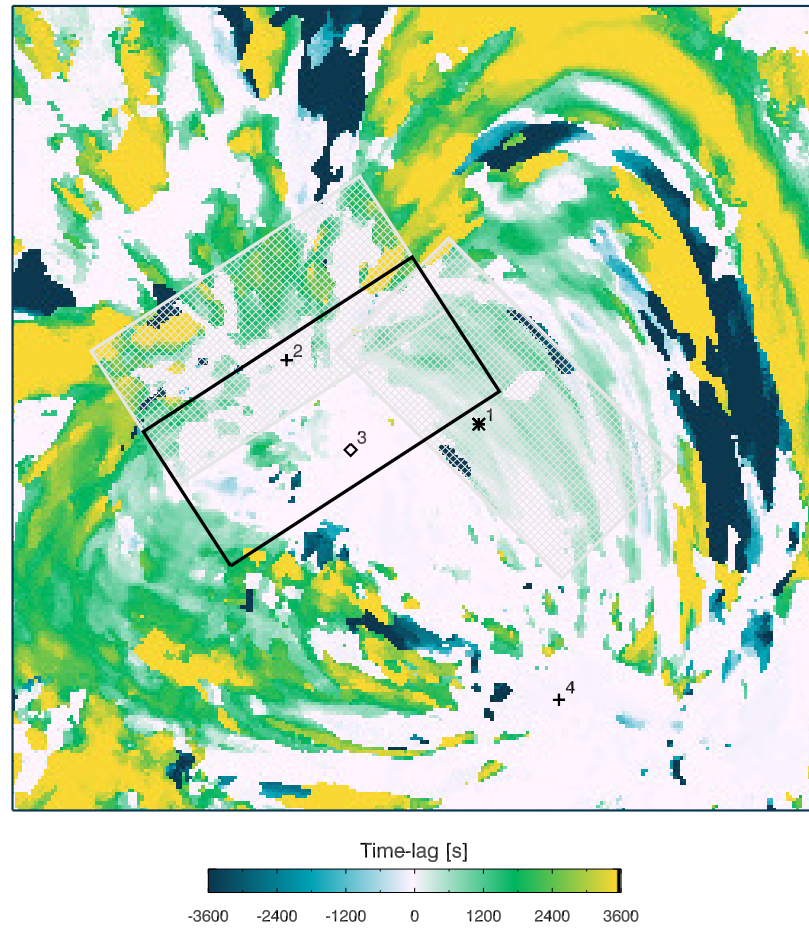


Figure 7.19:  $250 \times 250$  pixel time-lag map for the observed *SDO/AIA*  $193 \text{ \AA} - 171 \text{ \AA}$  channel pair with the four pixels of emission highlighted, as in Figure 6.23. The black rectangular box that encompasses the pixel of core loop emission used in later Figures, and additionally highlighted are the two rectangular regions from Pixels 1, 2.

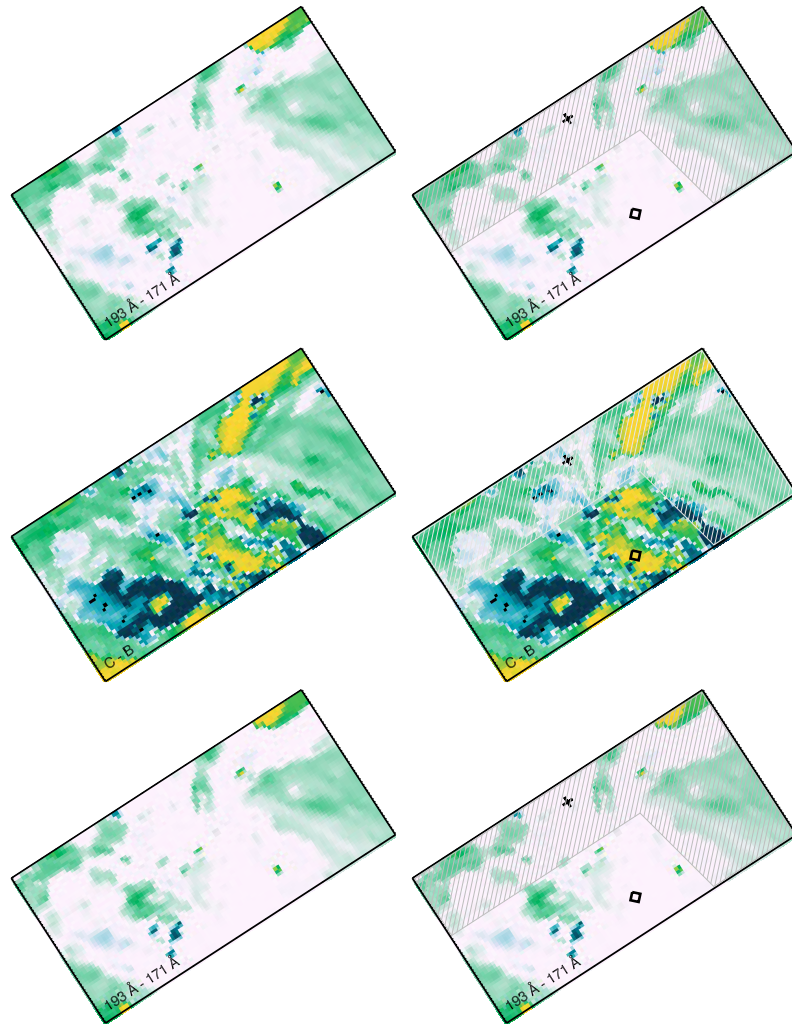


Figure 7.20: Time-lag analysis for the observed *SDO/AIA* 193 Å – 171 Å channel pair *top*, the corresponding EM time-lag map *middle*, and the DEM( $T,t$ )-synthesised 193 Å – 171 Å channel pair (*bottom*) for the  $100 \times 50$  pixel cutout chosen to include on the pixel of core loop emission. These time-lag maps are shown with-, and without the region of overlap (shown as a grey hatched region) between the region used in Pixel 1, 2 (*left, right*). EM time-lag analysis appears to assign non-zero values to some of the zero time-lags observed in *SDO/AIA* time-lag analysis, however the majority of the EM time-lags are at extreme values (maximum positive or negative time-lags). Regions where the observed and DEM-synthesised *SDO/AIA* time-lags agree indicate locations where the DEM inversion is reliable, and the EM time-lags are interpretable.

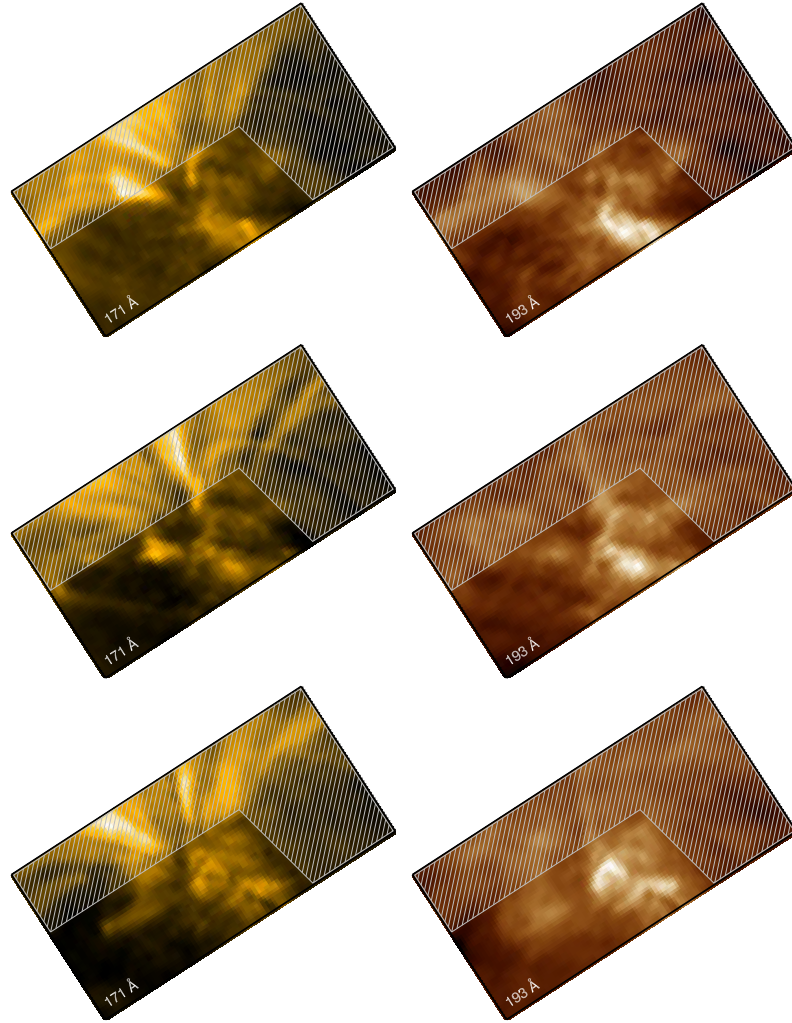


Figure 7.21: *SDO/AIA* observations of the rectangular cutout region chosen to encompass the pixel of core loop emission (Figure 7.19), for 171 Å, and 193 Å, at the beginning and end of the 12 hour time series (time-step = 0, *top*; 1439, *bottom*). Additionally, an image from the middle of the 2 hour time series ( $t \approx 4000$  s) is also shown (*middle*). All panels include the a grey hatched out region indicating where the rectangular regions from Pixel 1, and 2 overlap this region.

### 7.1.5 Loop Footpoint; Pixel 4

For the Pixel of loop footpoint emission, Pixel 4, over the 12-hour time series there are seven times at which the DEM was not recovered, and as a result, this would lead this pixel to be disregarded from analysis. However, in this section these missing values (in both the EM time series and the DEM-synthesised EM time series) will be interpolated over and this time series will be investigated.

Importantly, for this pixel there are a number of *zeros* within the recovered *SDO/AIA* time series that are the result no DEM being obtained at those time-steps. Figure 7.22 (*left*) shows the original time series (over the 2-hour period) plot in black, in comparison to the DEM-synthesised *SDO/AIA* observations (red). Figure 7.22 (*right*) shows the same time series with the *zeros* in the synthesised *SDO/AIA* observations interpolated over. As previously, these light curves have been offset in intensity to avoid overlap of the light curves, and from top to bottom these light curves are 94 Å; 335 Å; 211 Å; 193 Å; 171 Å; and 131 Å. In the complete 12-hour time series that is used for the time-lag maps in later figures there are seven instances where the DEM was not recovered, and therefore the predicted values in all six *SDO/AIA* channels are *zero*. The inability to recover the DEM at every time-step is different to the situation where certain temperature bins of the DEM are equal *zero*. In that case, a *zero* in a particular DEM (temperature) bin would lead to a set of *SDO/AIA* observations where the *zero* would have different effects on each channel due to the varying temperature sensitivity at the location where the *zero* is present.

With the exception of these locations, as with the pixel of diffuse emission, it is clear from Figure 7.22 that the variability is well-preserved through DEM(T,t) inversion, and these time series have the same qualities as previously: 171 Å, 193 Å, and 211 Å are generally well-reconstructed, while 131 Å, 94 Å, and 335 Å preserved the general variability, but fail to capture the complete short-scale variability. After interpolation over the *zero* values, Figure 7.23 shows that *all* channel pairs are seen to provide time-lag signatures that are consistent. This is most likely in part due to the large correlation of the original *SDO/AIA* time-lags (cross-correlation value > 0.9).

For the EM channel pairs (Figure 7.23, *bottom*) the cross-correlation as a function of offset is plotted for the three EM channel pairs which correspond to the *SDO/AIA* channel pairs that are well recovered through DEM-inversion (Figure 7.23, *top*). These are (as with other pixels) **B - A**, **D - C**, **C - B**, and are equivalent to 171 Å – 131 Å,

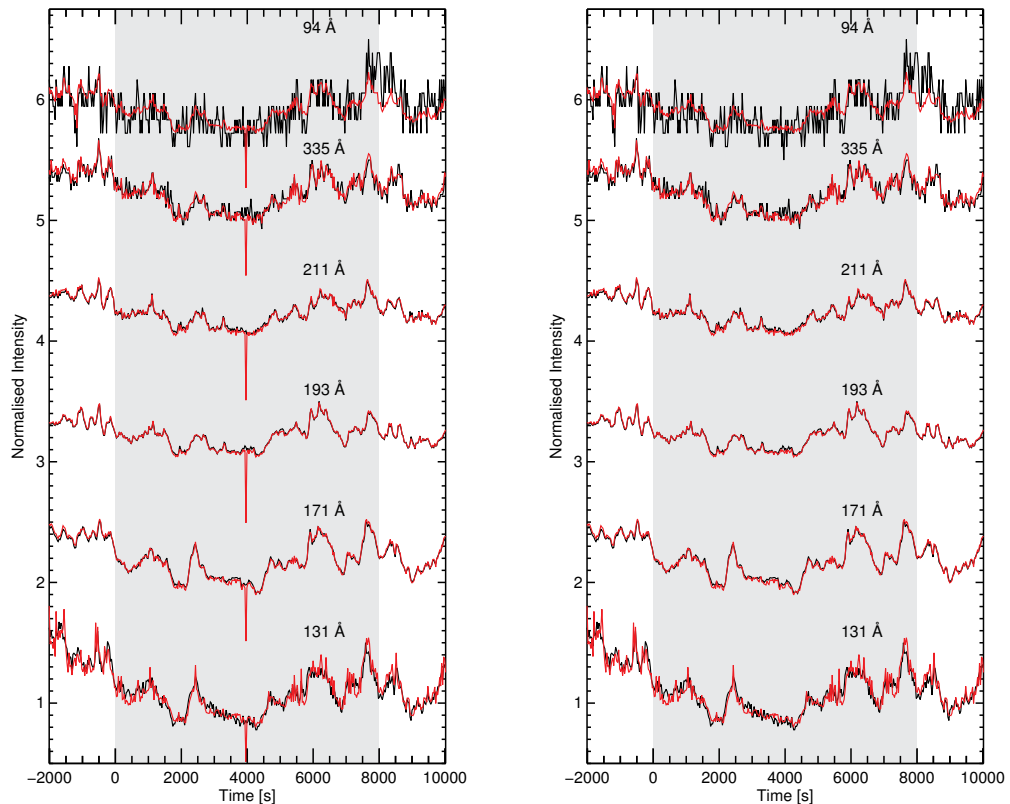


Figure 7.22: Light curves of a pixel of fan loop footpoint emission (Pixel 4; § 6.2.5) prior to interpolation over *zero* values (*left*), and after interpolation (*right*). These light curves are 94 Å; 335 Å; 211 Å; 193 Å; 171 Å; and 131 Å (*top to bottom*), where the original light curves (as in Figure 6.15) are shown in black, and the DEM-synthesised *SDO/AIA* observations are shown in red. The two-hour region used from time-lag and EM temperature analysis is shaded grey, and includes an additional  $\pm 2000$  s for context.

211 Å – 193 Å, and 193 Å – 171 Å. For EM time-lag analysis both **B** - **A** and **C** - **B** well-recover the *zero* time-lag observed in *SDO/AIA*. For the **D** - **C** pair the peak cross-correlation value is at  $\sim -1500$  s, with a slightly larger cross-correlation value than the secondary peak at 0 s. As there are two large peaks neither value can be regarded as significant in the EM time-lags. This again reinforces why trends in the time-lag maps should be considered rather than individual values.

It is these pixels (such as Pixel 4) that are on the edge of the active region, where a

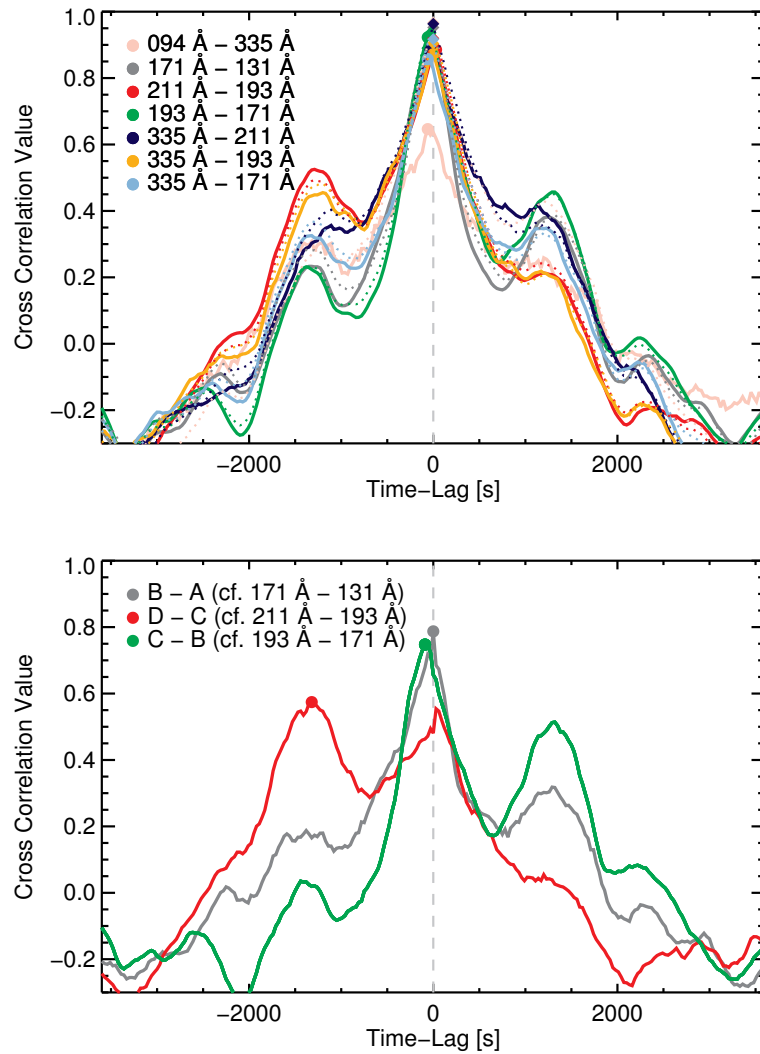


Figure 7.23: *Top*: Cross-correlation value as a function of temporal offset between the same seven channel pairs shown in Figure 6.16. The original cross-correlation value as a function of offset from Figure 6.5 (those for the *SDO/AIA* data) are shown as solid lines, and the cross-correlation value as a function of offset for the DEM-synthesised *SDO/AIA* observations are shown as dotted lines. For each channel pair the time-lag is defined as the point at which the cross-correlation value is maximum. Here, all sets of channel pairs have time-lags equal to *zero*. *Bottom*: As *top* but for the respective EM temperature bins that correspond to the peak temperature response functions where the time-lags are well-recovered from DEM inversion (dotted and solid lines agree, *top*).

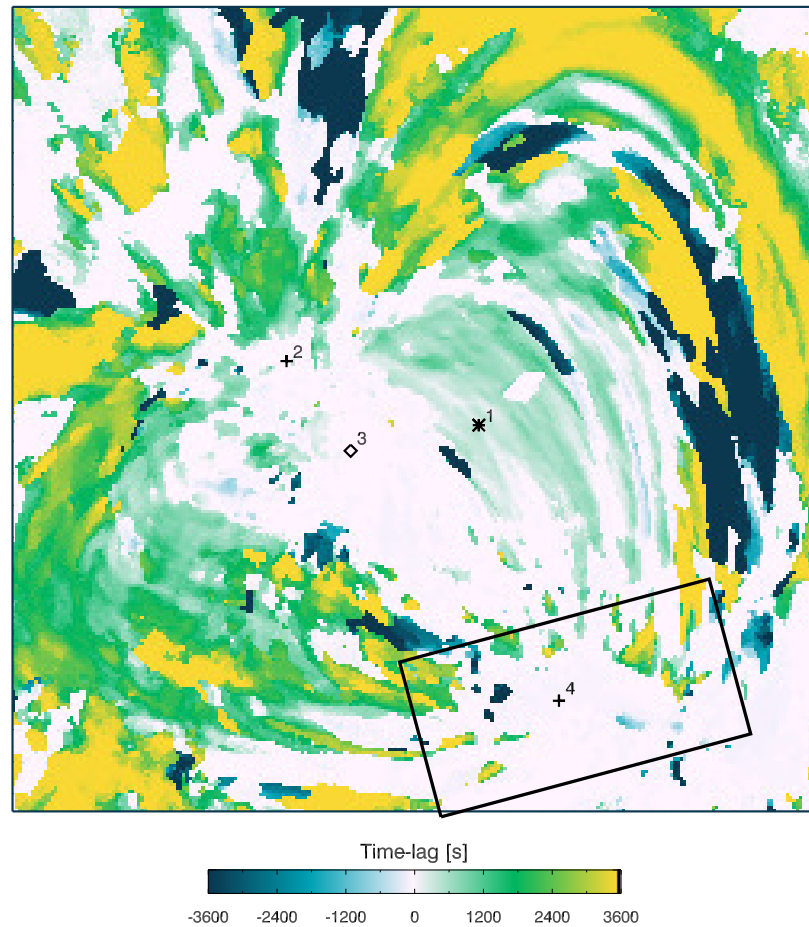


Figure 7.24:  $250 \times 250$  pixel time-lag map for the observed *SDO/AIA*  $193 \text{ \AA} - 171 \text{ \AA}$  channel pair with the four pixels highlighted, as in Figure 6.23. The rectangular region encompasses the pixel of loop footpoint emission (Pixel 4) which is presented in later Figures.

DEM solution cannot be reconstructed at every time-step, that leads to the majority of pixels outwith the core of the active region to have *zero* values (as was seen originally in Figure 7.8). The bottom panel of Figure 7.23 shows the three channel pairs as discussed previously, and the cross-correlation value as a function of time is generally well-preserved between all three pairs.

Figure 7.24 shows the same *SDO/AIA*  $193 \text{ \AA} - 171 \text{ \AA}$  time-lag map that has been presented previously, with the addition of the rectangular region around the pixel of fan loop emission (Pixel 4). The *SDO/AIA*  $193 \text{ \AA} - 171 \text{ \AA}$ , EM (C - B), and DEM-synthesised *SDO/AIA*  $193 \text{ \AA} - 171 \text{ \AA}$  time-lag maps are shown in Figure 7.25.

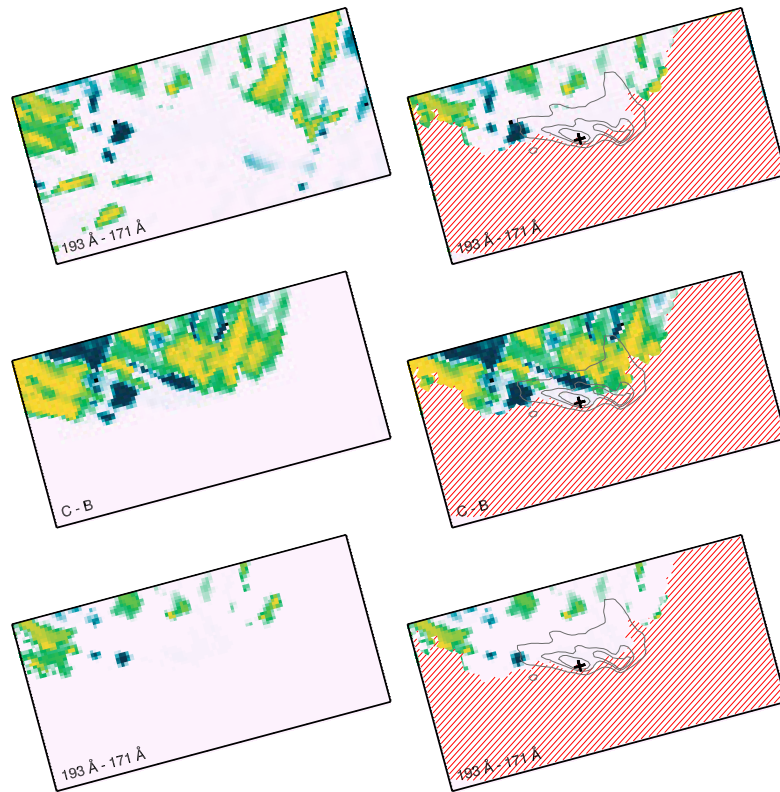


Figure 7.25: Time-lag analysis for the observed  $193 \text{ \AA} - 171 \text{ \AA}$  channel pair, the corresponding EM time-lags, and the  $193 \text{ \AA} - 171 \text{ \AA}$  pair synthesised from DEM inversion (*top to bottom*) for the  $100 \times 50$  pixel region chosen to encompass the pixel of loop footpoint emission. These time-lag maps are shown with and without a region of zero time-lags highlighted by a red hatched region (*left, right*), and also shown with an without contours of the brightest  $171 \text{ \AA}$  emission (*left, right*) extracted from the middle of the two-hour time series shown in Figure 7.22. Regions where the observed and DEM-synthesised *SDO/AIA* time-lags agree indicate locations where the DEM inversion is reliable, and the EM time-lags are interpretable.

Figure 7.25 (*top to bottom*), shows the *SDO/AIA*  $193 \text{ \AA} - 171 \text{ \AA}$ , EM **C – B**, and the DEM(*T,t*)-synthesised *SDO/AIA*  $193 \text{ \AA} - 171 \text{ \AA}$  time-lag maps, for the rectangular region in Figure 7.24. Figure 7.25 shows that DEM(*T,t*) generally preserves variability between observed and synthesised *SDO/AIA* time-lags. For the EM time-lag analysis (and therefore the synthesised *SDO/AIA* time-lag analysis, a large number of the time-lags are *zero*, which is a direct result of being unable to recover the DEM at  $\geq 1$  time-steps (out of 1440 time-steps). Figure 7.25 (*right*) therefore shows these time-lag maps

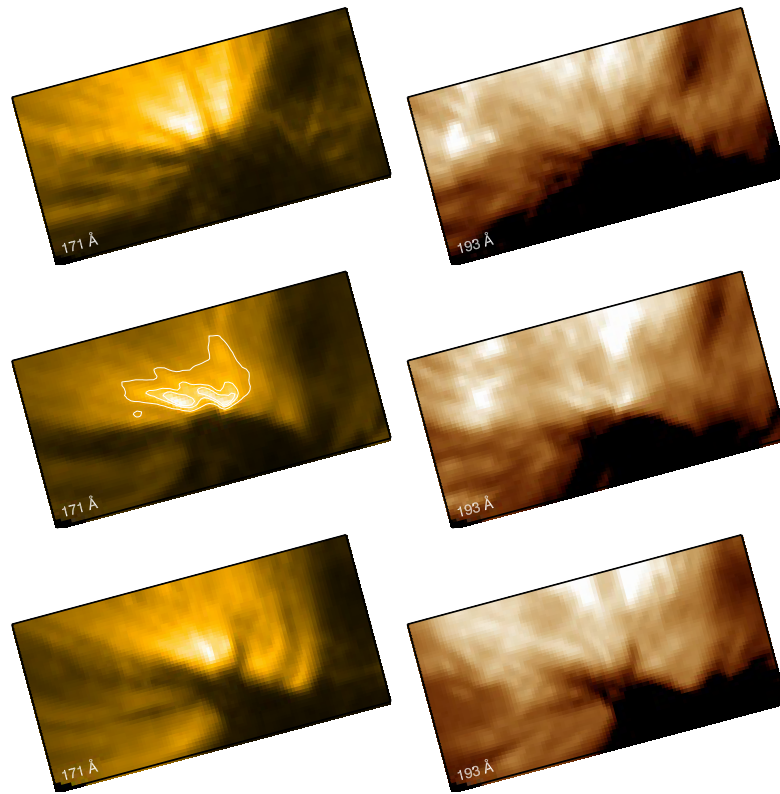


Figure 7.26: *SDO/AIA* 171 Å and 193 Å images for the cutout region shown in Figure 7.24, and Figure 7.25. These images are shown at three time-steps: the beginning (*top*), and end (*bottom*) of the 12 hour time series, and an image from the middle of the 2-hour time series shown earlier (*middle*). The 171 Å image from the middle of the two hour time series is shown with contours to highlight the brightest regions in the image.

with the addition of the red hatched region to indicate where at least one time-step in both EM time series returned a *zero* value. Also overplotted is the pixel considered in this section, and contours of the brightest 171 Å emission (see Figure 7.26, later). From these panels on the right-hand side of this Figure, it is clear that the EM time-lag map (*middle*) appears to perform some general interpolation of the the *SDO/AIA* time-lag maps (*top*) to regions that *SDO/AIA* time-lag maps are reported to be *zero*. As was seen in Figure 7.22, Pixel 4 had a number of *zero* values prior to interpolating, and is located within this red hatched region. Regardless, for this pixel, interpolating over these *zero*/missing values in the time series does not introduce a false time-lag, and therefore we still consider the time-lag of this pixel.

Figure 7.26 shows three observations of this cutout region at the beginning and end of the 12-hour time series (time-step = 0, 1439), and at a time-step in the middle of the 2-hour region presented in Figure 7.22 ( $t \approx 4000$  s). In addition to these observations, a contour of the brightest 171 Å emission (extracted from the middle of the two-hour time series) is overplotted (*middle, left*). With these context images, it is clear that the remaining *zero* values observed for the EM time-lag analysis (Figure 7.24) are co-spatially located with the brightest emission from 171 Å, which is observed to brighten in-phase with 193 Å.

### 7.1.6 Summary

Section 7.1 introduced the concept of EM time-lag analysis on the four pixels introduced with time-lag analysis (see, Chapter 6). The general idea of EM time-lag analysis is that by performing DEM(T,t) inversion, and extracting the time series from temperature bins chosen to coincide with the peak values of the temperature response functions the time-lag signature in temperature can be extracted (the signature that is potentially masked by time-lag analysis of the *SDO/AIA* data alone).

Here we have concentrated primarily on the 193 Å – 171 Å channel pair which corresponds to the EM time series **C** - **B**. From the four pixels presented it is clear that DEM inversion was able to recover the input time series which is important as for the DEM to be representative of the underlying temperature distribution it must return the data input. To summarise the results from EM time-lag analysis we address each pixel individually.

**Pixel 1** – Pixel 1 corresponds to a pixel of diffuse emission. DEM(T,t) inversion was able to accurately recover the time series in a number of channels including 171 Å, and 193 Å that were used to generate time-lag maps, and both the original *SDO/AIA* and DEM-synthesised 171 Å – 193 Å maps were in good agreement. For the EM time-lag, the time-lag maps **C** - **B** agree with *SDO/AIA* time-lag analysis in the majority of pixels where *SDO/AIA* time-lag analysis returned non-zero values. Importantly, in the vast majority of regions where *SDO/AIA* time-lag analysis returned zero values, EM time-lag analysis assigned non-zero values in these regions, and these non-zero values are similar to adjacent non-zero values seen in the *SDO/AIA* time-lag maps suggesting that the *SDO/AIA* time-lag analysis masks the underlying time-lag signature in tem-

perature.

**Pixel 2** – Pixel 2 corresponds to a pixel of fan loop emission. Similar behaviour was seen in Pixel 2 as with Pixel 1: DEM(T,t) inversion was able to accurately recover the time series in a number of channels including 171 Å, and 193 Å, and the EM time-lag maps show a smaller proportion on zero values in comparison to the *SDO/AIA* time-lag maps. This again is indicative of *SDO/AIA* time-lag analysis masking the underlying cooling that is observed in temperature space. Interestingly in this rectangular region there regions of zero time-lag values that are present in both the *SDO/AIA* and EM time-lag maps, one of which seems to trace out a fan loop, and this fan loop is seen to brighten in phase. Furthermore, in this region, [Uritsky \*et al.\* \(2013\)](#) observed propagating disturbances along the loops shown here which would result in zero time-lags in *SDO/AIA* time-lag analysis.

**Pixel 3** – Pixel 3 corresponds to active region core emission which is consistent with a brightening loop, and has significant emission consistent with the hotter component of the 94 Å emission. A significant number of the EM time-lags are at the extremities ( $\pm 3600$  s) which will be discussed later, however, it would be of interest to investigate these EM time-lags by performing analysis with a variety of DEM inversion methods in order to understand if this is physical or a result of the inversion method itself.

**Pixel 4** – Pixel 4 corresponds to a loop footpoint. Here both *SDO/AIA* and EM time-lag analysis return in-phase time series for the loop footpoint which is consistent with the transition region response to a coronal nanoflare, and this brightening is observed in the images.

## 7.2 Testing with Model Time Series

### 7.2.1 EBTEL Diffuse Emission Simulation: Corona

The EBTEL diffuse emission simulations in § 6.4 provide the ground truth  $\text{DEM}(T)$  over 30,000 time-steps. These simulations are ideal for testing the EM time-lag analysis that has been presented in this chapter.

For the 193 Å – 171 Å (1.6 – 0.9 MK) pair, Figure 7.27 shows the cross-correlation value as a function of offset for the “observed” *SDO/AIA* data (blue), which in this case has been simulated by EBTEL. This Figure also shows the cross-correlation value as a function of offset for the DEM-synthesised *SDO/AIA* data from  $\text{DEM}(T,t)$  inversion (pink). As with all four pixels presented in this chapter, it is clear that the  $\text{DEM}(T,t)$  inversion is able to preserve the variability observed by *SDO/AIA* in 171 Å, and 193 Å: that is, the cross-correlation values for the observed and synthesised *SDO/AIA* data (blue, pink) are in agreement as a function of offset, and specifically, the time-lag is consistent (this is a simple quality check on the DEM inversion). What is not clear without the EBTEL simulations is the ability for DEM inversion to *also* recover the underlying variability in the temperature distribution.

As the EBTEL simulations provide a ground-truth  $\text{DEM}(T,t)$ , it is also possible to directly compare the variability observed in EBTEL temperature bins (those that correspond to the peak temperature response of the channels) to the equivalent temperature bins from the  $\text{DEM}(T,t)$  that are recovered by inversion. This is performed in order to understand how well DEM inversion is preserving the underlying variability in temperature-space. If the *SDO/AIA* observations were masking the variability of the underlying plasma distribution then the EM cross-correlation value as a function of offset (and importantly, the reported time-lags) would differ from the *SDO/AIA* time-lags.

Figure 7.27 shows the EM time-lags for the EM **B – C** pair—the pair of temperature bins chosen to correspond to the 193 Å – 171 Å pair (see Figure 6.2 for the response functions and respective DEM bins). Here, it is clear that the EBTEL EM time-lag analysis reports a time-lag at a less positive value of offset than the corresponding *SDO/AIA* channel pair (210 s, *vs.* 230 s, respectively). This indicates that time-lag analysis on *SDO/AIA* data masks the true time-lag signatures that are recov-

ered by performing time-lag analysis on the temperature distribution (with these EM time series). It is also clear that after performing DEM inversion on the *SDO/AIA* observations, the (recovered) EM time-lag for **C** – **B** is consistent with that seen from the EBTEL EM time-lag, albeit at a higher cross-correlation value (Figure 7.27, *bottom*) which suggests noise suppression in DEM inversion.

What is also clear is that while the time-lags agree in offset, for the EM time-lag analysis the “observed” and recovered (by inversion) DEMs return different values of cross-correlation value as a function of offset. This implies that while DEM inversion can recover the input data (used to generate the DEM), the DEM(*T,t*) is not identical (there are, after-all, a large number of DEM(*T,t*) solutions that will return the original data).

The cross-correlation value as a function of offset for the **C** - **B** EM channel pair appears to have properties of both the “observed” (EBTEL-synthesised) *SDO/AIA* 193 Å – 171 Å channel pair, and the “observed” (EBTEL) EM **C** - **B** channel pair. For example, the time-lag derived from the “observed” (EBTEL) EM time-lag analysis is consistent with the *SDO/AIA* time-lag (at least in cross-correlation value), however, for the recovered EM cross-correlation value as a function of offset (between 2000 s and 3600 s) the EM channel pair appears to have similar variability to the *SDO/AIA* equivalent. Furthermore, over –3000 – –3600 s the cross-correlation value as a function of offset for the EM pair clearly has properties of both the observed EBTEL EM time series, and the EBTEL *SDO/AIA* time series.

Similarly to Figure 7.27, Figure 7.28 shows the same plot but for the 211 Å – 193 Å channel pair. In this channel pair it is observed that by performing EM time-lag analysis on the “observed” (EBTEL), and recovered DEMs, these are similar as a function of cross-correlation value, and ultimately have time-lags at similar values of time-lag (both shifted to more positive values, Figure 7.27 *bottom*). In Pixels 1 (Figure 7.6) and 2 (Figure 7.13), EM time-lag analysis showed that the time-lags for **D** - **C** (those equivalent to 211 Å – 193 Å) were significant in that they peaked at large cross-correlation values, and the cross-correlation value dropped off steeply as a function of offset. In both pixels, the EM (**D** - **C**) time-lag was observed to be shifted to a more positive time-lag than the *SDO/AIA* 211 Å – 193 Å time-lags. This behaviour is also observed in these EBTEL simulations (observed *SDO/AIA* time-lag, blue; “observed” EBTEL EM time-lag, green) and with the assumption that **D** - **C**

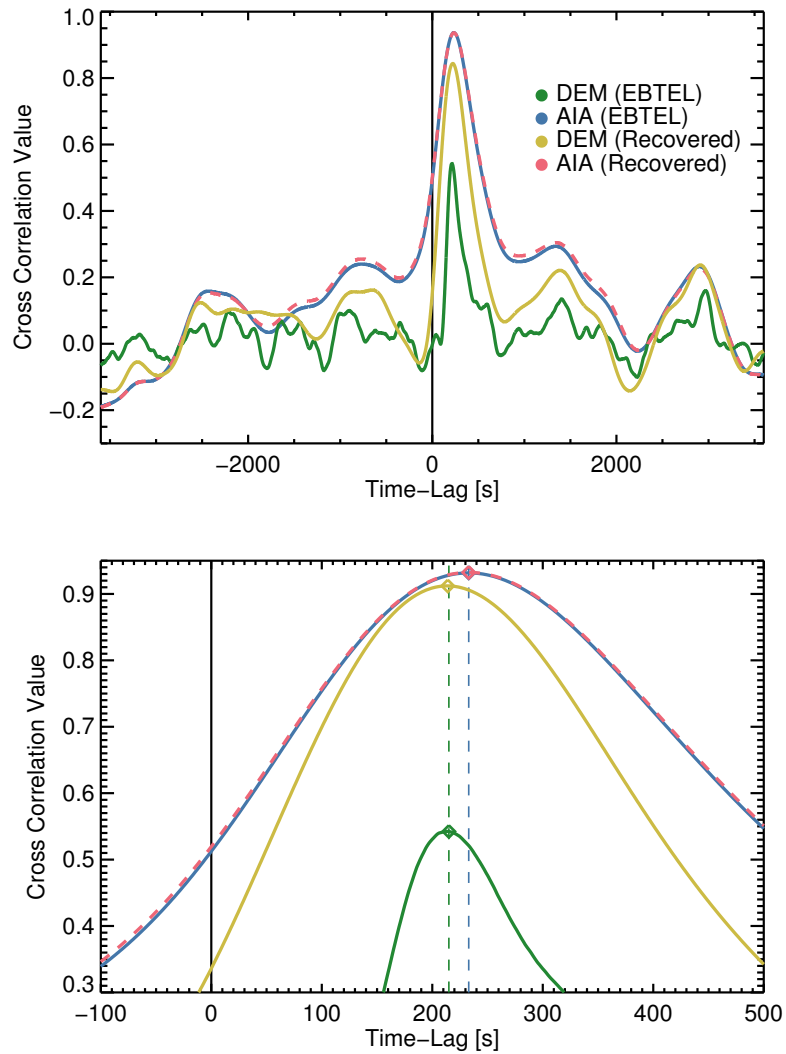


Figure 7.27: *Top*: Cross-correlation value as a function of offset for the  $193 \text{ \AA} - 171 \text{ \AA}$  channel pairs from the EBTEL simulations presented in § 6.4 (“observed”, blue; synthesised, pink). This is shown in comparison to the cross-correlation value as a function of offset derived from the equivalent temperature bins in the DEM (“observed”, green; recovered, yellow). *Bottom*: Magnified region of *top* to further highlight the agreement between DEM inversion and EBTEL EM Time-lag analysis, and the agreement between both input and recovered output. The dashed lines are overplotted to highlight the offset between *SDO/AIA* and DEM(T) time-lags.

is an accurate representation of the peaks of  $211 \text{ \AA}$ , and  $193 \text{ \AA}$ , this confirms that *SDO/AIA* time-lag analysis masks the true time-lag signature that is observed in EM

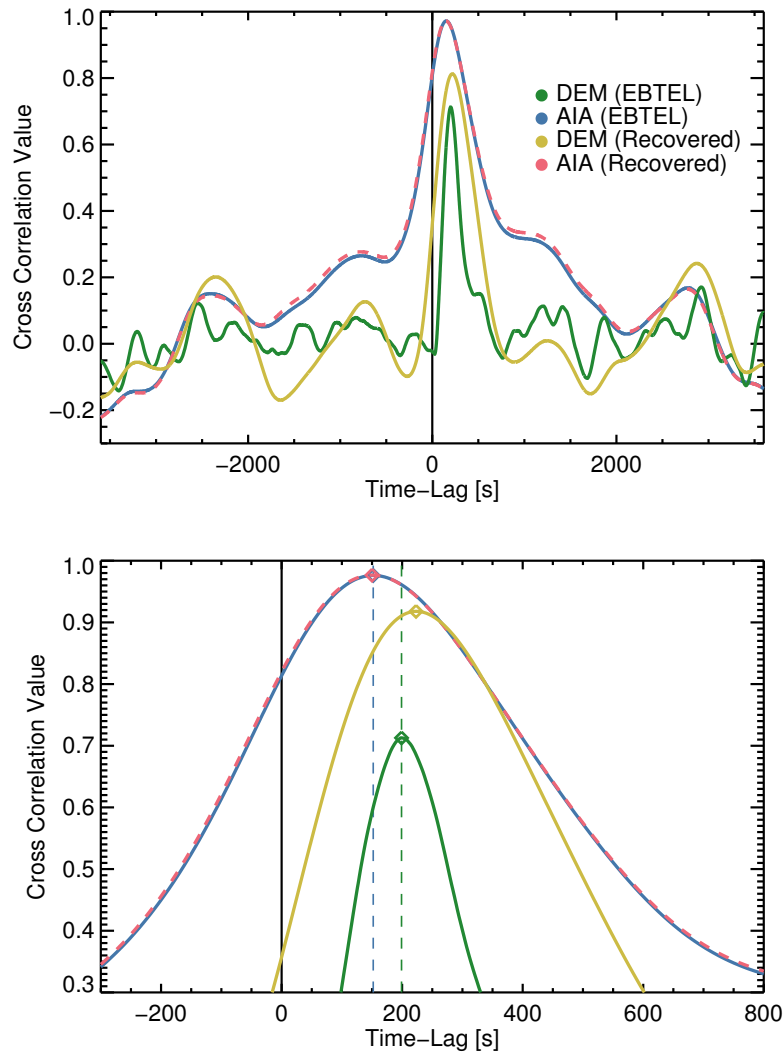


Figure 7.28: *Top*: Cross-correlation value as a function of offset for the  $211 \text{ \AA} - 193 \text{ \AA}$  channel pairs from the EBTEL simulations presented in § 6.4 (“observed”, blue; synthesised, pink). This is shown in comparison to the cross-correlation value as a function of offset derived from the equivalent temperature bins in the DEM (“observed”, green; recovered, yellow). *Bottom*: Magnified region of *top* to further highlight the agreement between DEM inversion and EBTEL EM Time-lag analysis, and the agreement between both input and recovered output. The dashed lines are overplotted to highlight the offset between *SDO/AIA* and *DEM(T)* time-lags.

time-lag analysis. As was seen in Figure 7.27, Figure 7.28 shows that for EM time-lag analysis on the recovered temperature distribution results in a cross-correlation curve

that has properties of both the EBTEL EM cross-correlation curve and the *SDO/AIA* cross-correlation curve.

### 7.2.2 EBTEL Diffuse Emission Simulation: Transition Region

In addition to the EBTEL coronal DEMs, § 6.4.2 presented the transition region DEMs. It is therefore also possible to test EM time-lag analysis and further test the ability for DEM inversion to recover  $\text{DEM}(T,t)$  from these simulations. This is particularly important as the EM time-lag analysis has returned fewer time-lags equal to *zero* than time-lag analysis on *SDO/AIA* data alone.

Returning to the  $193 \text{ \AA} - 171 \text{ \AA}$  and  $211 \text{ \AA} - 171 \text{ \AA}$  channels pairs, Figure 7.29 shows the cross-correlation value as a function of offset for the “observed” EBTEL DEM; the “observed” *SDO/AIA* data (synthesised by folding the EBTEL  $\text{DEM}(T,t)$  through the *SDO/AIA* response functions); the DEM from inversion; and finally the *SDO/AIA* data synthesised from DEMs obtained by inversion. Here, for both channel pairs, all four of the cross-correlation values as a function of offset peak at *zero* with the cross-correlation values near unity.

For these transition region simulations it is clear that for in-phase light-curves, the DEM rises and falls in each bin in phase, and this finally results in synthesised *SDO/AIA* observations that are in-phase. In comparison to coronal simulations, the EBTEL DEM bins are less noisy and therefore the cross-correlation is higher.

From the coronal and transition region EBTEL simulations ( $193 \text{ \AA} - 171 \text{ \AA}$ ) it is clear that the transition region response to nanoflare heating is not significantly masked by the *SDO/AIA* response functions. That is to say that the in-phase brightenings observed in *SDO/AIA* are also observed in the DEM bins themselves.

The time-lags observed in EM time-lag analysis of the transition region do not depend on the re-binning of the DEM. The original DEM is seen to rise and fall in-phase and this behaviour would be observed regardless of the exact re-binning chosen.

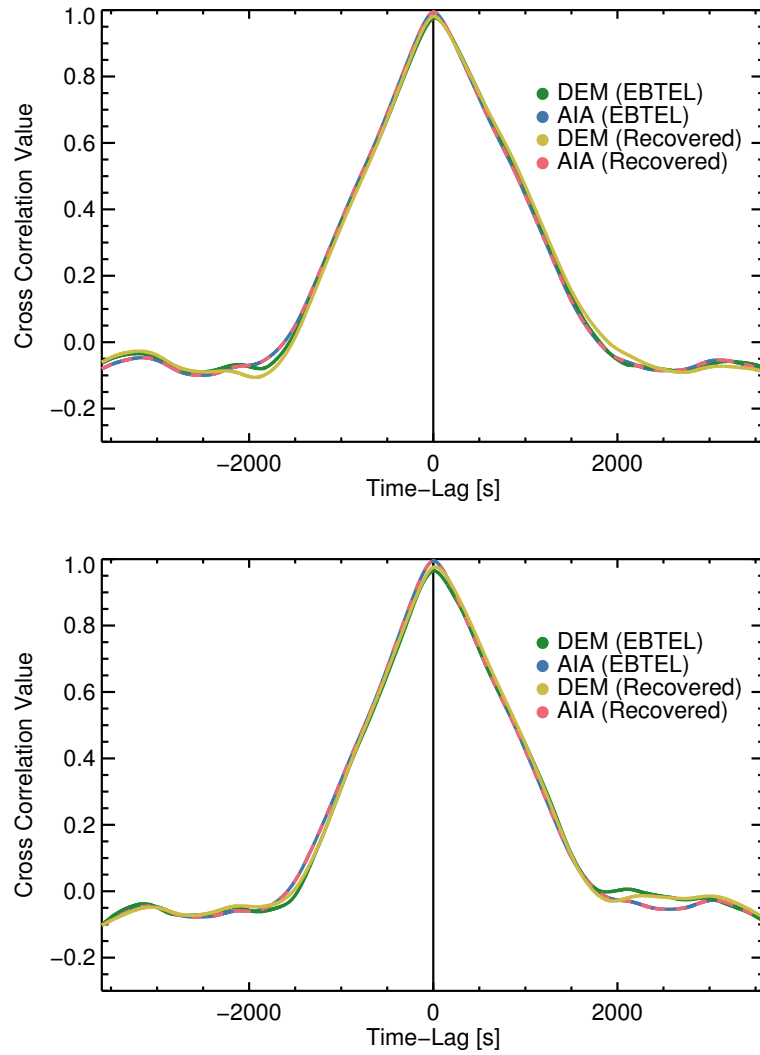


Figure 7.29: *Top*: Cross-correlation value as a function of offset for the 193 Å – 171 Å channel pairs (observed, blue; synthesised, pink) for the EBTEL Transition Region DEMs. *Bottom*: As *top*, but with cross-correlation value as a function of offset for 211 Å – 193 Å.

### 7.2.3 Steady Heating “Simulations”

Finally, it is also of interest to see how the injection of noise influences the results of time-lag analysis. Using the steady heating simulations presented in § 6.4.3 (Viall & Klimchuk, 2013), it is of interest to understand how the injected noise propagates through DEM( $T,t$ ) inversion.

If the method for DEM inversion was not relatively stable with regards to noise, this would lead to discrepancies between the original and DEM( $T,t$ )-synthesised *SDO/AIA* time-lags. The simulations outlined in § 6.4.3 consist of mean values with the addition of Poisson noise. Figure 7.30 shows the original time-lag results for the (simulated) *SDO/AIA* 193 Å – 171 Å channel pair, with the peak cross-correlation value at  $\sim -250$  s (blue). Additionally shown is the cross-correlation value as a function of time for the recovered 193 Å – 171 Å channel pair. In this case, a pink diamond indicates the time-lag. From these two curves, for this set of observations, the behaviour is preserved through DEM inversion, and the original time series and time-lags are recoverable in the DEM( $T,t$ )-synthesised data.

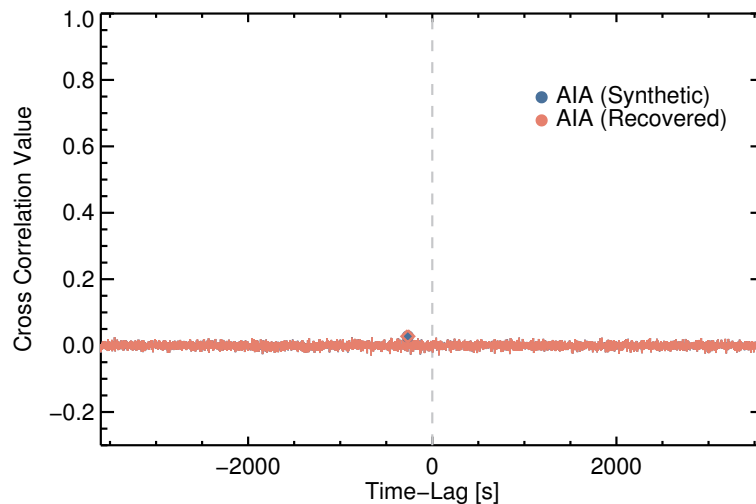


Figure 7.30: Cross-correlation value as a function of offset for the 193 Å – 171 Å channel pairs (observed, blue; synthesised, pink) for the simulated steady heating outlined in § 6.4.3. Both the observed and synthesised time-lags are in agreement.

## 7.3 Discussions and Conclusions

This chapter has concentrated on observations of NOAA AR 11082 that were used for the initial introduction of time-lag analysis by Viall & Klimchuk (2011, 2012). This chapter has used these same observations to introduce the concept of EM time-lag analysis on the four pixels of emission studied with time-lag analysis (see Chapter 6). The general idea is that by performing DEM( $T,t$ ) inversion and extracting the EM time series from locations near the peak of the *SDO/AIA* channels, the true (underlying) time-lag signature in temperature-space (the signature that is potentially masked by the *SDO/AIA* temperature response functions) can be extracted. To perform this analysis, this chapter has primarily concentrated on the *SDO/AIA* 193 Å – 171 Å channel pair, which corresponds to DEM bins **C**, and **B** (see, Figure 7.1). These channels were chosen as they have relatively isothermal response functions in a region of temperature-space that is well-constrained by *SDO/AIA* for DEM inversion. The idea was that the results from the *SDO/AIA* 193 Å – 171 Å channel pair and EM **C** – **B** time-lags should be similar due to the isothermal nature of the *SDO/AIA* temperature response functions. In this chapter it became clear that DEM inversion was able to well-recover the time series from a number of channels (171 Å, 193 Å, and 211 Å) without the need to consider uncertainties propagated from DEM inversion. This behaviour was clear as the cross-correlation value as a function of offset for both the observed *SDO/AIA* channel pairs, and the DEM-synthesised *SDO/AIA* channel pairs were nearly identical over time, and therefore the EM time-lags were interpretable: if the DEM cannot reconstruct the original (input) data, the DEM does not represent that data.

**Pixels 1 & 2** – Pixel 1 corresponds to a pixel of diffuse emission (similar in location to the pixel studied in Viall & Klimchuk, 2012), and Pixel 2 corresponds to an additional pixel of fan loop emission (See Figure 7.2). For these two pixels DEM( $T,t$ ) was able to accurately recover the time series originally observed in *SDO/AIA* 171 Å, 193 Å, 211 Å, and importantly, this was without the need to consider the uncertainties on the recovered data which cannot be used with time-lag analysis.

After excluding regions where the DEM  $\leq 0$  at  $\geq 1$  DEM bin (**C**, **B**) in the 12 hour time series, the time-lag maps for the original and synthesised *SDO/AIA* 193 Å –

171 Å channel pair were in good agreement. That is, the original *SDO/AIA* 171 Å, and 193 Å time series are accurately reproduced in the majority of pixels which leads to the synthetic time-lag map having nearly-identical time-lags to those observed with the original data. Significantly, EM time-lag analysis appears to assign non-zero values to a large number of time-lags that are reported as *zero* in both the observed and synthesised *SDO/AIA* 193 Å – 171 Å time-lag maps. This behaviour appears to be the result of the *SDO/AIA* temperature response functions masking the underlying time-lag signature, however further investigation of this is required with additional simulations. Within the EM and *SDO/AIA* time-lag maps there are a number of regions where *zero* values persist through DEM inversion. For Pixel 1 there is a  $8 \times 12$  pixel region that is observed to be co-spatially located with the brightening observed in all *SDO/AIA* channels at the beginning of the time series, and in Pixel 2 there are a number of similar regions including one that consistent with a fan loop brightening in-phase at the end of the 12 hour time series (See Figure 7.8, and Figure 7.15). These *zero* values appear to be consistent with the idea that a *zero* time-lag is the transition region response to heating. As discussed in § 6.4.2, while *zero* time-lags observed from *SDO/AIA* time-lag analysis can be related to the transition region response to a coronal nanoflare, Uritsky *et al.* (2013) observed propagating disturbances along the fan loops shown here. If the loops were to move in and out of a pixel region, this would result in in-phase behaviour, and this could be the reason for the large fraction of *zero* time-lags observed from *SDO/AIA* time-lag analysis in this region of the image.

**Pixel 3** – Pixel 3 corresponds to active region core emission which is consistent with a brightening loop, and has significant emission consistent with hot plasma. As with Pixels 1, and 2, DEM(T,t) was able to accurately recover the time series originally observed in *SDO/AIA* 171 Å, 193 Å, 211 Å.

Excluding the regions of overlap between the rectangular regions used in the analysis of Pixel 1 and Pixel 2, while the assignment of non-zero values to pixels which had time-lags of *zero* in *SDO/AIA* time-lag analysis is seen, the majority of EM time-lags obtained with the regularised inversion method are at the extremities ( $\pm 3600$  s). This behaviour needs further consideration, which will be discussed in § 7.3.2. As a first step to investigate these EM time-lags, it would be of interest to perform the same analysis with a number of other DEM inversion methods in order to understand if these

methods lead to the same EM time-lag signatures as seen here. Alternative methods for generating the EM time series will be discussed in § 7.3.2.

**Pixel 4** – Pixel 4 corresponds to a loop footpoint. As with Pixels 1, 2, and 3, DEM(T,t) was able to accurately recover the time series originally observed in *SDO/AIA* 171 Å, 193 Å, 211 Å. During the original 12 hour time series, there were seven instances at which the DEM was not recovered. This led the values for the reconstructed intensity in *all SDO/AIA* intensity to be *zero*. These values were interpolated over which did not significantly affect the analysis of these time series: the cross-correlation value as a function of time was nearly identical for the observed and synthetic 193 Å – 171 Å channel pair.

With the regions where the DEM was  $\leq 0$  for  $\geq 1$  DEM bin (**B**, **C**) in the 12 hour series (including the pixel studied here), the original and synthesised *SDO/AIA* time-lag maps were in good agreement as has been seen throughout these regions. Interestingly, while there are a number of pixels where the time-lag is at the maximum offset value ( $\pm 3600$  s), this behaviour is also seen in the original *SDO/AIA* time-lag maps, and there is also a large number of values that have been assigned non-zero, non-maximum time-lag values. Similarly to those maximum values seen in Pixel 3, the presence needs to be further investigated. In this rectangular region there is also a number of *zero* values that are not assigned non-zero values in EM time-lag analysis. These pixels are consistent with the loop footpoints that brighten in phase at  $t = 4000$ s.

**EBTEL Coronal Simulations** – For the 193 Å – 171 Å channel pair, as with the individual pixels, the “observed” and DEM-synthesised *SDO/AIA* cross-correlation value agrees as a function of offset, including the time-lag. This indicates that DEM inversion is able to recover the original input data. To understand how well the recovered temperature distribution represents the ground truth, the DEMs can be recovered from the “observed” *SDO/AIA* data, by inversion. Therefore we are performing the same time-lag analysis, but this time on the temperature distributions themselves. The cross-correlation value as a function of offset for the “observed” EBTEL EM time series, and the recovered EM time series shows that while the time-lag is identical in offset (albeit the recovered EM time-lag being located at a higher cross-correlation value), regularised inversion did not perfectly recover the DEM(T,t), which is not sur-

prising since there are many possible solutions. Importantly, as a function of offset, these two time series are different. The cross-correlation value as a function of offset for the EM time series appears to have properties of both the “observed” *SDO/AIA* cross-correlation curve and the “observed” EM curve for this channel pair. This is expected as the DEM is sensitive to the data (and the temperature response functions).

Similarly, the same method was applied to the 211 Å – 193 Å channel pair. This was done as for Pixels 1 and 2, the cross-correlation values for the *SDO/AIA* channel pair were well-recovered through DEM inversion, and the the results of EM time-lag analysis for the DEM bins that correspond to these channels were highly correlated, but shifted to more positive values. Performing the same analysis on this channel pair allowed us to investigate the difference between *SDO/AIA* time-lag analysis and EM time-lag analysis. As with the 193 Å – 171 Å channel pair the recovered EM cross-correlation values appear to be a convolution of the “observed” *SDO/AIA* and EM time-lag analysis. This is not surprising as there will be some sensitivity to the input data and the temperature response functions. Here, for the “observed” EM time-lag analysis the time-lag is located at a more positive value of offset when compared to the *SDO/AIA* time-lag as we observed in the active region data. The recovered EM time-lag analysis peaks at a similarly shifted value, again at higher cross-correlation value.

**EBTEL Transition Region Simulations** – The same analysis as for the EBTEL coronal simulations was applied to the transition region simulations. For both the “observed” (EBTEL-synthesised) and DEM-synthesised *SDO/AIA* channel pairs, the cross-correlation agrees as a function of offset, with a time-lag of  $\sim 0$  s. The same behaviour is also observed in the equivalent EM analysis, and this is seen in both the 193 Å – 171 Å and 211 Å – 193 Å channel pairs. This is not surprising as the EBTEL DEM is observed to only change in emission measure, and the temperature distribution remains relatively constant. This means that regardless of the re-binning of the DEM, these EM time-lags will be in-phase. The result is however important. In the EM time-lag maps presented in this chapter there are significantly fewer *zero* time-lags than in the *SDO/AIA* time-lag maps. Further investigation is needed with regards to the other possible causes of *zero* time-lags (see [Viall & Klimchuk, 2016](#)).

### 7.3.1 Summary

From the analysis of Pixels 1 and 2 (§ 7.1.2, § 7.1.3), the rectangular regions show that EM time-lag analysis recovers time-lag maps that are similar to the original *SDO/AIA* time-lag maps (especially in locations where the *SDO/AIA* time-lags were non-zero), and these EM time-lag maps appear to assign non-zero values to a significant portion of the pixels with zero values in the *SDO/AIA* time-lag maps. This behaviour tends to indicate that  $\text{DEM}(T,t)$  recovers the underlying time-lag, which in some cases has been masked by the temperature response functions of *SDO/AIA*. This behaviour is shown as a zero time-lag in the original and synthesised *SDO/AIA* time-lag pair, and non-zero in the EM time-lag. Importantly, the non-zero values in the EM time-lag maps are similar to the values for adjacent non-zero *SDO/AIA* pixels.

The time-lags observed in the active region core pixel (Pixel 3) display some general interpolation as seen in Pixels 1 and 2, however the majority of EM time-lags are at the maximum possible offset ( $\pm 3600$  s). There are a number of assumptions on the temperature response functions (and for DEM inversion), and it may be the case that these assumptions no longer hold. Furthermore, it could also be the case that this is a limitation of the DEM inversion method itself: due to the ill-posed nature of DEM reconstruction, there are a large number of DEM solutions that could accurately reconstruct the input *SDO/AIA* data. Therefore, the recovered temporal evolution of  $\text{DEM}(T)$  may not accurately represent the dynamics (the heating and cooling) along the line-of-sight even though it is able to reconstruct the original time series used to create the  $\text{DEM}(T,t)$ . By using alternative DEM inversion methods, a disagreement between EM time-lags derived from different inversion methods would highlight issues with DEM inversion.

### 7.3.2 Further Work: Alternative DEM Methods

In an attempt to understand if these extreme time-lag values are physical or a result of the DEM inversion itself, Figure 7.31, shows the DEM maps obtained through Basis Pursuit (BP Cheung *et al.*, 2015, § 3.4.4). These BP DEM maps were calculated as with the RI DEM Maps (Figure 7.3) for the *SDO/AIA* data presented in Figure 7.2. The BP DEM maps are in good agreement in temperature bins **B**, **C**, **D** (where **C**, **B** have been used extensively in this work). There is a significant amount of additional

emission measure in **A** which is a result of BP including a significant low-temperature component, and while **E** and **F** are in general agreement, there are slight differences outwith the active region core in bin **E**, and more emission measure in bin **F**. Again, this is however expected as the DEM is less well-constrained at the extremes (**A**, **F**).

Unfortunately, there are a significant number of *zero* values in temperature bin **B** in the core of the active region (the region of interest; shown as black pixels) which leads to complications when performing time-lag analysis with BP DEMs. While further investigation of DEM inversion with various sets of BP basis functions is required, a deep learning approach to DEM inversion, DeepEM (which will be briefly introduced in § 9.3), is able to provide non-*zero* DEMs for every *SDO/AIA* pixel. Using a single  $512 \times 512$  set of *SDO/AIA* images and the equivalent DEM maps (from BP), the neural network has learned a generalised mapping from the 6-dimensional observational-space to the 28-dimensional DEM-space. Using data that DeepEM has not seen previously, the solutions are comparable to BP (see Figure 9.1). It will therefore of interest to further investigate the results of EM time-lag analysis on DeepEM solutions as theoretically the DeepEM solutions will be relatively stable to noise perturbations if this generalised mapping has been learned correctly.

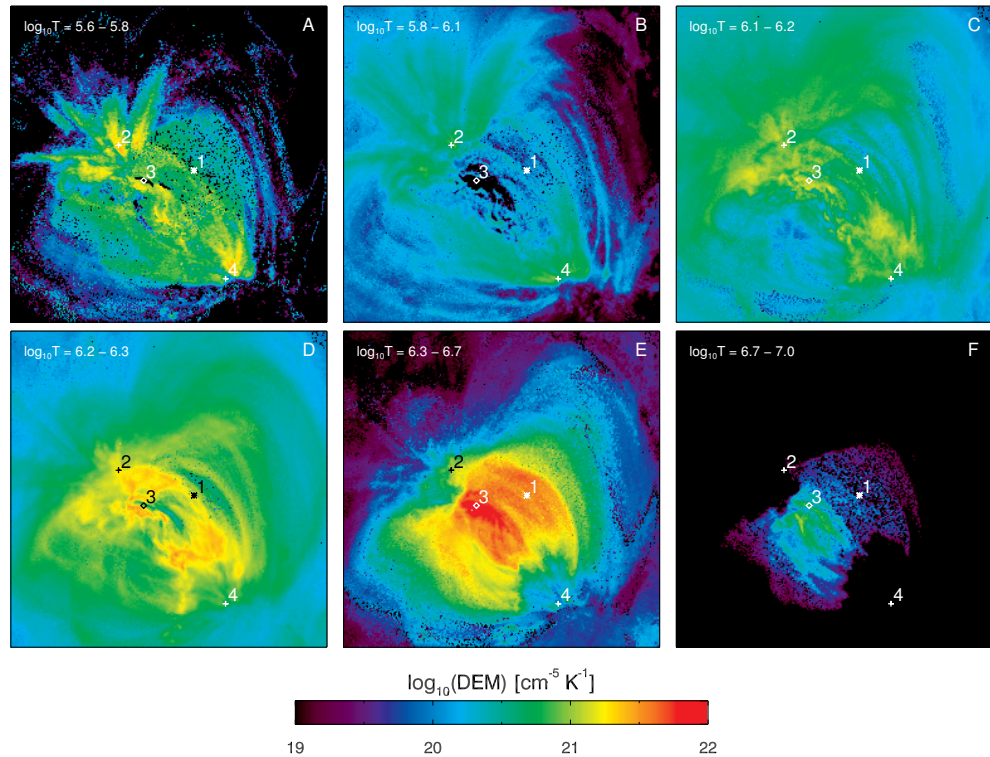


Figure 7.31: Basis Pursuit (BP) DEM maps rebinned from 28 temperature bins to six temperature bins chosen to coincide with the peak temperature response functions of the *SDO/AIA* response functions. These BP DEM maps can be directly compared to the RI DEM maps shown in Figure 7.3, and there is good agreement where the DEMs are generally well-constrained (temperature bins **B**, **C**, **D**).

# Chapter 8

## Wavelet Analysis

Solar coronal light curves are generated by complex systems so their study can elucidate the underlying processes. In particular, in this thesis we are interested in the signatures of coronal heating by small flares, however many mathematical methods used to examine these light-curves (e.g. Fourier analysis, or time-lag analysis; Chapter 6) identify persistent timescales of variation present throughout the time series. Wavelet analysis allows the relative importance of behaviour at different time-scales to vary throughout the time series so wavelet analysis is able to capture (for example) brief episodes of rapid fluctuations within an otherwise slowly evolving time series. This final chapter will introduce wavelet analysis before providing a *test-case demonstration* of how the wavelet transform can expand time-lag analysis in to the time-frequency domain for future investigations. Furthermore, Local Intermittency Measure (a modification of wavelet analysis suited to identifying periods of intermittent behaviour, [Farge, 1992](#)) will be briefly demonstrated on the 155-hour time series initially presented by [Froment et al. \(2015\)](#).

The wavelet coefficient  $W(i, \tau)$  for a discrete time series  $x_i = x(t_i)$ ;  $i = 0, \dots, N - 1$ , is given as:

$$W(i, \tau) = \sum_{j=0}^{N-1} x_j \psi^* \left[ \frac{(j-i)\delta t}{\tau} \right], \quad (8.1)$$

where  $W(i, \tau)$  indicates the time-frequency dependence ( $\tau$  is the time-scale on which the time series is varying);  $\psi^*$  represents the wavelet basis function complex conjugate; and  $\delta t = t_{i+1} - t_i \equiv t_1 - t_0$ , is the *constant* time-step in the time series. The Wavelet

Power Spectrum (WPS) is then described as

$$\text{WPS}(i, \tau) = |W(i, \tau) W^*(i, \tau)|, \quad (8.2)$$

whereas before, \* denotes the complex conjugate.

In practical applications of wavelet analysis, there are numerous wavelet basis functions ( $\psi$ ) that can be chosen for computation of the wavelet coefficient. Table 1 in [Torrence & Compo, 1998](#) provides details of three wavelet basis functions: the Morlet, Paul, and the derivative of the Gaussian (DOG). Each of these functions is governed by the classical version of Heisenberg's uncertainty principle: a trade-off between the time ( $\Delta t$ ) and frequency ( $\Delta \omega$ ) domains exists ( $\Delta t \cdot \Delta \omega$  has a defined minimum).

In this work we choose the commonly used Morlet wavelet as this wave function has good time-frequency localisation (e.g. [Grinsted \*et al.\*, 2004](#); [De Moortel \*et al.\*, 2004](#)).

## 8.1 Demonstrating Wavelet Analysis

In order to demonstrate Wavelet analysis we have utilised the wavelet software provided by [Torrence & Compo \(1998\)](#)<sup>1</sup>, and this section will concentrate on the observations initially introduced in [Froment \*et al.\* \(2015\)](#), and further analysed in [Auchère \*et al.\* \(2016\)](#). These are used to demonstrate wavelet analysis for two reasons: the first is that there is a clear periodicity in this data; secondly, these data have already been fitted with the background model that will be discussed later ([Auchère \*et al.\*, 2016](#)).

[Froment \*et al.\* \(2015\)](#) initially presented 155 hours of coronal *SDO/AIA* observations within a loop region that shows clear pulsations in the 335 Å channel. Using Fourier Analysis and a  $10\sigma$  detection threshold, [Froment \*et al.\* \(2015\)](#) detect a 9-hour period in all optically-thin *SDO/AIA* channels (with the exception of 171 Å), and this is most obviously seen in the 335 Å channel where there is a  $40.9\sigma$  detection at this period. Two explanations were put forward by [Froment \*et al.\* \(2015\)](#) to explain the periodicity in the data: an impulsive scenario with periodic changes in the frequency of heating events (the time between successive nanoflare events changes), or this behaviour could be the result of quasi-continuous heating at the loop footpoints which would drive a thermal non-equilibrium cycle. [Auchère \*et al.\* \(2016\)](#) reassessed the significance of the

---

<sup>1</sup>This software is available at <http://atoc.colorado.edu/research/wavelets/>.

pulsation detection made in [Froment \*et al.\* \(2015\)](#) by performing wavelet analysis on the 335 Å time series.

Figure 8.1 (*top*) shows the 155 hour *SDO/AIA* 335 Å time series normalised to the standard deviation as described in [Torrence & Compo \(1998\)](#). Prior to performing wavelet analysis, [Torrence & Compo \(1998\)](#) zero-pad the data (to reduce artefacts in the wavelet power spectrum), and for Fourier analysis these data have been apodized using the Hann window in order to smooth discontinuities at the beginning and end of the time series (which can lead to artefacts in the Fourier power spectrum). Figure 8.1 (*right*) therefore shows the Fourier Power Spectra (black histogram), and the average wavelet spectrum (thick black line).

To test the significance of peaks in the WPS, and the Fourier Power Spectrum (FPS), an appropriate background model must first be chosen as the confidence levels are linked to the background model. The wavelet code of [Torrence & Compo \(1998\)](#) provides models such as white noise which is represented by a flat power-spectrum. [Ireland \*et al.\* \(2015\)](#) and [Auchère \*et al.\* \(2016\)](#) note that any model needs to consider the power spectra of coronal time series as there is an inherent power-law property of coronal time series (as can be seen in Figure 8.1, *right*). [Gruber \*et al.\* \(2011\)](#); [Inglis \*et al.\* \(2015\)](#); [Ireland \*et al.\* \(2015\)](#) discuss that for quasi-periodic pulsation (QPP) observations of solar flares, numerous authors had not recognised the power-law dependence of the power spectra. As a result, a non-physical background model led to erroneous confidence levels in previous studies: 18 of 19 time series re-analysed by [Inglis \*et al.\* \(2015\)](#) were determined to no longer have significant periodicities.

Consequently, both [Ireland \*et al.\* \(2015\)](#) and [Auchère \*et al.\* \(2016\)](#) define models for the background spectrum which include a power-law component. The physical presence of this power-law component can be described as a manifestation of exponentially decaying pulses superimposed along the line of sight, consistent with the idea of nanoflare heating ([Ireland \*et al.\*, 2015](#)). Following the approach of [Auchère \*et al.\* \(2016\)](#), the FPS (Figure 8.1, *right*) is fitted with a three-component model. The model (of mean power) is of the form

$$\sigma(\nu) = A\nu^s + BK_p(\nu) + C, \quad (8.3)$$

with

$$K_\rho(\nu) = \left(1 + \frac{\nu^2}{\kappa\rho^2}\right)^{-\frac{\kappa+1}{2}}. \quad (8.4)$$

Here, the first term,  $A\nu^s$ , is the power-law which is the result of *stochastic* fluctuations; the second term,  $BK_\rho(\nu)$ , is a Kappa function chosen to simulate pulses within the time series; the constant term,  $C$ , corresponds to a background white-noise component that is physically expected through photon statistics. This is similar to the model of Ireland *et al.* (2015), where instead of the Kappa function, a Gaussian-shaped contribution is used:

$$G(\nu) = \alpha \exp\left[-\frac{(\ln(\nu) - \beta)^2}{2\delta^2}\right]. \quad (8.5)$$

In Figure 8.1 (*right*) the model in Equation 8.3 is fitted to the FPS, and is represented by a solid red line, with each component individually shown as dashed red lines. This model can be compared to the solid black line and the black histogram (the average wavelet spectrum, and the FPS). With a background model fitted, the whitened wavelet spectrum (the wavelet spectrum minus the background model) can then be plotted (Figure 8.1, *left*). In the whitened wavelet spectrum, the white hatched region is the “cone of influence” (COI) which arises as a result of using a time series with a finite length. The COI is the region where the edge effects become important (Torrence & Compo, 1998), and has larger influence as scales approach the length of the time series (and values within this hatched region cannot be trusted).

With the FPS, the whitened WPS, and the background model determined, confidence levels are then calculable. It is important to note that in addition to fitting a physically appropriate background model, Auchère *et al.* (2016) discuss that the confidence levels introduced by Torrence & Compo (1998) (“TC”) are local, and therefore do not take in to consideration the total number of degrees of freedom in the wavelet spectra. This can therefore produce false positive detections. For example, for the FPS, the 95% (TC) level is described as a 5% probability that by chance, the FPS is greater than the 95% local level in a given frequency bin. However, as each bin is independent with a sufficient number of frequency bins ( $\sim 512$ ), the probability that at least one bin has a value greater than the 95% local wavelet (TC) level approaches 1. Auchère *et al.* (2016) therefore derive the 95% global confidence level which takes in to account the total number of degrees of freedom (see § 4.1, Auchère *et al.*, 2016), and in Figure 8.1 this level is represented by a solid grey line.

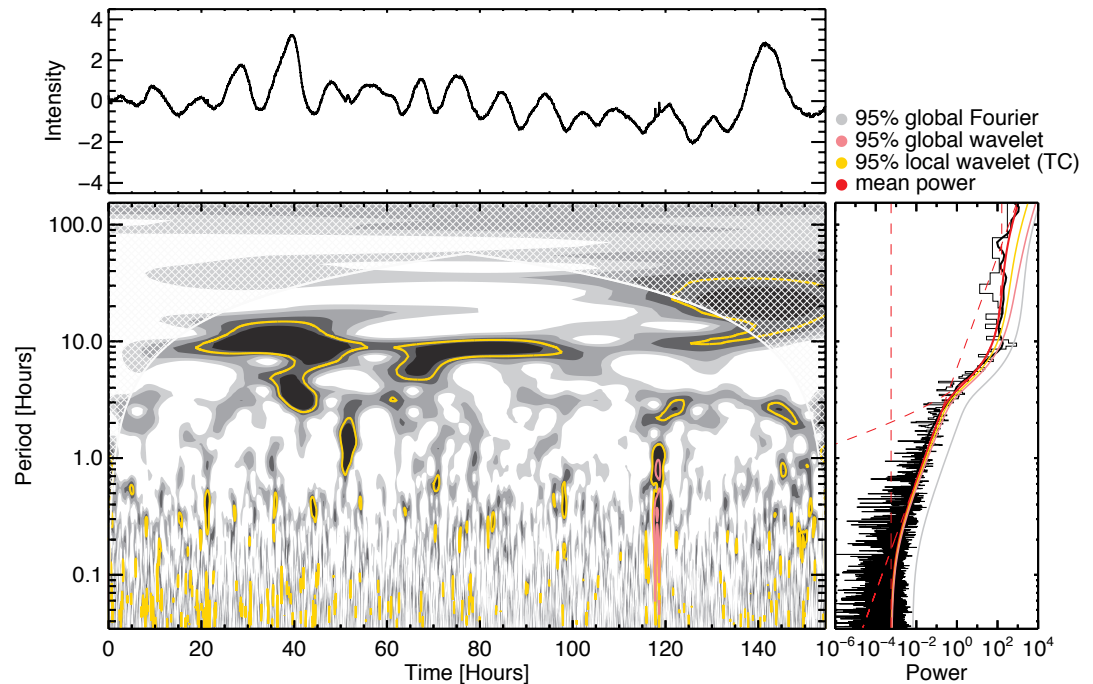


Figure 8.1: Wavelet (*left*) and Fourier analysis (*right*) of the 155-hour *SDO/AIA* 335 Å time series (*top*) initially presented in [Froment \*et al.\* \(2015\)](#). The Wavelet analysis (*left*) shows the whitened wavelet spectrum, where the background model is defined in Equation 8.3. As in [Froment \*et al.\* \(2015\)](#); [Auchère \*et al.\* \(2016\)](#), the peak of the Fourier Power is located at ( $\sim 9$  hr). Both the FPS and the time-averaged wavelet spectrum are above the respective global confidence levels (pink, grey).

Deriving similar confidence levels is more complicated for the wavelet spectrum as these bins are not statistically independent. The yellow contours in Figure 8.1 represent the 95% local wavelet (TC), and by performing Monte-Carlo simulations [Auchère \*et al.\* \(2016\)](#) derive a 95% global (wavelet) confidence level and a global time-averaged confidence level (pink in Figure 8.1).

With these calculated, Figure 8.1 displays the whitened wavelet spectrum (*left*), and the FPS (*right*), with the 95% local wavelet confidence level shown in yellow; the 95% global wavelet confidence level shown in pink; and the the 95% global Fourier confidence level shown in grey. Figure 8.1 shows both the FPS and time-averaged wavelet spectrum are above the respective global confidence levels at a period of  $\sim 9$  hours. In addition, there are two impulsive events located at  $t \sim 120$  hours, highlighted

by pink contours extending up to a period of  $\sim 2$  hours.

## 8.2 Wavelet Coherence

In addition to performing wavelet analysis on a single time series, it is also often desirable to examine two time series together as they are often linked. As has been seen in Chapter 6, the *SDO/AIA* EUV light curves in different wavelength channels have peak temperature response functions at different temperatures, and as material cools it will be more visible in different channels.

As in the previous section, here we use the Morlet wavelet, and in this case, the cross wavelet transform (XWT) is defined as:

$$\text{XWT}^{XY} = |W^X W^{Y*}|, \quad (8.6)$$

where  $X$  and  $Y$  are two time series, and  $W$  is the wavelet coefficient. The XWT exposes the common power (between  $X$  and  $Y$ ), and reveals a relative phase in time-frequency space (Grinsted *et al.*, 2004; Torrence & Webster, 1999)<sup>2</sup>.

The *wavelet coherence* of the two time series is then defined as the absolute value squared of the smoothed cross wavelet spectrum, which is normalised by the smoothed WPS (Appendix 2 Torrence & Webster, 1999):

$$R^2 = \frac{|\langle \tau^{-1} W^{XY}(i, \tau) \rangle|^2}{\langle \tau^{-1} |W^X(i, \tau)|^2 \rangle \langle s^{-1} |W^Y(i, \tau)|^2 \rangle} \quad (8.7)$$

with  $\langle \cdot \rangle$  indicating smoothing in time and scale (period), and results in values of  $0 \leq R^2 \leq 1$ . Furthermore the phase angle between the two time series, and the mean phase angle, in the time-frequency domain is calculable (Grinsted *et al.*, 2004).

For time-lag analysis (which was introduced in Chapter 6), the idea is by cross-correlating two time series for a set of offsets one is able to disentangle the lag between these channels, and as such, this analysis disregards the time-dependence of this behaviour. Using wavelet coherence on these two time series can then be studied in the time-frequency domain. Unfortunately, converting the phase angle to a time-lag is not trivial: there is a non-uniqueness problem in the conversion, and in order to perform this conversion the wavelength must be known, however, the phase angle is a function

<sup>2</sup><http://grinsted.github.io/wavelet-coherence/>

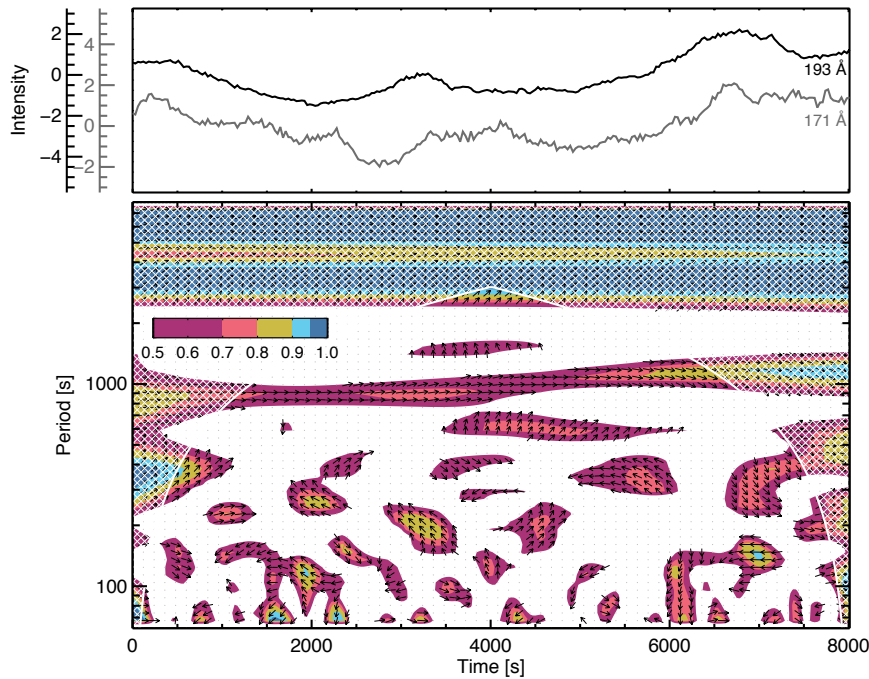


Figure 8.2: Wavelet Coherency and phase between *SDO/AIA* 193 Å, and 171 Å. Contours are shown for values of the wavelet squared coherency greater than 0.5. Vectors represented by arrows indicate the phase difference between the first and second time series. In order to provide clarity, vectors are plotted for values of coherency  $> 0.5$ , and have been down-sampled in time-frequency space (grey dots indicate the resolution at which phase angles are shown).

of both time and scale (period),  $\tau$ . Under the trigonometric usage (e.g. [Dolla \*et al.\*, 2012](#)),  $0$  ( $\rightarrow$ ) represents the two time series being in-phase, while  $\pi$  represents these two time series are in anti-phase ( $\leftarrow$ ). Furthermore,  $\frac{\pi}{4}$  ( $\nearrow$ ), indicates 171 Å lags 193 Å by  $\frac{\pi}{4}$ , and  $\frac{-\pi}{4}$  ( $\searrow$ ) indicates that 193 Å lags 171 Å by  $\frac{\pi}{4}$ .

Figure 8.2 shows wavelet coherence and phase between the *SDO/AIA* 193 Å ( $X$ ) and 171 Å ( $Y$ ) observations of the pixel of diffuse emission (§ 6.2.2; Figure 6.7). This is equivalent to the 193 Å – 171 Å channel pair for the pixel of diffuse emission in Chapter 6. Figure 8.2 (*top*) shows the two time series, which have been normalised to the standard deviation (as described in [Torrence & Compo, 1998](#)) with 193 Å plotted in black and 171 Å plotted in grey. Figure 8.2 (*bottom*) shows the cross wavelet power,

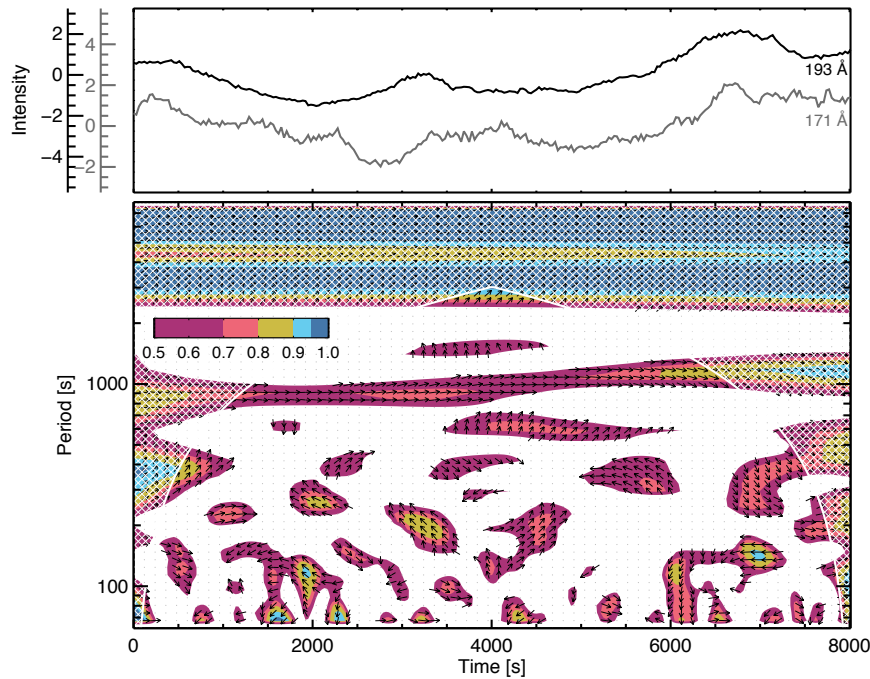


Figure 8.3: Wavelet Coherency and phase between the DEM-synthesised *SDO/AIA* 193 Å, and 171 Å channels. Contours are shown for values of the wavelet squared coherency greater than 0.5. Vectors represented by arrows indicate the phase difference between the first and second time series. In order to provide clarity, vectors are plotted for values of coherency  $> 0.5$ , and have been down-sampled in time-frequency space (grey dots indicate the resolution at which phase angles are shown).

which reveals areas of common power (contours are shown for areas where  $R^2 > 0.5$ ). In addition to the contours of cross wavelet power, a set of arrows indicating the phase angles are also shown. The underlying grid upon which these angles are determined is shown as grey dots, and for clarity the arrows are only shown for the regions where  $R^2 > 0.5$ .

For the longest periods that are not covered by the COI, the phase angle is constant as a function of time, and indicates that 193 Å leads, which is consistent with what was seen for time-lag analysis. In time-lag analysis, for these time series (see Figure 6.7), the lag between the two channels was  $\sim 250$  s, showing that 171 Å lags 193 Å, as shown in Figure 8.2. Interestingly, at other periods, it is observed that there are in-

phase time-lags extending diagonally from  $\sim 800$  s to up  $\sim 1500$  s (which is consistent with the period of time series increasing in unison), and at the smallest scales ( $\sim 60$  s) there are also regions of in-phase behaviour. These in-phase regions are located at  $\sim 250$  s,  $\sim 3500$  s, and  $\sim 6500$  s where brightenings are observed in the two time series.

Additionally, this same method can be applied to the equivalent DEM-synthesised time series, those that were used to quality check DEM inversion in Chapter 7. Performing the same analysis on the DEM-synthesised 193 Å, and 171 Å time series, Figure 8.3 shows that both plots agree on all scales, and this suggests that the DEM is able to reconstruct the input data without the need to consider uncertainties, which cannot be used with time-lag analysis in Chapter 6. Furthermore, this could eventually be performed on the EM time series (from simulations, and DEM inversion; e.g. C - B; see Chapter 7), however this is beyond the scope of this proof-of-concept chapter.

### 8.3 Local Intermittency Measure

While the Local Intermittency Measure (LIM, Farge, 1992) was introduced for analysis of turbulent fluids, this method has rarely been implemented for the study of solar physics time series data. In the most basic terms, intermittency is a feature of fluctuations for which energy at a given scale is not evenly distributed in space (Bruno *et al.*, 1999), and while readily used in interplanetary science (see Bruno & Carbone, 2016), LIM has so far only been used to study hard X-ray and submillimeter solar flare time series (Dinkelaker & MacKinnon, 2013a,b; Giménez de Castro *et al.*, 2016).

The LIM is defined for each  $t_i$  in a time series, and for each time scale  $\tau$  from the wavelet transform as

$$\text{LIM}(i, \tau) = \frac{\text{WPS}(i, \tau)}{\langle \text{WPS}(i, \tau) \rangle_t}, \quad (8.8)$$

where  $\langle \cdot \rangle_t$  is the mean over the time interval for a fixed  $\tau$ . While the condition of  $\text{LIM} > 1$  highlights an intermittent process, it is the square of the LIM, a proxy for kurtosis  $K_4$  (Meneveau, 1991), that is used here. As for a Gaussian random variable the expectation value of  $K_4 = 3$ , the condition of intermittent behaviour is therefore

$$\text{LIM}(i, \tau)^2 > 3, \quad (8.9)$$

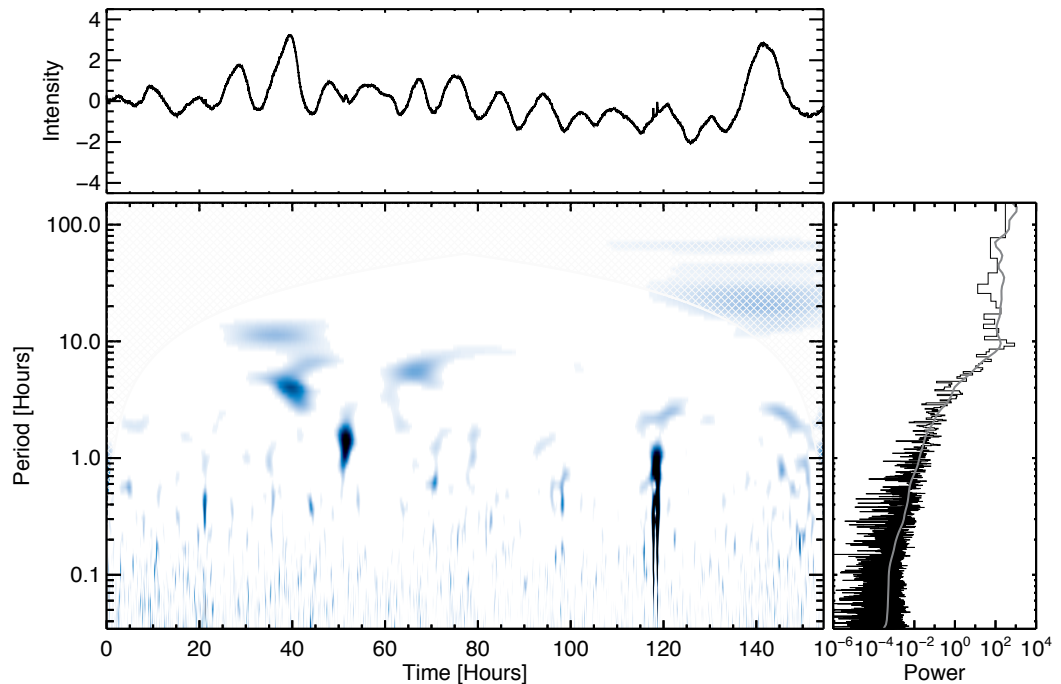


Figure 8.4: LIM<sup>2</sup> representation (*bottom*) of a 155 hour *SDO/AIA* 335 Å time series (*top*), plotted for values of LIM<sup>2</sup> > 3. Additionally shown is the FPS and the time-averaged wavelet power spectra (*right*). There are two main locations of intermimty observed, both coinciding with detections over the 95% local (and global) wavelet confidence levels (Figure 8.1). The first is located at  $\tau = 9$  hours (for a range of  $t$ ), and the second is located at  $t = 120$  hours (for a range of  $\tau$ ).

indicating a departure from Gaussianity—this signals that deterministic, rather than stochastic dynamics, are dominating (Bruno *et al.*, 1999; Marsch & Tu, 1994).

Here we present LIM<sup>2</sup> analysis on the *SDO/AIA* 335 Å coronal loop light curve (discussed earlier) that was seen to have regions of periodic behaviour on the order of  $\tau \sim 9$  hours between  $t = 20$  and  $t = 100$  hours in the time series. In addition, there is was an impulsive event observed at  $t \sim 120$  hours in the time series.

Figure 8.1 showed the 155-hour *SDO/AIA* 335 Å light curve (*top*), the FPS (*right*), and the whitened wavelet spectrum (*bottom*) with confidence levels derived from a background model. Figure 8.4 shows the equivalent LIM<sup>2</sup> analysis (LIM<sup>2</sup> > 3, *bottom*) for the same time series (*top*). For reference, the FPS and the time-averaged wavelet spectrum are plotted in black and grey respectively (*right*). It is clear in Figure 8.4

that without the need for background subtraction, the 9 hour periodicity observed by in Figure 8.1 is reproduced suggesting that this region is consistent with intermittency. Additionally, there is a large intermittent structure consistent with the location of the flaring ( $t \sim 120$  s), and a significant amount of disconnected intermittencies at scales of less than an hour.

## 8.4 Discussion and Future Work

This chapter has introduced wavelet analysis, and provided a *test-case demonstration* of how wavelet coherency can be applied to *SDO/AIA* EUV time series in the future. This chapter also introduced the concept of Local Intermittency Measure (LIM) on a time series, and here we present a number of avenues of further investigation.

Wavelet coherency is a powerful tool for the study of time series that are inherently linked, as is the case of two time series of different temperature coronal plasma. The power-law nature of the *SDO/AIA* time series are thought to be the result of unresolved exponential events superimposed along the line-of-sight (Ireland *et al.*, 2015), and by studying these time series together in the time-frequency domain the idea is that signatures of the coronal heating mechanism will be extracted. Unfortunately, calculating the time-lag from the phase angle is not trivial, and as such wavelet coherency has to be studied in a general sense. It will be of interest to expand this initial work to a set of simulations for different heating frequencies (such as those from EBTEL simulations) in order to understand if properties of the heating can be extracted from these time series when the heating properties are known.

Local Intermittency Measure has been introduced and applied to the 155-hour *SDO/AIA* 335 Å time series shown in Figure 8.1. LIM highlights intermittent processes, and here without the need for sophisticated background modelling and fitting. Figure 8.4 demonstrates that LIM can be applied to *SDO/AIA* time series and extracts regions that are consistent with the confidence levels in Figure 8.1. LIM could prove particularly useful for detecting intermittency as no model or background subtraction is required. This method could be applied to *SDO/AIA* coronal time series such as those in Chapters 6, and 7 in order to search for signatures of nanoflare heating.

# Chapter 9

## Conclusions and Future Work

This thesis has concentrated on a long-standing problem in heliophysics—the coronal heating problem. The work in this thesis investigated this problem in two main ways. The first has been to initiate the novel, yet highly successful, approach of trying to observe the smallest distinguishable heating events with a highly sensitive hard X-ray telescope, optimised for targets outside of the solar system (*NuSTAR*; Chapters 4, 5), and the second approach has been to study the unresolved ensemble of even smaller events (Chapters 6, 7, 8).

This final chapter brings together conclusions presented in the previous research chapters, and presents a number of potential future paths of investigation.

### 9.1 *NuSTAR* Microflares

Chapter 5 presented the first *NuSTAR* microflare that was observed in the EUV with *SDO/AIA*, soft X-rays with *Hinode/XRT*, and hard X-rays with *NuSTAR*. For three of the four *NuSTAR* observations of this region (pre-flare, decay, and post-flare phases), the spectrum is well fitted by a single thermal model of 3.2–3.5 MK, but the spectrum during the impulsive phase shows additional emission up to 10 MK, emission equivalent to the A0.1 GOES class.

As *SDO/AIA*, *Hinode/XRT*, and *NuSTAR* overlap in sensitivity this allowed the temperature distribution to be constrained over an unprecedented temperature range. Crucially this included the high-temperature component which is hard to constrain with *SDO/AIA* and *Hinode/XRT* alone. One of the by-products of this analysis was

that *Hinode*/XRT seemed to overestimate the contribution from high-Temperature emission in this microflare. This issue had been alluded to in the literature (Testa *et al.*, 2011; Cheung *et al.*, 2015; Schmelz *et al.*, 2015) however with *Hinode*/XRT alone, the high-temperature component of the temperature distribution is highly uncertain (e.g. Winebarger *et al.*, 2012), and was confirmed with these *NuSTAR* observations. We then find that the pre-flare DEM peaks at  $\sim 3$  MK and falls off sharply by  $\sim 5$  MK. During the microflare's impulsive phase, the emission above 3 MK is brighter and extends to 10 MK, giving a heating rate of about  $2.5 \times 10^{25}$  erg s $^{-1}$ .

Since these observations, Glesener *et al.* (2017) observed a similar GOES-class event (peak thermal energy of  $2.4 \times 10^{27}$  erg), again observing no non-thermal emission, but the observations show that the higher energy hard X-rays peak earlier indicating heating via non-thermal electrons or faint hotter plasma. Since 2015 smaller events have been detected, and there have also been indications of possible non-thermal emission (Hannah & Glesener, 2019).

In solar minimum, observations of microflares and non-flaring active regions will have higher livetimes (e.g. Hannah *et al.*, 2018, obtained a 3 s effective exposure from a one-minute observation), and these observations would greatly benefit from new, more sensitive, solar X-ray telescopes such as the *FOXSI* (Krucker *et al.*, 2014) and *MaGIXS* (Kobayashi *et al.*, 2011) sounding rockets, as well as the *MinXSS* CubeSats (Mason *et al.*, 2016). New data combined with *NuSTAR* observations during quieter periods of solar activity should provide detection of the high-temperature and possible non-thermal emission in even smaller microflares which should, in turn, provide a robust measure of their contribution to heating in active regions.

Finally, by obtaining observations from *Hinode*/EIS, *MaGIXS*, and *NuSTAR* the high-temperature component of the emission measure distribution for a non-flaring active region should be able to be fully constrained (as discussed in § 1.3).

## 9.2 Time-Lag Analysis

Chapter 6 introduced the concept of time-lag analysis (Viall & Klimchuk, 2011, 2012) on a pixel of diffuse emission (similar in location to the pixel studied by Viall & Klimchuk, 2012, Pixel 1, § 6.2.2). Following the introduction of time-lag analysis this

chapter expanded on the work of Viall & Klimchuk (2012) by presenting the same analysis for an additional three pixels. These pixels are studied throughout Chapter 6 and Chapter 7 and include a pixel of fan loop emission, Pixel 2, § 6.2.3; a pixel of active region core emission, Pixel 3, § 6.2.4; and an active region fan loop footpoint, Pixel 4, § 6.2.5. Pixels 1, 2, and 3 appear to display cooling through a wide range of channels pairs from varying peak temperatures, and are all consistent with the coronal response to low-frequency nanoflare heating. On the other hand, Pixel 4 reports time-lags of *zero* for each channel pair, consistent with transition region response to low-frequency nanoflare heating (§ 6.4).

One of the results presented in Viall & Klimchuk (2012) was that the *SDO/AIA* 94 Å acts as both a cool, and hot channel during time-lag analysis. This behaviour indicates that in some regions material is heated to the hotter  $\sim 7$  MK peak of 94 Å, and in other cases, material is only heated to  $\sim 2.5$  MK. This observed behaviour is a direct result of the bi-modal nature of the *SDO/AIA* 94 Å temperature response function and we therefore introduced the concept of the *SDO/AIA* 94 Å (Fe XVIII) – 335 Å channel pair for time-lag analysis. Using the empirical method outlined by Del Zanna (2013) (Equation 5.1), the *SDO/AIA* 94 Å (Fe XVIII) time series can be extracted from the 94 Å time series with using a combination of other *SDO/AIA* channels. By extending time-lag analysis to active region maps (§ 6.3), time-lag analysis is performed with the *SDO/AIA* 94 Å (Fe XVIII) – 335 Å in addition to the original 94 Å – 335 Å pair. From these observations it is clear that this method isolates the hottest material that is located in the core of the active region, with time-lags distributed over the complete range of possible time-lag values (with most cross-correlation values  $< 0.2$  outwith the core). Following the approach of Viall & Klimchuk (2012) time-lags were limited to  $> 0.2$ , which removed this apparent noise, further isolating *positive* time-lags to the core of the active region.

To further understand the time-lag results that were presented, § 6.4 discusses EBTEL simulations that were conducted by Viall & Klimchuk (2013, 2015). Such simulations are powerful as they allow varying heating scenarios to be simulated, and compared to observations. The simulations outlined in § 6.4 were performed by Viall & Klimchuk (2013, 2015) to simulate the pixel of diffuse emission (Pixel 1), and display similar cooling patterns to what was observed in NOAA AR 11082. As EBTEL returns both the coronal and transition region DEM at each time-step, these showed that

highly correlated in-phase time series (time-lag = *zero*) are indicative of the transition response to a coronal nanoflare (although, as discussed in Viall & Klimchuk (2016), and § 6.4.2.1, this is one of a few possibilities).

Looking to the future, the Fe XVIII approach introduced in this work could be applied additional active regions studied by Viall & Klimchuk (2017) (some of which have *Hinode*/EIS observations). While time-lag analysis cannot be applied directly to the *Hinode*/EIS observations, these observations could allow periodic checks between *SDO*/AIA and *Hinode*/EIS observations of Fe XVIII.

Furthermore, the method of recover the Fe XVIII from the *SDO*/AIA 94 Å filter channel is an empirical one (outlined in Del Zanna, 2013), with additional EBTEL simulations of various heating frequencies it would be a valuable exercise to compare how well this method isolates the 94 Å (Fe XVIII) time series in comparison to directly determining the relevant contribution from the simulated DEM.

### 9.3 EM Time-Lag Analysis

Chapter 7 builds on the work of Chapter 6 by introducing the concept of EM time-lag analysis. By first recovering the DEM ( $\log_{10}T = 5.6 - 7.0$ :  $\Delta\log_{10}T = 0.05$ ) at each pixel using in the  $250 \times 250$  *SDO*/AIA observations, the DEMs were re-binned into *six* temperature bins (**A - F**) chosen to correspond to peaks of the *SDO*/AIA temperature response functions over the temperature range that the DEM is recovered. Performing this as a function of time recovers the EM time series. Time-lag analysis can then be performed on the original and DEM-synthesised *SDO*/AIA data, and even on the EM time series (*EM time-lag analysis*).

By first performing time-lag analysis on the original *SDO*/AIA and DEM-synthesised *SDO*/AIA data the discrepancies between the original and DEM-synthesised time-lags indicate regions where DEM inversion was not able to accurately recover the original data. For the 193 Å – 171 Å channel pair, the original and DEM-synthesised *SDO*/AIA time-lags appear to generally agree. This indicates that DEM inversion was able to preserve the variability observed in the *SDO*/AIA 171 Å and 193 Å time series (without needing to consider uncertainties that propagate through DEM inversion). This is an important step as we are unable to assess the quality of the DEM inversion (without

simulations), and understanding if DEM inversion can recover the same time-lags as those observed in the original *SDO/AIA* data, is a basic quality indicator.

For the four pixels described in this chapter, DEM inversion was able to accurately preserve the variability in the *SDO/AIA* 171 Å, 193 Å, and 211 Å channels, and this was easily seen when plotting the cross-correlation as a function of offset. For each pixel a region of similar pixels was chosen, and time-lag maps for the original and DEM-synthesised *SDO/AIA* 193 Å – 171 Å pairs were presented in comparison to the EM **C - B** channel pair.

For the regions centred on Pixels 1 and 2 (the pixels of diffuse, and fan loop emission) the EM **C - B** channel pair reports similar time-lags in regions where the *SDO/AIA* time-lags were not equal to *zero*. For locations in the *SDO/AIA* time-lag maps where there were *zero* values, a large proportion of these values seem to be assigned non-zero values that are consistent with the non-*zero* values in adjacent pixels. The result is an apparent interpolation over a large portion of the *zero* values seen in *SDO/AIA* time-lag maps, and this indicates that time-lag analysis on the *SDO/AIA* 193 Å – 171 Å channel pair may mask the true time-lag signature. This is especially interesting in the case of Pixel 2: over this same region [Uritsky \*et al.\* \(2013\)](#) observed propagating disturbances along these fan loops. If a loop was to move in and out of a pixel then the time series would be in-phase and this would result in a *SDO/AIA* time-lag of *zero*. There are also regions that are not interpolated over, and have time-lag values of *zero* in both *SDO/AIA* and EM time-lag analysis. These regions do appear to be spatially located at regions where clear (in-phase) brightenings occur, however. For Pixel 1, there is an  $8 \times 12$  region that is consistent with a brightening observed at the beginning of the two-hour time series, and by performing the same analysis on this region it is clear that both the *SDO/AIA* and EM time-lags are strongly peaked at 0 s, indicating in-phase behaviour. For Pixel 2, the EM time-lag map traces out a part of a fan loop that is seen to brighten in-phase at the very end of the 12 hour time series that was used to generate time-lag maps.

Pixels 3 and 4 are associated with the active region core, and loop footpoint regions. The EM **C - B** pair reports a significant number of extreme time-lag values (those located at, or near, the maximum offset values) for Pixel 3. Similar behaviour is observed with Pixel 4, however in the *SDO/AIA* time-lags there are also a number of such pixels. Further investigation of these with coronal heating simulations is required

in order to understand if they are the result of the assumptions of DEM inversion no longer holding, or if the DEM inversion fails to recover the “ground-truth” EM time-lags (see § 7.2).

To investigate the ability for DEM inversion to recover the “ground-truth”, EM time-lag analysis was performed on *SDO/AIA* observations synthesised from EBTEL simulations. With the temperature range of temperature bins (**A** - **F**) defined in Figure 7.1, EM time-lag analysis on the EBTEL DEM returns a EM time-lag is less-positive by  $\sim 20$  s, but this would not necessarily be observable in a time-lag map. By performing DEM inversion, and EM time-lag analysis on the recovered DEM, and DEM-synthesised *SDO/AIA* observations, it is clear that DEM inversion well-recovers the original 171 Å, and 193 Å time series. Interestingly, EM time-lag analysis returns a time-lag that is identical in offset to EBTEL EM time-lag analysis, but at a higher value of cross-correlation; it is seen that the cross-correlation as a function of offset for the recovered EM time series appears to have properties of both of the equivalent relationships between the EBTEL *SDO/AIA* time-lags and the EBTEL EM time-lags. This indicates that DEM inversion recovers the temperature distribution over time that can accurately recover the underlying time series but the DEM form *is not* identical to the underlying temperature distribution.

Similar analysis was performed for the *SDO/AIA* 211 Å – 193 Å channel pair as for Pixels 1 and 2 the equivalent (**D** - **C**) EM time-lags showed high-correlation and a more positive time-lag value than for *SDO/AIA* time-lag analysis (see Figure 7.6 and Figure 7.13). From the EBTEL *SDO/AIA* and EM time-lags, similar behaviour was observed in these simulated time series as in *SDO/AIA* observations (and from DEM-inversion) confirming that *SDO/AIA* time-lag analysis appears to mask the EM time-lags.

Furthermore with the transition region DEMs in Figure 7.29 all four methods to calculate *SDO/AIA* and EM time-lags resulted in *zero* values that are highly correlated. This is not surprising as the DEM is observed to change only emission measure (the form of the DEM remains constant), and for the steady heating simulations, DEM inversion is relatively insensitive to noise in the data.

For EM time-lag analysis, this method should first be applied to the additional active regions in Viall & Klimchuk (2017) in order to understand if the same signatures

for the channel pairs used here are seen in other active regions. This work will then be extended to additional channel pairs such as  $211 \text{ \AA} - 193 \text{ \AA}$ , which is still well-constrained through DEM inversion, however in Figure 6.23, a large fraction of these time-lags are *zero*.

Using alternative DEM inversion techniques such as Basis Pursuit (§ 3.4.4) should allow us to understand if the extreme EM time-lags seen in the core of the active region are a result of the DEM inversion method. Furthermore, as seen for Pixel 4 (§ 7.1.5), the DEM is not recovered in all pixels, leading to *zero* values in *all* EM time series. For the analysis in this work, these regions have been excluded (shown as red hatched regions), however, it would be beneficial to have more example pixels. While these times when the DEM was not recovered could be interpolated over (as performed for Pixel 4, § 7.1.5), in order to obtain DEM solutions in each pixel we are currently employing the use of neural networks. While the details of neural networks are outwith the scope of this thesis, they can be seen as a technique that enables complex transformations of the input data that takes advantage of the informational content contained in those data. This means that it is possible for neural networks to learn physically meaningful relationships.

DeepEM (Wright *et al.*, 2018, 2019) is a (supervised) deep learning approach to DEM inversion that is currently under development on GitHub<sup>1</sup>, and is available as part of the Heliophysics Machine Learning (HelioML) e-book: *Machine Learning, Statistics, and Data Mining for Heliophysics*<sup>2</sup>. DeepEM has been designed to both accelerate the computation of DEM solutions, and reduce erroneous solutions provided by *pre-existing* inversion methods, such as those described in this thesis. The underlying idea is that a neural network should be able to learn a generalised mapping from a set of training examples in order to transform an *SDO/AIA* input vector ( $6 \times 1 \times 1$ ) to the DEM output vector ( $N_T \times 1 \times 1$ ; where  $N_T$  is the number of temperature bins of the DEM solution), and this should be done with similar fidelity to the original DEM method.

Figure 9.1 shows the Basis Pursuit and DeepEM temperature maps for a set of test data (20th March 2011) at  $\log_{10}T = 5.9, 6.2$  K. These are shown in comparison to the *SDO/AIA*  $171 \text{ \AA}$  and  $193 \text{ \AA}$  images. Importantly, as the model was trained on a single set of images obtained on 27th January 2011, and tested on data from 20th March

<sup>1</sup><https://github.com/PaulJWright/DeepEM>

<sup>2</sup><https://helioML.github.io/HelioML/04/1/notebook>

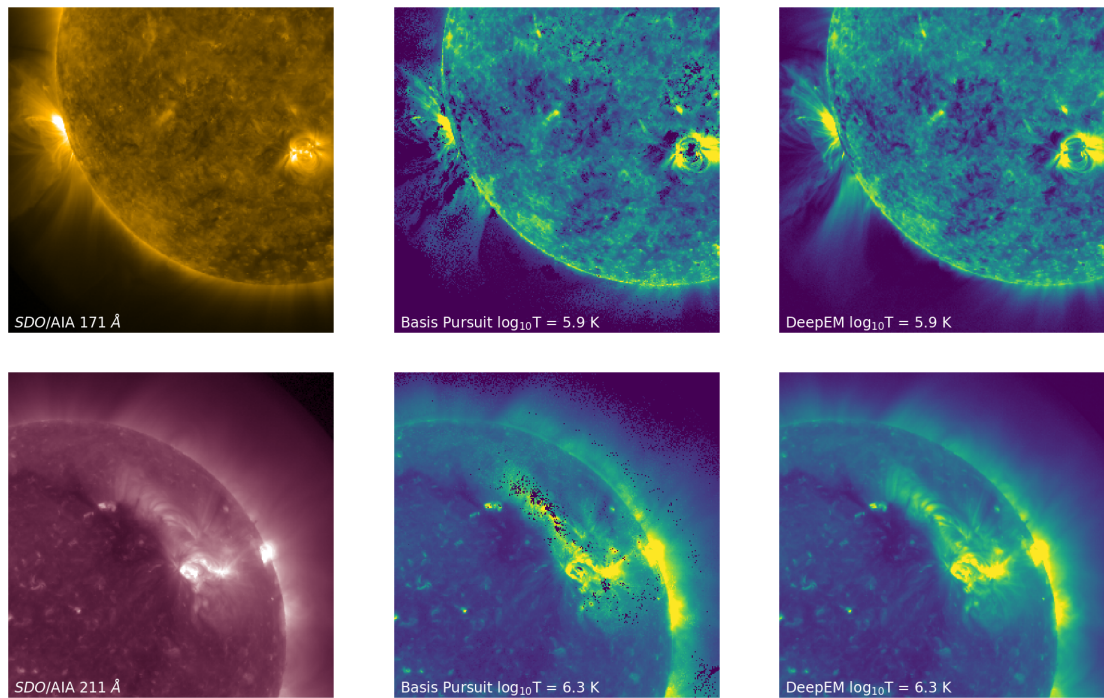


Figure 9.1: *Left:*  $300 \times 300$  pixel *SDO/AIA* cutouts of the test set (20-March-2011) for  $171 \text{ \AA}$  and  $193 \text{ \AA}$  ( $\log_{10} T_{peak} = 5.9, 6.2 \text{ K}$ ; *top, bottom*), plotted on a linear scale. Also shown are the corresponding temperature maps observed by Basis Pursuit (*middle*) and DeepEM (*right*) for the temperature bins at  $\log_{10} T = 5.9, 6.2 \text{ K}$  (*top, bottom*). DeepEM provides solutions that are similar in fidelity to Basis Pursuit, but importantly, DeepEM provides DEM solutions for every pixel.

2011 (two synodic rotations later, Figure 9.1), in order to produce DeepEM maps that agree with the DEMs obtained by Basis Pursuit (where Basis Pursuit found solutions) DeepEM has learned a generalised mapping from the  $512^2$  examples in the training set. Additionally, DeepEM is able to obtain solutions in pixels where Basis Pursuit was unable to (within set tolerances).

We are able to trust the DeepEM solutions provided in regions where Basis Pursuit failed to provide a solution as DeepEM agrees (within uncertainties) in regions where Basis Pursuit provided a solution. Further testing of DeepEM is required, and DeepEM can be used to accelerate and improve the solutions provided by any DEM code as long as there are enough training examples.

## 9.4 Wavelet Analysis

Chapter 8 presented a brief introduction to wavelet analysis, leading on to two methods that could be used to analyse the wealth of data provided by instruments such as the *Solar Dynamics Observatory*. Wavelet analysis was first introduced on a 155-hour time series (first presented by Froment *et al.*, 2015) in order to introduce the basic idea where a clear (significant) region was observed. After this brief introduction, test case demonstrations of wavelet coherence and local intermittency measure were provided.

In chapter 6, time-lag analysis was used to understand the time-delay between two channels of varying peak temperatures. Wavelet coherence expands this analysis in to the time-frequency domain where relationships between the two time series can be studied at different scales. Figure 8.2 shows the wavelet coherency and phase between *SDO/AIA* 193 Å, and 171 Å. It is clear on the largest scales there is a general lag between these channels with 171 Å lagging 193 Å. At shorter scales (between 800 and 1000 s, these two time series were seen to be in-phase, and this seen as a diagonal region between  $\sim 800$  s, and  $\sim 1000$  s which implies that both time series are increasing in period. Interestingly on the shortest time-scales ( $\sim 60$  s) there were regions of in-phase behaviour at times when there were distinct (yet small) brightenings in the *SDO/AIA* time series. This approach needs to be compared to heating models in order to understand if there are general trends that could be extracted from *SDO/AIA* that could highlight the properties of the heating mechanism.

Local Intermittency Measure (LIM, a modification of wavelet analysis suited to identifying periods of intermittent behaviour, Farge, 1992) was introduced on the 155 hour time series, demonstrating that within the time series there were regions of intermittent behaviour on all scales. Importantly, without the need to first model, and then background subtract that model, LIM was able to highlight regions for further analysis. While further testing of LIM needs to be conducted on additional simulated light curves, LIM is a powerful tool to quickly understand intermittent events and could prove to be very useful for determining the periodicity/intermittency with solar data as no model or background subtraction is required. This could be applied to quiescent *SDO/AIA* time series from different active regions, again looking for the signatures of nanoflare heating as well as intermittent periodicities (such as those observed by Froment *et al.*, 2015).

---

*This thesis utilises colour-blind friendly colour-tables ([Wright, 2017](#)).*

# Bibliography

- ABBE, E. (1881). Vii.—on the estimation of aperture in the microscope. *Journal of the Royal Microscopical Society*, **1**, 388–423.
- ACTON, L.W., CULHANE, J.L., GABRIEL, A.H., BENTLEY, R.D., BOWLES, J.A., FIRTH, J.G., FINCH, M.L., GILBRETH, C.W., GUTTRIDGE, P., HAYES, R.W., JOKI, E.G., JONES, B.B., KENT, B.J., LEIBACHER, J.W., NOBLES, R.A., PATRICK, T.J., PHILLIPS, K.J.H., RAPLEY, C.G., SHEATHER, P.H., SHERMAN, J.C., STARK, J.P., SPRINGER, L.A., TURNER, R.F. & WOLFSON, C.J. (1980). The soft X-ray polychromator for the Solar Maximum Mission. *Solar Physics*, **65**, 53–71.
- ARNAUD, K.A. (1996). XSPEC: The First Ten Years. In G.H. Jacoby & J. Barnes, eds., *Astronomical Data Analysis Software and Systems V*, vol. 101 of *Astronomical Society of the Pacific Conference Series*, 17.
- ASCHENBACH, B. (1985). X-ray telescopes. *Reports on Progress in Physics*, **48**, 579.
- ASCHWANDEN, M.J. (2004). *Physics of the Solar Corona. An Introduction*. Praxis Publishing Ltd.
- ASCHWANDEN, M.J. & BOERNER, P. (2011). Solar Corona Loop Studies with the Atmospheric Imaging Assembly. I. Cross-sectional Temperature Structure. *The Astrophysical Journal*, **732**, 81.
- ASCHWANDEN, M.J., TARBELL, T.D., NIGHTINGALE, R.W., SCHRIJVER, C.J., TITTE, A., KANKELBORG, C.C., MARTENS, P. & WARREN, H.P. (2000). Time Variability of the “Quiet” Sun Observed with TRACE. II. Physical Parameters, Temperature Evolution, and Energetics of Extreme-Ultraviolet Nanoflares. *The Astrophysical Journal*, **535**, 1047–1065.

- ATTWOOD, D. (2007). *Soft X-Rays and Extreme Ultraviolet Radiation: Principles and Applications*. Cambridge University Press, New York, NY, USA, 1st edn.
- AUCHÈRE, F., FROMENT, C., BOCCHIALINI, K., BUCHLIN, E. & SOLOMON, J. (2016). On the Fourier and Wavelet Analysis of Coronal Time Series. *The Astrophysical Journal*, **825**, 110.
- BATTAMS, K., GALLAGHER, B.M. & WEIGEL, R.S. (2019). A Global Survey of EUV Coronal Power Spectra. *Solar Physics*, **294**, 11.
- BENZ, A.O. & KRUCKER, S. (2002). Energy Distribution of Microevents in the Quiet Solar Corona. *The Astrophysical Journal*, **568**, 413–421.
- BENZ, A.O., KRUCKER, S., HURFORD, G.J., ARNOLD, N.G., ORLEANSKI, P., GRÖBELBAUER, H.P., KLOBER, S., ISELI, L., WIEHL, H.J., CSILLAGHY, A., ETESI, L., HOCHMUTH, N., BATTAGLIA, M., BEDNARZIK, M., RESANOVIC, R., GRIMM, O., VIERTEL, G., COMMICHAU, V., MEURIS, A., LIMOUSIN, O., BRUN, S., VILMER, N., SKUP, K.R., GRACZYK, R., STOLARSKI, M., MICHALSKA, M., NOWOSIELSKI, W., CICHOCKI, A., MOSDORF, M., SEWERYN, K., PRZEPIÓRKA, A., SYLWESTER, J., KOWALINSKI, M., MROZEK, T., PODGORSKI, P., MANN, G., AURASS, H., POPOW, E., ONEL, H., DIONIES, F., BAUER, S., RENDTEL, J., WARMUTH, A., WOCHE, M., PLÜSCHKE, D., BITTNER, W., PASCHKE, J., WOLKER, D., VAN BEEK, H.F., FARNIK, F., KASPAROVA, J., VERONIG, A.M., KIENREICH, I.W., GALLAGHER, P.T., BLOOMFIELD, D.S., PIANA, M., MASSONE, A.M., DENNIS, B.R., SCHWARZ, R.A. & LIN, R.P. (2012). The spectrometer telescope for imaging x-rays on board the Solar Orbiter mission. In *Space Telescopes and Instrumentation 2012: Ultraviolet to Gamma Ray*, vol. 8443 of *Society of Photo-Optical Instrumentation Engineers (SPIE) Conference Series*, 84433L.
- BERGER, T.E., DE PONTIEU, B., FLETCHER, L., SCHRIJVER, C.J., TARBELL, T.D. & TITLE, A.M. (1999). What is Moss? *Solar Physics*, **190**, 409–418.
- BERTERO, M., DEMOL, C. & PIKE, E.R. (1985). Linear inverse problems with discrete data. I. General formulation and singular system analysis. *Inverse Problems*, **1**, 301–330.

- BHALERAO, V.B. (2012). *Neutron stars and NuSTAR: A systematic survey of neutron star masses in high mass x-ray binaries Characterization of CdZnTe detectors for NuSTAR*. Ph.D. thesis, California Institute of Technology.
- BOERNER, P., EDWARDS, C., LEMEN, J., RAUSCH, A., SCHRIJVER, C., SHINE, R., SHING, L., STERN, R., TARBELL, T., TITLE, A., WOLFSON, C.J., SOUFLI, R., SPILLER, E., GULLIKSON, E., MCKENZIE, D., WINDT, D., GOLUB, L., PODGORSKI, W., TESTA, P. & WEBER, M. (2012). Initial Calibration of the Atmospheric Imaging Assembly (AIA) on the Solar Dynamics Observatory (SDO). *Solar Physics*, **275**, 41–66.
- BOERNER, P.F., TESTA, P., WARREN, H., WEBER, M.A. & SCHRIJVER, C.J. (2014). Photometric and Thermal Cross-calibration of Solar EUV Instruments. *Solar Physics*, **289**, 2377–2397.
- BRADSHAW, S.J. & CARGILL, P.J. (2013). The Influence of Numerical Resolution on Coronal Density in Hydrodynamic Models of Impulsive Heating. *The Astrophysical Journal*, **770**, 12.
- BRADSHAW, S.J. & KLIMCHUK, J.A. (2011). What Dominates the Coronal Emission Spectrum During the Cycle of Impulsive Heating and Cooling? *The Astrophysical Journal Supplement Series*, **194**, 26.
- BRADSHAW, S.J. & VIAL, N.M. (2016). Patterns of Activity in a Global Model of a Solar Active Region. *The Astrophysical Journal*, **821**, 63.
- BRADSHAW, S.J., KLIMCHUK, J.A. & REEP, J.W. (2012). Diagnosing the Time-dependence of Active Region Core Heating from the Emission Measure. I. Low-frequency Nanoflares. *The Astrophysical Journal*, **758**, 53.
- BRAY, R.J., CRAM, L.E., DURRANT, C. & LOUGHHEAD, R.E. (1991). *Plasma Loops in the Solar Corona*.
- BROOKS, D.H., WARREN, H.P. & UGARTE-URRA, I. (2012). Solar Coronal Loops Resolved by Hinode and the Solar Dynamics Observatory. *The Astrophysical Journal Letters*, **755**, L33.

- BROSIUS, J.W., DAW, A.N. & RABIN, D.M. (2014). Pervasive Faint Fe XIX Emission from a Solar Active Region Observed with EUNIS-13: Evidence for Nanoflare Heating. *The Astrophysical Journal*, **790**, 112.
- BROWN, J.C. (1971). The Deduction of Energy Spectra of Non-Thermal Electrons in Flares from the Observed Dynamic Spectra of Hard X-Ray Bursts. *Solar Physics*, **18**, 489–502.
- BRUNER, M.E. & MCWHIRTER, R.W.P. (1988). Radiating properties of solar plasmas. *The Astrophysical Journal*, **326**, 1002–1016.
- BRUNO, R. & CARBONE, C. (2016). *Turbulence in the Solar Wind*. Springer International Publishing.
- BRUNO, R., BAVASSANO, B., PIETROPAOLO, E., CARBONE, V. & VELTRI, P. (1999). Effects of intermittency on interplanetary velocity and magnetic field fluctuations anisotropy. *Geophysical Research Letters*, **26**, 3185–3188.
- BUITRAGO-CASAS, J.C., ELSNER, R., GLESENER, L., CHRISTE, R., RAMSEY, B., COURTADE, S., ISHIKAWA, S., NARUKAGE, N., TURIN, P., VIEVERING, J., ATHIRAY, P.S., MUSSET, S. & KRUCKER, S. (2017). Methods for reducing singly reflected rays on the wolter-i focusing mirrors of the foxsi rocket experiment.
- CADAVID, A.C., LAWRENCE, J.K., CHRISTIAN, D.J., JESS, D.B. & NIGRO, G. (2014). Heating Mechanisms for Intermittent Loops in Active Region Cores from AIA/SDO EUV Observations. *The Astrophysical Journal*, **795**, 48.
- CANDÈS, E.J. & TAO, T. (2006). Near-optimal signal recovery from random projections: Universal encoding strategies? *IEEE Transactions on Information Theory*, **52**, 5406–5425.
- CANDÈS, E.J. & TAO, T. (2007). The Dantzig selector: Statistical estimation when p is much larger than n. *Annals of Statistics*, **35**, 2313–2351.
- CARGILL, P.J. (1994). Some Implications of the Nanoflare Concept. *The Astrophysical Journal*, **422**, 381.
- CARGILL, P.J. (2014). Active Region Emission Measure Distributions and Implications for Nanoflare Heating. *The Astrophysical Journal*, **784**, 49.

- CARGILL, P.J. & KLIMCHUK, J.A. (2004). Nanoflare Heating of the Corona Revisited. *The Astrophysical Journal*, **605**, 911–920.
- CARGILL, P.J., MARISKA, J.T. & ANTIOCHOS, S.K. (1995). Cooling of Solar Flare Plasmas. I. Theoretical Considerations. *The Astrophysical Journal*, **439**, 1034.
- CARGILL, P.J., BRADSHAW, S.J. & KLIMCHUK, J.A. (2012). Enthalpy-based Thermal Evolution of Loops. II. Improvements to the Model. *The Astrophysical Journal*, **752**, 161.
- CARGILL, P.J., BRADSHAW, S.J. & KLIMCHUK, J.A. (2012). Enthalpy-based Thermal Evolution of Loops. III. Comparison of Zero-dimensional Models. *The Astrophysical Journal*, **758**, 5.
- CASH, W. (1979). Parameter estimation in astronomy through application of the likelihood ratio. *The Astrophysical Journal*, **228**, 939–947.
- CASPI, A., WOODS, T.N. & WARREN, H.P. (2015). New Observations of the Solar 0.5-5 keV Soft X-Ray Spectrum. *The Astrophysical Journal Letters*, **802**, L2.
- CHEN, S.S., DONOHO, D.L. & SAUNDERS, M.A. (1998). Atomic decomposition by basis pursuit. *SIAM Journal on Scientific Computing*, **20**, 33–61.
- CHEN, S.S., DONOHO, D.L. & SAUNDERS, M.A. (2001). Atomic Decomposition by Basis Pursuit. *SIAM Review*, **43**, 129–159.
- CHEUNG, M.C.M., BOERNER, P., SCHRIJVER, C.J., TESTA, P., CHEN, F., PETER, H. & MALANUSHENKO, A. (2015). Thermal Diagnostics with the Atmospheric Imaging Assembly on board the Solar Dynamics Observatory: A Validated Method for Differential Emission Measure Inversions. *The Astrophysical Journal*, **807**, 143.
- CHRISTE, S., HANNAH, I.G., KRUCKER, S., MCTIERNAN, J. & LIN, R.P. (2008). RHESSI Microflare Statistics. I. Flare-Finding and Frequency Distributions. *The Astrophysical Journal*, **677**, 1385–1394.
- CHRISTE, S., GLESENER, L., BUITRAGO-CASAS, C., ISHIKAWA, S.N., RAMSEY, B., GUBAREV, M., KILARU, K., KOLODZIEJCZAK, J.J., WATANABE, S., TAKAHASHI, T., TAJIMA, H., TURIN, P., SHOURT, V., FOSTER, N. & KRUCKER, S. (2016).

- FOXSI-2: Upgrades of the Focusing Optics X-ray Solar Imager for its Second Flight. *Journal of Astronomical Instrumentation*, **5**, 1640005–625.
- CHRISTENSEN, F.E., HORNSTRUP, A., WESTERGAARD, N.J., SCHNOPPER, H.W., WOOD, J. & PARKER, K. (1992). A graded d-spacing multilayer telescope for high energy X-ray astronomy. In R.B. Hoover, ed., *Multilayer and Grazing Incidence X-Ray/EUV Optics*, vol. 1546 of *Proceedings of SPIE*, 160–167.
- CHRISTENSEN, F.E., JAKOBSEN, A.C., BREJNHOLT, N.F., MADSEN, K.K., HORNSTRUP, A., WESTERGAARD, N.J., MOMBERG, J., KOGLIN, J., FABRICANT, A.M., STERN, M., CRAIG, W.W., PIVOVAROFF, M.J. & WINDT, D. (2011). Coatings for the NuSTAR mission. In *Society of Photo-Optical Instrumentation Engineers (SPIE) Conference Series*, vol. 8147 of *Proceedings of the SPIE*, 81470U.
- CIRTAİN, J.W., GOLUB, L., WINEBARGER, A.R., DE PONTIEU, B., KOBAYASHI, K., MOORE, R.L., WALSH, R.W., KORRECK, K.E., WEBER, M., MCCAULEY, P., TITLE, A., KUZIN, S. & DEFOREST, C.E. (2013). Energy release in the solar corona from spatially resolved magnetic braids. *Nature*, **493**, 501–503.
- COURANT, R. & HILBERT, D. (1953). *Methods of mathematical physics - Vol.1; Vol.2*.
- CRAIG, I.J.D. (1977). The use of a-priori information in the derivation of temperature structures from X-ray spectra. *Astronomy & Astrophysics*, **61**, 575–590.
- CRAIG, I.J.D. & BROWN, J.C. (1976). Fundamental limitations of X-ray spectra as diagnostics of plasma temperature structure. *Astronomy & Astrophysics*, **49**, 239–250.
- CRAIG, I.J.D. & BROWN, J.C. (1977). Why measure astrophysical X-ray spectra? (reply). *Nature*, **267**, 411–412.
- CULHANE, J.L., HIEI, E., DOSCHEK, G.A., CRUISE, A.M., OGAWARA, Y., UCHIDA, Y., BENTLEY, R.D., BROWN, C.M., LANG, J., WATANABE, T., BOWLES, J.A., DESLATTES, R.D., FELDMAN, U., FLUDRA, A., GUTTRIDGE, P., HENINS, A., LAPINGTON, J., MAGRAW, J., MARISKA, J.T., PAYNE, J., PHILLIPS, K.J.H., SHEATHER, P., SLATER, K., TANAKA, K., TOWNDROW, E., TROW, M.W. & YAMAGUCHI, A. (1991). The Bragg Crystal Spectrometer for SOLAR-A. *Solar Physics*, **136**, 89–104.

- CULHANE, J.L., HARRA, L.K., JAMES, A.M., AL-JANABI, K., BRADLEY, L.J., CHAUDRY, R.A., REES, K., TANDY, J.A., THOMAS, P., WHILLOCK, M.C.R., WINTER, B., DOSCHEK, G.A., KORENDYKE, C.M., BROWN, C.M., MYERS, S., MARISKA, J., SEELY, J., LANG, J., KENT, B.J., SHAUGHNESSY, B.M., YOUNG, P.R., SIMNETT, G.M., CASTELLI, C.M., MAHMOUD, S., MAPSON-MENARD, H., PROBYN, B.J., THOMAS, R.J., DAVILA, J., DERE, K., WINDT, D., SHEA, J., HAGOOD, R., MOYE, R., HARA, H., WATANABE, T., MATSUZAKI, K., KOSUGI, T., HANSTEEN, V. & WIKSTOL, Ø. (2007). The EUV Imaging Spectrometer for Hinode. *Solar Physics*, **243**, 19–61.
- DADASHI, N., TERIACA, L., TRIPATHI, D., SOLANKI, S.K. & WIEGELMANN, T. (2012). Doppler shift of hot coronal lines in a moss area of an active region. *Astronomy & Astrophysics*, A115.
- DANTZIG, G., ORDEN, A. & WOLFE, P. (1955). The generalized simplex method for minimizing a linear form under linear inequality restraints. *Pacific Journal of Mathematics*, **5**, 183–195.
- DATLOWE, D.W. (1975). Pulse pile-up in hard X-ray detector systems. *Space Science Instrumentation*, **1**, 389–406.
- DE MOORTEL, I., MUNDAY, S.A. & HOOD, A.W. (2004). Wavelet Analysis: the effect of varying basic wavelet parameters. *Solar Physics*, **222**, 203–228.
- DE PONTIEU, B., TITLE, A.M., LEMEN, J.R., KUSHNER, G.D., AKIN, D.J., ALLARD, B., BERGER, T., BOERNER, P., CHEUNG, M., CHOU, C., DRAKE, J.F., DUNCAN, D.W., FREELAND, S., HEYMAN, G.F., HOFFMAN, C., HURLBURT, N.E., LINDGREN, R.W., MATHUR, D., REHSE, R., SABOLISH, D., SEGUIN, R., SCHRIJVER, C.J., TARBELL, T.D., WÜLSER, J.P., WOLFSON, C.J., YANARI, C., MUDGE, J., NGUYEN-PHUC, N., TIMMONS, R., VAN BEZOOIJEN, R., WEINGROD, I., BROOKNER, R., BUTCHER, G., DOUGHERTY, B., EDER, J., KNAGENHJELM, V., LARSEN, S., MANSIR, D., PHAN, L., BOYLE, P., CHEIMETS, P.N., DELUCA, E.E., GOLUB, L., GATES, R., HERTZ, E., MCKILLOP, S., PARK, S., PERRY, T., PODGORSKI, W.A., REEVES, K., SAAR, S., TESTA, P., TIAN, H., WEBER, M., DUNN, C., ECCLES, S., JAEGGLI, S.A., KANKELBORG, C.C., MASHBURN, K., PUST, N., SPRINGER, L., CARVALHO, R., KLEINT, L., MARMIE, J.,

- MAZMANIAN, E., PEREIRA, T.M.D., SAWYER, S., STRONG, J., WORDEN, S.P., CARLSSON, M., HANSTEEN, V.H., LEENAARTS, J., WIESMANN, M., ALOISE, J., CHU, K.C., BUSH, R.I., SCHERRER, P.H., BREKKE, P., MARTINEZ-SYKORA, J., LITES, B.W., MCINTOSH, S.W., UITENBROEK, H., OKAMOTO, T.J., GUMMIN, M.A., AUKER, G., JERRAM, P., POOL, P. & WALTHAM, N. (2014). The Interface Region Imaging Spectrograph (IRIS). *Solar Physics*, **289**, 2733–2779.
- DEL ZANNA, G. (2013). The multi-thermal emission in solar active regions. *Astronomy & Astrophysics*, **558**, A73.
- DEL ZANNA, G. & MASON, H.E. (2003). Solar active regions: SOHO/CDS and TRACE observations of quiescent coronal loops. *Astronomy & Astrophysics*, **406**, 1089–1103.
- DEL ZANNA, G. & MASON, H.E. (2014). Elemental abundances and temperatures of quiescent solar active region cores from X-ray observations. *Astronomy & Astrophysics*, **565**, A14.
- DEL ZANNA, G. & MASON, H.E. (2018). Solar UV and X-ray spectral diagnostics. *Living Reviews in Solar Physics*, **15**, 5.
- DEL ZANNA, G., LANDINI, M. & MASON, H.E. (2002). Spectroscopic diagnostics of stellar transition regions and coronae in the XUV: AU Mic in quiescence. *Astronomy & Astrophysics*, **385**, 968–985.
- DEL ZANNA, G., O'DWYER, B. & MASON, H.E. (2011). SDO AIA and Hinode EIS observations of "warm" loops. *Astronomy & Astrophysics*, **535**, A46.
- DEL ZANNA, G., TRIPATHI, D., MASON, H., SUBRAMANIAN, S. & O'DWYER, B. (2015). The evolution of the emission measure distribution in the core of an active region. *Astronomy & Astrophysics*, **573**, A104.
- DELABOUDINIÈRE, J.P., ARTZNER, G.E., BRUNAUD, J., GABRIEL, A.H., HOCHEDÉZ, J.F., MILLIER, F., SONG, X.Y., AU, B., DERE, K.P., HOWARD, R.A., KREPLIN, R., MICHELS, D.J., MOSES, J.D., DEFISE, J.M., JAMAR, C., ROCHUS, P., CHAUVINEAU, J.P., MARIOGE, J.P., CATURA, R.C., LEMEN, J.R., SHING, L., STERN, R.A., GURMAN, J.B., NEUPERT, W.M., MAUCHERAT, A.,

- CLETTE, F., CUGNON, P. & VAN DESSEL, E.L. (1995). EIT: Extreme-Ultraviolet Imaging Telescope for the SOHO Mission. *Solar Physics*, **162**, 291–312.
- DERE, K.P., LANDI, E., MASON, H.E., MONSIGNORI FOSSI, B.C. & YOUNG, P.R. (1997). CHIANTI - an atomic database for emission lines. *Astronomy & Astrophysics Supplement series*, **125**, 149–173.
- DERE, K.P., LANDI, E., YOUNG, P.R., DEL ZANNA, G., LANDINI, M. & MASON, H.E. (2009). CHIANTI - an atomic database for emission lines. IX. Ionization rates, recombination rates, ionization equilibria for the elements hydrogen through zinc and updated atomic data. *Astronomy & Astrophysics*, **498**, 915–929.
- DINKELAKER, A.N. & MACKINNON, A.L. (2013a). Wavelets, Intermittency and Solar Flare Hard X-rays 1. Local Intermittency Measure in Cascade and Avalanche Scenarios. *Solar Physics*, **282**, 471–481.
- DINKELAKER, A.N. & MACKINNON, A.L. (2013b). Wavelets, Intermittency and Solar Flare Hard X-rays 2. LIM Analysis of High Time Resolution BATSE Data. *Solar Physics*, **282**, 483–501.
- DOLLA, L., MARQUÉ, C., SEATON, D.B., VAN DOORSSELAERE, T., DOMINIQUE, M., BERGHMANS, D., CABANAS, C., DE GROOF, A., SCHMUTZ, W., VERDINI, A., WEST, M.J., ZENDER, J. & ZHUKOV, A.N. (2012). Time Delays in Quasi-periodic Pulsations Observed during the X2.2 Solar Flare on 2011 February 15. *The Astrophysical Journal*, **749**, L16.
- DOMINGO, V., FLECK, B. & POLAND, A.I. (1995). The SOHO Mission: an Overview. *Solar Physics*, **162**, 1–37.
- DONOHO, D.L. (2006). Compressed sensing. *IEEE Transactions on Information Theory*, **52**, 1289–1306.
- EDLÉN, B. (1943). Die Deutung der Emissionslinien im Spektrum der Sonnenkorona. Mit 6 Abbildungen. *Zeitschrift für Astrophysik*, **22**, 30.
- FARGE, M. (1992). Wavelet transforms and their applications to turbulence. *Annual Review of Fluid Mechanics*, **24**, 395–457.

- FELDMAN, U. (1992). Elemental abundances in the upper solar atmosphere. *Physica Scripta*, **46**, 202–220.
- FELDMAN, U., DOSCHEK, G.A. & SEELY, J.F. (1988). Solar spectroscopy in the far-ultraviolet - X-ray wavelength regions: status and prospects. *Journal of the Optical Society of America B Optical Physics*, **5**, 2237–2251.
- FELDMAN, U., MANDELBAUM, P., SEELY, J.F., DOSCHEK, G.A. & GURSKY, H. (1992). The potential for plasma diagnostics from stellar extreme-ultraviolet observations. *The Astrophysical Journal Supplement Series*, **81**, 387–408.
- FLETCHER, L., DENNIS, B.R., HUDSON, H.S., KRUCKER, S., PHILLIPS, K., VERONIG, A., BATTAGLIA, M., BONE, L., CASPI, A., CHEN, Q., GALLAGHER, P., GRIGIS, P.T., JI, H., LIU, W., MILLIGAN, R.O. & TEMMER, M. (2011). An Observational Overview of Solar Flares. *Space Science Reviews*, **159**, 19–106.
- FLUDRA, A., GRIFFIN, D., CALDWELL, M., ECCLESTON, P., CORNABY, J., DRUMMOND, D., GRAINGER, W., GREENWAY, P., GRUNDY, T., HOWE, C., MCQUIRK, C., MIDDLETON, K., POYNTZ-WRIGHT, O., RICHARDS, A., ROGERS, K., SAWYER, C., SHAUGHNESSY, B., SIDHER, S., TOSH, I., BEARDSLEY, S., BURTON, G., MARSHALL, A., WALTHAM, N., WOODWARD, S., APPOURCHAUX, T., PHILIPPON, A., AUCHERE, F., BUCHLIN, E., GABRIEL, A., VIAL, J.C., SCHÜHLE, U., CURDT, W., INNES, D., MEINING, S., PETER, H., SOLANKI, S., TERIACA, L., GYO, M., BÜCHEL, V., HABERREITER, M., PFIFFNER, D., SCHMUTZ, W., CARLSSON, M., HAUGAN, S.V., DAVILA, J., JORDAN, P., THOMPSON, W., HASSLER, D., WALLS, B., DEFOREST, C., HANLEY, J., JOHNSON, J., PHELAN, P., BLECHA, L., COTTARD, H., PACIOTTI, G., AUTISSIER, N., ALLEMAND, Y., RELECOM, K., MUNRO, G., BUTLER, A., KLEIN, R. & GOTTWALD, A. (2013). SPICE EUV spectrometer for the Solar Orbiter mission. In *Solar Physics and Space Weather Instrumentation V*, vol. 8862 of *Proceedings of the SPIE*, 88620F.
- FRIEDMAN, H. (1963). Ultraviolet and X Rays from the Sun. *Annual Review of Astronomy & Astrophysics*, **1**, 59.
- FRIEDRICH, P. (2008). *Wolter Optics*, 41–50. Springer Berlin Heidelberg, Berlin, Heidelberg.

- FROMENT, C., AUCHÈRE, F., BOCCHIALINI, K., BUCHLIN, E., GUENNOU, C. & SOLOMON, J. (2015). Evidence for Evaporation-incomplete Condensation Cycles in Warm Solar Coronal Loops. *The Astrophysical Journal*, **807**, 158.
- GBUREK, S., SYLWESTER, J., KOWALINSKI, M., BAKALA, J., KORDYLEWSKI, Z., PODGORSKI, P., PLOCINIENIAK, S., SIARKOWSKI, M., SYLWESTER, B., TRZEBINSKI, W., KUZIN, S.V., PERTSOV, A.A., KOTOV, Y.D., FARNIK, F., REALE, F. & PHILLIPS, K.J.H. (2011). SphinX soft X-ray spectrophotometer: Science objectives, design and performance. *Solar System Research*, **45**, 189–199.
- GEHRELS, N. (1986). Confidence limits for small numbers of events in astrophysical data. *The Astrophysical Journal*, **303**, 336–346.
- GIMÉNEZ DE CASTRO, G., SIMÕES, P.J.A., RAULIN, J.P. & GUIMARÃES, O.M. (2016). Analysis of Intermittency in Submillimeter Radio and Hard X-Ray Data During the Impulsive Phase of a Solar Flare. *Solar Physics*, **291**, 2003–2016.
- GIORGINI, J.D., YEOMANS, D.K., CHAMBERLIN, A.B., CHODAS, P.W., JACOBSON, R.A., KEESEY, M.S., LIESKE, J.H., OSTRO, S.J., STANDISH, E.M. & WIMBERLY, R.N. (1996). JPL's On-Line Solar System Data Service. In *AAS/Division for Planetary Sciences Meeting Abstracts #28*, AAS/Division for Planetary Sciences Meeting Abstracts, 25.04.
- GLESENER, L., KRUCKER, S., HANNAH, I.G., HUDSON, H., GREFENSTETTE, B.W., WHITE, S.M., SMITH, D.M. & MARSH, A.J. (2017). NuSTAR Hard X-Ray Observation of a Sub-A Class Solar Flare. *The Astrophysical Journal*, **845**, 122.
- GOLUB, L., NOCI, G., POLETTI, G. & VAIANA, G.S. (1982). Active region coronal evolution. *The Astrophysical Journal*, **259**, 359–365.
- GOLUB, L., DELUCA, E.E., SETTE, A. & WEBER, M. (2004). Differential Emission Measure Reconstruction with the SolarB X-Ray Telescope. In T. Sakurai & T. Sekii, eds., *The Solar-B Mission and the Forefront of Solar Physics*, vol. 325 of *Astronomical Society of the Pacific Conference Series*, 217.
- GOLUB, L., DELUCA, E., AUSTIN, G., BOOKBINDER, J., CALDWELL, D., CHEIMETS, P., CERTAIN, J., COSMO, M., REID, P., SETTE, A., WEBER, M.,

- SAKAO, T., KANO, R., SHIBASAKI, K., HARA, H., TSUNETA, S., KUMAGAI, K., TAMURA, T., SHIMOJO, M., MCCrackEN, J., CARPENTER, J., HAIGHT, H., SILER, R., WRIGHT, E., TUCKER, J., RUTLEDGE, H., BARBERA, M., PERES, G. & VARISCO, S. (2007). The X-Ray Telescope (XRT) for the Hinode Mission. *Solar Physics*, **243**, 63–86.
- GORENSTEIN, P. (2012). Grazing incidence telescopes for x-ray astronomy. *Optical Engineering*, **51**, 011010–011010–15.
- GREFENSTETTE, B.W., GLESENER, L., KRUCKER, S., HUDSON, H., HANNAH, I.G., SMITH, D.M., VOGEL, J.K., WHITE, S.M., MADSEN, K.K., MARSH, A.J., CASPI, A., CHEN, B., SHIH, A., KUHAR, M., BOGGS, S.E., CHRISTENSEN, F.E., CRAIG, W.W., FORSTER, K., HAILEY, C.J., HARRISON, F.A., MIYASAKA, H., STERN, D. & ZHANG, W.W. (2016). The First Focused Hard X-ray Images of the Sun with NuSTAR. *The Astrophysical Journal*, **826**, 20.
- GRINSTED, A., MOORE, J.C. & JEVREJEVA, S. (2004). Application of the cross wavelet transform and wavelet coherence to geophysical time series. *Nonlinear Processes in Geophysics*, **11**, 561–566.
- GROTRIAN, W. (1939). Zur Frage der Deutung der Linien im Spektrum der Sonnenkorona. *Naturwissenschaften*, **27**, 214–214.
- GRUBER, D., LACHOWICZ, P., BISSALDI, E., BRIGGS, M.S., CONNAUGHTON, V., GREINER, J., VAN DER HORST, A.J., KANBACH, G., RAU, A., BHAT, P.N., DIEHL, R., VON KIENLIN, A., KIPPEN, R.M., MEEGAN, C.A., PACIASAS, W.S., PREECE, R.D. & WILSON-HODGE, C. (2011). Quasi-periodic pulsations in solar flares: new clues from the Fermi Gamma-Ray Burst Monitor. *Astronomy & Astrophysics*, **533**, A61.
- GUENNOU, C., AUCHÈRE, F., KLIMCHUK, J.A., BOCCHIALINI, K. & PARENTI, S. (2013). Can the Differential Emission Measure Constrain the Timescale of Energy Deposition in the Corona? *The Astrophysical Journal*, **774**, 31.
- HANDY, B.N., ACTON, L.W., KANKELBORG, C.C., WOLFSON, C.J., AKIN, D.J., BRUNER, M.E., CARVALHO, R., CATURA, R.C., CHEVALIER, R., DUNCAN, D.W., EDWARDS, C.G., FEINSTEIN, C.N., FREELAND, S.L., FRIEDLAENDER,

- F.M., HOFFMANN, C.H., HURLBURT, N.E., JURCEVICH, B.K., KATZ, N.L., KELLY, G.A., LEMEN, J.R., LEVAY, M., LINDGREN, R.W., MATHUR, D.P., MEYER, S.B., MORRISON, S.J., MORRISON, M.D., NIGHTINGALE, R.W., POPE, T.P., REHSE, R.A., SCHRIJVER, C.J., SHINE, R.A., SHING, L., STRONG, K.T., TARBELL, T.D., TITLE, A.M., TORGERSON, D.D., GOLUB, L., BOOKBINDER, J.A., CALDWELL, D., CHEIMETS, P.N., DAVIS, W.N., DELUCA, E.E., McMULLEN, R.A., WARREN, H.P., AMATO, D., FISHER, R., MALDONADO, H. & PARKINSON, C. (1999). The transition region and coronal explorer. *Solar Physics*, **187**, 229–260.
- HANNAH, I.G. & GLESENER, L. (2019). private communication.
- HANNAH, I.G. & KONTAR, E.P. (2012). Differential emission measures from the regularized inversion of Hinode and SDO data. *Astronomy & Astrophysics*, **539**, 146.
- HANNAH, I.G., CHRISTE, S., KRUCKER, S., HURFORD, G.J., HUDSON, H.S. & LIN, R.P. (2008). RHESSI Microflare Statistics. II. X-Ray Imaging, Spectroscopy, and Energy Distributions. *The Astrophysical Journal*, **677**, 704–718.
- HANNAH, I.G., HUDSON, H.S., HURFORD, G.J. & LIN, R.P. (2010). Constraining the Hard X-ray Properties of the Quiet Sun with New RHESSI Observations. *The Astrophysical Journal*, **724**, 487–492.
- HANNAH, I.G., HUDSON, H.S., BATTAGLIA, M., CHRISTE, S., KAŠPAROVÁ, J., KRUCKER, S., KUNDU, M.R. & VERONIG, A. (2011). Microflares and the Statistics of X-ray Flares. *Space Science Reviews*, **159**, 263–300.
- HANNAH, I.G., GREFENSTETTE, B.W., SMITH, D.M., GLESENER, L., KRUCKER, S., HUDSON, H.S., MADSEN, K.K., MARSH, A., WHITE, S.M., CASPI, A., SHIH, A.Y., HARRISON, F.A., STERN, D., BOGGS, S.E., CHRISTENSEN, F.E., CRAIG, W.W., HAILEY, C.J. & ZHANG, W.W. (2016). The First X-Ray Imaging Spectroscopy of Quiescent Solar Active Regions with NuSTAR. *The Astrophysical Journal Letters*, **820**, L14.
- HANNAH, I.G., KLEINT, L., KRUCKER, S., GREFENSTETTE, B.W., GLESENER, L., HUDSON, H.S., WHITE, S.M. & SMITH, D.M. (2018). Joint X-ray, EUV and UV Observations of a Small Microflare. *arXiv e-prints*, arXiv:1812.09214.

- HANSEN, P.C. (1992). Numerical tools for analysis and solution of Fredholm integral equations of the first kind. *Inverse Problems*, **8**, 849–872.
- HARA, H., TSUNETA, S., LEMEN, J.R., ACTON, L.W. & MCTIERNAN, J.M. (1992). High-Temperature Plasmas in Active Regions Observed with the Soft X-Ray Telescope aboard YOHKOH. *Publications of the Astronomical Society of Japan*, **44**, L135–L140.
- HARP, D.I., LIEBE, C.C., CRAIG, W., HARRISON, F., KRUSE-MADSEN, K. & ZOGLAUER, A. (2010). NuSTAR: system engineering and modeling challenges in pointing reconstruction for a deployable x-ray telescope. In *Modeling, Systems Engineering, and Project Management for Astronomy IV*, vol. 7738 of *Proceedings of SPIE*, 77380Z.
- HARRISON, F.A., CRAIG, W.W., CHRISTENSEN, F.E., HAILEY, C.J., ZHANG, W.W., BOGGS, S.E., STERN, D., COOK, W.R., FORSTER, K., GIOMMI, P., GREFENSTETTE, B.W., KIM, Y., KITAGUCHI, T., KOGLIN, J.E., MADSEN, K.K., MAO, P.H., MIYASAKA, H., MORI, K., PERRI, M., PIVOVAROFF, M.J., PUC CETTI, S., RANA, V.R., WESTERGAARD, N.J., WILLIS, J., ZOGLAUER, A., AN, H., BACHETTI, M., BARRIÈRE, N.M., BELLM, E.C., BHALERAO, V., BREJNHOLT, N.F., FUERST, F., LIEBE, C.C., MARKWARDT, C.B., NYNKA, M., VOGEL, J.K., WALTON, D.J., WIK, D.R., ALEXANDER, D.M., COMINSKY, L.R., HORNSCHEMEIER, A.E., HORNSTRUP, A., KASPI, V.M., MADEJSKI, G.M., MATT, G., MOLENDI, S., SMITH, D.M., TOMSICK, J.A., AJELLO, M., BALLANTYNE, D.R., BALOKOVIĆ, M., BARRET, D., BAUER, F.E., BLANDFORD, R.D., BRANDT, W.N., BRENNEMAN, L.W., CHIANG, J., CHAKRABARTY, D., CHENEVEZ, J., COMASTRI, A., DUFOUR, F., ELVIS, M., FABIAN, A.C., FARRAH, D., FRYER, C.L., GOTTHELF, E.V., GRINDLAY, J.E., HELFAND, D.J., KRIVONOS, R., MEIER, D.L., MILLER, J.M., NATALUCCI, L., OGLE, P., OFEK, E.O., PTAK, A., REYNOLDS, S.P., RIGBY, J.R., TAGLIAFERRI, G., THORSETT, S.E., TREISTER, E. & URRY, C.M. (2013). The Nuclear Spectroscopic Telescope Array (NuSTAR) High-energy X-Ray Mission. *The Astrophysical Journal*, **770**, 103.
- HARRISON, R.A., SAWYER, E.C., CARTER, M.K., CRUISE, A.M., CUTLER, R.M., FLUDRA, A., HAYES, R.W., KENT, B.J., LANG, J., PARKER, D.J., PAYNE,

- J., PIKE, C.D., PESKETT, S.C., RICHARDS, A.G., GULHANE, J.L., NORMAN, K., BREEVELD, A.A., BREEVELD, E.R., AL JANABI, K.F., MCCALDEN, A.J., PARKINSON, J.H., SELF, D.G., THOMAS, P.D., POLAND, A.I., THOMAS, R.J., THOMPSON, W.T., KJELDSETH-MOE, O., BREKKE, P., KARUD, J., MALTBY, P., ASCHENBACH, B., BRÄUNINGER, H., KÜHNE, M., HOLLANDT, J., SIEGMUND, O.H.W., HUBER, M.C.E., GABRIEL, A.H., MASON, H.E. & BROMAGE, B.J.I. (1995). The Coronal Diagnostic Spectrometer for the Solar and Heliospheric Observatory. *Solar Physics*, **162**, 233–290.
- HIRSH, R.F. (1983). *Glimpsing an invisible universe. The emergence of x-ray astronomy*.
- HÖGBOM, J.A. (1974). Aperture Synthesis with a Non-Regular Distribution of Interferometer Baselines. *Astronomy & Astrophysics Supplement Series*, **15**, 417.
- HOLMAN, G.D., ASCHWANDEN, M.J., AURASS, H., BATTAGLIA, M., GRIGIS, P.C., KONTAR, E.P., LIU, W., SAINT-HILAIRE, P. & ZHARKOVA, V.V. (2011). Implications of X-ray Observations for Electron Acceleration and Propagation in Solar Flares. *Space Science Reviews*, **159**, 107–166.
- HUDSON, H.S. (1991). Solar flares, microflares, nanoflares, and coronal heating. *Solar Physics*, **133**, 357–369.
- HUDSON, H.S., ACTON, L.W., DELUCA, E.E., HANNAH, I.G., REARDON, K. & VAN BIBBER, K. (2012). X-Ray Searches for Solar Axions. In L. Bellot Rubio, F. Reale & M. Carlsson, eds., *4th Hinode Science Meeting: Unsolved Problems and Recent Insights*, vol. 455 of *Astronomical Society of the Pacific Conference Series*, 25.
- INGLIS, A.R. & CHRISTE, S. (2014). Investigating the Differential Emission Measure and Energetics of Microflares with Combined SDO/AIA and RHESSI observations. *The Astrophysical Journal*, **789**, 116.
- INGLIS, A.R., IRELAND, J. & DOMINIQUE, M. (2015). Quasi-periodic Pulsations in Solar and Stellar Flares: Re-evaluating their Nature in the Context of Power-law Flare Fourier Spectra. *The Astrophysical Journal*, **798**, 108.

- IRELAND, J., MCATEER, R.T.J. & INGLIS, A.R. (2015). Coronal Fourier Power Spectra: Implications for Coronal Seismology and Coronal Heating. *The Astrophysical Journal*, **798**, 1.
- JEFFERIES, J.T., ORRALL, F.Q. & ZIRKER, J.B. (1972). The Interpretation of Total Line Intensities from Optically Thin Gases. I: A General Method. *Solar Physics*, **22**, 307–316.
- JESS, D.B., MATHIOUDAKIS, M. & KEYS, P.H. (2014). Nanoflare Activity in the Solar Chromosphere. *The Astrophysical Journal*, **795**, 172.
- JORDAN, C. (1976). The Structure and Energy Balance of Solar Active Regions. *Philosophical Transactions of the Royal Society of London Series A*, **281**, 391–404.
- JORDAN, C., AYRES, T.R., BROWN, A., LINSKY, J.L. & SIMON, T. (1987). The chromospheres and coronae of five G-K main-sequence stars. *Monthly Notices of the Royal Astronomical Society*, **225**, 903–937.
- KANO, R., SAKAO, T., HARA, H., TSUNETA, S., MATSUZAKI, K., KUMAGAI, K., SHIMOJO, M., MINESUGI, K., SHIBASAKI, K., DELUCA, E.E., GOLUB, L., BOOKBINDER, J., CALDWELL, D., CHEIMETS, P., CERTAIN, J., DENNIS, E., KENT, T. & WEBER, M. (2008). The Hinode X-Ray Telescope (XRT): Camera Design, Performance and Operations. *Solar Physics*, **249**, 263–279.
- KASHYAP, V. & DRAKE, J.J. (1998). Markov-Chain Monte Carlo Reconstruction of Emission Measure Distributions: Application to Solar Extreme-Ultraviolet Spectra. *The Astrophysical Journal*, **503**, 450–466.
- KASHYAP, V. & DRAKE, J.J. (2000). PINTofALE : Package for the interactive analysis of line emission. *Bulletin of the Astronomical Society of India*, **28**, 475–476.
- KATSUKAWA, Y. & TSUNETA, S. (2001). Small Fluctuation of Coronal X-Ray Intensity and a Signature of Nanoflares. *The Astrophysical Journal*, **557**, 343–350.
- KITAGUCHI, T., GREFENSTETTE, B.W., HARRISON, F.A., MIYASAKA, H., BHALERAO, V.B., COOK, W.R., III, MAO, P.H., RANA, V.R., BOGGS, S.E. & ZOGLAUER, A.C. (2011). Spectral calibration and modeling of the NuSTAR CdZnTe

- pixel detectors. In *Society of Photo-Optical Instrumentation Engineers (SPIE) Conference Series*, vol. 8145 of *Proceedings of SPIE*, 814507.
- KITAGUCHI, T., BHALERAO, V., COOK, W.R., FORSTER, K., GREFENSTETTE, B.W., HARRISON, F.A., MADSEN, K.K., MAO, P.H., MIYASAKA, H. & RANA, V.R. (2014). Inflight performance and calibration of the NuSTAR CdZnTe pixel detectors. In *Space Telescopes and Instrumentation 2014: Ultraviolet to Gamma Ray*, vol. 9144 of *Proceedings of SPIE*, 91441R.
- KLIMCHUK, J.A. (2006). On Solving the Coronal Heating Problem. *Solar Physics*, **234**, 41–77.
- KLIMCHUK, J.A. (2015). Key Aspects of Coronal Heating. *Philosophical Transactions of the Royal Society A: Mathematical*, **373**.
- KLIMCHUK, J.A., PATSOURAKOS, S. & CARGILL, P.J. (2008). Highly Efficient Modeling of Dynamic Coronal Loops. *The Astrophysical Journal*, **682**, 1351–1362.
- KO, Y.K., DOSCHEK, G.A., WARREN, H.P. & YOUNG, P.R. (2009). Hot Plasma in Nonflaring Active Regions Observed by the Extreme-Ultraviolet Imaging Spectrometer on Hinode. *The Astrophysical Journal*, **697**, 1956–1970.
- KOBAYASHI, K., CIRTAIN, J., GOLUB, L., WINEBARGER, A., HERTZ, E., CHEIMETS, P., CALDWELL, D., KORRECK, K., ROBINSON, B., REARDON, P., KESTER, T., GRIFFITH, C. & YOUNG, M. (2011). The Marshall Grazing Incidence X-ray Spectrograph (MaGIXS). In *Society of Photo-Optical Instrumentation Engineers (SPIE) Conference Series*, vol. 8147, 81471M.
- KOBAYASHI, K., CIRTAIN, J., WINEBARGER, A.R., KORRECK, K., GOLUB, L., WALSH, R.W., DE PONTIEU, B., DEFOREST, C., TITLE, A., KUZIN, S., SAVAGE, S., BEABOUT, D., BEABOUT, B., PODGORSKI, W., CALDWELL, D., MCCRACKEN, K., ORDWAY, M., BERGNER, H., GATES, R., MCKILLOP, S., CHEIMETS, P., PLATT, S., MITCHELL, N. & WINDT, D. (2014). The High-Resolution Coronal Imager (Hi-C). *Solar Physics*, **289**, 4393–4412.
- KOBAYASHI, K., WINEBARGER, A.R., SAVAGE, S., CHAMPEY, P., CHEIMETS, P.N., HERTZ, E., BRUCCOLERI, A.R., SCHOLVIN, J., GOLUB, L., RAMSEY, B., RANGANATHAN, J., MARQUEZ, V., ALLURED, R., PARKER, T., HEILMANN, R.K. &

- SCHATTENBURG, M.L. (2018). The Marshall Grazing Incidence X-ray Spectrometer (MaGIXS). In *Society of Photo-Optical Instrumentation Engineers (SPIE) Conference Series*, vol. 10699, 1069927.
- KOBELSKI, A.R., SAAR, S.H., WEBER, M.A., MCKENZIE, D.E. & REEVES, K.K. (2014). Calibrating Data from the Hinode/X-Ray Telescope and Associated Uncertainties. *Solar Physics*, **289**, 2781–2802.
- KOSUGI, T., MAKISHIMA, K., MURAKAMI, T., SAKAO, T., DOTANI, T., INDA, M., KAI, K., MASUDA, S., NAKAJIMA, H., OGAWARA, Y., SAWA, M. & SHIBASAKI, K. (1991). The Hard X-ray Telescope (HXT) for the SOLAR-A Mission. *Solar Physics*, **136**, 17–36.
- KOSUGI, T., MATSUZAKI, K., SAKAO, T., SHIMIZU, T., SONE, Y., TACHIKAWA, S., HASHIMOTO, T., MINESUGI, K., OHNISHI, A., YAMADA, T., TSUNETA, S., HARA, H., ICHIMOTO, K., SUEMATSU, Y., SHIMOJO, M., WATANABE, T., SHIMADA, S., DAVIS, J.M., HILL, L.D., OWENS, J.K., TITLE, A.M., CULHANE, J.L., HARRA, L.K., DOSCHEK, G.A. & GOLUB, L. (2007). The Hinode (Solar-B) Mission: An Overview. *Solar Physics*, **243**, 3–17.
- KREPLIN, R.W. (1961). Solar X-rays. *Annales de Geophysique*, **17**, 151.
- KRUCKER, S., BENZ, A.O., BASTIAN, T.S. & ACTON, L.W. (1997). X-Ray Network Flares of the Quiet Sun. *The Astrophysical Journal*, **488**, 499–505.
- KRUCKER, S., CHRISTE, S., GLESENER, L., ISHIKAWA, S., RAMSEY, B., GUBAREV, M., SAITO, S., TAKAHASHI, T., WATANABE, S., TAJIMA, H., TANAKA, T., TURIN, P., GLASER, D., FERMIN, J. & LIN, R.P. (2013). The focusing optics x-ray solar imager (FOXSI): instrument and first flight. In *Solar Physics and Space Weather Instrumentation V*, vol. 8862 of *Proceedings of SPIE*, 88620R.
- KRUCKER, S., CHRISTE, S., GLESENER, L., ISHIKAWA, S.N., RAMSEY, B., TAKAHASHI, T., WATANABE, S., SAITO, S., GUBAREV, M., KILARU, K., TAJIMA, H., TANAKA, T., TURIN, P., MCBRIDE, S., GLASER, D., FERMIN, J., WHITE, S. & LIN, R. (2014). First Images from the Focusing Optics X-Ray Solar Imager. *The Astrophysical Journal Letters*, **793**, L32.

- KUHAR, M., KRUCKER, S., HANNAH, I.G., GLESENER, L., SAINT-HILAIRE, P., GREFENSTETTE, B.W., HUDSON, H.S., WHITE, S.M., SMITH, D.M., MARSH, A.J., WRIGHT, P.J., BOGGS, S.E., CHRISTENSEN, F.E., CRAIG, W.W., HAILLEY, C.J., HARRISON, F.A., STERN, D. & ZHANG, W.W. (2017). Evidence of Significant Energy Input in the Late Phase of a Solar Flare from NuSTAR X-Ray Observations. *The Astrophysical Journal*, **835**, 6.
- KUHAR, M., KRUCKER, S., GLESENER, L., HANNAH, I.G., GREFENSTETTE, B.W., SMITH, D.M., HUDSON, H.S. & WHITE, S.M. (2018). NuSTAR Detection of X-Ray Heating Events in the Quiet Sun. *The Astrophysical Journal Letters*, **856**, L32.
- LANDI, E., FELDMAN, U. & DERE, K.P. (2002). CHIANTI-An Atomic Database for Emission Lines. V. Comparison with an Isothermal Spectrum Observed with SUMER. *The Astrophysical Journal Supplement Series*, **139**, 281–296.
- LANDI, E., YOUNG, P.R., DERE, K.P., DEL ZANNA, G. & MASON, H.E. (2013). CHIANTI—An Atomic Database for Emission Lines. XIII. Soft X-Ray Improvements and Other Changes. *The Astrophysical Journal*, **763**, 86.
- LEMEN, J.R., TITLE, A.M., AKIN, D.J., BOERNER, P.F., CHOU, C., DRAKE, J.F., DUNCAN, D.W., EDWARDS, C.G., FRIEDLAENDER, F.M., HEYMAN, G.F., HURLBURT, N.E., KATZ, N.L., KUSHNER, G.D., LEVAY, M., LINDGREN, R.W., MATHUR, D.P., MCFEATERS, E.L., MITCHELL, S., REHSE, R.A., SCHRIJVER, C.J., SPRINGER, L.A., STERN, R.A., TARBELL, T.D., WUELSENER, J.P., WOLFSON, C.J., YANARI, C., BOOKBINDER, J.A., CHEIMETS, P.N., CALDWELL, D., DELUCA, E.E., GATES, R., GOLUB, L., PARK, S., PODGORSKI, W.A., BUSH, R.I., SCHERRER, P.H., GUMMIN, M.A., SMITH, P., AUKER, G., JERRAM, P., POOL, P., SOUFLI, R., WINDT, D.L., BEARDSLEY, S., CLAPP, M., LANG, J. & WALTHAM, N. (2012). The Atmospheric Imaging Assembly (AIA) on the Solar Dynamics Observatory (SDO). *Solar Physics*, **275**, 17–40.
- LEMEN, J.R., TARBELL, T.D., DE PONTIEU, B. & WUELSENER, J.P. (2017). MUSE, the Multi-Slit Solar Explorer. In *AGU Fall Meeting Abstracts*, vol. 2017, SH51B–2494.
- LIN, R.P., SCHWARTZ, R.A., KANE, S.R., PELLING, R.M. & HURLEY, K.C. (1984). Solar hard X-ray microflares. *The Astrophysical Journal*, **283**, 421–425.

- LIN, R.P., DENNIS, B.R., HURFORD, G.J., SMITH, D.M., ZEHNDER, A., HARVEY, P.R., CURTIS, D.W., PANKOW, D., TURIN, P., BESTER, M., CSILLAGHY, A., LEWIS, M., MADDEN, N., VAN BEEK, H.F., APPLEBY, M., RAUDORF, T., MC-TIERNAN, J., RAMATY, R., SCHMAHL, E., SCHWARTZ, R., KRUCKER, S., ABIAD, R., QUINN, T., BERG, P., HASHII, M., STERLING, R., JACKSON, R., PRATT, R., CAMPBELL, R.D., MALONE, D., LANDIS, D., BARRINGTON-LEIGH, C.P., SLASSI-SENNOU, S., CORK, C., CLARK, D., AMATO, D., ORWIG, L., BOYLE, R., BANKS, I.S., SHIREY, K., TOLBERT, A.K., ZARRO, D., SNOW, F., THOMSEN, K., HENNECK, R., MCHEDLISHVILI, A., MING, P., FIVIAN, M., JORDAN, J., WANNER, R., CRUBB, J., PREBLE, J., MATRANGA, M., BENZ, A., HUDSON, H., CANFIELD, R.C., HOLMAN, G.D., CRANNELL, C., KOSUGI, T., EMSLIE, A.G., VILMER, N., BROWN, J.C., JOHNS-KRULL, C., ASCHWANDEN, M., METCALF, T. & CONWAY, A. (2002). The Reuven Ramaty High-Energy Solar Spectroscopic Imager (RHESSI). *Solar Physics*, **210**, 3–32.
- LIONELLO, R., ALEXANDER, C.E., WINEBARGER, A.R., LINKER, J.A. & MIKIĆ, Z. (2016). Can Large Time Delays Observed in Light Curves of Coronal Loops Be Explained in Impulsive Heating? *The Astrophysical Journal*, **818**, 129.
- LÓPEZ FUENTES, M. & KLIMCHUK, J.A. (2016). A Nanoflare-based Cellular Automaton Model and the Observed Properties of the Coronal Plasma. *The Astrophysical Journal*, **828**, 86.
- MACNEICE, P., PALLAVICINI, R., MASON, H.E., SIMNETT, G.M., ANTONUCCI, E., SHINE, R.A., RUST, D.M., JORDAN, C. & DENNIS, B.R. (1985). Multiwavelength Analysis of a Well Observed Flare from Solar Maximum Mission. *Solar Physics*, **99**, 167–188.
- MADSEN, K.K., HARRISON, F.A., MAO, P.H., CHRISTENSEN, F.E., JENSEN, C.P., BREJNHOLT, N., KOGLIN, J. & PIVOVAROFF, M.J. (2009). Optimizations of Pt/SiC and W/Si multilayers for the Nuclear Spectroscopic Telescope Array. In *Optics for EUV, X-Ray, and Gamma-Ray Astronomy IV*, vol. 7437 of *Proceedings of the SPIE*, 743716.
- MADSEN, K.K., HARRISON, F.A., MARKWARDT, C.B., AN, H., GREFENSTETTE, B.W., BACHETTI, M., MIYASAKA, H., KITAGUCHI, T., BHALERAO, V., BOGGS,

- S., CHRISTENSEN, F.E., CRAIG, W.W., FORSTER, K., FUERST, F., HAILEY, C.J., PERRI, M., PUC CETTI, S., RANA, V., STERN, D., WALTON, D.J., JØRGEN WESTERGAARD, N. & ZHANG, W.W. (2015). Calibration of the NuSTAR High-energy Focusing X-ray Telescope. *The Astrophysical Journal Supplement Series*, **220**, 8.
- MADSEN, K.K., CHRISTENSEN, F.E., CRAIG, W.W., FORSTER, K.W., GREFENSTETTE, B.W., HARRISON, F.A., MIYASAKA, H. & RANA, V. (2017). Observational Artifacts of NuSTAR: Ghost Rays and Stray Light. *ArXiv e-prints*.
- MANDRINI, C.H., DÉMOULIN, P. & KLIMCHUK, J.A. (2000). Magnetic Field and Plasma Scaling Laws: Their Implications for Coronal Heating Models. *The Astrophysical Journal*, **530**, 999–1015.
- MARSCH, E. & TU, C.Y. (1994). Non-Gaussian probability distributions of solar wind fluctuations. *Annales Geophysicae*, **12**, 1127–1138.
- MARSH, A.J., SMITH, D.M., GLESENER, L., HANNAH, I.G., GREFENSTETTE, B.W., CASPI, A., KRUCKER, S., HUDSON, H.S., MADSEN, K.K., WHITE, S.M., KU HAR, M., WRIGHT, P.J., BOGGS, S.E., CHRISTENSEN, F.E., CRAIG, W.W., HAILEY, C.J., HARRISON, F.A., STERN, D. & ZHANG, W.W. (2017). First NuSTAR Limits on Quiet Sun Hard X-Ray Transient Events. *The Astrophysical Journal*, **849**, 131.
- MARSH, A.J., SMITH, D.M., GLESENER, L., KLIMCHUK, J.A., BRADSHAW, S.J., VIEVERING, J., HANNAH, I.G., CHRISTE, S., NOSUKE ISHIKAWA, S. & KRUCKER, S. (2018). Hard x-ray constraints on small-scale coronal heating events. *The Astrophysical Journal*, **864**, 5.
- MARTENS, P.C.H., KANKELBORG, C.C. & BERGER, T.E. (2000). On the Nature of the “Moss” Observed by TRACE. *The Astrophysical Journal*, **537**, 471–480.
- MASON, J.P., WOODS, T.N., CASPI, A., CHAMBERLIN, P.C., MOORE, C., JONES, A., KOHNERT, R., LI, X., PALO, S. & SOLOMON, S.C. (2016). Miniature X-Ray Solar Spectrometer: A Science-Oriented, University 3U CubeSat. *Journal of Spacecraft and Rockets*, **53**, 328–339.

- MAZZOTTA, P., MAZZITELLI, G., COLAFRANCESCO, S. & VITTORIO, N. (1998). Ionization balance for optically thin plasmas: Rate coefficients for all atoms and ions of the elements H to NI. *Astronomy & Astrophysics Supplement Series*, **133**, 403–409.
- MCINTOSH, S.W., DE PONTIEU, B., CARLSSON, M., HANSTEEN, V., BOERNER, P. & GOOSSENS, M. (2011). Alfvénic waves with sufficient energy to power the quiet solar corona and fast solar wind. *Nature*, **475**, 477–480.
- MCTIERNAN, J.M. (2009). RHESSI/GOES Observations of the Nonflaring Sun from 2002 to 2006. *The Astrophysical Journal*, **697**, 94–99.
- MENEVEAU, C. (1991). Analysis of turbulence in the orthonormal wavelet representation. *Journal of Fluid Mechanics*, **232**, 469–520.
- METROPOLIS, N., ROSENBLUTH, A.W., ROSENBLUTH, M.N., TELLER, A.H. & TELLER, E. (1953). Equation of State Calculations by Fast Computing Machines. *Journal of Chemical Physics*, **21**, 1087–1092.
- MEYER, J.P. (1985). Solar-stellar outer atmospheres and energetic particles, and galactic cosmic rays. *The Astrophysical Journal Supplement Series*, **57**, 173–204.
- MICELI, M., REALE, F., GBUREK, S., TERZO, S., BARBERA, M., COLLURA, A., SYLWESTER, J., KOWALINSKI, M., PODGORSKI, P. & GRYCIUK, M. (2012). X-ray emitting hot plasma in solar active regions observed by the SphinX spectrometer. *Astronomy & Astrophysics*, **544**, A139.
- MOORE, C. (2019). private communication.
- MOORE, C.S., CASPI, A., WOODS, T.N., CHAMBERLIN, P.C., DENNIS, B.R., JONES, A.R., MASON, J.P., SCHWARTZ, R.A. & TOLBERT, A.K. (2018). The Instruments and Capabilities of the Miniature X-Ray Solar Spectrometer (MinXSS) CubeSats. *Solar Physics*, **293**, 21.
- MOROZOV, V. (1967). *Dokladi Akademii SSSR*, **175**, 1225.
- MÜLLER, D., MARSDEN, R.G., ST. CYR, O.C. & GILBERT, H.R. (2013). Solar Orbiter . Exploring the Sun-Heliosphere Connection. *Solar Physics*, **285**, 25–70.

- MULU-MOORE, F.M., WINEBARGER, A.R. & WARREN, H.P. (2011). Can a Long Nanoflare Storm Explain the Observed Emission Measure Distributions in Active Region Cores? *The Astrophysical Journal Letters*, **742**, L6.
- NARUKAGE, N., SAKAO, T., KANO, R., HARA, H., SHIMOJO, M., BANDO, T., URAYAMA, F., DELUCA, E., GOLUB, L., WEBER, M., GRIGIS, P., CIRTAIN, J. & TSUNETTA, S. (2011). Coronal-Temperature-Diagnostic Capability of the Hinode/X-Ray Telescope Based on Self-Consistent Calibration. *Solar Physics*, **269**, 169–236.
- NARUKAGE, N., SAKAO, T., KANO, R., SHIMOJO, M., WINEBARGER, A., WEBER, M. & REEVES, K.K. (2014). Coronal-Temperature-Diagnostic Capability of the Hinode/ X-Ray Telescope Based on Self-consistent Calibration. II. Calibration with On-Orbit Data. *Solar Physics*, **289**, 1029–1042.
- O'DWYER, B., DEL ZANNA, G., MASON, H.E., STERLING, A.C., TRIPATHI, D. & YOUNG, P.R. (2011). Hinode extreme-ultraviolet imaging spectrometer observations of a limb active region. *Astronomy & Astrophysics*, **525**, A137.
- OGAWARA, Y., TAKANO, T., KATO, T., KOSUGI, T., TSUNETTA, S., WATANABE, T., KONDO, I. & UCHIDA, Y. (1991). The SOLAR-A Mission - An Overview. *Solar Physics*, **136**, 1–16.
- PARKER, E.N. (1983). Magnetic neutral sheets in evolving fields. I - General theory. *The Astrophysical Journal*, **264**, 635–647.
- PARKER, E.N. (1988). Nanoflares and the solar X-ray corona. *The Astrophysical Journal*, **330**, 474–479.
- PARNELL, C.E. (2004). The Role of Dynamic Brightenings in Coronal Heating. In R.W. Walsh, J. Ireland, D. Danesy & B. Fleck, eds., *SOHO 15 Coronal Heating*, vol. 575 of *ESA Special Publication*, 227.
- PARNELL, C.E. & DE MOORTELE, I. (2012). A Contemporary View of Coronal Heating. *Philosophical Transactions of the Royal Society A: Mathematical*, 3217–3240.
- PARNELL, C.E. & JUPP, P.E. (2000). Statistical Analysis of the Energy Distribution of Nanoflares in the Quiet Sun. *The Astrophysical Journal*, **529**, 554–569.

- PECCEI, R.D. & QUINN, H.R. (1977). CP conservation in the presence of pseudoparticles. *Physical Review Letters*, **38**, 1440–1443.
- PERES, G. (2000). Models of dynamic coronal loops. *Solar Physics*, **193**, 33–52.
- PESNELL, W.D., THOMPSON, B.J. & CHAMBERLIN, P.C. (2012). The Solar Dynamics Observatory (SDO). *Solar Physics*, **275**, 3–15.
- PETRE, R. & SERLEMITSOS, P.J. (1985). Conical imaging mirrors for high-speed x-ray telescopes. *Applied Optics*, **24**, 1833–1837.
- PHILLIPS, K.J.H. (2004). The Solar Flare 3.8-10 keV X-Ray Spectrum. *The Astrophysical Journal*, **605**, 921–930.
- PHILLIPS, K.J.H., FELDMAN, U. & LANDI, E. (2012). *Ultraviolet and X-ray Spectroscopy of the Solar Atmosphere*. Cambridge University Press.
- POTTASCH, S.R. (1963). The Lower Solar Corona: Interpretation of the Ultraviolet Spectrum. *The Astrophysical Journal*, **137**, 945.
- REALE, F., MCTIERNAN, J.M. & TESTA, P. (2009a). Comparison of Hinode/XRT and RHESSI Detection of Hot Plasma in the Non-Flaring Solar Corona. *The Astrophysical Journal*, **704**, L58–L61.
- REALE, F., TESTA, P., KLIMCHUK, J.A. & PARENTI, S. (2009b). Evidence of Widespread Hot Plasma in a Nonflaring Coronal Active Region from Hinode/X-Ray Telescope. *The Astrophysical Journal*, **698**, 756–765.
- REALE, F., GUARRASI, M., TESTA, P., DELUCA, E.E., PERES, G. & GOLUB, L. (2011). Solar Dynamics Observatory Discovers Thin High Temperature Strands in Coronal Active Regions. *The Astrophysical Journal Letters*, **736**, L16.
- REEP, J.W., BRADSHAW, S.J. & KLIMCHUK, J.A. (2013). Diagnosing the Time Dependence of Active Region Core Heating from the Emission Measure. II. Nanoflare Trains. *The Astrophysical Journal*, **764**, 193.
- REEVES, E.M., HUBER, M.C.E. & TIMOTHY, J.G. (1977a). Extreme UV spectroheliometer on the Apollo Telescope Mount. *Applied Optics*, **16**, 837–848.

- REEVES, E.M., TIMOTHY, J.G., HUBER, M.C.E. & WITHBROE, G.L. (1977b). Photometric calibration of the EUV spectroheliometer on ATM. *Applied Optics*, **16**, 849–857.
- ROSNER, R., TUCKER, W.H. & VAIANA, G.S. (1978). Dynamics of the quiescent solar corona. *The Astrophysical Journal*, **220**, 643–645.
- SAKAMOTO, Y., TSUNETA, S. & VEKSTEIN, G. (2008). Observational Appearance of Nanoflares with SXT and TRACE. *The Astrophysical Journal*, **689**, 1421–1432.
- SARKAR, A. & WALSH, R.W. (2008). Hydrodynamic Simulation of a Nanoflare-heated Multistrand Solar Atmospheric Loop. *The Astrophysical Journal*, **683**, 516–526.
- SCHMELZ, J.T. & PATHAK, S. (2012). The Cold Shoulder: Emission Measure Distributions of Active Region Cores. *The Astrophysical Journal*, **756**, 126.
- SCHMELZ, J.T. & WINEBARGER, A.R. (2015). What can observations tell us about coronal heating? *Philosophical Transactions of the Royal Society A: Mathematical, Physical and Engineering Sciences*, **373**, 20140257–20140257.
- SCHMELZ, J.T., KASHYAP, V.L., SAAR, S.H., DENNIS, B.R., GRIGIS, P.C., LIN, L., DE LUCA, E.E., HOLMAN, G.D., GOLUB, L. & WEBER, M.A. (2009a). Some Like It Hot: Coronal Heating Observations from Hinode X-ray Telescope and RHESSI. *The Astrophysical Journal*, **704**, 863–869.
- SCHMELZ, J.T., SAAR, S.H., DELUCA, E.E., GOLUB, L., KASHYAP, V.L., WEBER, M.A. & KLIMCHUK, J.A. (2009b). Hinode X-Ray Telescope Detection of Hot Emission from Quiescent Active Regions: A Nanoflare Signature? *The Astrophysical Journal Letters*, **693**, L131–L135.
- SCHMELZ, J.T., ASGARI-TARGHI, M., CHRISTIAN, G.M., DHALIWAL, R.S. & PATHAK, S. (2015). Hot Plasma from Solar Active Region Cores: a Test of AC and DC Coronal Heating Models? *The Astrophysical Journal*, **806**, 232.
- SCHWARTZ, R.A., CSILLAGHY, A., TOLBERT, A.K., HURFORD, G.J., MCTIERNAN, J. & ZARRO, D. (2002). RHESSI Data Analysis Software: Rationale and Methods. *Solar Physics*, **210**, 165–191.

- SHIMIZU, T. (1995). Energetics and Occurrence Rate of Active-Region Transient Brightenings and Implications for the Heating of the Active-Region Corona. *Publications of the Astronomical Society of Japan*, **47**, 251–263.
- SHIMIZU, T. (2009). Hinode Mission Status. In B. Lites, M. Cheung, T. Magara, J. Mariska & K. Reeves, eds., *The Second Hinode Science Meeting: Beyond Discovery-Toward Understanding*, vol. 415 of *Astronomical Society of the Pacific Conference Series*, 1.
- SMITH, D.M., LIN, R.P., TURIN, P., CURTIS, D.W., PRIMBSCH, J.H., CAMPBELL, R.D., ABIAD, R., SCHROEDER, P., CORK, C.P., HULL, E.L., LANDIS, D.A., MADDEN, N.W., MALONE, D., PEHL, R.H., RAUDORF, T., SANGSINGKEOW, P., BOYLE, R., BANKS, I.S., SHIREY, K. & SCHWARTZ, R. (2002). The RHESSI Spectrometer. *Solar Physics*, **210**, 33–60.
- SNODGRASS, H.B. (1983). Magnetic rotation of the solar photosphere. *The Astrophysical Journal*, **270**, 288–299.
- STRONG, K. (1979). *Studies of the solar corona and certain galactic X-ray sources*. Ph.D. thesis, University College London, UK.
- SU, Y., VERONIG, A.M., HANNAH, I.G., CHEUNG, M.C.M., DENNIS, B.R., HOLMAN, G.D., GAN, W. & LI, Y. (2018). Determination of Differential Emission Measure from Solar Extreme Ultraviolet Images. *The Astrophysical Journal*, **856**, L17.
- TANAKA, K. (1983). Flares on the sun - Selected results from HINOTORI. In P.B. Byrne & M. Rodono, eds., *IAU Colloq. 71: Activity in Red-Dwarf Stars*, vol. 102 of *Astrophysics and Space Science Library*, 307–319.
- TARBELL, T.D. (2017). A New Approach to Observing Coronal Dynamics: MUSE, the Multi-Slit Solar Explorer. In *AGU Fall Meeting Abstracts*, vol. 2017, SH41C–08.
- TARBELL, T.D. & DE PONTIEU, B. (2017). MUSE: the Multi-Slit Solar Explorer. In *AAS/Solar Physics Division Abstracts #48*, AAS/Solar Physics Division Meeting, 110.08.

- TERIACA, L., WARREN, H.P. & CURDT, W. (2012). Spectroscopic Observations of Fe XVIII in Solar Active Regions. *The Astrophysical Journal Letters*, **754**, L40.
- TERZO, S., REALE, F., MICELI, M., KLIMCHUK, J.A., KANO, R. & TSUNETTA, S. (2011). Widespread Nanoflare Variability Detected with Hinode/X-Ray Telescope in a Solar Active Region. *The Astrophysical Journal*, **736**, 111.
- TESTA, P. & REALE, F. (2012). Hinode/EIS Spectroscopic Validation of Very Hot Plasma Imaged with the Solar Dynamics Observatory in Non-flaring Active Region Cores. *The Astrophysical Journal Letters*, **750**, L10.
- TESTA, P., REALE, F., LANDI, E., DELUCA, E.E. & KASHYAP, V. (2011). Temperature Distribution of a Non-flaring Active Region from Simultaneous Hinode XRT and EIS Observations. *The Astrophysical Journal*, **728**, 30.
- TESTA, P., DE PONTIEU, B., MARTÍNEZ-SYKORA, J., HANSTEEN, V. & CARLSSON, M. (2012). Investigating the Reliability of Coronal Emission Measure Distribution Diagnostics using Three-dimensional Radiative Magnetohydrodynamic Simulations. *The Astrophysical Journal*, **758**, 54.
- TESTA, P., DE PONTIEU, B., ALLRED, J., CARLSSON, M., REALE, F., DAW, A., HANSTEEN, V., MARTINEZ-SYKORA, J., LIU, W., DELUCA, E.E., GOLUB, L., MCKILLOP, S., REEVES, K., SAAR, S., TIAN, H., LEMEN, J., TITLE, A., BOERNER, P., HURLBURT, N., TARBELL, T.D., WUELSER, J.P., KLEINT, L., KANKELBORG, C. & JAEGGLI, S. (2014). Evidence of nonthermal particles in coronal loops heated impulsively by nanoflares. *Science*, **346**, 1255724.
- TIKHONOV, A.N. (1963). *Soviet Math. Dokl.*, **4**, 1035.
- TORRENCE, C. & COMPO, G.P. (1998). A Practical Guide to Wavelet Analysis. *Bulletin of the American Meteorological Society*, **79**, 61–78.
- TORRENCE, C. & WEBSTER, P.J. (1999). Interdecadal Changes in the ENSO-Monsoon System. *Journal of Climate*, **12**, 2679–2690.
- TOUSEY, R. (1963). The Extreme Ultraviolet Spectrum of the Sun. *Space Science Reviews*, **2**, 3–69.

- TOUSEY, R., WATANABE, K. & PURCELL, J.D. (1951). Measurements of solar extreme ultraviolet and x-rays from rockets by means of a  $\text{CaSO}_4$ :Mn phosphor. *Physical Review*, **83**, 792–797.
- TRIPATHI, D., KLIMCHUK, J.A. & MASON, H.E. (2011). Emission Measure Distribution and Heating of Two Active Region Cores. *The Astrophysical Journal*, **740**, 111.
- TRIPATHI, D., MASON, H.E. & KLIMCHUK, J.A. (2012). Active Region Moss: Doppler Shifts from Hinode/Extreme-ultraviolet Imaging Spectrometer Observations. *The Astrophysical Journal*, **753**, 37.
- TSUNETA, S., ACTON, L., BRUNER, M., LEMEN, J., BROWN, W., CARVALHO, R., CATURA, R., FREELAND, S., JURCEVICH, B., MORRISON, M., OGAWARA, Y., HIRAYAMA, T. & OWENS, J. (1991). The Soft X-ray Telescope for the SOLAR-A Mission. *Solar Physics*, **136**, 37–67.
- UGARTE-URRA, I. & WARREN, H.P. (2012). Is Active Region Core Variability Age Dependent? *The Astrophysical Journal*, **761**, 21.
- UGARTE-URRA, I., WINEBARGER, A.R. & WARREN, H.P. (2006). An Investigation into the Variability of Heating in a Solar Active Region. *The Astrophysical Journal*, **643**, 1245–1257.
- URITSKY, V.M., DAVILA, J.M., VIAL, N.M. & OFMAN, L. (2013). Measuring Temperature-dependent Propagating Disturbances in Coronal Fan Loops Using Multiple SDO/AIA Channels and the Surfing Transform Technique. *The Astrophysical Journal*, **778**, 26.
- VAIANA, G.S. & ROSNER, R. (1978). Recent advances in coronal physics. *Annual Review of Astronomy & Astrophysics*, **16**, 393–428.
- VAIANA, G.S., REIDY, W.P., ZEHNPENNIG, T., VAN SPEYBROECK, L. & GIACCONI, R. (1968). X-ray Structures of the Sun during the Importance 1N Flare of 8 June 1968. *Science*, **161**, 564–567.
- VAIANA, G.S., DAVIS, J.M., GIACCONI, R., KRIEGER, A.S., SILK, J.K., TIMOTHY, A.F. & ZOMBECK, M. (1973a). X-Ray Observations of Characteristic Structures and

- Time Variations from the Solar Corona: Preliminary Results from SKYLAB. *The Astrophysical Journal Letters*, **185**, L47.
- VAIANA, G.S., KRIEGER, A.S. & TIMOTHY, A.F. (1973b). Identification and Analysis of Structures in the Corona from X-Ray Photography. *Solar Physics*, **32**, 81–116.
- VAN BEEK, H.F., HOYNG, P., LAFLEUR, B. & SIMNETT, G.M. (1980). The Hard X-ray Imaging Spectrometer (HXIS). *Solar Physics*, **65**, 39–52.
- VANSPEYBROECK, L.P. & CHASE, R.C. (1972). Design parameters of paraboloid-hyperboloid telescopes for x-ray astronomy. *Applied Optics*, **11**, 440–445.
- VECK, N.J., STRONG, K.T., JORDAN, C., SIMNETT, G.M., CARGILL, P.J. & PRIEST, E.R. (1984). The development and cooling of a solar limb-flare. *Monthly Notices of the Royal Astronomical Society*, **210**, 443–462.
- VERNAZZA, J.E. & REEVES, E.M. (1978). Extreme ultraviolet composite spectra of representative solar features. *The Astrophysical Journal Supplement Series*, **37**, 485–513.
- VESECKY, J.F., ANTIOCHOS, S.K. & UNDERWOOD, J.H. (1979). Numerical modeling of quasi-static coronal loops. I. Uniform energy input. *The Astrophysical Journal*, **233**, 987–997.
- VIAL, N.M. & KLIMCHUK, J.A. (2011). Patterns of Nanoflare Storm Heating Exhibited by an Active Region Observed with Solar Dynamics Observatory/Atmospheric Imaging Assembly. *The Astrophysical Journal*, **738**, 24.
- VIAL, N.M. & KLIMCHUK, J.A. (2012). Evidence for Widespread Cooling in an Active Region Observed with the SDO Atmospheric Imaging Assembly. *The Astrophysical Journal*, **753**, 35.
- VIAL, N.M. & KLIMCHUK, J.A. (2013). Modeling the Line-of-sight Integrated Emission in the Corona: Implications for Coronal Heating. *The Astrophysical Journal*, **771**, 115.
- VIAL, N.M. & KLIMCHUK, J.A. (2015). The Transition Region Response to a Coronal Nanoflare: Forward Modeling and Observations in SDO/AIA. *The Astrophysical Journal*, **799**, 58.

- VIALL, N.M. & KLIMCHUK, J.A. (2016). Signatures of Steady Heating in Time Lag Analysis of Coronal Emission. *The Astrophysical Journal*, **828**, 76.
- VIALL, N.M. & KLIMCHUK, J.A. (2017). A Survey of Nanoflare Properties in Active Regions Observed with the Solar Dynamics Observatory. *The Astrophysical Journal*, **842**, 108.
- WALTON, D.J., TOMSICK, J.A., MADSEN, K.K., GRINBERG, V., BARRET, D., BOGGS, S.E., CHRISTENSEN, F.E., CLAVEL, M., CRAIG, W.W., FABIAN, A.C., FUERST, F., HAILEY, C.J., HARRISON, F.A., MILLER, J.M., PARKER, M.L., RAHOU, F., STERN, D., TAO, L., WILMS, J. & ZHANG, W. (2016). The Soft State of Cygnus X-1 Observed with NuSTAR: A Variable Corona and a Stable Inner Disk. *The Astrophysical Journal*, **826**, 87.
- WARREN, H.P., WINEBARGER, A.R. & HAMILTON, P.S. (2002). Hydrodynamic Modeling of Active Region Loops. *The Astrophysical Journal*, **579**, L41–L44.
- WARREN, H.P., BROOKS, D.H. & WINEBARGER, A.R. (2011). Constraints on the Heating of High-temperature Active Region Loops: Observations from Hinode and the Solar Dynamics Observatory. *The Astrophysical Journal*, **734**, 90.
- WARREN, H.P., WINEBARGER, A.R. & BROOKS, D.H. (2012). A Systematic Survey of High-temperature Emission in Solar Active Regions. *The Astrophysical Journal*, **759**, 141.
- WEBER, M.A., DELUCA, E.E., GOLUB, L. & SETTE, A.L. (2004). Temperature diagnostics with multichannel imaging telescopes. In A.V. Stepanov, E.E. Benevolenskaya & A.G. Kosovichev, eds., *Multi-Wavelength Investigations of Solar Activity*, vol. 223 of *IAU Symposium*, 321–328.
- WIK, D.R., HORNSTRUP, A., MOLENDI, S., MADEJSKI, G., HARRISON, F.A., ZOGLAUER, A., GREFENSTETTE, B.W., GASTALDELLO, F., MADSEN, K.K., WESTERGAARD, N.J., FERREIRA, D.D.M., KITAGUCHI, T., PEDERSEN, K., BOGGS, S.E., CHRISTENSEN, F.E., CRAIG, W.W., HAILEY, C.J., STERN, D. & ZHANG, W.W. (2014). NuSTAR Observations of the Bullet Cluster: Constraints on Inverse Compton Emission. *The Astrophysical Journal*, **792**, 48.

- WINEBARGER, A., TRIPATHI, D., MASON, H.E. & DEL ZANNA, G. (2013). Doppler Shifts in Active Region Moss Using SOHO/SUMER. *The Astrophysical Journal*, **767**, 107.
- WINEBARGER, A.R., SCHMELZ, J.T., WARREN, H.P., SAAR, S.H. & KASHYAP, V.L. (2011). Using a Differential Emission Measure and Density Measurements in an Active Region Core to Test a Steady Heating Model. *The Astrophysical Journal*, **740**, 2.
- WINEBARGER, A.R., WARREN, H.P., SCHMELZ, J.T., CERTAIN, J., MULU-MOORE, F., GOLUB, L. & KOBAYASHI, K. (2012). Defining the “Blind Spot” of Hinode EIS and XRT Temperature Measurements. *The Astrophysical Journal*, **746**, L17.
- WITHBROE, G.L. (1975). The analysis of XUV emission lines. *Solar Physics*, **45**, 301–317.
- WITHBROE, G.L. & NOYES, R.W. (1977). Mass and energy flow in the solar chromosphere and corona. *Annual Review of Astronomy & Astrophysics*, **15**, 363–387.
- WOLTER, H. (1952). Spiegelsysteme streifenden Einfalls als abbildende Optiken für Röntgenstrahlen. *Annalen der Physik*, **445**, 94–114.
- WRIGHT, P.J. (2017). Colourblind: A Collection Of Colour Blind Friendly Colour Tables.
- WRIGHT, P.J., HANNAH, I.G., GREFENSTETTE, B.W., GLESENER, L., KRUCKER, S., HUDSON, H.S., SMITH, D.M., MARSH, A.J., WHITE, S.M. & KUCHAR, M. (2017). Microflare Heating of a Solar Active Region Observed with NuSTAR, Hinode/XRT, and SDO/AIA. *The Astrophysical Journal*, **844**, 132.
- WRIGHT, P.J., CHEUNG, M.C.M., THOMAS, R., GALVEZ, R., SZENICER, A., JIN, M., MUÑOZ-JARAMILLO, A. & FOUHEY, D. (2018). DeepEM: A Deep Learning Approach for DEM Inversion. In M. Bobra & J. Mason, eds., *Machine Learning, Statistics, and Data Mining for Heliophysics*, chap. 4.
- WRIGHT, P.J., CHEUNG, M.C.M., THOMAS, R., GALVEZ, R., SZENICER, A., JIN, M., MUÑOZ-JARAMILLO, A. & FOUHEY, D. (2019). DeepEM: A Deep Learning Approach to DEM Inversion. *The Astrophysical Journal Letters*, **in prep**.

- 
- YOSHIMORI, M., OKUDAIRA, K., HIRASIMA, Y., IGARASHI, T., AKASAKA, M., TAKAI, Y., MORIMOTO, K., WATANABE, T., OHKI, K., NISHIMURA, J., YAMAGAMI, T., OGAWARA, Y. & KONDO, I. (1991). The Wide Band Spectrometer on the SOLAR-A. *Solar Physics*, **136**, 69–88.